

**NONLINEAR FINITE ELEMENT ANALYSIS OF
FLEXURE-DOMINANT REINFORCED CONCRETE STRUCTURES**

by

Ali Kheyroddin

March 1996



Department of Civil Engineering and Applied Mechanics
McGill University
Montreal, Canada

A thesis submitted to
the Faculty of Graduate Studies and Research
in partial fulfilment of the requirements for the degree of
Doctor of Philosophy

© Ali Kheyroddin, 1996

IN THE NAME OF GOD

To

My Parents, My Wife

and

My Children: Farzaneh and Mehdi

ABSTRACT

This thesis demonstrates the capabilities of the nonlinear finite element method as a tool for predicting the flexural response of reinforced concrete (R C) structures. The layered finite element program, NONLACS2, developed in the present study, includes the different modelling options including the proposed model for eliminating mesh size dependency, the compressive stress-strain curves of normal and high-strength concrete, new models for concrete in tension and tension-stiffening, and the concrete ultimate compressive and tensile strains.

The effects of finite element size, tension and compression reinforcement ratios and strengths, loading types and stages, tensile and compressive strengths of the concrete, cracking and tension-stiffening on the flexural response of different structural elements (i.e., simple and continuous beams, shear panels and frames) are investigated. The effect of these parameters on the different behavioral aspects such as the load-displacement, moment-curvature and load-strain characteristics, the flexural rigidity, cracking pattern, cracking, yielding and the ultimate load, mode of failure, plastic hinge rotations, equivalent plastic hinge length, yielding length and ductility are discussed along with a comparison with the experimental data where available.

The various analyses indicate that the value of the concrete ultimate tensile strain, ϵ_u , has a significant effect on the computed results and if the value of ϵ_u is adjusted appropriately according to the element size, it can help eliminate the mesh sensitivity drawback. To adjust an appropriate value for ϵ_u , two models have been used: a) crack band model and b) a new proposed model as a function of the element size. The analytical results obtained using the different models are compared with the experimental results; the proposed model gives good agreement. In particular, the new model can be used effectively with relatively large element sizes with reasonable accuracy.

Based on the analytical results, new equations are proposed to calculate the analytical cracking moment, cracking flexural rigidity, tangent flexural rigidity, and the deflection of R C beams. In addition, new simple equations are proposed to consider the effect of tension reinforcement index, ω , and the loading type in the calculation of plastic hinge rotations.

The proposed flexural rigidity equations are utilized to develop a nonlinear finite element program, NAFS, based on the modified stiffness approach. The NAFS program provides a more efficient, speedy, and economical method, for a complete analysis of large frame structures.

The NONLACS2 and NAFS programs and the proposed methods can be used for nonlinear analysis of R C structures with sufficient accuracy. Finally, this research study indicates the usefulness of the nonlinear finite element analysis as a powerful tool to study the behaviour of different types of structural elements subjected to loads increasing monotonically until failure.

SOMMAIRE

Cette thèse démontre l'efficacité d'un nouveau modèle d'éléments finis non-linéaires pour la prédiction du comportement en flexion des structures en béton armé. Le modèle d'éléments finis NONLACS2 idéalise les composantes par le biais de couches multiples pour le béton et l'armature. Le modèle inclue une procédure pour éliminer la dépendance sur le degré de la discrétisation, des courbes contraintes-déformations pour le béton normal et le béton hautes performances en compression, de nouveaux modèles pour le béton en tension et l'augmentation de la résistance en tension, et pour les déformations ultimes en tension et en compression du béton.

L'effet du degré de discrétisation, du ratio entre l'acier en tension et en compression, des résistances, du type et de l'historique du chargement, de la résistance du béton en compression et en tension, de la fissuration et du raidissement en tension sur le comportement en flexion de différentes composantes structurales (poutres simples et continues, murs de cisaillement et cadres) sont analysés. Les effets de ces paramètres sur différents aspects de la réponse des éléments (courbes forces-déformations, moment-courbure, contraintes-déformations, la rigidité en flexion, le patron de fissuration, la limite d'écoulement, la charge ultime, le mode de rupture, les rotations aux rotules plastiques, la longueur équivalente des rotules plastiques, et la ductilité) sont examinés et comparés à des résultats expérimentaux lorsque disponibles.

Les analyses indiquent que la déformation ultime du béton en tension $\epsilon_{u,c}$ a un effet significatif sur les résultats et peut être utilisée pour contrôler l'effet du degré de discrétisation sur les résultats. Deux procédures ont été utilisées afin d'estimer la valeur de $\epsilon_{u,c}$: a) le modèle de fissuration en bande et b) un nouveau modèle en fonction du degré de discrétisation. Les résultats obtenus par les deux modèles sont en accord avec les résultats expérimentaux disponibles. En particulier, les modèles proposés peuvent être utilisés avec une discrétisation large sans perte appréciable de précision.

Sur la base de ces résultats, de nouvelles équations sont proposées pour le calcul du moment de fissuration, de la rigidité en flexion fissuré, du module tangent en flexion, et la déflexion des poutres en béton armé. De plus, des équations simplifiées sont proposées pour l'effet de l'index ω pour l'acier en tension, et pour le type de chargement pour le calcul des rotations des rotules plastiques.

Les équations proposées pour la rigidité en flexion sont utilisées pour développer un programme non-linéaire d'éléments finis, NAFS, basé sur l'approche de la rigidité modifiée. Le logiciel NAFS est plus efficace, rapide et économique pour l'analyse complète d'une structure.

Les logiciels NONLACS et NAFS peuvent être utilisés pour l'analyse des structures en béton armé avec une précision acceptable. Finalement, cette recherche illustre l'utilité des éléments finis non-linéaires pour l'analyse de différents types d'éléments structuraux soumis à des charges monotoniques jusqu'à la rupture.

ACKNOWLEDGEMENTS

I am thankful to God the Almighty, from whom I always receive help and protection.

I would like to express my deepest gratitude to my supervisor, Prof. M.S. Mirza, for his valuable supervision, encouragement, assistance and guidance during all stages of this research program. He was always available, during the week or over holidays, as if I was the only student being supervised by him. He surprised me several times by returning the marked drafts of my chapters with significant constructive criticism within a day or two of my handing the draft to him. For the countless and productive hours involved in technical discussion, review and related research activities, and his dedicated and extremely helpful supervision of my research program and his kind disposition towards me and my family, I shall always remember him with utmost gratefulness and warmest sincerely.

The author would like to thank Dr. A. G. Razaqpur of the Department of Civil Engineering, Carleton University, Ottawa, for making available the computer program NONLACS.

Special thanks are due to the consultants and operations staff of the McGill University Computer Center, especially Dr. H. Young, for their assistance and generous allocation of the required computer funds.

The excellent French translation of the abstract by Prof. L.E. Chouinard is very much appreciated. The author also would like to thank Prof. L.E. Chouinard for his assistance in the numerical analysis part of Chapter 5 of this thesis.

The author wishes to extend his sincere thanks to Dr. M.A. Shayanfar for his useful comments, suggestions and help in the development of the computer program NONLACS2 and the related mainframe operations. The assistance and guidance provided by Dr. M.A. Shayanfar at the early stage of this work and his collaboration in investigating the element size effect phenomenon are also gratefully acknowledged. The assistance of Mr. H. Ahmad in the analysis of portal frame, FP4, is gratefully appreciated.

The author is very grateful to the Ministry of Culture and Higher Education of the Islamic Republic of Iran for the continuing financial support.

Finally, this undertaking could never have been achieved without the patience, understanding, and encouragement of my parents, wife and children: Farzaneh and Mehdi.

TABLE OF CONTENTS

ABSTRACT	i
SOMMAIRE	ii
ACKNOWLEDGEMENTS	iii
LIST OF FIGURES	xi
LIST OF TABLES	xviii
LIST OF SYMBOLS	xx

CHAPTER 1

INTRODUCTION	1
1.1 GENERAL	1
1.2 OBJECTIVES	5
1.3 THESIS ORGANIZATION	6

CHAPTER 2

REVIEW OF DEFLECTION, FLEXURAL RIGIDITY AND ULTIMATE DEFORMATION OF REINFORCED CONCRETE BEAMS	10
2.1 REVIEW OF DEFLECTION CALCULATION PROCEDURES	10
2.1.1 Use of Cracked Transformed Section Ignoring Tension-Stiffening ..	12
2.1.2 Yu and Winter's Method	14
2.1.3 European Concrete Committee (CEB) Procedure	15
2.1.4 Granholm General Flexural Theory	16
2.1.5 Branson's Empirical Equation	17
2.1.6 Beeby's Method	19
2.1.7 Recent Investigations	19

2.1.8 Deflection of High-Strength Concrete Beams	21
2.1.9 Discussion and Basis for Further Studies	22
2.2 ULTIMATE DEFORMATION CHARACTERISTICS	23
2.2.1 Brief Review of Limit Design Methods	23
2.2.2 Plastic Hinge Length and Rotation	24
2.2.3 Governing Parameters for the Rotation Capacity of Plastic Hinges . .	26
2.2.4 Definitions of the Yielding and Ultimate Limit States	27
2.2.5 Ultimate Compressive Strain of Concrete	28
2.2.6 Empirical Expressions for Plastic Hinge Length and Rotations	30
2.2.7 Ductility	37
2.2.8 Ultimate Deformation of High-Strength Concrete Beams	38
2.2.9 Discussion and Basis for Further Studies	39

CHAPTER 3

NONLINEAR LAYERED FINITE ELEMENT PROGRAM	44
3.1 DESCRIPTION AND CLASSIFICATION OF NONLINEAR ANALYSIS METHODS	44
3.1.1 Lumped-Plasticity Approach	45
3.1.2 "Microscopic" Finite Element Approach	45
3.1.3 "Macroscopic" Finite Element Approach	46
3.2 FINITE ELEMENT PROGRAMS DEVELOPED IN THE PRESENT STUDY	47
3.3 GENERAL DESCRIPTION OF NONLACS2 PROGRAM	47
3.4 MATERIAL MODELLING	49
3.4.1 Constitutive Relationship for Concrete	49
3.4.2 Compressive Stress-Strain Curves for Concrete	54
3.4.2.1 Saenz and Smith's equation	55
3.4.2.2 Popovics' equation	56
3.4.3 Crushing of Concrete	58

3.4.4	Crack Modelling Techniques	59
3.4.5	Proposed Models for Concrete in Tension	61
3.4.6	Failure Criteria for Concrete	64
3.4.7	Constitutive Relationship for Steel Reinforcement	65
3.5	THE NONLINEAR LAYERED FINITE ELEMENT FORMULATION	66
3.5.1	Displacement Based Formulation in Finite Element	66
3.5.2	Element Library	69
3.5.3	Layered Discretization	70
3.5.4	Nonlinear Analysis Method	71
3.5.5	Unbalanced Forces	71
3.5.6	Convergence Criteria	71
3.5.7	Divergence Criteria	72
3.6	IMPLEMENTATION OF PROPOSED MODELS IN THE COMPUTER PROGRAM	72

CHAPTER 4

	FINITE ELEMENT SIZE EFFECT PHENOMENON	80
4.1	PARAMETERS INFLUENCING THE COMPUTED RESULTS	81
4.2	EFFECT OF FINITE ELEMENT SIZE ON COMPUTED RESPONSES	82
4.2.1	Example 1: Reinforced Concrete Beams	82
4.2.2	Example 2: Reinforced Concrete Shear Panel W-2	85
4.3	PHYSICAL DESCRIPTION OF MESH SIZE DEPENDENCY	86
4.4	ANALYTICAL SOLUTIONS FOR ELEMENT SIZE DEPENDENCY	87
4.4.1	The Proposed Model	87
4.4.2	Crack Band Model	90
4.5	IMPLEMENTATION OF THE MODELS INTO THE NONLACS2 PROGRAM	92
4.5.1	General Modifications	92
4.5.2	The Proposed Model	93
4.5.3	Crack Band Model	93

4.6	COMPARISON OF COMPUTED AND EXPERIMENTAL RESULTS	95
4.6.1	Beam T2LA	95
4.6.2	Shear Panel W-2	96
4.6.3	Beams T4LA, T1HB, C2W, C3YNA, and C3YNB	97
4.6.4	Crack Patterns	99

CHAPTER 5

	PARAMETRIC STUDY OF FLEXURAL BEHAVIOUR OF REINFORCED CONCRETE BEAMS	116
5.1	PROPOSED MODELS FOR CALCULATION OF FLEXURAL RIGIDITY, EI	116
5.1.1	Reinforced Concrete Beams Tested by Gaston	118
5.1.2	Reinforced Concrete Beam Tested by Mattock	120
5.1.3	Parametric Study	122
5.1.4	Pre-cracking Stage ($M_a \leq M_{cr,anl}$)	122
5.1.4.1	Effect of influencing parameters on the I_{ucr}/I_g , $M_{cr,anl}$ and (EI) _{cr}	122
5.1.4.2	Proposed model for analytical cracking moment, $M_{cr,anl}$	126
5.1.4.3	Proposed model for cracking flexural rigidity, (EI) _{cr}	127
5.1.5	Post-cracking Stage ($M_{cr} < M_a < M_y$)	128
5.1.5.1	Effect of tension reinforcement ratio on EI	128
5.1.5.2	Influence of compression reinforcement ratio on EI	129
5.1.5.3	Effect of concrete compressive strength on EI	130
5.1.5.4	Effect of yield strength of steel on EI	131
5.1.5.5	Influence of tension-stiffening	131
5.1.5.6	Effect of loading type on EI	132
5.1.5.7	Proposed equations for post-cracking stage ($M_{cr} \leq M_a \leq M_y$)	133
5.1.6	Post-Yielding Stage ($M_y \leq M_a \leq M_u$)	136
5.1.7	Comparison of Results	137
5.1.8	Predicting Short-Term Deflections	138

CHAPTER 6

ANALYTICAL INVESTIGATION OF PLASTIC HINGE ROTATION

CAPACITY	157
6.1 FINITE ELEMENT MODELLING, BEAM C5	157
6.2 INFLUENCE OF TENSION REINFORCEMENT INDEX, ω	158
6.2.1 Yielding Curvature	159
6.2.2 Ultimate Curvature and Curvature Ductility Ratio	160
6.2.3 Plastic Hinge Rotation and Length	163
6.3 INFLUENCE OF BENDING MOMENT DISTRIBUTION (LOADING TYPE)	165
6.3.1 Proposed Equations	168

CHAPTER 7

NONLINEAR ANALYSIS OF HIGH-STRENGTH

CONCRETE BEAMS	180
7.1 DESCRIPTION OF THE BEAMS ANALYZED	181
7.2 FINITE ELEMENT IDEALIZATION	182
7.3 INFLUENCE OF CONCRETE TENSILE STRENGTH	182
7.3.1 Computed Response of Beam HUCB	184
7.3.2 Computed Response of Beams Tested by Leslie et al.	186
7.3.3 Recommended Value of f_t for Finite Element Analysis	187
7.4 TENSION-STIFFENING MODEL WITH DISCONTINUOUS SOFTENING ..	188
7.4.1 Response of High-Strength Concrete Beam HUCB	188
7.4.2 Response of High-Strength Concrete Beam LS1	190
7.5 COMPARISON OF NORMAL AND HIGH-STRENGTH CONCRETE BEAMS	191

CHAPTER 8

FINITE ELEMENT ANALYSIS OF REINFORCED

CONCRETE FRAMES	200
8.1 PREVIOUS STUDIES	200
8.2 CCA SPECIMENS	202
8.3 EFFECT OF FINITE ELEMENT SIZE	203
8.4 EFFECT OF CONCRETE ULTIMATE TENSILE STRAIN	205
8.5 RESPONSE OF REINFORCED CONCRETE FRAME FP4	206
8.5.1 Load-Deflection Curve	206
8.5.2 Load -Strain Curves for Concrete and Steel	207
8.5.3 Cracking Pattern and Formation Sequence of Plastic Hinges	208
8.5.4 Available Plastic Hinge Rotations	209

CHAPTER 9

NAFS- A FINITE ELEMENT PROGRAM FOR NONLINEAR

ANALYSIS OF FRAMED STRUCTURES	220
9.1 MODIFIED STIFFNESS APPROACH	220
9.2 VARIATION OF FLEXURAL RIGIDITY ALONG BEAM LENGTH	221
9.3 MODIFIED STIFFNESS MATRIX FOR BEAM ELEMENT WITH BOTH ENDS- FIXED	222
9.3.1 Hinge at Left End	223
9.3.2 Hinge at Right End	224
9.4 COMPUTER PROGRAMMING AND SOLUTION PROCEDURE	224
9.4.1 Solution Procedure	225
9.4.2 Plastic Hinge Rotation	226
9.5 APPLICATION OF NAFS PROGRAM	227

9.5.1 Analysis of Two-Span Continuous Beams	227
9.5.2 Analysis of Fixed-Base Portal Frames	229

CHAPTER 10

SUMMARY AND CONCLUSIONS	241
--------------------------------------	------------

10.1 SUMMARY	241
10.2 CONCLUSIONS	242
10.2.1 Finite Element Size Effect	243
10.2.2 Flexural Rigidity and Deflection of Reinforced Concrete Beams ..	244
10.2.3 Rotation Capacity of Plastic Hinges	245
10.2.4 High-Strength Concrete Beams	247
10.2.5 Nonlinear Analysis of Frame Structures	248
10.2.6 Modified Stiffness Approach (NAFS Program)	249
10.3 RECOMMENDATIONS FOR FUTURE RESEARCH	251

STATEMENT OF ORIGINALITY	252
---------------------------------------	------------

REFERENCES	253
-------------------------	------------

APPENDIX A

INPUT DATA FILE FOR THE NONLACS2 PROGRAM	268
---	------------

APPENDIX B

INPUT DATA FILE FOR THE NAFS PROGRAM	285
---	------------

LIST OF FIGURES

Figure 2.1:	Stress distribution and cracking in different regions of a reinforced concrete beam	40
Figure 2.2:	CEB bilinear moment-deflection curve	40
Figure 2.3:	Typical moment-deflection curve for a reinforced concrete flexural member	41
Figure 2.4:	Qualitative moment-curvature relationship	41
Figure 2.5:	Schematic curvature distribution along beam at ultimate stage: (a) beam, (b) bending moment diagram, (c) curvature diagram	42
Figure 2.6:	Existing moment-curvature constitutive laws	42
Figure 2.7:	Inelastic rotations versus relative depth of neutral axis at ultimate load adopted by CEB MC 78 (Siviero 1974)	43
Figure 3.1:	Nonlinear analysis methods: (a) lumped-plasticity approach (Riva 1988), (b) discrete model (Ngo and Scordelis 1967), (c) layered finite element, and (d) modified stiffness approach	74
Figure 3.2:	Analytical uniaxial stress-strain curve for plain concrete: (a) Saenz and Smith equation, (b) modified Popovics equation (Collins and Porasz 1989)	74
Figure 3.3:	Classification of cracking models	75
Figure 3.4:	Idealization of Cracks: (a) nodal separation using two or four coincident nodes, (b) smeared crack (ASCE 1982)	75
Figure 3.5:	Different proposed models for concrete in tension: (a) linear softening, (b) proposed model, (c) discontinuous softening, and (d) small stress when $\epsilon_t > \epsilon_{tm}$	76
Figure 3.6:	Typical biaxial failure envelope for concrete (Kupfer and Gerstle 1973) . .	76
Figure 3.7:	Typical steel representations in finite element models of concrete structures, (a) smeared, (b) embedded, and (c) discrete (ASCE 1982) . . .	77
Figure 3.8:	Idealized steel stress-strain curves: (a) elastic-perfectly plastic, (b) elastic-strain hardening, (c) elastic-plastic strain-hardening	77
Figure 3.9:	Some typical finite elements in the NONLACS2 program	78

Figure 3.10:	A schematic representation of the incremental-iterative tangent stiffness method	78
Figure 3.11:	Flow chart of the NONLACS2 program	79
Figure 4.1:	Effect of element size on post-peak softening	100
Figure 4.2:	Geometry and reinforcement details of Gaston's beams (After Gaston et al. 1952)	100
Figure 4.3:	Mesh configurations for beams T2LA and T5L	101
Figure 4.4:	Load-deflection curve at mid-span for beam T2LA ($\epsilon_u = 0.0007$)	102
Figure 4.5:	Effect of element size on computed ultimate load for beam T2LA ($\epsilon_u=0.0007$)	103
Figure 4.6:	Load-concrete strain at mid-span top for beam T2LA ($\epsilon_u = 0.0007$)	103
Figure 4.7:	Details of reinforcement and geometry for shear panel W-2 (After Cervenka, 1970)	104
Figure 4.8:	Mesh configurations for shear panel W-2	105
Figure 4.9:	Load-deflection curve for shear panel W-2 ($\epsilon_u = 0.002$)	105
Figure 4.10:	Effect of mesh size on crack pattern of shear panel W-2 (P=24,000 lb, $\epsilon_u=0.002$)	106
Figure 4.11:	Qualitative influence of element size on the response of a tension member	107
Figure 4.12:	Ultimate tensile strain of concrete, ϵ_u , versus width of element, h	107
Figure 4.13:	A flow chart for the changes on subroutines: TENSION and CYCMAT	108
Figure 4.14:	Load-deflection curves for beam T2LA idealized using 4 elements	109
Figure 4.15:	Load-deflection curves for beam T2LA idealized using 320 elements	109
Figure 4.16:	Comparison of ultimate loads computed using different models for beam T2LA	110
Figure 4.17:	Load-deflection curves for shear panel W-2 using 35 elements	110
Figure 4.18:	Load-deflection curves for shear panel W-2 using 120 elements	111
Figure 4.19:	Load-deflection curve for beam T4LA idealized using 80 elements	111
Figure 4.20:	Load-deflection curve for beam T1HB idealized using 80 elements	112
Figure 4.21:	Load-deflection curve for beam C2W idealized using 80 elements	112
Figure 4.22:	Load-deflection curve for beam C3YNA idealized using 80 elements	113
Figure 4.23:	Load-deflection curve for beam C3YNB idealized using 80 elements	113

Figure 4.24:	Comparison of analytical cracking patterns for beam T2LA at load $P=0.9 P_{u,exp}=14000$ lb.	114
Figure 4.24:	Comparison of analytical and experimental cracking patterns for shear panel at load $P=0.96 P_{u,exp}=25,500$ lb.	115
Figure 5.1:	Schematic variation of flexural rigidity versus moment, M	142
Figure 5.2:	Comparison of analytical and experimental load-deflection response of beam T2LA	142
Figure 5.3:	Variation of flexural rigidity versus M_g/M_{cr} ratio for beam T2LA	143
Figure 5.4:	Geometry, reinforcement details and mesh configuration for beam C5 . . .	144
Figure 5.5:	Comparison of analytical and experimental load-deflection response of beam C5	145
Figure 5.6:	Variation of flexural rigidity versus $M_g/M_{cr,anl}$ ratio for beam C5	145
Figure 5.7:	Effect of compression reinforcement and compressive strength of concrete on analytical cracking moment, $M_{cr,anl}$	146
Figure 5.8:	Effect of compression reinforcement and compressive strength of concrete on cracking flexural rigidity, $(EI)_{cr}$	146
Figure 5.9:	Effect of tension reinforcement on flexural rigidity of Gaston beams . . .	147
Figure 5.10:	Theoretical variation of the flexural rigidity ratio with the level of loading (Mattock beams, Group No. 1)	147
Figure 5.11:	Variation of the cracked length ratio with level of loading (Group No.1)	148
Figure 5.12:	Effect of compression reinforcement on flexural rigidity of Gaston beams	148
Figure 5.13:	Effect of compression reinforcement on flexural rigidity of over-reinforced beams	149
Figure 5.14:	Effect of compression reinforcement on flexural rigidity of under-reinforced beams	149
Figure 5.15:	Effect of compression reinforcement ratio on the flexural rigidity ratio (Mattock beams, concentrated loads)	150
Figure 5.16:	Effect of concrete compressive strength on flexural rigidity of over-reinforced beams	150

Figure 5.17:	Effect of concrete compressive strength on flexural rigidity of under-reinforced beams	151
Figure 5.18:	Effect of tension stiffening on flexural rigidity of beam C5	151
Figure 5.19:	Effect of loading type on post-cracking flexural rigidity of beam C3YNA	152
Figure 5.20:	Variation of the cracked length ratio with the type of loading, beam C3YNA	152
Figure 5.21:	Effect of different loading types on flexural rigidity of under-reinforced beams	153
Figure 5.22:	Effect of different loading types on flexural rigidity of over-reinforced beams	153
Figure 5.23:	Effect of different parameters on the value of "n" for proposed equation	154
Figure 5.24:	Effect of tension reinforcement ratio on the value of " α " for proposed equation	154
Figure 5.25:	Effect of reinforcement ratios and compressive strength of concrete on ultimate moment for Mattock beams	155
Figure 5.26:	Comparison of experimental, analytical, and proposed flexural rigidity for beam T2LA	155
Figure 5.27:	Comparison of experimental, analytical, and proposed flexural rigidity for beam C5	156
Figure 5.28:	Comparison of experimental and computed (proposed model) short-term deflections	156
Figure 6.1:	172-element mesh configuration for beam C5	170
Figure 6.2:	Comparison of experimental and analytical results for beam C5: (a) load-deflection curve, (b) moment-curvature curve	170
Figure 6.3:	Load-deflection curves at mid-span for beams with different reinforcement index (Group No. 1)	171
Figure 6.4:	Variation of yielding curvature with tension reinforcement index, ω	171
Figure 6.5:	Effect of ω on ultimate concrete and reinforcing steel strains (Group No. 1)	172

Figure 6.6:	Variation of ultimate curvature with respect to tension reinforcement index, ω (Group No. 1)	172
Figure 6.7:	Effect of tension reinforcement index, ω , on the ductility factor (Group No. 1)	173
Figure 6.8:	Calculation of plastic rotation for beam M13F ($\omega=0.206$) at ultimate stage: (a) crack pattern and crushing of concrete, (b) plastic hinge rotation	174
Figure 6.9:	Variation of curvature along the length of beam for two different values of ω	175
Figure 6.10:	Comparison of existing plastic hinge rotation formulations for simply supported beams subjected to concentrated load at midspan ($z/d=5.5$)	175
Figure 6.11:	Comparison of existing plastic hinge length equations (Group No. 1, $z/d=5.5$)	176
Figure 6.12:	Influence of different loading types on the plastic rotation	176
Figure 6.13:	Variation of yielding length with respect to tension reinforcement index	177
Figure 6.14:	Effect of loading type on the plastic rotation of beam with $\omega=0.412$	177
Figure 6.15:	Effect of loading type on the failure mechanism of beams with $\omega=0.412$	178
Figure 6.16:	Influence of different loading types on the equivalent plastic hinge length	179
Figure 6.17:	Analytical and estimated values of plastic rotations	179
Figure 7.1:	Geometry and reinforcement details of beams tested by Abrishami et al. (1995)	192
Figure 7.2:	Geometry and reinforcement details of beams tested by Leslie et al.	192
Figure 7.3:	Effect of concrete tensile strength on the load-deflection response of beam HUCB	193
Figure 7.4:	Crack patterns for beam HUCB at load $P=30$ kN using different values of f_t	193
Figure 7.5:	Effect of concrete tensile strength on load-deflection response of beam LS1	194
Figure 7.6:	Crack patterns for beam LS1 at failure using different values of f_t	194
Figure 7.7:	Effect of concrete tensile strength on the load-deflection response of the LS2	195
Figure 7.8:	Effect of tensile softening branch factor, α_2 , on the response of beam HUCB	195

Figure 7.9:	Load-concrete compressive strain curve at the top of beam HUCB at midspan	196
Figure 7.10:	Load-steel tensile strain curve at the bottom of beam HUCB at midspan .	196
Figure 7.11:	Crack patterns for beam HUCB at initial cracking using different values of α_2	197
Figure 7.12:	Effect of tensile softening branch factor, α_2 , on response of beam LS1 .	198
Figure 7.13:	Crack patterns for beam LS1 at load level of P=180 kN using different values of α_2	198
Figure 7.14:	Comparison of normal and high-strength concrete beams, UCB and HUCB	199
Figure 8.1:	Geometry of frames FP4, FP3, and FP2 tested by Cranston and Cracknell	211
Figure 8.2:	Reinforcement details for frame FP4	211
Figure 8.3:	Reinforcement details for frame FP3	212
Figure 8.4:	Reinforcement details for frame FP2	212
Figure 8.5:	Mesh configurations for frame FP4	213
Figure 8.6:	Load-deflection curves for different mesh sizes for frame FP4 ($\epsilon_u = 0.0021$).	214
Figure 8.7:	Load-deflection curve for frame FP4 idealization 89-elements with different values of the concrete ultimate tensile strain, ϵ_u	214
Figure 8.8:	Effect of tension-stiffening on the response of the frame FP4 (212-element model)	215
Figure 8.9:	Load-steel and concrete strain curves at the mid-span of the beam in the frame FP4	215
Figure 8.10:	Initial crack pattern at load level of 6.67 kN	216
Figure 8.11:	First hinge formation at the right hand corner of the frame at load level of 39.4 kN	216
Figure 8.12:	Development of the second hinge at the right foot at load level of 41.15 kN	217
Figure 8.13:	Development of the third hinge before the collapse at load level of 42.25 kN	217
Figure 8.14:	Last hinge formed at ultimate load of 43.6 kN	218
Figure 8.15:	Deformed shape of frame FP4 at the failure ($P_u=43.6$ kN)	218

Figure 8.16:	Distribution the yield and ultimate curvatures at the critical sections of frame FP4	219
Figure 8.17:	Experimental and analytical location of plastic hinges for frame FP4	219
Figure 9.1:	Variation of flexural rigidity over half of beam M11 subjected to concentrated loads	233
Figure 9.2:	Variation of flexural rigidity over half of beam M81 subjected to uniform loads	233
Figure 9.3:	Linear variation of flexural rigidity over the length of element	234
Figure 9.4:	Numbering of member end forces and end displacements in local axes. . .	234
Figure 9.5:	Flow chart for the NAFS program	235
Figure 9.6:	Analysis of continuous beams (a) geometry and loading, (b) finite element model using NAFS program, and (c) finite element model using NONLACS2 program	236
Figure 9.7:	Comparison of analytical and experimental load-deflection curves for beam C1	236
Figure 9.8:	Comparison of analytical and experimental load-deflection curves for beam C3	237
Figure 9.9:	Location and sequence of the plastic hinges for continuous beams	237
Figure 9.10:	Finite element mesh for analysis of portal frames using NAFS program . .	238
Figure 9.11:	Comparison of analytical and experimental load-deflection curves for frame FP4	238
Figure 9.12:	Comparison of analytical and experimental load-deflection curves for frame FP3	239
Figure 9.13:	Comparison of analytical and experimental load-deflection curves for frame FP2	239
Figure 9.14:	Experimental and analytical locations of the plastic hinges for portal frames	240

LIST OF TABLES

Table 3.1:	Analytical models for stress-strain relations for concrete (After Bahlis and Mirza 1987)	52
Table 3.2:	Cracking models (Bello, 1992)	62
Table 4.1:	Dimensions and properties of Gaston's beams and Cervenka's shear panel	83
Table 4.2:	Effect of element size and ϵ_{tu} on the ultimate load of beam T5L.	85
Table 4.3:	Effect of ϵ_{tu} on ultimate load for under-reinforced beam T2LA	89
Table 4.4:	Effect of ϵ_{tu} on ultimate load of shear panel W-2	89
Table 4.5:	Optimum value of ϵ_{tu} for different mesh sizes for beam T2LA and shear panel W-2	90
Table 4.6:	Ultimate load for the beam T2LA and the shear panel W-2 for different models	96
Table 4.7:	Ultimate load for singly and doubly reinforced beams tested by Gaston et. al.	98
Table 5.1:	Comparison of experimental and analytical results, Gaston and Mattock beams.	120
Table 5.2:	Dimensions and properties of Mattock's beam, C5.	121
Table 5.3:	Details of Mattock beams used in parametric study.	123
Table 5.4:	Sectional properties of Mattock beams, Group No. 1	125
Table 5.5:	Variation of n for Mattock beam under different loading types	135
Table 5.6:	Details of test beams for comparison of test and calculated short-term deflections	140
Table 5.7:	Comparison of experimental and calculated short-term deflections	141
Table 6.1:	Analytical results obtained using the NONLACS2 program (Group No. 1).	159
Table 6.2:	Comparison of existing ϵ_{cu} and θ_p formulations (θ_p is the plastic rotation on one side of section).	162
Table 6.3:	Analytical and estimated values of plastic rotation, θ_p (rad), for different loading types.	169
Table 7.1:	Sectional details and material properties of beams analyzed	181

Table 7.2:	Effect of concrete tensile strength on the cracking behaviour of beams HUCB and UCB	184
Table 7.3:	Summary of analytical results at yielding and ultimate of beams HUCB, LS1, and LS2186
Table 7.4:	Summary of analytical results at yielding and ultimate of beam HUCB190
Table 8.1:	Material properties used in the analysis of frames	203
Table 8.2:	The yielding and ultimate loads of frame FP4 for different meshes	205
Table 8.3:	Summary of cracking, yielding and ultimate loads for different values of ϵ_u	206
Table 8.4:	Comparison of experimental and analytical plastic hinge rotations	210
Table 9.1:	Sectional and material properties of beams C1 and C3 (Adaszkiwicz 1977)	229
Table 9.2:	Summary of analytical and experimental results at cracking, yielding and ultimate stage of continuous beams tested by Adaszkiwicz (1977)	232
Table 9.3:	Summary of analytical and experimental results at cracking, yielding and ultimate of frames	232
Table 9.4:	Comparison of experimental and analytical plastic hinge rotation	232

LIST OF SYMBOLS

A	=	finite element area
A_s	=	area of tension reinforcement
A'_s	=	area of compression reinforcement
b	=	width of element
b_w	=	web width
$c=kd$	=	neutral axis depth
C_{ijkl}	=	material constant (component of the constitutive matrix)
$d\varepsilon_{kl}$	=	incremental strain
$d\sigma_{ij}$	=	incremental stress
d_a	=	maximum aggregate size
D_{ijkl}	=	fourth-order tangential material stiffness tensor
E'_c	=	reduced modulus of elasticity equal to $0.57E_c$
E_0	=	initial concrete modulus of elasticity
E_{0i}	=	initial modulus of elasticity in i th direction; $i=1, 2$
EA	=	axial rigidity
E_c	=	secant modulus of elasticity of concrete
$E_c I_c$	=	flexural rigidity using Branson's equation
$E_c I_g$	=	flexural rigidity of uncracked gross section (ignoring reinforcement)
$E_c I_{ucr}$	=	flexural rigidity of uncracked transformed section
E_i	=	tangent moduli in principal directions i ; $i=1, 2$
EI	=	flexural rigidity
EI_c	=	flexural rigidity at the yielding stage
EI_u	=	flexural rigidity at the ultimate load stage
E_s	=	initial tangent modulus for reinforcing steel
E_s^*	=	tangent modulus for reinforcing steel in the strain hardening region (bi-modulus)
E_{sc}	=	secant modulus at peak stress
E_t	=	modulus of elasticity of concrete in tension
f_t	=	concrete uniaxial tensile strength
f_{ct}	=	splitting tensile strength

f_{eq}	=	equivalent tensile strength
F_{ij}	=	elastic response factor
f_r	=	modulus of rupture of concrete
f_y	=	yield strength of reinforcing steel
f_{yh}	=	yield strength of the hoop reinforcement
f'_c	=	concrete uniaxial compressive strength
G	=	shear modulus
G_f	=	fracture energy
h	=	element size
h_0	=	element size corresponding to the vertical drop on concrete tensile stress-strain curve
I_{cr}	=	second moment of cross-sectional area of cracked transformed section
I_e	=	effective second moment of cross-sectional area
I_{exp}	=	experimental second moment of cross-sectional area
I_g	=	second moment of area of uncracked gross section ignoring the reinforcement
I_{ucr}	=	second moment of cross-sectional area of uncracked transformed section
k_i	=	decay factor
L	=	length of element
l_c	=	crack spacing
L_{cr}	=	cracked length
L_{cr}/L	=	cracked length ratio
l_p	=	equivalent plastic hinge length
l_y	=	yielding length
m	=	power index in Branson's equation
$M_g/M_{cr,anl}$	=	moment ratio
M_a	=	maximum moment
M_{cr}	=	moment at first cracking
$M_{cr,anl}$	=	analytical cracking moment
MDEP	=	mesh dependency analysis option
M_Q	=	moment corresponding to the failure load
M_u	=	ultimate moment
M_y	=	yielding moment
n	=	power of the proposed equation
n_i	=	curve fitting factor in principal direction i

P_0	=	axial load capacity in compression
P_{cr}	=	cracking load
P_u	=	ultimate load
$P_{u,ani}$	=	analytical ultimate load
$P_{u,exp}$	=	experimental ultimate load
P_y	=	yielding load
r	=	correlation coefficient
R_i	=	$(EI)_i/L^3$
R_j	=	$(EI)_j/L^3$
S^e	=	surface area of any element
t	=	depth of element
t_{si}	=	thickness of smeared steel layer i
u, v, w	=	displacements in X, Y, and Z directions
V^e	=	volume area of any element
w	=	magnitude of the uniformly distributed load
W_1	=	vertical load
W_2	=	lateral load
w_c	=	crack band width
X	=	distance of the section A from the left end (end i)
y_t	=	distance from neutral axis to extreme fiber in tension
z	=	distance from the location of the maximum moment to the point of zero moment
α	=	loading type factor
α_1	=	tensile strain ratio (ϵ_w/ϵ_{cr})
α_2	=	tensile softening branch factor
α_{hk}	=	flexibility coefficients
α_u	=	loading type factor at the ultimate load stage
β	=	shear retention factor
β'	=	curvature distribution factor (shape factor)
γ	=	shear strain
γ_c	=	remaining compressive strength factor
γ_t	=	remaining tensile strength factor
Δ	=	short-term deflection

$\Delta\delta_i$	=	incremental nodal displacements
$\Delta\theta_p$	=	incremental plastic hinge rotation
ΔF_i	=	incremental external loads
δ_p	=	inelastic deflection
δW_e	=	variation in the work done by the external forces
ϵ_1 (ϵ_2)	=	strain corresponding to σ_1 (σ_2)
ϵ_{max}	=	concrete compressive strain at peak stress
ϵ_c	=	strain in concrete
ϵ_{ce}	=	concrete compressive strain at yielding
ϵ_{cr}	=	cracking strain of concrete
ϵ_{cu}	=	ultimate concrete compressive strain
ϵ_i	=	strain corresponding to σ_i
ϵ_{ic}	=	equivalent uniaxial strain corresponding to σ_{ic}
ϵ_{ij}	=	strain tensor
ϵ_{iu}	=	equivalent uniaxial strain in ith direction; i=1, 2
ϵ_p	=	plastic strain
ϵ_s	=	strain in steel
ϵ_{su}	=	ultimate steel strain
ϵ_{sy}	=	steel strain at yield
ϵ_t	=	tensile strain of concrete
ϵ_{tu}	=	ultimate tensile strain of concrete
ϵ_u	=	ultimate compressive strain of concrete in ith direction; i=1, 2
θ_e	=	elastic rotation
θ_p	=	plastic hinge rotation
θ_t	=	total rotation
θ_u	=	rotations of member corresponding to the maximum load
θ_x	=	normal plate rotation about X-axis
θ_y	=	normal plate rotation about Y-axis
μ_Δ	=	deflection ductility ratio
μ_ϕ	=	curvature ductility ratio
ν	=	equivalent Poisson's ratio
ν_i	=	initial Poisson's ratio in ith direction; i=1, 2

ρ	=	<i>tension reinforcement ratio</i>
ρ'	=	<i>compression reinforcement ratio</i>
ρ_b	=	<i>balanced reinforcement ratio</i>
ρ_s	=	<i>ratio of volume of confining steel to the volume of the concrete core</i>
$\sigma_1(\sigma_2)$	=	<i>major (minor) principal stress</i>
σ_{ic}	=	<i>compressive strength of biaxially loaded concrete in direction i, i=1, 2</i>
σ_{ij}	=	<i>stress tensor</i>
σ_{it}	=	<i>tensile strength of concrete in ith direction; i=1, 2</i>
τ_{xy}	=	<i>shear stress</i>
$\phi(x)$	=	<i>curvature at distance of x from the critical section</i>
ϕ_{cr}	=	<i>cracking curvature</i>
ϕ_p	=	<i>plastic curvature</i>
ϕ_u	=	<i>ultimate curvature</i>
ϕ_y	=	<i>yielding curvature</i>
ω	=	<i>tension reinforcement index</i>
w_c	=	<i>unit weight of the concrete</i>
$\Delta\varepsilon$	=	<i>incremental strain</i>
$\Delta\sigma$	=	<i>incremental stress</i>
$(EI)_0$	=	<i>initial analytical flexural rigidity</i>
$(EI)_A$	=	<i>tangent flexural rigidity of the section A</i>
$(EI)_{cr}$	=	<i>cracking flexural rigidity</i>
$(EI)_i$	=	<i>flexural rigidity at end i of element</i>
$(EI)_j$	=	<i>flexural rigidity at end j of element</i>
$(EI)_p$	=	<i>proposed flexural rigidity</i>
$(EI)_{tan}$	=	<i>tangent flexural rigidity</i>
$(EI)_{tan}/(EI)_{cr}$	=	<i>flexural rigidity ratio</i>
$\{\delta\varepsilon\}$	=	<i>virtual strains at any point of the element</i>
$\{\Delta\varepsilon\}$	=	<i>incremental strain vector in local coordinate system</i>
$\{\Delta\varepsilon_i\}$	=	<i>strain increment vector during the iteration i</i>
$\{\Delta\varepsilon_{iu}\}$	=	<i>incremental equivalent uniaxial strain vector</i>
$\{\Delta\sigma_i\}$	=	<i>the "true" stress increment obtained from the stress -strain relationship.</i>
$\{\delta u\}$	=	<i>virtual displacement vector at any point of the element</i>

$\{\varepsilon\}$	=	strain vector at any point within the finite element
$\{\varepsilon_0\}$	=	vector of initial strains
$\{\sigma_0\}$	=	vector of initial stresses
$\{b\}$	=	body force (per unit volume)
$\{F\}$	=	equivalent nodal force vector
$\{f_{\varepsilon_0}\}$	=	equivalent nodal force vector due to initial strains
$\{f_{\sigma_0}\}$	=	equivalent nodal force vector due to initial stresses
$\{F_0\}$	=	norm vector components
$\{f_b\}$	=	equivalent nodal force vector due to body forces
$\{\overline{F}_{i+1}\}$	=	equivalent unbalanced forces
$\{f_p\}$	=	external applied nodal load vector
$\{f_s\}$	=	equivalent nodal force vectors due to surface traction
$\{s\}$	=	surface traction
$\{u\}$	=	displacements at any point within the element
$\{U\}$	=	structure nodal displacement vector
$\{U\}_n$	=	element nodal displacement vector
$[B]$	=	matrix relating strains and element nodal displacements
$[D_{i-1}]$	=	tangent constitutive matrix at the beginning of iteration i
$[D]$	=	constitutive matrix
$[K]$	=	structure stiffness matrix in global coordinate system
$[k]_{bb}$	=	bending element stiffness matrix
$[K]^e$	=	element stiffness matrix
$[k]_{pb}$	=	coupling element stiffness matrix
$[k]_{pp}$	=	in-plane element stiffness matrix
$[L]$	=	linear-operator matrix
$[N]$	=	shape function matrix

CHAPTER 1

INTRODUCTION

1.1 GENERAL

A good understanding of the fundamental behaviour of reinforced concrete (R C) substructures such as beams, columns, frames, and structural walls is needed for effective design. The present practice of designing structural concrete systems normally involves linear elastic analysis to calculate the internal forces and moments, followed by strength design of the member sections. In linear elastic analysis, concrete is assumed to be an uncracked homogeneous isotropic material. In reality, the cracking of structural elements such as beams occurs at an early stage of loading and as cracking progresses with increasing load, the stiffness of the structure decreases gradually. It is evident that elastic analysis cannot predict critical failure modes or other behavioral aspects such as the complete load-deflection characteristics, which are very important in design.

Several reinforced concrete design tools are based on empirical formulations derived from extensive experimental programs, which are normally expensive, time-consuming and require considerable human and physical resources. Using nonlinear finite element analysis, it is now possible, at a comparatively low cost and effort, to predict the complete response of more complex R C members and structures such as tall structural walls, coupled elevator core systems and large slab systems with unusual layouts and supports. In recent year, nonlinear finite element analysis of structural concrete has been used successfully for such systems to obtain their complete response including load-deflection characteristics, strain distributions and cracking patterns at different load levels, failure modes, etc. Computer-based nonlinear finite element analysis can be used as a supplement to the experimental investigations, and it offers a computational tool to study the effect of the various influencing parameters and to achieve a better understanding of the

behaviour of R C structures. For the results of these nonlinear analysis to be considered reliable, it is necessary that the behaviour of R C elements is modeled accurately, besides verifying the accuracy of the analytical results of some selected structures for which detailed experimental data is available.

The use of the finite element method to predict the behaviour of R C beams has been increasing ever since the pioneering work of Ngo and Scordelis (1967). This was followed by considerable work in this area by investigators such as Nilson (1968), Jofriet and McNeice (1971), Mufti et al. (1971), Scanlon (1971), Houde (1973), Lin and Scordelis (1975), Cedolin et al. (1977), Ghoneim (1978), Appleton et al. (1983), Al-Manaseer and Phillips (1987), Bazant et al. (1987), Balakrishnan et al. (1988), Vecchio (1989), Kim and Lee (1993), Polak (1994) and others. A review of different finite element methods is available in the report of the ASCE Committee on Finite Element Analysis of Reinforced Concrete Structures (1982 and 1991).

The versatility of the finite element method as a tool for analysis of concrete structures has been enhanced significantly by incorporation of nonlinear material behaviour, geometric nonlinearities and time dependent effects which has facilitated prediction of the structural response of a member at all stages of its loading history. In this respect, the influence of the "numerical" effects, such as the element size, load steps, integration order, etc., on the various classes of structures needs to be studied. Despite the extensive research effort, there exists a need to determine a simple material model that best represents the behaviour of the various classes of structural elements and their assemblages. Such an extensive verification will result in improving the level of confidence in the nonlinear finite element analysis of structural concrete, while at the same time pointing out areas that need further research and development.

Some investigators have indicated that the computed results are not the same with regard to the element size used, i.e., the results change significantly if the mesh is refined (Bazant 1976, Bazant and Cedolin 1979, 1980, 1983, Bazant and Oh 1983, Darwin 1985, Rots et al. 1985, Choi and Kwak 1990, Shayanfar et al. 1993, and Kheyroddin et al. 1994). Various analyses indicated that if the value of ϵ_m is adjusted appropriately according to the element size, it can help eliminate the mesh dependency drawback. Some researchers such as Lin and Scordelis (1975), Gilbert and Warner (1978), Hanna and Mirza (1983), Bazant and Oh (1983), and Rots et al. (1985) have suggested different values for the ultimate tensile strain of the concrete, ϵ_m , but a detailed survey of the literature shows that there exist neither a universally accepted value for ϵ_m , nor a suitable method for its determination (Kheyroddin and Mirza 1994). Therefore, a new method of

evaluating ϵ_m to idealize the tension stiffening effect and to remove the mesh dependency drawback is required. In the present study, attempts have been made to eliminate the mesh dependency phenomenon by defining the ultimate tensile strain, ϵ_m , and the associated descending branch of the stress-strain curve.

The most important factors affecting the short-term deflection and the flexural rigidity of an R C beam are its span length, end constraints, magnitude and type of loads, section geometry and material properties, tension and compression steel percentages, tension-stiffening, the type and extent of cracking, bond-slip characteristics, and the aggregate interlock at the cracks. One of the earliest proposed models for calculation of the flexural rigidity of R C beams was proposed by Maney (1914). This was followed by considerable work in the area of deflection and flexural rigidity of R C beams by Yu and Winter (1960), Branson (1963), Corley and Sozen (1966), Beeby (1968), Mirza and Sabnis (1971), Hsu (1974), Grossman (1981), Rangan (1982), Cosenza (1990), Al-Shaikh and Al-Zaid (1993), and others. Extensive review of deflection and flexural rigidity of R C beams has been reported by ACI publications (Symposium on the Deflection of Concrete Structures, 1974, 1984, 1995), Branson (1966, 1977), and Kheyroddin and Mirza (1994).

Branson (1963) suggested a well-known empirical expression for the effective second moment of area to determine the flexural rigidity over the entire length of a simply supported, uniformly loaded R C beam subjected to service loads. Although Branson's equation is simple to use and it is widely accepted, it has some weaknesses. This equation is not suitable for nonlinear finite element analysis of structural concrete members subjected principally to flexure. In addition, it gives a constant flexural rigidity along the length of element and does not take into account the effect of loading type.

The main problem in the evaluation of deflections in R C beams is the definition of an appropriate moment-curvature relationship, and the resulting section flexural rigidity for each stage of loading. Most of the difficulties arise from the assumptions involved in assessing whether the section is cracked or uncracked. Most of the previous investigators used the effective second moment of area and constant value of the secant modulus of elasticity of concrete to calculate the deflection of R C beams while the flexural rigidity, EI , is a sectional characteristic which depends on factors such as the geometry of section, the properties of the concrete and the reinforcing steel, and the type and magnitude of the applied loads. A review of the state-of-the-art in the area of evaluation of deflection and flexural rigidity of concrete beams, reported by Kheyroddin and Mirza (1994), suggests a need for further modification of the equation for flexural rigidity, EI , and a

more representative value of the flexural rigidity, EI , of the section beyond the service load level at the various load stages up to the ultimate load to obtain the best estimate of deflection. It is also important to study the distribution and the magnitude of the flexural rigidity along the length of the member through the various load stages.

It is well established that the inelastic behaviour of R C sections leads to a redistribution of moments and forces, resulting in an increased load bearing capacity of the indeterminate structure. As the applied load is increased, hinges start forming in succession at locations where the hinge moment capacity is reached; with further increase in the applied load, these hinges continue to rotate until the last hinge forms converting the structure into a mechanism at failure. Most of the ultimate flexural strength design equations have been derived using an "equivalent stress-block" for the concrete. These equations give satisfactory "ultimate strength" values, however, they cannot be used for considering the deformational behaviour in the inelastic range for any limit design methods. The components of well designed and detailed indeterminate system normally possess adequate rotation capacity at the "plastic" hinges to enable transformation of the structure into a mechanism with increasing loads.

Some equations have been proposed to calculate the plastic hinge length and the inelastic rotation capacity, however, there is no general agreement on the techniques to evaluate the inelastic behavioural characteristics of indeterminate concrete structures. The nature and complexities of the problems discussed in Chapter 2 are such that further research is needed to clarify the influence of the different factors on the response of indeterminate structures near the ultimate load, and in particular on the rotation capacity of the plastic hinge, θ_p .

For nonlinear analysis of R C structures using the finite element method, both the modified stiffness and the layered discretization approaches have been used recently. In the layered approach, the structure is idealized as an assemblage of shell elements with each element subdivided into a number of layers (e.g., Ghoneim 1978, Al-Manaseer and Phillips 1987, Bazant et al. 1987, Balakrishnan et al. 1988, Razaqpur et al. 1989, Hu and Schnobrich 1990). The considerable computational effort required makes this method unsuitable for practical application, and therefore, it is not very efficient to use in a design office for nonlinear analysis of large structures, such as a multistorey framed system. For planar frames, the modified stiffness approach implies the use of beam elements that account approximately for the nonlinear behaviour of structural concrete (e.g., Aparicio et al. 1983, Pulmano and Shin 1987, Kim and Lee 1992). With the development of the tangent flexural rigidity equation, the modified stiffness approach can be

implemented in the program, which will reduce the required computational time considerably. The present work is aimed at demonstrating the capabilities of both the layered finite element and the modified stiffness approaches as tools for predicting the nonlinear response of concrete structures.

1.2 OBJECTIVES

The main objectives of the present study can be summarized as follows:

- 1) To review and discuss the previously proposed equations with emphasis on deflection, flexural rigidity and ultimate deformation of normal and high-strength concrete beams.
- 2) To verify the effect of finite element size on the computed response of selected concrete structural elements subjected to monotonically increasing loads.
- 3) To establish a new simple procedure to evaluate the value of ϵ_{cu} and remove the mesh dependency phenomenon permitting analysis of structural elements using relatively large size elements with an adequate level of confidence and savings in the required computational time.
- 4) To incorporate the proposed model for mesh dependency, the compressive stress-strain curves of normal and high-strength concrete, new models for concrete in tension and tension-stiffening, and concrete ultimate compressive and tensile strains into a nonlinear layered finite element formulation.
- 5) To carry out detailed parametric studies in order to investigate the influence of cracking, the various tension-stiffening models, tension and compression reinforcement ratios, concrete tensile and compressive strengths, and three different types of loading conditions including the midspan-concentrated loading, the third-point loading, and the uniform loading on the overall behaviour of R C beams in three stages of loading:
 - a) pre-cracking ($M_a < M_{cr}$),
 - b) post-cracking ($M_{cr} \leq M_a < M_y$), and
 - c) post-yielding ($M_y \leq M_a < M_u$).

- 6) To develop appropriate equations for the calculation of the analytical cracking moment, flexural rigidity and the deflection of R C beams at the serviceability limit state.
- 7) To examine the plastic rotation capacity of beams and frames and to propose new simple equations to evaluate the rotation capacity of plastic hinges.
- 8) To investigate the effect of finite element size, concrete ultimate tensile strain, and tension-stiffening on the overall behaviour of the R C frames.
- 9) To develop a nonlinear finite element program (NAFS) to formulate a 2-node beam element based on modified stiffness approach with a degrading stiffness matrix to analyze large scale structural frame systems with savings in the required computational time.
- 10) To demonstrate the accuracy and reliability of the proposed models, NONLACS2 and NAFS programs by comparison of the computed and the experimental results.

1.3 THESIS ORGANIZATION

The thesis is organized in ten chapters and two appendices.

Chapter 1 "Introduction" discusses briefly some of the reasons responsible for the limited use of nonlinear finite element analysis programs, and the need for development of new equations for elimination of mesh dependency phenomenon, flexural rigidity and plastic hinge rotations of R C members. It also includes the objectives and organization of the thesis.

Chapter 2 "Review of Deflection, Flexural Rigidity and Ultimate Deformation of Reinforced Concrete Beams" provides a general state-of-the-art report on the flexural behaviour of R C beams and reviews and discusses the previously proposed equations with emphasis on deflection, flexural rigidity, and ultimate deformations. Finally, based on the previous procedures, the basis for further studies and establishing an appropriate model for flexural rigidity and plastic hinge rotations of R C members are discussed.

Chapter 3 "Nonlinear Layered Finite Element Program" describes the key features of the

nonlinear layered finite element analysis program, NONLACS2 (NONLinear Analysis of Concrete and Steel structures), developed in the present study. First, a classification and description of existing nonlinear analysis methods of R C structures are discussed. Then, the history and capabilities of the NONLACS2 program, constitutive models for uncracked and cracked concrete, the compressive stress-strain curves for normal and high-strength concrete, crack modelling techniques, new proposed models for concrete in tension, proposed concrete ultimate compressive and tensile strains and the failure criteria for the concrete are presented in this chapter, along with a discussion of the constitutive model for the steel reinforcement. The nonlinear finite element formulation in the NONLACS2 program including the element library, layered discretization technique, numerical algorithms, and convergence and divergence criteria are also outlined.

Chapter 4 "Finite Element Size Effect Phenomenon" is aimed at evaluating and finding the key parameters that can help to remove the influence of the finite element size in the nonlinear finite element analysis of R C structures. For elimination of the element size effect phenomenon, both the new proposed model and the crack band model proposed by Bazant and Oh (1983) are implemented into the NONLACS2 program to analyze different structural elements. The analytical results obtained using the different models are also compared with the experimental data where available.

Chapter 5 "Parametric Study of Flexural Behaviour of Reinforced Concrete Beams" presents the results of a parametric study into the effects of tension and compression reinforcement ratios and steel yield strengths, loading types and stages, compressive strength of concrete, cracking and tension-stiffening in nonlinear finite element analysis of R C beams. New equations are proposed to calculate the analytical cracking moment, cracking flexural rigidity, tangent flexural rigidity and the deflection of R C beams at the serviceability limit state. The accuracy of the proposed models is also investigated along with a comparison with the analytical results obtained from the NONLACS2 program and the experimental data.

Chapter 6 "Analytical Investigation of Plastic Hinge Rotation Capacity" examines the influence of tension reinforcement index, ($\omega = \rho f_s / f_c$), and bending moment distribution (loading type) on the ultimate deformation characteristics of R C beams. The analytical results of 15 simply supported beams with different amounts of tension reinforcement ratio under three different

loading conditions are presented and the predictions using the new formulation are compared with the experimental data, where available. Based on the analytical results, new simple equations as a function of tension reinforcement index and the loading type are proposed.

Chapter 7 "Nonlinear Analysis of High-Strength Concrete Beams" demonstrates the capability of the NONLACS2 program for nonlinear finite element analysis of high-strength concrete beams using analysis of three high-strength concrete beams, specimens: LS1 and LS2 tested by Leslie et al. (1976) and HUCB tested by Abrishami et al. (1995). The influence of the concrete tensile strength and the tensile softening branch factor, α_2 , on the computed response of high-strength concrete beams including the cracking behaviour, yielding, ductility and failure mechanism is studied. The computed results for the normal and high-strength concrete beams are compared with the experimental results for the beams, UCB and HUCB, tested by Abrishami et al. (1995).

Chapter 8 "Finite Element Analysis of Reinforced Concrete Frames" investigates the nonlinear behaviour of a R C single-bay portal frame, FP4, tested by Cranston and Cracknell (1969) under monotonically increasing vertical and lateral loads. The capability and accuracy of the finite element program, NONLACS2, in predicting the nonlinear response of R C frame structures is verified along with a comparison between the analytical and the corresponding experimental results. The effect of the finite element size, concrete ultimate tensile strain, and tension-stiffening on the response of the R C frame, FP4, is also investigated. In addition, the program is used to carry out a plastic analysis of the frame to define the mechanism of failure, the plastic hinge rotations, and their yielding and equivalent plastic hinge lengths. The location and the sequence of formation of plastic hinges for frame FP4 is also discussed.

Chapter 9 "NAFS- A Finite Element Program for Nonlinear Analysis of Framed Structures" presents the key features of a nonlinear finite element analysis computer program, NAFS (Nonlinear Analysis of Frame Structures), as a practical engineering tool based on the modified stiffness approach. The variation of the flexural rigidity at the section at different loading stages and along the length of the element are studied. The new 2-node nonlinear beam element with a degrading stiffness matrix is developed to model cracking and other nonlinear effects throughout the entire loading range from zero to the ultimate load. The accuracy and efficiency

of the NAFS program is also verified through comparison with the experimental data from tests on R C frames (Cranston and Cracknell 1969) and continuous beams (Adaszkievicz 1977).

Chapter 10 "Summary and Conclusions" includes a brief summary of the work, highlights of the key results, and makes recommendations for future investigations.

Appendix A presents a list of the input data file required for the NONLACS2 program.

Appendix B presents a detailed description of the input data required to run the NAFS program.

CHAPTER 2

REVIEW OF DEFLECTION, FLEXURAL RIGIDITY AND ULTIMATE DEFORMATION OF REINFORCED CONCRETE BEAMS

A general state-of-the-art report on deflection, flexural rigidity and ultimate deformation of reinforced concrete (R C) beams is presented in this chapter. First, some of the major procedures, previously proposed for calculation of flexural rigidity, EI, and short term deflection are reviewed along with their advantages and disadvantages. Then the ultimate deformation characteristics including empirical expressions for the ultimate concrete compressive strain, plastic hinge length and plastic rotations are presented. Finally, based on the previous procedures, the basis for further studies and establishing an appropriate model for flexural rigidity and plastic hinge rotation of R C members are discussed.

2.1 REVIEW OF DEFLECTION CALCULATION PROCEDURES

The most important factors affecting the short-term deflection and the flexural rigidity of an R C beam are its span length, end constraints, magnitude and type of loads, section geometry and material properties, steel percentages, tension-stiffening, the type and extent of cracking, bond-slip characteristics, and the aggregate interlock at the cracks. Also, because of the varying amounts of reinforcement and the extent of cracking along the span length of the beam, the flexural rigidity of R C beams at different load stages is difficult to predict accurately.

The short term deflection of a R C beam can be expressed as

$$\Delta = k \frac{M_a L^2}{EI} \quad (2.1)$$

where L is span length, EI is the flexural rigidity, M_a is the maximum moment at service load,

and k is a constant which depends on the type of loading and the member end conditions. The flexural rigidity, EI , is a sectional characteristic which depends on factors such as the section geometry, steel reinforcement details and the material properties of concrete and steel. It should be noted that the flexural rigidity, EI , is a load dependent property which decreases gradually with an increase in the applied load.

The various cross sections of an R C beam along the span are subjected to different stress configurations during bending (Fig. 2.1). The largest bending moment acting on the member, M_s , is usually greater than the cracking moment, M_{cr} , (say, M_s/M_{cr} ratio values up to about 3 or 4), and the subsequent formation of cracks in the high moment region decreases the flexural rigidity and stiffness of the R C beam. Therefore, using the flexural rigidity based on the gross concrete section (ignoring the reinforcement), or more accurately the uncracked transformed section (Zone 1 in Fig. 2.1) would underestimate the deflection of the beam. On the other hand, using an EI value based on a fully cracked cross section, (Section 2 in Fig. 2.1) would overestimate the deflection of the beam, because the tension-stiffening effect is ignored. However, for values of bending moments larger than the cracking moment, the depth and width of the cracks vary in accordance with the variation of the bending moments along the span. In addition, the concrete between cracks still resists some tension, which contributes both to the strength and the stiffness of the beam- a phenomenon termed tension-stiffening. As a result, an intermediate value for the flexural rigidity is needed at a given cross section, which is normally between its uncracked and fully cracked values.

Due to the complex nature of the flexural behaviour of R C beams and the need for a simplified method for calculating the short-term deflections, different procedures have been proposed in the literature. Generally, two approaches have been used to predict the flexural rigidity and deflection of a R C beam.

In the first approach described as "empirical methods", most of the investigators used the "effective second moment of the area, I_e ," and a constant value of the concrete modulus of elasticity, E_c , to calculate the flexural rigidity and the deflection of the beam. To allow for the nonlinear behaviour of the section, it is usual to utilize a pre- and post-cracked value of EI . Beeby (1968) has summarized four of the more commonly accepted versions of this approach together with a further proposal of his own method. The second method, which may be referred to as a "direct sectional analysis", uses assumed material properties, compatibility relationships, etc. to predict the curvature and consequently the flexural rigidity at a given moment. Integration of the

curvature over the specimen length and consideration of the boundary conditions yields rotations between two selected sections. Another integration of these rotation and accounting for the boundary conditions and some algebra lead to the value of the deflection at the appropriate beam section. The second method is generally more accurate than the first but it requires considerably more computational effort. Hsu (1974) reviewed the different procedures based on the second approach and also derived the moment-curvature relationship for under-reinforced and over-R C sections. The deformations were evaluated using the complete moment-curvature characteristics at a given section.

A bibliography on the deflection of concrete structures was presented by Sabnis for the ACI Committee 435, "Deflection of Concrete Structures" (1974). Extensive review of deflection of R C beams has been reported by ACI Committee 435 (1974, 1995) and Branson (1977). The deflection and flexural rigidity of R C beams was also reviewed by Kheyroddin and Mirza (1994). Some of the commonly used procedures are presented here for completeness. This review is limited to the flexural rigidity and short-term deflection of normal and high strength R C beams.

2.1.1 Use of Cracked Transformed Section Ignoring Tension-Stiffening

One of the earliest proposed model for calculation of flexural rigidity of R C beams was proposed by Maney in 1914. The second moment of area was calculated using the cracked transformed section (ignoring tension-stiffening), I_{cr} , throughout the length of the span and the following equation was proposed for calculating deflection, Δ :

$$\Delta = \frac{KM_a L^2}{E_c I_{cr}} \quad (2.2)$$

where M_a is maximum moment in member at the load stage at which the deflection is being computed, and I_{cr} is the second moment of area of the cracked section transformed to concrete and can be calculated as:

$$I_{cr} = \frac{b(kd)^3}{3} + nA_s(d-kd)^2 + (n-1)A'_s(kd-d')^2 \quad (2.3)$$

where the neutral axis factor

$$k = \sqrt{2n(\rho + 2\rho'd'/d) + n^2(\rho + 2\rho')^2} - n(\rho + 2\rho') \quad (2.4)$$

and b is the width of beam, d is the effective depth, n is the modular ratio defined as E_s/E_c and A_s and A'_s are cross-sectional areas of the tension and compression reinforcements, respectively.

Also d' is the distance from the extreme compression fibre to centroid of the compression steel reinforcement and ρ and ρ' are the tension and compression reinforcement ratios, respectively.

The assumption that the concrete is cracked to the neutral axis is used to calculate the value of I_{cr} . In other words, the tension zone below the neutral axis and above the upper tip of the crack is neglected. Since Eq. 2.3 does not take into account the tension-stiffening effect, the beam deflection is overestimated. This error increases with a decrease in the tension steel percentage. With steel percentages of about 0.75%, the error at working load is of the order of 100% (Beeby, 1968).

In 1940, Murashev proposed an equation for the cracked transformed second moment of area, I_{cr} , based on a modular ratio $n=E_s^*/E_c$, where E_s^* is an increased effective modulus of elasticity of steel in order to take into account the tension-stiffening and is given by

$$E_s^* = \frac{E_s}{\Psi} \quad (2.5)$$

where $\Psi = 1-2/3 (M_{cr}/M)^2 \leq 1.0$, and M is the maximum bending moment at the service load.

On the basis of an experimental study, the Portland Cement Association, (PCA, 1947), recommended the use of the uncracked gross second moment of the area, I_g , ignoring the effect of the steel.

The ACI 318-63 (1963) specifies that where short-time deflections are to be computed, the second moment of area should be taken as:

$$I_e = I_g \quad \text{when } \rho f_y \leq 500 \quad (2.6)$$

$$I_e = I_{cr} \quad \text{when } \rho f_y > 500 \quad (2.7)$$

In these equations, the effect of the steel reinforcement is neglected before cracking, and by utilizing the cracked second moment of area after the cracking of concrete, it is assumed that the concrete does not resist any tension. Therefore, the value of the calculated deflection based on these equations is on the higher side.

Corley and Sozen (1966) proposed the following equation for curvature at a given section:

$$\phi = \frac{M}{E_c I_{cr}} = \frac{\epsilon_c}{kd} \quad (2.8)$$

where $\epsilon_c=f_c/E_c$ is the concrete strain in the extreme fibre in compression. Equation 2.8 must be used when the value of moment is above the cracking moment, M_{cr} . If the applied moment is

smaller than the cracking moment, the beam section should be considered uncracked along beam length.

Kordina (1970) suggested reduction factors for flexural rigidity of structural members which are parts of a frame as:

$$\text{Reduction factor} = \frac{\text{Effective flexural rigidity, } (EI)_{\text{eff}}}{\text{Flexural rigidity of uncracked section}} \quad (2.9)$$

For normal ratios of reinforcement, Kordina's equations suggest that the second moment of area of beam sections should be taken as 0.4 to 0.5 I_g and that of columns as about 0.8 I_g (for more information, see Kheyroddin and Mirza 1994). Commonly, the section flexural rigidity values used in structural analysis are based on the gross concrete section and no allowance is made for cracking of the concrete, and the steel reinforcement is ignored. It may seem that this is a considerable approximation because when a member section cracks, the flexural rigidity and stiffness change. For example, Park and Paulay (1975) showed that for a rectangular section with a modular ratio of 10, the reduction in the flexural rigidity from the gross section value ($E_c I_g$) on cracking may be 30 to 60% for sections with $\rho = \rho' = 0.01$, and 40 to 60% for sections with $\rho = 0.01$ and $\rho' = 0$, depending on the location of steel in the section.

2.1.2 Yu and Winter's Method

Yu and Winter (1960) suggested the following two methods for calculation of short-term deflections on the basis of a cracked section:

Method A: The cracked transformed second moment of area, I_{cr} at midspan is used as a constant value along the length of the span for simple spans, and the average second moment of area for the positive and negative moment regions is used for calculating deflections in continuous beams.

Method B: In order to take into account the tension-stiffening effect, the instantaneous deflections calculated by Method A are multiplied by the correction factor in the form

$$I_e = \frac{I_{cr}}{\left(1 - \frac{M_1}{M_{\max}}\right)} \quad (2.10)$$

where

$$M_1 = 0.1 (f'_c)^{2/3} h (h - kd) \quad (\text{psi units}) \quad (2.11)$$

and b is the width of beam on the tension side, h is the total depth of the beam and kd is the

depth of neutral axis. As can be seen, Equation 2.10 is applicable only for values of $M_{max} \geq bM_1$. The Method B was considered satisfactory by the ACI Committee 435 for prediction of short-term deflections of R C beams. The use of this method in the finite element analysis is limited because a measure of the "actual" flexural rigidity rather than a value based on the effective second moment of area is required. The effective second moment of the area, I_e , is related to the second moment of area of the cracked and gross concrete sections, I_{cr} and I_g , respectively, and several other factors, such as the tension-stiffening effect, the type of load, etc. Comparison of test and calculated results of 90 beams by Yu and Winter (1960) showed that the standard deviation of calculated to measured deflections was 0.151 and 0.14 for methods A and B, respectively.

2.1.3 European Concrete Committee (CEB) Procedure

The European Concrete Committee (CEB, 1961) recommended that deflections can be determined in two parts as shown in Fig. 2.2.

$$\Delta = \Delta_1 + \Delta_2 + \Delta_3 \quad (2.12)$$

Part I: For the initial loading stage, $M < M_{cr}$, the evaluation of deflection is based on the uncracked section, with:

$$K_1 = E_c I_g \quad (2.13)$$

where K_1 is the equivalent elastic flexural rigidity. The value of Δ_1 is calculated using M_{cr} and K_1 .

Part II: For the loading stage after the beam has cracked, $M > M_{cr}$, the deflection Δ_2 is calculated using the values of the maximum moment at service load, M_2 , and K_2' . Here, K_2' is equal to 0.75 K_2 and is given by:

$$K_2 = E_s A_s d^2 (1 - 2\omega)(1 - 2/3 \omega) \quad (2.14)$$

where E_s is modulus of elasticity of steel and ω is tension reinforcement index and equal to $(A_s/bd)(f_y/f'_c)$, but not more than 0.25. The value of Δ_3 is calculated using the values of M , the moment corresponding to the total load, and K_2 . The use of the tension reinforcement index may be incorrect since the yield strength of the steel cannot possibly be a factor in the calculation of section properties at loads which are well below the value causing any of the steel reinforcement to yield. This method does not account for the variation of flexural rigidity along the length of the beam, however, it considers the behaviour of the structure in two extreme load stages. There is no recommendation for evaluation of deflections in continuous beams using this approach.

The European Concrete Committee (CEB, 1968) modified the 1961 CEB bilinear equation (Eq. 2.12) as follows:

When $\rho \geq 0.005$ for rectangular beams, and
 $\rho \geq 0.001$ for T-beams with $b/b_w \geq 10.0$,

the deflection, Δ , is given by:

$$\Delta = \frac{KM_a L^2}{E_c I_{cr}} \quad (2.15)$$

When the value of ρ is less than the above values,

$$\Delta = \frac{KL^2}{E_c} \left[\frac{M_{cr}}{I_g} + \frac{4}{3} \frac{M_a - M_{cr}}{I_{cr}} \right] \leq \frac{KM_a L^2}{E_c I_{cr}} \quad (2.16)$$

2.1.4 Granholm General Flexural Theory

In 1965, Granholm presented a general flexural theory based on neglecting the tension part of concrete in the form

$$\frac{EI}{E_s A_s d^2} = \left(1 - \frac{c}{d}\right) \left(1 - \frac{c}{3d}\right) + \frac{\rho'}{\rho} \left(\frac{c}{d} - \frac{d'}{d}\right) \left(\frac{c}{3d} - \frac{d'}{d}\right) \quad (2.17)$$

For concrete with a high value of E_c and for weakly reinforced sections, the flexural rigidity, EI , approaches the theoretical maximum value of

$$EI = E_s A_s d^2 \left[1 + \frac{\rho'}{\rho} \left(\frac{d'}{d}\right)^2\right] \quad (2.18)$$

The flexural rigidity of weakly reinforced sections is affected only slightly by the modulus elasticity of the concrete, E_c . For a section with $\rho=0.005$ and $\rho'=0$, the flexural rigidity thus increases from a value of $0.75 E_s A_s d^2$ when the value of n decreases from 20 to 5. An increase in the value of the modulus of elasticity of the concrete by a factor of four results in the flexural rigidity being increased by a factor of only about 1.3. For $\rho=0.01$, the flexural rigidity increases by a factor of about 1.5. The depth of the concrete compression zone increases as the modulus of elasticity decreases. The flexural rigidity of under-reinforced beams when a beam is loaded until the tensile reinforcement yields does not remain constant; it decreases as the strains in the reinforcement increase. In this case, the flexural rigidity can be calculated using the equation:

$$EI = M \frac{d}{(\epsilon_c + \epsilon_s)} \quad (2.19)$$

2.1.5 Branson's Empirical Equation

Branson (1963) used an effective second moment of area to include the effect of stiffness variation caused by the cracking of the concrete along the length of the beam. Branson suggested the use of the following well-known empirical expression for the effective second moment of area to determine the section flexural rigidity of a simply supported R C beam subjected to service loads

$$I_e = \left(\frac{M_{cr}}{M_a}\right)^m I_g + \left[1 - \left(\frac{M_{cr}}{M_a}\right)^m\right] I_{cr} \leq I_g \quad (2.20)$$

which can be applied when $M_a \geq M_{cr}$, otherwise $I_e = I_g$. Here, M_a is the maximum moment at the section, I_{cr} and I_g are the second moments of area of the cracked transformed and gross sections, respectively. M_{cr} is the flexural cracking moment and can be computed as:

$$M_{cr} = \frac{f_t I_g}{y_t} \quad (2.21)$$

where f_t is the modulus of rupture and equal to $0.62\sqrt{f'_c}$ in which f'_c is the compressive strength of concrete in MPa and y_t is the distance from the neutral axis to the extreme fibre in tension. In fact, the second term in Eq. 2.20 takes into account empirically the effect of tension-stiffening. This equation was developed from a statistical study of 54 test specimens which had M_{max}/M_{cr} values ranging from 2.2 to about 4 and I_g/I_{cr} values ranging from 1.3 to 3.5. The study included simple-span rectangular and T-beams and two-span continuous rectangular beams. The Newmark's numerical procedure together with the test results was used to determine an empirical value of $m=4$ for individual sections. It was further determined that the same type of equation but with the power index equal to 3 could be used for the average value of I_e over the entire length of a simply supported, uniformly loaded, rectangular or T-beams (or between inflection points of continuous beams), with an average value weighted at 2/3 for the positive and at 1/3 for the negative moment regions for the two-span continuous beams. It is noted that the slope of the moment (or load) versus deflection curve as shown typically in Fig. 2.3 changes sharply after cracking, and this is reflected in a sharp decrease in the value of I_e (I_e is proportional to the slope of the secant line to any point on the load-deflection curve above the first cracking). As the ratio M_a/M_{cr} increases, the value of I_e rapidly approaches the value of I_{cr} .

According to the ACI Committee 435 (1966), the second moment of area of uncracked transformed section, I_{ucr} , might be more accurately used instead of I_g in Eq. 2.20, especially for

heavily reinforced members. Based on Eq. 2.21, the principal effect of using I_{ucr} instead of I_g is an increase in the second moment of the area and a decrease in the distance from centroidal axis to the extreme tension fibre, y_t , and consequently an increase in the moment at first cracking, M_{cr} . Also, the ratio I_{ucr}/I_g may be as high as 1.30 due to the inclusion of tension steel and 1.15 due to the inclusion of compression steel.

Branson's equation is simple to use for evaluation of deflection at the serviceability limit state and it is widely accepted, for example, this formula has been adopted by the ACI Code since 1971 and by the CSA Standard A23.3 (1977). In order to calculate the flexural rigidity, Branson used the value of I_e (Eq. 2.20), and a constant secant modulus of elasticity of concrete, E_c (corresponding to a stress value of $0.50f'_c$ and equal to $57000\sqrt{f'_c}$, psi), for different load stages. It must be emphasized that the tangent modulus of elasticity of the concrete is a load dependent material property which decreases gradually with an increase in the applied load. It is also well established that the flexural rigidity, EI , is a sectional characteristic which depends on factors such as the geometry of the section, the material properties of the concrete and the reinforcing steel and the type and magnitude of applied load.

The present study questions the assumption of a constant flexural rigidity for the pre-cracking stage adopted by Branson and other investigators. This equation is not suitable for nonlinear finite element analysis of structural concrete members subjected principally to flexure, because it does not yield directly the tangent flexural rigidity of a given section at the various load stages (Fig. 2.3). In addition, it can be seen from Branson's equation, that the only load parameter included is the maximum moment, M_u , at the section for which the effective second moment of area, I_e , is estimated. This means that the effective second moment of area is the same for all identical beams loaded to the same level of moment, regardless of the type of loading applied. It is well known that the value of the effective second moment of area of a section is affected by the reinforcement ratios, ρ and ρ' , especially for heavily R C members. The most time-consuming value to compute is the cracking second moment of area, I_{cr} , especially for flanged members. It should be noted that Branson (1963) derived his equation for evaluation of deflection at the service load level, however, several investigators, have attempted to use it in their nonlinear analysis formulation with the obvious problems mentioned above.

According to the ACI Committee 435 (1972), "using deflection criteria of ACI 318-71, there is approximately a 90 percent chance that the deflections of a particular beam will be within the range of 20 percent less than to 30 percent more than the calculated value". However, several

investigators have shown that Branson's equation is the best practice-oriented tool to calculate deflections in normal and high-strength concrete beams (Mirza and Sabnis 1971, Pastor 1986).

2.1.6 Beeby's Method

Beeby (1968) proposed two methods to compute deflections based on a number of beam tests conducted at the British Cement and Concrete Association:

Method 1: The following equation represents an empirically modified bilinear model (see Fig. 2.2)

$$\Phi = \frac{M_{cr}}{E_c I_{ucr}} + \frac{(M - M_{cr})}{E'_c I'_c} \quad (2.22)$$

where $M_{cr} = f_r I_{ucr} / y$, $f_r = 0.62 \sqrt{f'_c}$, $E_c = 5000 \sqrt{f'_c}$ all in MPa, and I'_c is the second moment of area of the cracked transformed section using E'_c which is a reduced modulus of elasticity equal to $0.57E_c$. This equation can be used for calculating the curvature at an individual section based on the total moment at the section, M . A numerical procedure is then used to compute the deflections.

Method 2: An alternate and improved empirical method for constructing the bilinear moment-curvature diagram at individual sections is to define three coordinate points as $(0,0)$, $(M_{cr}, M_{cr}/E_c I_g)$, and $(M_Q, M_Q/E_c I_g)$, where M_Q = the ultimate moment resistance of the section, and M_{cr} is calculated using the gross second moment of area, I_g . The Beeby formula is in a form that can be incorporated directly into the finite element analysis because it introduces the flexural rigidity of a section. Jofriet and McNeice (1971) used Beeby and Branson's equations in nonlinear finite element analysis of R C slabs. They concluded that the Beeby method appears to give a better estimate of the flexural rigidity of a R C section than the Branson's method.

2.1.7 Recent Investigations

Other recent studies have established more simplified equations for evaluation of deflection. Grossman (1981) proposed the following relationships:

$$\frac{I_e}{I_g} = \left(\frac{M_{cr}}{M_a} \right)^2 \leq 1.0 \quad \text{if} \quad \left(\frac{M_a}{M_{cr}} \right) \leq 1.6 \quad (2.23)$$

$$\frac{I_e}{I_g} = 0.1 \left(\frac{M_a}{M_{cr}} \right) \quad \text{if} \quad \left(\frac{M_a}{M_{cr}} \right) > 1.6 \quad (2.24)$$

A lower bound for I_e/I_g of 0.35 was suggested. The value of I_e can be estimated without the need

to compute either the reinforcing steel or the value of I_{cr} for the member. Branson's equation was used to determine the "exact" values for the effective second moment of area in his study. Although Grossman's equations are simple to use, the effect of tension and compression reinforcements and loading type are neglected. In other words, they depend only on the gross second moment of area and the maximum and cracking moments at the section.

Another simple equation was proposed by Rangan (1982) as:

$$I_e = kbd^3 \quad (2.25)$$

where

$$k = 0.0019 / n\rho \leq 0.067 \quad \text{if } n\rho \leq 0.045 \quad (2.26)$$

$$k = 0.1955 \sqrt{n\rho} \leq 0.111 \quad \text{if } n\rho > 0.045 \quad (2.27)$$

where ρ is the tension reinforcement ratio, and n is the modular ratio. Although Eq. 2.25 recognizes the effect of the reinforcement ratio, ρ , it neglects other important parameters such as the load level which is represented by the moment ratios, M_s/M_{cr} , and the second moment of area of the cracked section I_{cr} .

Pulmano and Shin (1987) presented a simple finite-element method for predicting the instantaneous deflections of R C beams. The effective flexural rigidity, $E_c I_e$, proposed by Branson was adopted in their investigation.

According to the final version of the CEB-FIP Model Code (Final Draft, 1990), the deformations are calculated from the curvatures by applying appropriate procedures, such as the principle of virtual work or double integration.

Cosenza (1990) used different definitions of the effective second moment of area given by the CEB and Branson's equations to evaluate the stiffness matrix for R C beams by means of the flexibility coefficients, α_{hk} . The constant initial modulus of elasticity of concrete, E_c , was used to calculate the value of the flexural rigidity, EI_e , in the uncracked and cracked regions.

Al-Zaid et al. (1991) investigated experimentally the effect of three types of loading on the effective second moment of area, I_e . All beams were reinforced with the same amount of tension reinforcement ($\rho=0.01$). The results showed that the value of I_e was significantly affected by the type of loading. A simple modified form of Eq. 2.20 was proposed to account for the effect of the type of loading. The average values of power m in Eq. 2.20 have been suggested as 2.8, 2.3, and 1.8 for uniformly distributed loading, third point loading, and the midspan-concentrated

loading, respectively. A new model was proposed to account the effect of the loading type by considering the variations in the cracked length, L_{cr} , in the form

$$I_e = \left(\frac{L_{cr}}{L}\right)^{m'} I_{cr} + \left[1 - \left(\frac{L_{cr}}{L}\right)^{m'}\right] I_g \quad (2.28)$$

where $m' = M_{cr}/M_a$ and L is the beam span. The cracked length, L_{cr} , is defined as the beam segment over which the maximum moment exceeds the cracking moment, M_{cr} (Fig. 2.1). The cracked length formula for the different loaded beams are derived by Kheyroddin and Mirza (1994). Al-Zaid et al. did not consider the effect of the reinforcement ratio and variation of the flexural rigidity along the length of the beam in their studies. Also, the conventional elastic deflection formula was used to calculate the experimental second moment of area, I_{exp} .

The effective second moment of area of rectangular R C beams with different tension reinforcement ratios under a midspan concentrated load was evaluated experimentally by Al-Shaikh and Al-Zaid (1993). The values of m equal to 2.3, 1.9, and 1.4 in Branson's equation (Eq. 2.20) have been suggested for lightly, normally, and heavily reinforced sections, respectively. They observed that the use of the second moment of area of the uncracked transformed section, I_{ucr} , in Eq. 2.20, instead of the second moment of area of the gross section, I_g , for heavily reinforced section did not significantly improve the estimation of I_e . The effect of different types of loading, compression reinforcement ratio, ρ' , concrete tensile and compressive strengths, and the variation of the modulus of elasticity of the concrete during the loading were ignored in their investigations. As Branson mentioned, the power m does not have significant effect on the total calculation, especially for the values of the ratio M_a/M_{cr} larger than 2.5.

2.1.8 Deflection of High-Strength Concrete Beams

The increasing use of high strength concrete has resulted in the design of smaller sections which are more likely to contravene the serviceability criteria. The higher strength of materials is not accompanied by a proportional increase in the elastic modulus, and leads to greater strains and consequently larger deflections at the service load level. Thus, in structural design with high strength materials, serviceability conditions may be more critical than the strength considerations.

Swamy and Anand (1974) investigated experimentally the influence of the steel stress and the concrete strength on the deflection characteristics of high-strength concrete beams. Under short term loading, the measured deflections agreed closely with those predicted by the ACI standards. The ACI Committee 363 (State-of-the-Art Report on High Strength Concrete, 1992) reaccepted

Branson's equation (Eq. 2.20) for high-strength concrete beams.

Recent studies at Cornell University (Pastor 1986 and Paulson et al. 1989) showed that Branson's equation can be used to evaluate the deflections in high-strength concrete beams with reasonable accuracy. Paulson et al. (1989) compared the measured short term deflection of nine high-strength concrete beams with the values calculated using the ACI 318-83 Code method. The measured values were greater than those predicted using the ACI Code with a maximum difference of 21%.

2.1.9 Discussion and Basis for Further Studies

Some of the methods and guidelines to calculate the deflection of R C members have been discussed briefly in this chapter. A study of the previously proposed procedures showed that the use of the gross section second moment of area, I_g , underestimates the deflection, and the use of cracked transformed second moment of the area, I_{cr} , leads to an overestimation of deflection. For obvious reasons, most investigators have evaluated deflections only at the service load levels and they have not considered the post-yielding and failure stages. Also, they used a constant value of the secant modulus of elasticity of the concrete, E_c , for calculation of the flexural rigidity and deflection. However, the flexural rigidity, EI , is a sectional characteristic which depends on factors such as the geometry of the section, the material properties of the concrete and the steel and decreases gradually with an increase in the applied load. Most models do not yield directly the tangent flexural rigidity of a section after cracking but rather the secant rigidity, therefore they are not suitable for nonlinear finite element analysis of structural concrete. The effect of loading type, tension and compression reinforcement ratios, compressive strength of concrete, the concrete ultimate tensile strain, ϵ_m and the variation of EI along the beam length are normally not included explicitly in the previous models.

A review of the state-of-the-art in the area of evaluation of deflection of concrete beams, suggests a need for further modification of the EI equation for simple and continuous beams. New models are required to predict the flexural rigidity beyond the service load level at the various load stages up to the ultimate load. The effect of the influencing parameters including tension and compression reinforcement ratios and strengths, loading types and stages, compressive strength of the concrete, cracking and tension-stiffening must be investigated analytically.

The main objective of this research program is to establish new equations for calculation of flexural rigidity and deflection of reinforced concrete beams. In Chapter 5, an analytical

investigation of the flexural behaviour of R C beams has been undertaken and new equations are proposed to calculate the analytical cracking moment, $M_{cr,anal}$, cracking flexural rigidity, $(EI)_{cr}$, tangent flexural rigidity and the deflection of R C beams with reasonable accuracy. The tangent flexural rigidity equation can be incorporated in the modified stiffness approach for nonlinear finite element analysis of large R C frame structures subjected principally to flexure which would lead to significant savings in the required computational time. In Chapter 9, the proposed equations are implemented in the nonlinear finite element program, NAFS.

2.2 ULTIMATE DEFORMATION CHARACTERISTICS

It is well established that the inelastic behaviour of R C sections leads to a redistribution of moments which can increase the load bearing capacity of indeterminate structures. The degree of moment redistribution achieved depends on the rotation capacity of plastic hinging regions over which the steel yields or member has become inelastic. A properly designed member possesses adequate rotation capacity so that a successful redistribution of moments can occur. In this regard, Cohn (1964) pointed out:

"It would be ignoring reality to neglect the existence of strength reserve due to the inelasticity of reinforced concrete and not to take advantage of it only because imperfect, rather than ideal plasticity is proper to this material."

Inelastic behaviour of R C structures has also played an important role in the limit design methods.

2.2.1 Brief Review of Limit Design Methods

Limit design theories for R C structures have been proposed by Baker (1956), Macchi (1960), Sawyer (1964), Cohn (1965), and others. A historical review of the existing limit design theories in R C structures has been made by Hsu (1974) and Park and Paulay (1975). An annotated bibliography on limit design for R C structures was reported by Cohn in 1969.

Three basic requirements are specific to the limit design of concrete structures, namely:

- 1) Limit equilibrium implying that the distribution of bending moment is statically admissible.
- 2) Rotation compatibility implying that the rotation capacity of the plastic hinge regions is sufficient to enable the assumed distribution of moments to be developed at the ultimate load.
- 3) Serviceability implying that the cracking and deflections at the service load are not excessive.

The limit design methods will normally be used for frames and continuous beams. This method allows extensive moment redistribution using the elastic moment diagram. The main advantage of a limit design method is to choose the pattern of moment so as to avoid congestion of reinforcement at the supports of the member, which consequently results in an economical design. Kodur (1992) conducted a parametric study of redistribution of moments in continuous concrete beams. The effect of span-depth ratio, shape of the cross-section, position and type of loading, prestressing, concrete strength, confinement of the concrete and tension-stiffening were studied analytically. Extensive literature review of the redistribution of moment is also included in his thesis (Kodur 1992). Model clauses suitable for inclusion in a building code has presented by ACI-ASCE Committee 428 (1968), in a progress report on limit design. The model clauses presented can be used as the provisions for inelastic design in any code, along with the upper and the lower limits of force-deformation relationship. However, limit design methods have not been accepted by the building codes because the service load behaviour including cracking and deflections may not be satisfactory, also because the available limit design procedures are extremely complex to use in practice.

Any limit design method requires a knowledge of the plastic hinge length, l_p , and plastic hinge rotation, θ_p , in order to achieve full redistribution of bending moments. Here, the review is only restricted to the rotation compatibility.

2.2.2 Plastic Hinge Length and Rotation

Limit design methods for structural concrete normally assume that members have an elastic-perfectly plastic behaviour with limited ductility. The ultimate limit state is defined for the structure, or a part of it, and a collapse mechanism is normally developed at this load level. The occurrence of a collapse mechanism can be ensured only if at each structural joint the plastic rotation capacity of the section is larger than the plastic rotation required by the mechanism condition. The required rotations depend initially on the values of the bending moments and the flexural rigidity of the structural members. Here, the review is limited to the plastic rotation capacity of R C beams.

The moment-curvature characteristics of a given cross-section can represent the deformation properties of an R C section. As can be seen from Fig. 2.4, the schematic moment-curvature curve for under-reinforced beams which fail due to tension in the reinforcing steel consists of three stages. Typically, point "A" indicates the cracking point where the concrete starts

cracking (ϕ_{cr} and M_{cr}). In the initial stages ($M < M_{cr}$), the response is elastic and linear. With an increase in the applied moment, the cracking of the concrete reduces the flexural rigidity of the section and this reduction depends on the amount of the reinforcement. At a higher load level, (point "B"), the tension steel begins to yield (ϕ_y and M_y), followed by the crushing of the concrete (ϕ_u and M_u at point "C"). A large increase in curvature and ductility normally occurs beyond the yield load.

The rotation of the member can be determined from curvature distribution along the member length. Based on first moment area theorem, the rotation (change of slope) between any two points, e.g., along the beam is equal to the area under the curvature diagram between these two points. It is given by

$$\theta_{AB} = \int_A^B \phi dx \quad (2.29)$$

where x is the distance of element dx from A. This equation can be applied whether elastic or inelastic curvatures are involved.

The conditions at the ultimate load stage of a cantilever beam subjected to uniform load is shown in Fig. 2.5. For values of loads smaller than the yielding moment, M_y , the curvature increases gradually from the free end of a cantilever (point A) to the column face (point B). There is a large increase in curvature at first yield of the tension steel. At the ultimate load stage, the value of the curvature at the support increases suddenly so that it causes a large inelastic deformation. Since the concrete between the cracks can carry some tension (tension-stiffening), the curvature fluctuates along the beam length. Each of the peaks of curvature corresponds to a crack location. The actual distribution of curvature at the ultimate load stage can be idealized into elastic and inelastic (plastic) regions (Fig. 2.5c), thus the total rotation, θ_t , over the beam length can be divided into elastic, θ_e , and plastic, θ_p , rotations. The elastic rotation, θ_e , (until yielding of steel) can be obtained using the curvature at yielding (Eq. 2.29). According to Eq. 2.29, the plastic rotation can be determined, on each side of the critical section, as:

$$\theta_p = \int_0^{l_y} [\phi(x) - \phi_y] dx \quad (2.30)$$

in which $\phi(x)$ is the curvature at the distance of x from the critical section at the ultimate load stage. The yielding length, l_y , is defined as the beam segment over which the maximum moment exceeds the yield moment, M_y , or the distance between the critical section and the location where

tension steel first yields (Fig. 2.5).

The shaded area in Fig. 2.5c is the plastic (inelastic) rotation, θ_p , that occurs in addition to the elastic rotation at the plastic hinge at the ultimate load stage. The plastic hinge rotation can be determined either by the calculation of shaded area or by an equivalent rectangle of height $(\phi_u - \phi_y)$ and width l_p . Using Eq. 2.30, the equivalent plastic hinge length, l_p , can be defined as:

$$l_p = \frac{1}{(\phi_u - \phi_y)} \int_0^{l_y} [\Phi(x) - \phi_y] dx \quad (2.31)$$

Therefore, the value of plastic hinge rotation, θ_p , at ultimate stage can be calculated easily by the following well-known equation:

$$\theta_p = (\phi_u - \phi_y) l_p = \phi_p l_p = \beta' \phi_p l_y \quad (2.32)$$

where ϕ_u and ϕ_y are the curvatures at the ultimate load and yielding, respectively and l_p is the equivalent length of the plastic hinge over which the plastic curvature, $(\phi_p = \phi_u - \phi_y)$, is assumed to be constant. Equation 2.32 results in the same area as the actual plastic curvature distribution (Shaded area in Fig. 2.5c). The dimensionless factor β' is a shape factor or curvature distribution factor for the curvature diagram near the support and is less than 1. It may also be called a reduction factor of the yielding length over which the steel reinforcement yields, so that $\beta' l_y = l_p$.

2.2.3 Governing Parameters for the Rotation Capacity of Plastic Hinges

The plastic hinge rotation, θ_p , of R C beams depends on a number of parameters including the definition of yielding and ultimate curvatures, section geometry, material properties, compression and tension reinforcement, transverse reinforcement, cracking and tension-stiffening, the stress-strain curve for the concrete in tension and compression, the stress-strain curve for steel, bond-slip characteristics between the concrete and the reinforcing steel, support conditions and the magnitude and type of loading, axial force, width of the loading plate, influence of shear, and the presence of column. The steel type and the concrete strength affect the shape of moment-curvature and consequently they will influence the yielding length and distribution of curvature in the yielding zone.

As shown by Macchi (1964) and other investigators, a limited reduction of the rotation capacity occurs if a column is present at the support section of a beam. Inclined cracks due to shear cause spreading of the plastic zone and thus to increase the rotation capacity, provided that

the shear failure is prevented. Also, the value of z , the distance between critical section and the point of contraflexure, has a significant effect on the plastic hinge length, l_p . An increase in the value of z , results in an increase in the value of l_p . Based on the experimental study carried out by CEB (1968), the neutral axis depth at the ultimate limit state was observed to be the main governing parameter among those investigated. A discussion of the parameters governing the plastic rotation capacity, and of the existing θ_p expressions can be found in the work by Burnett (1973), Park and Paulay (1975), and Riva and Cohn (1990, 1994).

2.2.4 Definitions of the Yielding and Ultimate Limit States

Generally, the proposed method for calculation of θ_p is developed by accepting the various idealizations of the moment-curvature constitutive relationships, as shown in Fig. 2.6. In the limit design method, a bilinear $M-\phi$ curve (elastic-perfectly plastic behaviour) is used (Fig. 2.6a, Baker and Amarakone 1964). The limits L_1 and L_2 are idealized as elastic and plastic limits, respectively. Bilinear curve in Fig. 2.6b was used by Sawyer et al. (1956), tri-linear $M-\phi$ curve in Fig. 2.6c adopted by Chan (1955), and the more elaborate $M-\phi$ curve in Fig. 2.6d utilized by Riva and Cohn (1990, 1994). The common features of these models are the definition of the yielding and the ultimate load stages. In R C sections, the yielding curvature is well defined as a point that coincides with the yielding of the reinforcing steel. Generally, there are four common definitions for the ultimate limit state in the literature:

a) The deformation corresponding to a particular limiting values for the concrete compressive strain or for both steel and concrete ultimate strains. Although this approach is simple to use and it is widely accepted (for example, this formula has been adopted by the ACI Code since 1963), ϵ_{cu} depends on several variables and is difficult to predict exactly.

In the ACI 318-83 Building Code, the ultimate limit state is based implicitly on the assumption of a limit strain for concrete ($\epsilon_{cu}=0.003$), while in CEB Model Code (1978) it is based explicitly on both the steel and the concrete ultimate strains i.e. $\epsilon_{su}=0.01$, and $\epsilon_{cu}=0.0035$. Although the ultimate concrete strain values ($\epsilon_{cu}=0.003$ or 0.0035) are satisfactory for the evaluation of the ultimate strength, they are very conservative for deformation analysis and moment redistribution. The ultimate steel strain limitation of $\epsilon_{su}=0.01$ in the CEB Model Code (1978) is excessively conservative, while the absence of a steel strain limitation in the ACI (1983) and the CSA Standards (1984) is unconservative.

b) The definition corresponding to the maximum moment capacity,

- c) The definition based on the post-peak deformation when the load carrying capacity has undergone a small reduction, and
- d) the definition based on the deformation when the longitudinal or transverse reinforcing steel fractures, or the longitudinal compression reinforcement buckles.

However, the most realistic definition for the available deformation at the ultimate load is given by Items c and d above.

2.2.5 Ultimate Compressive Strain of Concrete

As mentioned in Section 2.2.4, the ultimate limit state and the ultimate curvature of a structural concrete member is usually assumed to be reached when an ultimate compressive strain, ϵ_{cu} , is reached in the concrete. A difficulty with this method is that ϵ_{cu} depends on several variables, including the shape of compressed area of the member section, the ratio of neutral axis depth to the member section depth, confined or unconfined concrete stress-strain relationship and the stress-strain curve of steel. Since the effect of all variables cannot be included in one expression, generally the ϵ_{cu} values, which have been suggested, have resulted in conservative estimates of the ultimate curvature. For example, the ACI 318-63 Building Code adopted a single and very conservative value of 0.003 for ϵ_{cu} . Although the moment capacity of the beam is relatively independent of the range of values assumed for the concrete ultimate strain, the value of ultimate curvature depends very much on ϵ_{cu} .

Adopting Eq. 2.32, the study of the plastic hinge rotation will be limited to the calculation of plastic curvature ($\phi_u - \phi_y$) and the equivalent plastic hinge length. Plastic curvature depends on the deformational properties of the concrete section (including the shape of the concrete section, the strength of the concrete and the steel, and the amount of tension and compression reinforcement) and the depth of neutral axis at yield and ultimate loads. The plastic rotation at the ultimate load stage is given by

$$\theta_p = (\Phi_u - \Phi_y) l_p = \left(\frac{\epsilon_{cu}}{c} - \frac{\epsilon_{ce}}{kd} \right) l_p \quad (2.33)$$

where c and ϵ_{cu} are neutral axis depth and the ultimate compressive strain of the concrete at the ultimate moment, respectively. kd and ϵ_{ce} are the neutral axis depth and the concrete compressive strain when the yield curvature is reached, respectively. Experimental study by a number of investigators has resulted in the development of several empirical equations for ϵ_{cu} .

Mattock (1964) reported the results of 37 tests on simply-supported under-reinforced

beams subjected to concentrated and two-point loading. The effects of the concrete strength, depth of beam, the distance from the location of the maximum moment to the point of zero moment, z , and the amount and yield strength of reinforcement on the $M-\phi$ relationship were investigated. He proposed a safe method to calculate the ultimate concrete compressive strain as:

$$\epsilon_{cu} = 0.003 + \left(\frac{0.5}{z} \right) \quad (2.34)$$

where z is measured in inches. The ultimate compressive strain of the concrete and the ultimate curvature in a R C beam subjected to concentrated load at critical section can be very much in excess of that for the usually assumed values of 0.003 for ϵ_{cu} . In a region of constant moment this equation provides a value of 0.003, as suggested by the ACI 318-83 Building Code. The effect of confinement of the concrete in compression, and the effect of the member size were not included in Mattock's equation (Eq. 2.34). Mattock calculated the values of ultimate curvature, ϕ_u , from the experimental data using the equation:

$$\phi_u = \frac{\epsilon_{cu}}{c} \quad (2.35)$$

where c is neutral axis depth. In his derivation, Mattock employed the concept of the equivalent stress-block for the concrete compression zone. For a given span, the curvature at the ultimate load decreases as the tension reinforcement index, ω , increases. Based on Eq. 2.35, the curvature is inversely proportional to the value of c , which at ultimate stage varies directly as the tension reinforcement index, ω . Therefore, the ultimate curvature decreases as the tension reinforcement index increases. An increase in the compression reinforcement will reduce the neutral axis depth and hence increase the curvature. This equation was confirmed by Corley (1966) and verified by Ghosh (1972).

Based on the results of 77 tests on simply supported beams, Corley (1966) suggested the following empirical equation as the lower bound of the maximum concrete strain:

$$\epsilon_{cu} = 0.003 + 0.02 \frac{b}{z} + \left(\frac{\rho_s f_y}{20} \right)^2 \quad (2.36)$$

where b is width of beam, and z is equal to half span length for simply supported beam, d is the effective depth at the critical section in inches, ρ_s is the ratio of volume of confining steel including the compression steel to the volume of the concrete core, and f_y is the yield strength of the confining steel in kips per square inch. The value of z depends on the span length and the type

and position of loading. The simpler and more conservative form of Eq. 2.36, was suggested by Mattock (1967) as:

$$\epsilon_{cu} = 0.003 + 0.02 \frac{b}{z} + 0.2 \rho_s \quad (2.37)$$

Scott et al. (1982) proposed, as an approximate lower bound, that the ultimate concrete compressive strain for confined concrete can be taken as:

$$\epsilon_{cu} = 0.004 + 0.9 \rho_s \left(\frac{f_{yh}}{300} \right) \quad (2.38)$$

where ρ_s is the ratio of volume of hoop reinforcement to the volume of the core measured to the outside of the hoops and f_{yh} is the yield strength of the hoop reinforcement (MPa). For a beam in a typical plastic hinge region, ϵ_{cu} can be even greater than 0.01. For unconfined concrete, where ρ_s is zero, the maximum usable strain value is 0.004.

Some procedures for determination of the yielding and the ultimate moment and curvatures have been proposed by Cohn (1964), Mattock (1964) and Park and Paulay (1975).

2.2.6 Empirical Expressions for Plastic Hinge Length and Rotations

The plastic hinge length, l_p , depends on a number of parameters and a number of empirical relationships are available for predicting this length. The length of a plastic hinge is difficult to calculate in most cases, because of its sensitivity to some factors such as the loading conditions. General expression for the plastic hinge length, l_p , is valid at loads above the yielding loads, provided l_y and $\phi(x)$ are known at these load stages (Eq. 2.31). Both l_y and $\phi(x)$ are functions of the material and sectional properties as well as the loading history. Due to the complexity of the problem, the appropriate procedures have been defined for practical purposes. In this section, some popular expressions for the calculation of plastic hinge length and rotation are presented for completeness.

In order to estimate θ_p using equation 2.32, the equivalent plastic hinge length, l_p , must be known. By relating the actual behaviour to the idealized behaviour, a safe empirical method of calculating l_p was first suggested by Baker (1956) as:

$$l_p = k_1 k_2 k_3 \left(\frac{z}{d} \right)^{0.25} d \quad (2.39)$$

where k_1 is equal to 0.7 for mild steel or 0.9 for cold-worked steel, $k_2 = 1 + (0.5P_u/P_0)$ in which P_u

is axial compressive force and P_0 is load capacity as an axially loaded column, and k_3 is 0.6 when $f'_c=5100$ psi or k_3 is 0.9 when $f'_c=1700$ psi. This equation was developed for members with unconfined concrete. For a broad range of structural members, this equation results in a range of values for l_p from about 0.4 to 2.4 d .

For members confined by transverse steel, Baker and Amarakone (1964) proposed an expression for l_p for members with tension over part of the section

$$l_p = 0.8 k_1 k_3 \left(\frac{z}{d} \right) c \quad (2.40)$$

where c is the neutral axis depth at the ultimate moment.

Chan (1962) suggested the following empirical equation in terms of a curvature distribution factor, β' (measured from tests):

$$\theta_p = \beta' l_y M_u \left(\frac{1}{EI_u} - \frac{1}{EI_e} \right) \quad (2.41)$$

where EI_u and EI_e are flexural rigidity at the ultimate and the yielding stages, respectively (limit L_2 and L_1 as shown in Fig. 2.6a) .

From the test results of 37 simply supported beams, Mattock (1964) developed an empirical form for the prediction of the rotational capacity of the hinging regions which assumed the length of a plastic hinge to be equal to the half of the effective depth of beam i.e. $d/2$ at the support section for simply supported beams under a central (midspan) load. The ultimate plastic hinge rotation, θ_u , at the critical section obtained from Eq. 2.32 using an average curvature over a length of $0.5d$. The total inelastic rotation at ultimate, θ_m , over the length, z , was assumed to be concentrated at the point of maximum moment and obtained from the measured plastic deflection at midspan. The spread of plasticity along the beam away from critical section was found to increase with an increase in the ratio z/d , and with a decrease in the net tension reinforcement index ($\omega-\omega'$) at the critical section. If strain-hardening of the reinforcement is not taken into account, the depth of the neutral axis will probably be underestimated, and hence the available rotation will be overestimated. The assumption of the concentration of inelastic rotation at the critical section can lead to inaccurate results.

Corley (1966) investigated the effect of size, beam width, reinforcement index, and binding by closed stirrups on the inelastic behaviour of 77 simply supported beams and proposed the following equation for the equivalent plastic hinge length:

$$l_p = 0.5 d + 0.2 \sqrt{d} \left(\frac{z}{d} \right) \quad (2.42)$$

A measure of total inelastic rotation was obtained in the same manner as that used by Mattock (1964).

Later, the following equation was proposed by Mattock (1967), which is conservative in nature and of a simpler form of Eq. 2.42:

$$l_p = 0.5 d + 0.05 z \quad (2.43)$$

Sawyer (1964) suggested the following equation:

$$l_p = 0.25 d + 0.075 z \quad (2.44)$$

The zone of yielding was assumed to extend a distance $d/4$ beyond the section where the bending moment is reduced to M_y . It is noted that l_p is the equivalent plastic hinge length on one side of the critical section.

Extensive experimental and analytical investigations show large variations in the plastic hinge length in R C hinges assumed to be between $0.4d$ to $2.4d$ in length (Hsu 1974). In fact, the assumption of a constant plastic hinge length implies that the effects of the structural layout, magnitude and the type of load on the inelastic rotation are neglected. Most proposed equations have been presented as function of z , which is constant only for simply supported and cantilever beams. For statically indeterminate beams, however, the value of z varies throughout the loading history; it can either increase or decrease with the loading, depending on the reinforcement detailing of beam, span length, the type and position of loading, the section considered, and the end constraints.

Cohn (1964) proposed a simple and rational technique to check the rotation compatibility of plastic hinges in R C continuous beams designed using the limit design method,- referred to as "optimum limit design approach". Appropriate expressions for both the plastic rotations and the rotation capacities of plastic hinges were derived. Constant values of $l_p = (1/15)L$ and $\epsilon_{cu} = 0.0035$ were adopted in the calculation, where L is the span length. For beams subjected to concentrated loads, the following simple equation was proposed:

$$\frac{l_p}{z} = 1 - \frac{M_y}{M_u} \quad (2.45)$$

Macchi (1964) suggested an upper and lower limit of θ_p as functions of c/d . Based on the experimental study, the neutral axis depth at the ultimate limit state appeared to be the main governing parameter among those investigated. Siviero (1974) proposed an empirical θ_p - c/d curve (Fig. 2.7), derived based on the statistical evaluation of 350 available experimental results (performed by different investigators between 1960 and 1970). The rotation capacity increases significantly with a decrease in the c/d ratio values. This expression of θ_p was later adopted by the CEB-FIP Model Code 78 (1978). The limitation of formulation adopted by the CEB is that important factors such as the type of structure, the height-to-span ratio and the distribution of curvature are not considered. The scatter of experimental measurements used by Siviero was very large (Fig. 2.7), indicating that the various authors measured the limit rotation of the specimens in different ways. In this case, a statistical evaluation is relatively meaningless.

Influence of the width of loading plate on the rotation capacity of R C members was studied experimentally by Chandrasekhar and Falkner (1974). Plastic rotation of simply supported beams was calculated using two methods:

1) Using the midspan deflections:

$$\theta_p = (\Delta_u - \Delta_y) / (L/2) \quad (2.46)$$

where L is span length and Δ_y and Δ_u are deflection at midspan corresponding to the yield load and the maximum load, respectively.

2) Using the end slopes

$$\theta_p = (\theta_u - \theta_y) \quad (2.47)$$

where θ_y and θ_u are rotations of the member corresponding to the yield load and the maximum load, respectively. It was figured out that the rotation capacity of the hinging regions is influenced considerably by the width of the loading plate. The inelastic rotation is considerably reduced when loads are applied to test beams through narrow bearing plates (because of the decreased length of the plastic hinge).

The influence of the length of the constant bending moment zone on the plastic rotation of beams subjected to third-point loadings was studied by Lenkei (1974). It was noted that the

inelastic rotation were considerably lower for longer constant bending moment lengths.

In a more recent study, Eligehausen and Langer (1987a, 1987b) and Eligehausen et. al. (1993) investigated the effect of the stress-strain curve for steel, percentage of reinforcement, beam span and depth, concrete confinement, shear cracks, and the width of the loading plate. They pointed out that the degree of moment redistribution allowed by the expression adopted in CEB (1978) may be unconservative in some cases such as lightly reinforced sections and for beam reinforced with cold worked deformed bars. The plastic rotation capacity was significantly influenced by the stress-strain relationship of the tension reinforcement. They suggested a modification of the CEB curve to account for the variations in the behaviour of such sections when brittle or ductile steels are used. This proposal has been adopted in the latest versions of the CEB-FIP Model Code (final draft, 1991). The model is based on the integration of the section curvature along the beam. In this approach, the effects of loading distribution, and the section shape are neglected. A recent experimental investigation of the CEB plastic rotation formula has been conducted on simply supported beams subjected to one or three symmetrical loads by Bosco and Debernardi (1993). It was observed that, in general, when comparing experimental and theoretical values, the agreement is closer when dealing with deep beams while the scatter in the results is much higher when low-depth beams are tested.

Based on an analytical study on continuous beams, Scholz (1993) defined the following expression for plastic hinge rotation to one side of the hinge:

$$\theta_p = \frac{L}{2EI} \left(\frac{wL^2}{12} - M'_u \right) \quad (2.48)$$

where L is beam span, EI is constant and is the product of the modulus of elasticity and the second moment of area, w is the magnitude of the uniformly distributed load and M'_u is the ultimate design moment at the support. He used Mattock's equation (Eq. 2.43) for calculation of l_p with an assumed value of $z=0.18L$. The variation of EI along the beam span and the variation of z throughout the loading history were neglected.

It has been suggested by many researchers, e.g. Hillerborg (1989), that the rotational capacity is size-dependent, approximately inversely proportional to the beam depth. Bigaj and Walraven (1993) investigated experimentally the size effect on the rotational capacity of plastic hinges in R C beams. It was found that the complete stress-strain curve of concrete in compression is size-dependent, thus it has a significant effect on the rotation capacity. Elements with smaller dimensions show a much more ductile response to the load, i.e. much higher plastic rotations, than

the elements with the same characteristics but larger dimensions. For a reinforcement ratio of 1.12%, a decrease by a factor of 4 was observed in rotational capacity, as the effective height of the beam was increased from 90 mm to 450 mm.

The recent comprehensive research work on rotation capacity of structural concrete members was undertaken by Riva and Cohn (1990, 1994). The relatively simple lumped-plasticity model was used in all of this work (Riva and Cohn 1990, 1994). In this model, the structure is discretized by linear-elastic elements, with the behavioral nonlinearity lumped at rigid-plastic joints, for which a piecewise linearized rigid-plastic moment-rotation law is assumed. In fact, the model assumes linear elastic elements, with the material nonlinearity lumped at the element ends. The local moment-curvature constitutive relationship is determined from the study of an element length equal to the crack spacing l_c , assuming the moment to be constant along the element, and expressing the compatibility and equilibrium conditions at the cracked section. For sections failing due to the concrete crushing (highly reinforced rectangular sections), the ultimate limit state was assumed to correspond to the maximum moment capacity. For other sections, the ultimate limit state was identified by reinforcing steel reaching a limiting strain (i.e., $\epsilon_{st}=0.03$).

Riva (1988) and Riva and Cohn (1990) performed a parametric study of the moment-curvature relationship and the plastic hinge length by nonlinear analysis of 56 simply supported beams and 32 cantilevered reinforced and prestressed beams. The influence of load distribution, percentage of tension steel, shape of the section, support conditions and prestressing were studied. Since the distance z in continuous beams varies throughout loading history, statically determinate R C beams were studied. The plastic rotation was obtained considering a constant plastic curvature distribution along the half-element (i.e., $\theta_p = \phi_p l_e / 2$, where l_e is the element length and equal to approximately $z/100$). The influence of the various material parameters was not investigated. It was noted that the values of the plastic rotation at the critical section were quite sensitive to the adopted element length in the analysis, because of the assumption of constant curvature over the element length. The results showed that the l_p/z ratio is not sensibly affected by the variation of the z/h ratio (where h is the section height), and is influenced mostly by the bending moment distribution and the steel percentage. Based on the analytical results, the approximate expressions were proposed for l_p/z for three different loading phases:

- 1) From cracking to yielding limit state:

$$\frac{l_p}{z} = \left(A - \frac{B}{800 \omega} \right) \left(\frac{\phi_p}{\phi_{py}} \right)^{(c/80 \omega)} \left(\frac{b'}{b_w} \right)^{-(D/640 \omega^2)} f(\gamma) \quad (2.49)$$

2) From yielding to reinforcement strain-hardening:

$$\frac{l_p}{z} = \left(\frac{l_p}{z} \right)_y \left(\frac{\phi_p}{\phi_{py}} \right)^{-(0.9-0.8\gamma)} \quad (2.50)$$

3) Ultimate limit state (only if $\phi_{pu} / \phi_{py} > 7.0$):

$$\frac{l_p}{z} = \left(\frac{E}{100} + \frac{F}{1000} \frac{\phi_{pu}}{\phi_{py}} \right) \left(\frac{b}{b_w} \right)^G \quad (2.51)$$

where $(l_p/z)_y$ in Eq. 2.50 is the value of l_p/z from Eq. 2.49 when $\phi_{pu}/\phi_{py}=1$, b is width of the compression flange, and b_w is web width. The constants A, B, C, D, E, F, G and $f(\gamma)$ depend on the bending moment distribution considered and can be found elsewhere (Riva 1988). The parameters ϕ_{pu} and ϕ_{py} are shown in Fig. 2.6d. For example, for simply supported beam subjected to uniformly distributed load, the values of A, B, C, D, E, F, G are 0.58, 3.0, 3.5, 3.0, 5.0, 6.5, and 0.5, respectively.

In the latest published research work on rotation capacity of structural concrete members by Riva and Cohn (1994), attention was given to the plastic rotation capacity at the ultimate limit state. It was noted that neglecting the influence of the loading distribution may lead to non-conservative results. It was found that for lightly reinforced sections ($\rho < 0.004$, steel failure), plastic rotation capacities increase, while for highly reinforced sections ($\rho > 0.004$, failure of compression zone), plastic rotation capacities decrease, with increasing reinforcement index values. Distributed loads on a simply supported beam lead to θ_p values varying from five times to twice as high as those corresponding for a concentrated load on a simply supported beam or a distributed load on a cantilever beam respectively (Riva and Cohn 1994).

Although Riva and Cohn's proposed formulation is valid at any load stage, and considers the effect of moment distribution and shape section, it is difficult to use in practice due to complexities of the model. However, the proposed model (Eq. 2.49 through Eq. 2.51) was implemented into the lumped-plasticity program, STRUPL-1C, developed by Riva (1988) and comparison of the experimental and analytical results showed that the new model can be used with reasonable accuracy. The plastic rotation obtained from Eqs. 2.50 and 2.51 is the total inelastic rotation from the onset of inelastic behaviour i.e. cracking of concrete. Limitations of the STRUPL-1C program are related to the fact that only first-order, flexural, static actions are considered (Riva and Cohn 1990).

2.2.7 Ductility

The term "ductility" refers to the ability of a structure to undergo large deformations in inelastic range (after yielding). Generally, the ductility ratio is defined by the ratio of the ultimate limit state deformation to that at yielding. Ductility ratios have been commonly defined in terms of displacement, rotation and curvature. A measure of the ductility required of a structure or member is the displacement ductility ratio, μ_{Δ} , defined as $\mu_{\Delta}=\Delta_u/\Delta_y$. The ductility of R C section can be defined by the curvature ductility ratio, $\phi_{\mu}=\phi_u/\phi_y$. The relationship between these two factors is illustrated by Park and Paulay (1975). Several researchers investigated the ductility of R C structures in seismic design and the related energy absorbing characteristics, inelastic moment redistribution, detailing, etc. A state-of-the-art report on ductility has been prepared by Park (1988).

In fact, all factors affecting plastic curvature, ($\phi_p=\phi_u-\phi_y$), would also influence the curvature ductility ratio. Major factors affecting the ductility are:

- a) Definition of yielding and ultimate curvatures, and the ultimate limit state,
- b) Material properties such as the stress-strain curve of the concrete in tension and compression, steel type and the stress-strain curve, bond-slip characteristics, and the strain-hardening behaviour,
- c) Geometric parameters such as the shape of the section, tension and compression reinforcement index, and stirrups, and
- d) Loading parameters such as axial force, loading distribution and loading repetition.

Experimental work on ductility was carried out by several investigators including Cohn (1964) and Mattock (1964). The effect of the different variables such as stirrups, steel fibers and compression reinforcement on the ductility was investigated experimentally by Shah and Rangan (1970). The results showed that stirrups were most effective in increasing the ductility of the over-reinforced beams. Use of fibers were less effective, while the compression reinforcement was the least effective. Later, Ghosh (1971) criticized Shah and Rangan's conclusions (1970) and pointed out that based on the experimental results, compression reinforcement was found to be more effective than the lateral ties in providing sectional ductility.

The available ductility of doubly R C beam sections with a range of tension and compression reinforcement ratios and strengths of steel and concrete were derived by Park and Ruitong (1988). The value for the ultimate concrete compression strain was assumed to be $\epsilon_{cu}=0.004$. It was found that, with other variables maintained constant, the available curvature ductility ratio, $\phi_{\mu}=\phi_u/\phi_y$, is increased, with a decrease in the tension steel ratio ρ , an increase in

the compression steel ratio ρ' , a decrease in the steel yield strength f_y , and an increase in the concrete compressive strength f'_c .

A parametric study was conducted by Cohn and Riva (1991) to examine the effect of the basic parameters that govern the curvature ductility ratio. Based on the analytical results, some ACI Code revisions were proposed.

A simple expression for the ratio of curvature at the ultimate load and at the first yield, ϕ_u/ϕ_y , for continuous beams was proposed by Scholz (1993). He figured out that for many practical continuous beams, it is sufficient to concentrate on meeting the deflection limit. The ductility requirement and thus the capacity for moment redistribution are then automatically satisfied.

2.2.8 Ultimate Deformation of High-Strength Concrete Beams

Perhaps the earliest study on the deformability of high-strength concrete beams was undertaken by Leslie et al. (1976). The results of 12 under-reinforced rectangular beams showed that with an increase in the concrete strength, the ultimate compressive strain becomes progressively smaller. As the tension reinforcement ratio increased (from 0.01 to 0.027), the displacement ductility ratio decreased from 6.0 to 1.8.

A comprehensive investigation on the ultimate deformation of high-strength concrete beams was carried out by Pastor (1986). As mentioned in Section 2.2.5, expressions most commonly used to predict ϵ_{cu} are generally independent of the concrete compressive strength, f'_c . The test results showed that the limiting compressive strain of unconfined concrete in flexure, ϵ_{cu} , decreases with increasing concrete strength. A new expression was proposed as:

$$\epsilon_{cu} = 0.00364 - 4.086 \times 10^{-8} f'_c \quad (2.52)$$

for rectangular unconfined concrete sections with $f'_c \leq 12,000$ psi. This equation is not as conservative for high-strength concrete as it is for normal-strength concrete. It was observed that an overall reduction in both curvature and displacement ductility factors with increasing tension reinforcement.

The flexural ductility of ultra-high-strength concrete members (concrete strength ranging up to 103.4 MPa) was studied experimentally by Shin et. al. (1989). The test variables were concrete strength, amount of longitudinal reinforcement, and spacing of ties. The confinement reinforcement spacing, within the range studied, did not have an appreciable effect on member

ductility. The ductility of high-strength concrete beams was generally higher than those of beams with moderate concrete strength.

2.2.9 Discussion and Basis for Further Studies

Test results for θ_p show considerable scatter, due mainly to the definition of ultimate limit state, different testing procedures, dimensions of specimen and loading plate, and the method of application of load on the beam. Although it has become common practice to use the terms "plastic hinge" and "critical section" or concentration of plastic rotations in critical sections, the properties of the plastic hinge are not actually the properties of individual critical sections. In fact, the assumption of a constant plastic hinge length implies that the effects of the structural layout, magnitude and the type of load on the inelastic rotation are neglected.

Although some procedures have been proposed to calculate the plastic hinge length and the inelastic rotation capacity, there is no general agreement on the inelastic behavioral characteristics of R C beams. The nature and complexities of the problems discussed in this chapter are such that further research is needed to clarify the influence of different factors such as loading type and the reinforcement ratio. In fact, the effect of the reinforcement ratios, concrete tensile and compressive strengths, loading types and stages, cracking and tension-stiffening, the effect of magnitude and type of loading on the plastic hinge rotation, θ_p , should be taken into account.

A nonlinear layered finite element program (NONLACS2) is used for determination of the yielding length, plastic hinge length and the plastic hinge rotation. The advantage of the present study is that the yielding length and the "exact" value of plastic rotation (shaded area in Fig. 2.6) can be determined without using the idea of an equivalent plastic hinge length. The effect of the tension reinforcement index and the loading type on the ultimate deformations of R C beams is investigated in Chapter 6 and new equations are developed to consider the influence of the various parameter on the calculation of the plastic hinge rotation.

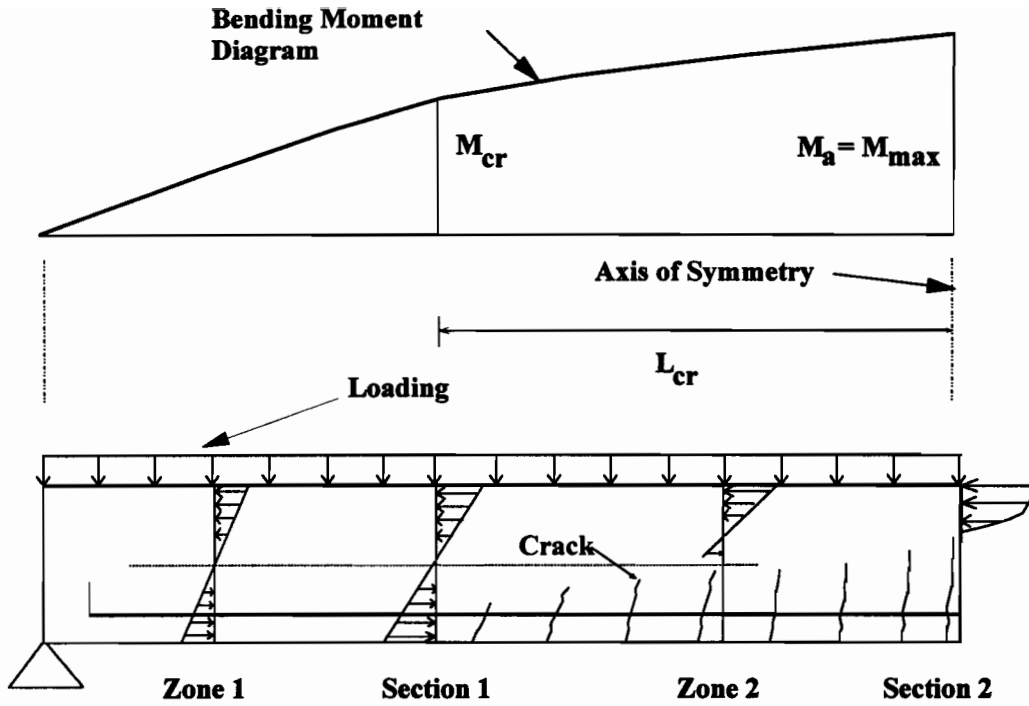


Figure 2.1: Stress distribution and cracking in different regions of a reinforced concrete beam

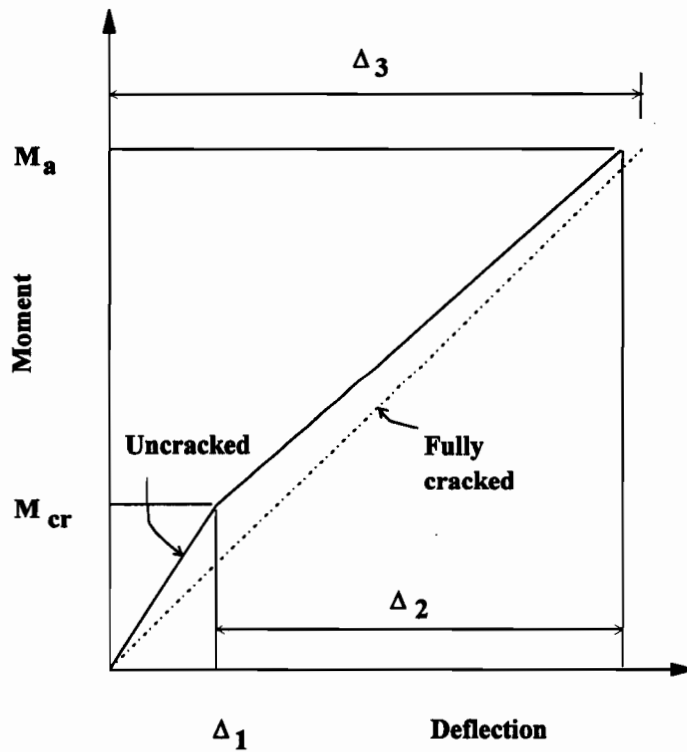


Figure 2.2: CEB bilinear moment-deflection curve

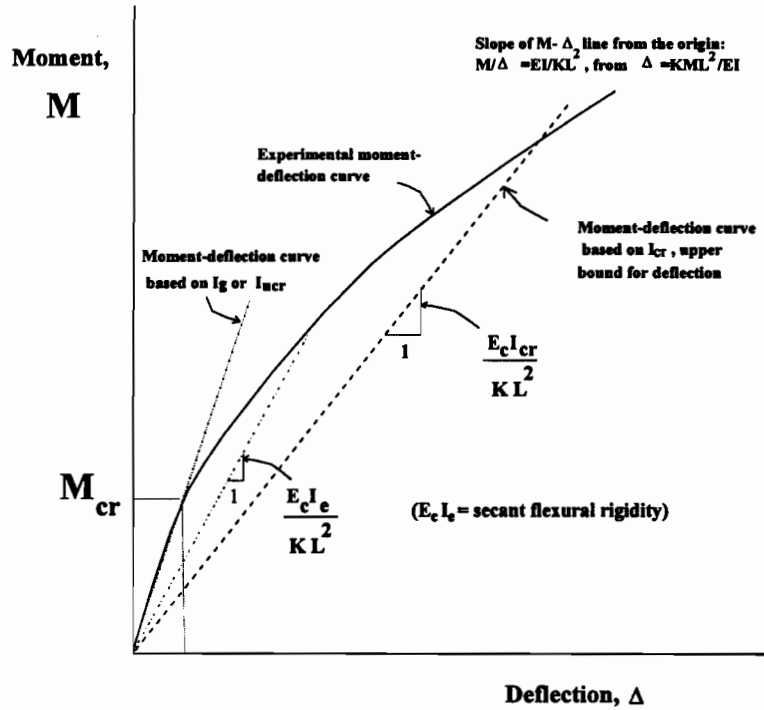


Figure 2.3: Typical moment-deflection curve for a reinforced concrete flexural member

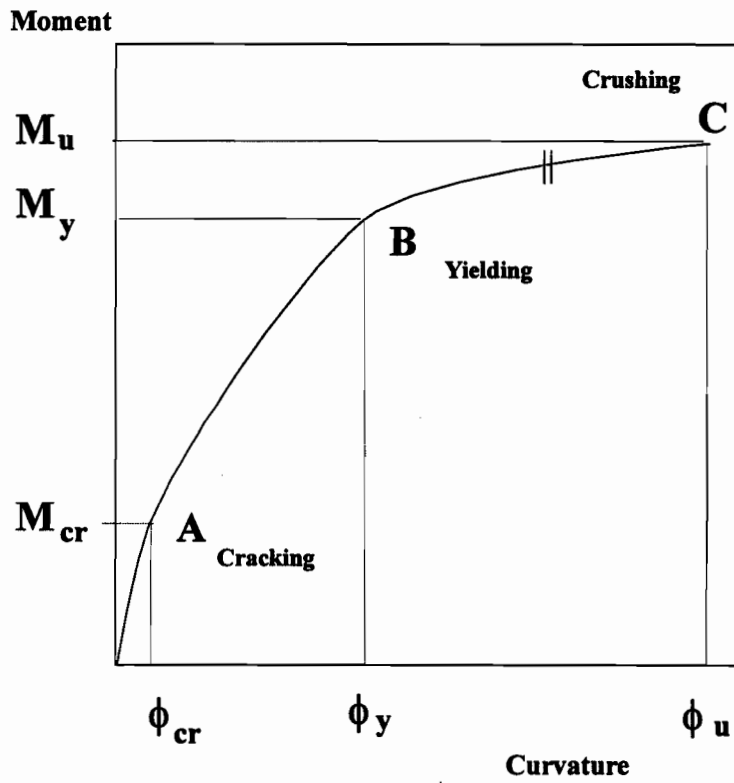


Figure 2.4: Qualitative moment-curvature relationship

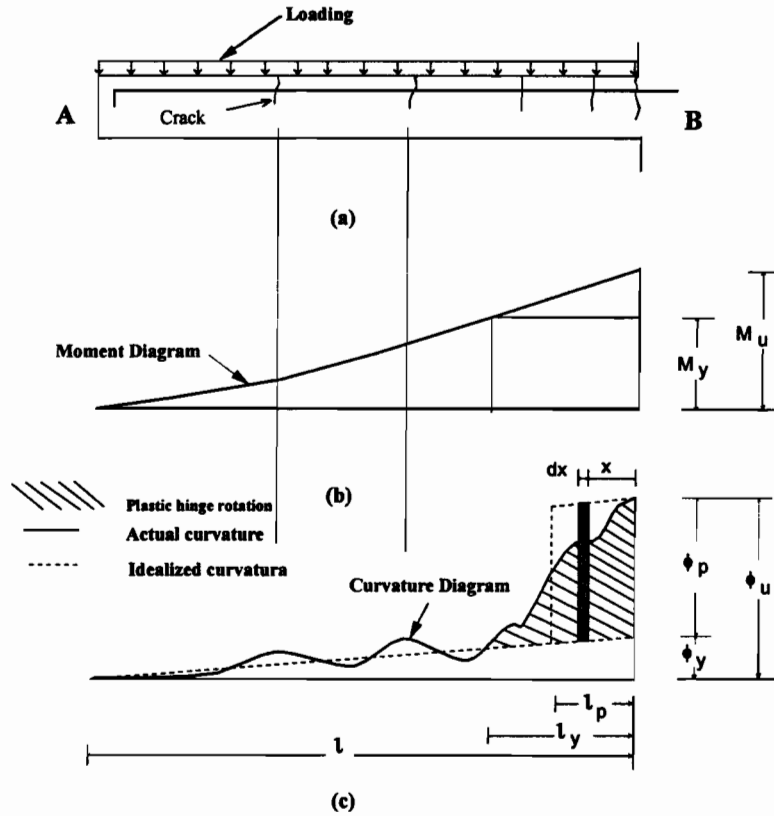


Figure 2.5: Schematic curvature distribution along beam at ultimate stage: (a) beam, (b) bending moment diagram, (c) curvature diagram

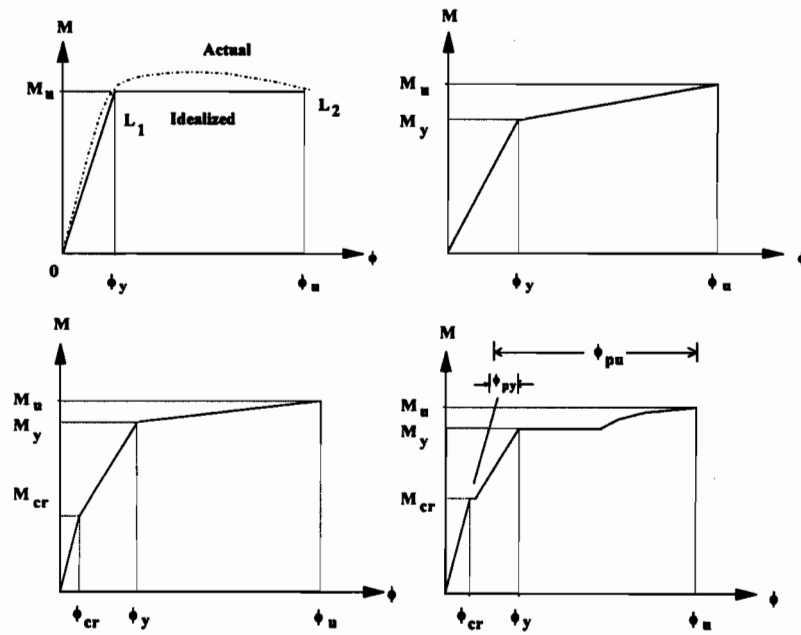


Figure 2.6: Existing moment-curvature constitutive laws

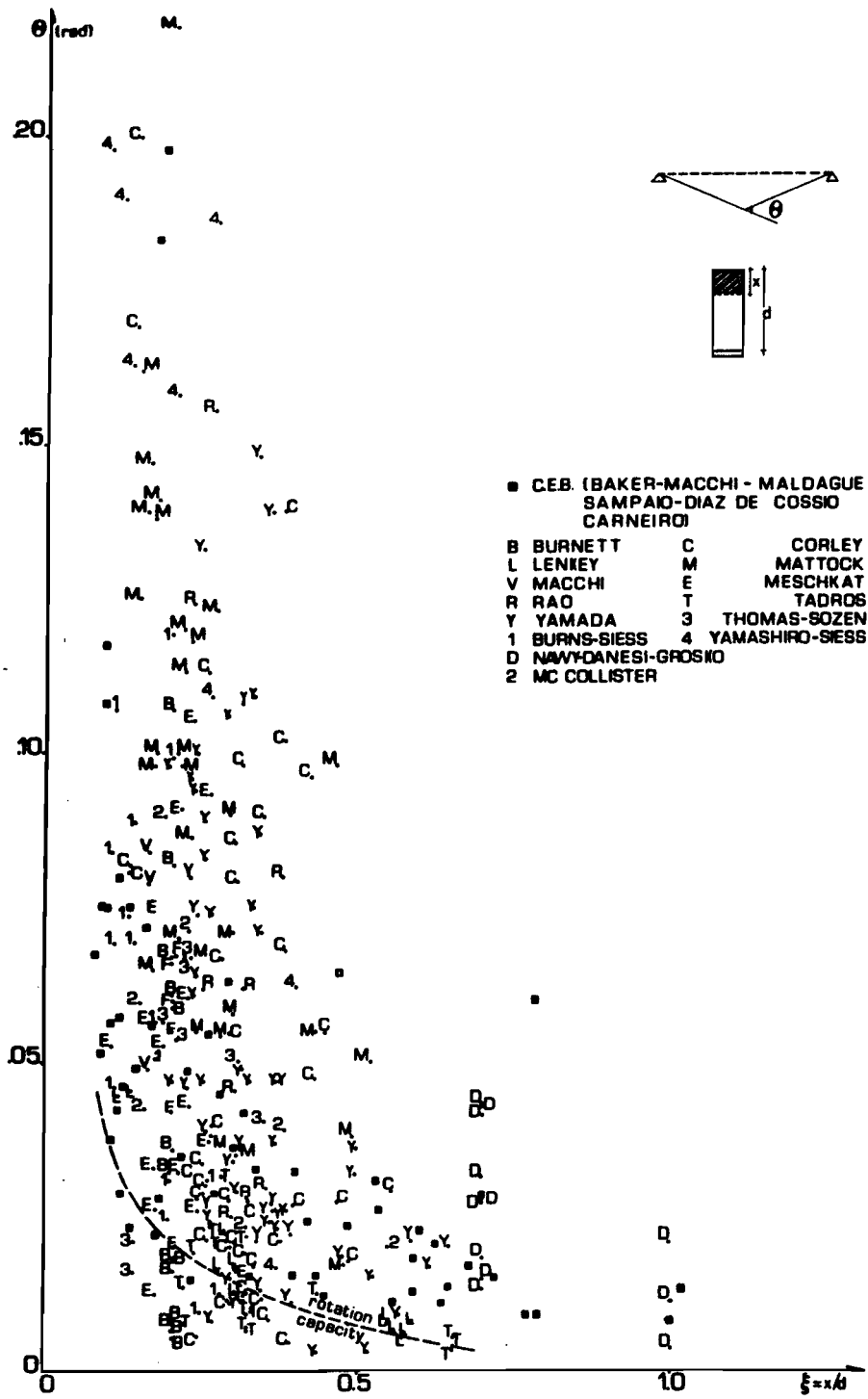


Figure 2.7: Inelastic rotations versus relative depth of neutral axis at ultimate load adopted by CEB MC 78 (Siviero 1974)

CHAPTER 3

NONLINEAR LAYERED FINITE ELEMENT PROGRAM

The key features of the nonlinear layered finite element analysis program, NONLACS2 (NONLinear Analysis of Concrete and Steel structures), developed in the present study, are described in this chapter. First, a classification and description of the existing nonlinear analysis methods of reinforced concrete (R C) structures are discussed. Then, the history and capabilities of the NONLACS2 program, constitutive models for uncracked and cracked concrete, the compressive stress-strain curves of normal and high-strength concrete, crack modelling techniques, new proposed models for concrete in tension, proposed concrete ultimate compressive and tensile strains and failure criteria for the concrete are presented, along with a discussion of constitutive model for the steel reinforcement. The nonlinear finite element formulation in the NONLACS2 program including element library, layered finite element, numerical algorithms, and convergence and divergence criteria is also discussed.

3.1 DESCRIPTION AND CLASSIFICATION OF NONLINEAR ANALYSIS METHODS

Although the experimental methods can provide useful information about the behaviour of R C structures, they are expensive and time-consuming. Using the nonlinear analysis methods, it is now possible, at comparatively low cost and effort, to predict the complete response of more complex R C members and structures such as tall structural walls, coupled elevator core systems and large slab systems with unusual layouts and supports.

Existing computer nonlinear analysis methods for structural concrete may be classified based on the constitutive laws accepted by the program, discretization techniques, and the degree of complexity. Generally three major categories are available in the literature:

3.1.1 Lumped-Plasticity Approach

The relatively simple lumped-plasticity model was used by some researchers such as Macchi (1972), Cohn and Franchi (1979), Hung (1984), Riva (1988) and Riva and Cohn (1990, 1994). In this model as shown in Fig. 3.1a, the structure is discretized by linear-elastic elements, with the behavioral nonlinearity lumped at the "rigid-plastic" joints, for which a piecewise linearized rigid-plastic moment-rotation law is assumed. The lumped-plasticity program, STRUPL-1C, developed by Riva (1988) used for nonlinear analysis of reinforced and prestressed concrete structures and comparison of experimental and analytical results showed that this method can be used with reasonable accuracy. For more information, see Section 2.2.6, and the work reported by Riva (1988).

3.1.2 "Microscopic" Finite Element Approach

Development of powerful numerical methods over the past three decades and the advent of increasingly fast computers with large capacities have led to the use of the finite element method as a supplement to the experimental work, and in situations where experiments are difficult to perform. Nonlinear finite element analysis of structural concrete has been used successfully for such systems to obtain their complete response including the load-deflection characteristics, strain distributions and cracking patterns at different load levels, failure modes, etc. Extensive research has resulted in significant advances in the area of concrete constitutive relationships which have led to the development of a substantial number of finite element programs with nonlinear analysis capabilities. A partial listing of such programs is available in the report of the ASCE Committee on Finite Element Analysis of Reinforced Concrete Structures, referred to as "ASCE", (1982 and 1991). For nonlinear analysis of R C structures using the finite element method, both the "macroscopic" (modified stiffness) and the "microscopic" finite element approaches are used widely.

The "microscopic" finite element approach appears to be the most accurate of the available approaches. In this approach, the structure is idealized as an assemblage of shell elements and the structural behaviour is studied in detail at each load level. The time-dependent behaviour of concrete, geometric nonlinearity and material nonlinearities including stress-strain curves of concrete and steel, tension-stiffening, the type and extent of cracking, bond-slip, stress redistribution due to cracking or crushing of concrete or yielding of steel, dowel action and the aggregate interlock at the cracks may be considered. Detailed reviews of the previous work have

been presented by Scordelis (1972) and ASCE (1982 and 1991).

Implementation of nonlinear concrete and reinforcement properties into a finite element analysis system was first undertaken over two decades ago by Ngo and Scordelis (1967) (Fig. 3.1b). Two-dimensional plane stress analyses of R C beams were developed in which the concrete and the steel were assumed to have linearly elastic stress-strain relationship. The concrete and steel were represented by triangular finite elements and the steel-concrete connections (bond-slip) was simulated by special linkage elements, spaced along the bar length. The nonlinear behaviour of the material was later considered by Nilson (1968) in a similar model. The discrete crack model was used and the structural topology was redefined after each load increment.

Recently some models have been developed based on the layered finite element approach using smeared cracking models. As can be seen from Fig. 3.1c, the structure is discretized using a number of shell elements, and each shell element subdivided into a number of imaginary concrete and steel layers (Scanlon 1971, Cedolin et al. 1977, Ghoneim 1978, Balakrishnan et al. 1988, Razaqpur et al. 1989, Lin and Scordelis 1975, Vecchio 1989, Hu and Schnobrich 1990, and Shayanfar, Kheyroddin and Mirza 1993). Each layer is assumed to be in a state of plane stress. The proposed material models are then applied to each layer individually.

For beams failing in flexure, the simplest finite element model (layered cross-section method) consists of dividing the beam longitudinally into a series of segmental elements. Each element cross-section is then subdivided into a number of discrete concrete and steel layers. Obviously, this kind of idealization can predict only the vertical cracks that occurs in the beam. Bazant et al. (1987) showed that for beams failing in flexure, where vertical cracks predominate the behaviour, this model can give an accurate prediction of the response up to the ultimate load.

The considerable computational effort required makes the "microscopic" finite element approach unsuitable for practical application especially for nonlinear analysis of large structures, such as a multistorey framed systems. However this method is valuable in research for better understanding of the nonlinear behaviour of R C structures.

3.1.3 "Macroscopic" Finite Element Approach

For beams and planar frames, the macroscopic finite element (modified stiffness) approach is based on an overall moment-curvature relationship reflected in the various stages of the material behaviour. Jofriet and McNeice (1971) used a bilinear moment-curvature relationship based on an empirically determined effective second moment of area of the cracked slab section. For beams

and frame analysis, this method implies the use of beam elements (one-dimensional elements) that account approximately for the nonlinear behaviour of structural concrete (Aparicio et al. 1983, Appleton et al. 1983, Cauvin 1983, Kim and Lee 1992 and 1993). For example, Pulmano and Shin (1987) presented a modified stiffness approach for predicting the instantaneous deflections of R C beams. The effective flexural rigidity, $E_c I_e$, proposed by Branson was adopted for calculation of the stiffness matrix in their investigation. Since most previous researchers assumed constant curvature in an element, the structure must be discretized in short elements (Fig. 3.1d).

3.2 FINITE ELEMENT PROGRAMS DEVELOPED IN THE PRESENT STUDY

The present work is aimed at demonstrating the capabilities of the finite element method as a tool for predicting the nonlinear response of R C structures. The NONLACS2 program as an ideal research-oriented tool (more comprehensive, high accuracy) employs a layered finite element approach. The response of selected R C members is predicted using the finite element program, NONLACS2. Based on the analytical results obtained from this program, new models are proposed. The key features of this program including constitutive models, material modelling and finite element formulation are presented in the following sections.

Another objective of the research described here is to develop a nonlinear finite element program, NAFS (Nonlinear Analysis of Frame Structures), as a practical engineering tool based on modified stiffness approach. A new 2-node nonlinear beam element (3 degrees of freedom per node, Fig. 3.1d) with a degrading stiffness matrix is developed to model cracking and other nonlinear effects throughout the entire loading range from zero to the ultimate load. The variation of curvature and flexural rigidity at the section at different loading stages and along the length of element are considered. With these modifications, the NAFS program can provide a speedy and economical method for analysis of large frame structures with adequate solution accuracy. Chapter 9 presents the key features and applications of the NAFS program. The results obtained from the layered finite element approach, NONLACS2, are compared with the results obtained from the modified stiffness approach, NAFS, in Chapter 9.

3.3 GENERAL DESCRIPTION OF NONLACS2 PROGRAM

Like most of the other nonlinear finite element analysis programs, the NONLACS2

program was developed within the university environment. The origin of this program can be traced back to the earlier programs: NARCS, NOTACS, FELARC and NONLACS developed by Lin (1973), Kabir (1976), Ghoneim (1978) and Razaqpur and Nofal (1990), respectively. Recently, Shayanfar (1995) modified the NONLACS program and developed it significantly into a new program called "HODA", which includes a new hypoelasticity constitutive relationship utilizing the rotation of material axis, employment of both fixed and rotating crack models, normal and high strength concrete compressive stress-strain curves, post-cracking compressive strength degradation, new uniaxial stress-strain relationships for concrete under monotonically increasing and reversed cyclic loadings, accounting for mesh sensitivity, and utilizing the tensile strength degradation due to extensive internal microcracking of the concrete. The model implemented in the program can also account for high nonlinearity of the compression stress-strain behaviour of concrete in the pre-peak regime, the softening behaviour of concrete in the post-peak region, the stiffness degradation caused by the extension of microcracks during subsequent unloadings and reloadings and the irrecoverable volume dilatation at high levels of compressive load.

The NONLACS2 program utilizes the basic structure of the NONLACS program with the same finite element formulation and differs from the previous programs in terms of its versatility to analyze both normal and high-strength concretes, to eliminate the element size effect (mesh size dependency) using both the fracture mechanics and strength-based approaches, to utilize different models for concrete in compression and tension, and to determine the ultimate concrete tensile and compressive strain, ϵ_{tu} and ϵ_{cu} , respectively.

The program can be used to predict the nonlinear behaviour of any plain, reinforced or prestressed concrete, steel, or composite concrete-steel structure that is composed of thin plate members with plane stress conditions. This includes beams, slabs (plates), shells, folded plates, box girders, shear walls, or any combination of these structural elements. Time-dependent effects such as creep and shrinkage can also be considered. The program, however, has its limitations, it cannot account for large displacements or geometric nonlinearities, transverse shear deformations in plate bending problems, fatigue type effects, punching shear, dynamic loads, and the slip between the concrete and the reinforcing steel. Also, its element library does not include one dimensional beam element which is appropriate for analysis of frame and shear wall-frame structures. While the required finite element model for this program can have a three-dimensional geometry, it must be ensured that each element is subjected to a plane stress condition.

While the general purpose nonlinear finite element program, NONLACS2, is a relatively

new program, the results of analyses conducted so far using original version of NONLACS (Nofal, 1988) are quite interesting and useful. Analyses by Razaqpur et al. (1989) resulted in very good correlation with the experimental results of prestressed concrete box girder bridges tested at McGill University by Hadj-Arab (1987) and Joucдар (1988). The recent work undertaken at McGill University by Risha (1991), Bello (1992), Shariatmadar (1992), Shayanfar et al. (1993), Kheyroddin and Mirza (1994, 1995a, 1995b), and Manatakos (1995) showed that the results computed using the NONLACS program were in good agreement with the experimental results for load-deflection characteristics, cracking patterns and the mode of failure at the ultimate load for R C structural walls and beams.

3.4 MATERIAL MODELLING

Generally, nonlinearities in R C structures can be classified in two categories:

- 1) Geometric nonlinearities, where large deflection can introduce significant secondary moments, and hence stresses in the structure. This kind of nonlinearity is associated only with special structural elements such as thin plates, shell elements and long columns.
- 2) Material nonlinearities caused by cracking of the concrete, nonlinear stress-strain relationship of concrete and steel, tension-stiffening, tension-softening, bond-slip, stress redistribution due to cracking or crushing of concrete or yielding of the steel, dowel action, aggregate interlock, multiaxial stress state, and the time-dependent effects such as creep, shrinkage, temperature and loading history. Reinforced concrete behaves almost linearly up to about 20% of the ultimate load and then exhibits highly nonlinear behaviour. Cracking is generally believed to be the most influential factor that contributes to the nonlinear response of reinforced concrete. Since the geometric nonlinearity is of little importance in normal R C structures (beams, shear walls, etc.) because of their robustness, there is comparatively little risk of stability failures, and only the material nonlinearities will be discussed hereafter.

3.4.1 Constitutive Relationship for Concrete

Extensive research over the last two decades has produced numerous constitutive models capable of representing various aspects of concrete behaviour. These models can be grouped into five main categories: (1) elasticity-based models, which are the most widely used. They can be linear or nonlinear based elastic models, (2) plasticity-based models, that takes into account the

plastic deformations of concrete when it is stressed beyond its elastic limit, (3) plastic-fracturing models, which combines the plasticity and fracturing material theory to obtain a nonlinear constitutive relationship, (4) endochronic models, which are based on the inelastic accumulation, and (5) boundary surface models which are simpler than the endochronic or plastic-fracturing models. It predicts the constitutive behaviour of concrete under a multiaxial cyclic state of stress. Comprehensive reviews of these models are provided by Chen (1982), the report of the ASCE Committee on Finite Element Analysis of Reinforced Concrete Structures (1982, 1991), and Shareef and Buyukozturk (1983). The principal features of these models as summarized by Bahlis and Mirza (1987) are presented in Table 3.1.

With regards to computer implementation, elasticity-based models are the easiest to implement and this is one of the reasons why these models are very popular. Elasticity-based models are based on a Hookean formulation and can be implemented either in a total or incremental form. In the total (secant) stress-strain models, the state of stress, σ_{ij} , depends only on the current state of strain, ϵ_{kl} . The constitutive relation is expressed as:

$$\sigma_{ij} = F_{ij}(\epsilon_{kl}) \quad (3.1)$$

where F_{ij} is the elastic response factor. The path independence of this relationship is a major drawback that restricts the application of these models to situations in which loadings are increasing monotonically, or are proportional.

In the incremental hypoelastic stress-strain form, the stress state depends not only on the current strain state but also on the stress path followed to reach that state. The constitutive relationship is expressed as:

$$d\sigma_{ij} = D_{ijkl} d\epsilon_{kl} \quad (3.2)$$

where $d\sigma_{ij}$ and $d\epsilon_{kl}$ are the stress and strain increment tensors, respectively, and D_{ijkl} is the fourth-order tangential material stiffness tensor that depends on the stress and (or) the strain tensor. The path dependence of these models makes them very appropriate to handle non-monotonically increasing and non-proportional type of loads.

While elasticity-based models exist for uniaxial, biaxial and triaxial stress conditions, biaxial models are probably the most popular. The biaxial models are either isotropic or orthotropic. Common formulations are the isotropic total stress-strain models, the incremental isotropic and the incremental orthotropic stress-strain models. While the isotropic models have been found to produce satisfactory results (Gerstle 1981), these models are incapable of representing stress induced anisotropy. This deficiency has led to the development of orthotropic biaxial models to handle cases

in which anisotropy is important. Examples of such models include those developed by Liu et al. (1972) and Darwin and Pecknold (1976, 1977).

The basic structure of the various constitutive models can be expressed as

$$\begin{Bmatrix} d\sigma_1 \\ d\sigma_2 \\ d\tau_{12} \end{Bmatrix} = \begin{bmatrix} d_{11} & d_{12} & 0 \\ d_{21} & d_{22} & 0 \\ 0 & 0 & d_{33} \end{bmatrix} \begin{Bmatrix} d\epsilon_1 \\ d\epsilon_2 \\ d\gamma_{12} \end{Bmatrix} \quad (3.3)$$

These equations contain 5 coefficients d_{ij} , however, these are not all independent coefficients. It follows from the principle of the conservation of energy, that the matrix of coefficients in Eq. 3.3 should be symmetric. Thus the number of independent variables reduces to 4.

When the generalized Hooke's law (Eq. 3.3) is specialized for an orthotropic material under a biaxial state of stress in the plane consisting of coordinates 1 and 2, the following form is obtained

$$\begin{Bmatrix} d\sigma_1 \\ d\sigma_2 \\ d\tau_{12} \end{Bmatrix} = \frac{1}{(1-\nu_1\nu_2)} \begin{bmatrix} E_1 & \nu_2 E_1 & 0 \\ \nu_1 E_2 & E_2 & 0 \\ 0 & 0 & (1-\nu_1\nu_2)G \end{bmatrix} \begin{Bmatrix} d\epsilon_1 \\ d\epsilon_2 \\ d\gamma_{12} \end{Bmatrix} \quad (3.4)$$

where $\nu_1 E_2 = \nu_2 E_1$ and subscripts 1, 2 denote the current principal stress axes; E_1 , E_2 are the Young's moduli of elasticity with respect to directions 1 and 2, respectively; G is the elastic shear modulus for the plane parallel to coordinates 1 and 2; and ν_1 and ν_2 are the Poisson's ratios in directions 1 and 2, respectively.

The various models differ in the following respects: definition of the moduli of elasticity in the principal directions, consideration of the Poisson's effect (i.e, the coupling between the principal directions), and the definition of the shear modulus of elasticity. The model of Darwin and Pecknold (1976,1977) is adopted in the NONLACS2 program. Two modifications were adopted by Darwin and Pecknold (1976,1977), in Eq. 3.4. Firstly, they introduced an "equivalent Poisson's ratio", ν , defined as:

$$\nu^2 = \nu_1 \nu_2 \quad (3.5)$$

Secondly, since no information was available on the shear modulus of elasticity, G , for plain concrete under a general state of biaxial stress, they assumed that it is independent of the orientation of the principal axes.

Table 3.1: Analytical models for stress-strain relations for concrete (After Bahlis and Mirza 1987)

Model	Approach	Stress-strain relations	Advantages	Disadvantages
Elasticity-based models	Linear elastic	$\sigma_{ij} = C_{ijkl} \epsilon_{kl}$ where C_{ijkl} = material constants $f(E, \nu)$	-Simple, easy to formulate and use -Gives good results for reinforced concrete beams and panels where stress condition are predominantly biaxial tension or tension-compression.	-Fails to identify inelastic deformation -Must be combined with a failure criterion -State of stress depends only on current state of strain
	Nonlinear elastic total (secant) model	$\sigma_{ij} = F_{ij}(\epsilon_{ij})$ where F_{ij} = elastic response factor, which is a function of stress or strain tensor	-Provides simple approach for problems in which monotonically increasing proportional* loads prevail	-State of stress depends only on current state of strain -Limited to structures subjected to specific type of loading (monotonic, proportional)
	Incremental: hypoelastic model	$\sigma_{ij} = D_{ijkl} \epsilon_{kl}$ where D_{ijkl} = material property matrix, which is a function of stress or strain tensor	-Simple in comparison to plastic, elastic-fracturing and endochronic models -Model many of the characteristics of concrete behaviour -Capable of modelling concrete under monotonic and cyclic loadings	-Does not apply in situations where the principal stress axes or the principal directions rotate -Cannot account for behaviour of concrete in the strain softening region -Cannot describe accurately the behaviour of concrete under cyclic loading
Plasticity-based models	Elastic-perfectly plastic	$d\epsilon_{ij} = \lambda \partial f / \partial \sigma_{ij}$ where λ = scalar proportionality vector and $\partial f / \partial \sigma_{ij}$ = yield surface	-Simple in comparison with more sophisticated models -Improvement over elastic models since it can represent inelastic strains in concrete	-Normality rule used in these models does not apply to fractured concrete -Cannot account for the behaviour of concrete in the strain softening region -Must be associated with yield and failure criteria
	Based on yield surface and evolution of subsequent loading surfaces	Elastic hardening plastic		-Difficulty in choosing yield and failure criteria -Complex functions required to describe stress-strain relationships of concrete -Difficulty in choosing the hardening rule -Effects of internal friction

Table 3.1: (Cont'd)

Model	Approach	Stress-strain relation	Advantages	Disadvantages
<i>Plastic fracturing model</i>	Plastic fracture	Based on plastic slip and microcracking	-Provides powerful tool for modelling a wide range of nonlinear multiaxial cyclic behaviour of concrete -Reflects microcracking in concrete	-Involves a large number of functions and material parameters resulting in heavy computational effort in a finite element program -Does not take time or strain rate into account
<i>Endochronic theory</i>	Endochronic	Based on the concept of intrinsic time, which describes inelastic strain accumulation	-Provides a powerful tool for modelling a wide range of nonlinear multiaxial cyclic behaviour of concrete	-Involves a large number of functions and material parameters that are incrementally nonlinear, resulting in heavy computational iteration in a finite element program -Used in association with a tension cutoff criterion to model concrete failure in tension
<i>Boundary surface</i>	Boundary surface	Based on the concept of boundary surface (equivalent to failure surface in monotonic loadings) that shrinks in a stress space as a function of maximum strain	-Simple in comparison with plastic fracture and endochronic models -Models many of the characteristic behaviour of concrete, namely, stiffness degradation, nonlinear stress-strain response, plastic deformation, shear compaction, and dilatancy, and aggregate interlock	-Can possibly lead to erroneous predictions for particular stress paths -Ability to analyze reinforced concrete structures have not yet been demonstrated

* Monotonic: no unloading or reversal in load direction. Proportional: no rotation of principal stress axes during loading.

This leads to the following relationship

$$(1 - \nu^2) G = \frac{1}{4} (E_1 + E_2 - 2\nu \sqrt{E_1 E_2}) \quad (3.6)$$

Equation 3.4 then takes the form:

$$\begin{Bmatrix} d\sigma_1 \\ d\sigma_2 \\ d\tau_{12} \end{Bmatrix} = \frac{1}{(1-\nu^2)} \begin{bmatrix} E_1 & \nu\sqrt{E_1E_2} & 0 \\ \nu\sqrt{E_1E_2} & E_2 & 0 \\ 0 & 0 & \frac{1}{4}(E_1+E_2-2\nu\sqrt{E_1E_2}) \end{bmatrix} \begin{Bmatrix} d\epsilon_1 \\ d\epsilon_2 \\ d\gamma_{12} \end{Bmatrix} \quad (3.7)$$

If incremental equivalent uniaxial strains, $d\epsilon_{1u}$ and $d\epsilon_{2u}$, are defined as:

$$\begin{aligned} d\epsilon_{1u} &= \frac{1}{1-\nu^2} [d\epsilon_1 + \nu \sqrt{\frac{E_2}{E_1}} d\epsilon_2] \\ d\epsilon_{2u} &= \frac{1}{1-\nu^2} [\nu \sqrt{\frac{E_1}{E_2}} d\epsilon_1 + d\epsilon_2] \end{aligned} \quad (3.8)$$

then Eq. 3.7 becomes:

$$\begin{aligned} d\sigma_1 &= E_1 d\epsilon_{1u} \\ d\sigma_2 &= E_2 d\epsilon_{2u} \\ d\tau_{12} &= G d\gamma_{12} \end{aligned} \quad (3.9)$$

These relationships have the same form as for the uniaxial stress condition, hence the name "equivalent uniaxial strain" has been selected for $d\epsilon_{1u}$ and $d\epsilon_{2u}$. The definition of equivalent uniaxial strain can be restated, using Eq. 3.9 as:

$$\epsilon_{iu} = \int \frac{d\sigma_i}{E_i} \quad (3.10)$$

or its discrete equivalent,

$$\epsilon_{iu} = \sum_{\substack{\text{Load} \\ \text{increments}}} \frac{\Delta\sigma_i}{E_i} \quad (3.11)$$

where $\Delta\sigma_i$ is incremental change in principal stress σ_i and E_i is the tangent modulus in the principal direction i . Once the stress-strain relationship has been written in a form similar to that of the uniaxial stress-strain curve, the values of E_1 and E_2 for a given principal stress ratio are found as the slopes of the σ_1 - ϵ_{1u} and σ_2 - ϵ_{2u} curves given by Eq. 3.14 at the current values of ϵ_{1u} and ϵ_{2u} , which are accumulated during the loading history in Eq. 3.11. In the NONLACS2 program, the value of the equivalent Poisson's ratio, ν , is taken to be constant during the loading history.

3.4.2 Compressive Stress-Strain Curves for Concrete

Experimental results indicate that concrete behaves differently under different types and

combinations of stress conditions due to the progressive microcracking at the interface between the mortar and the aggregates (transition zone). Microcracks exist at the transition zone even before any load has been applied, which are normally caused by differential drying and thermal shrinkage between the cement paste and the aggregates. Microcracks can develop further during loading due to the difference in stiffness between the aggregate and the mortar. The propagation of these cracks under the applied loads contributes to the nonlinear behaviour of the concrete. At about 30% of the compressive strength ($0.3f'_c$), concrete essentially behaves as a linear elastic material. Beyond that, concrete becomes softer until it reaches the peak stress where the curve start to descend until crushing occurs (Fig. 3.2a). Different states of stress-strain curve of concrete depending on the stress level, are indicated by indices KC= 1, 2, 3, 4, 5, and 6 in the NONLACS2 program as shown in Fig. 3.2a.

The following two compressive stress-strain curves for normal and high-strength concrete are formulated in the NONLACS2 program:

3.4.2.1 Saenz and Smith's equation

As shown in Fig. 3.2a, the compressive uniaxial stress-strain curve is made of two distinct parts. The first part up to the peak compressive strength is represented by the Saenz's model (1965) given by Eq. 3.12, while the strain-softening part is modeled by the model of Smith and Young (1955), represented by Eq. 3.13.

Part I of the curve in Fig. 3.2a is given by:

$$\sigma_i = \frac{E_0 \epsilon_{iu}}{1 + \left(\frac{E_0}{E_{sc}} - 2 \right) \left(\frac{\epsilon_{iu}}{\epsilon_{ic}} \right) + \left(\frac{\epsilon_{iu}}{\epsilon_{ic}} \right)^2} \quad (3.12)$$

where σ_i is the current principal stress in direction i , E_0 is the initial modulus of elasticity of concrete, E_{sc} is the secant modulus of concrete at peak stress, ϵ_{iu} is the equivalent uniaxial strain in the i th principal direction, σ_{ic} is compressive strength of biaxially loaded concrete in the principal direction i , and ϵ_{ic} is the equivalent uniaxial strain corresponding to σ_{ic} .

Part II of the curve is given by:

$$\sigma_i = \sigma_{ic} \left(\frac{\epsilon_{iu}}{\epsilon_{ic}} \right) \exp(1 - \epsilon_{iu} / \epsilon_{ic}) \quad (3.13)$$

The strength of concrete, σ_{ic} , the values of E_1 and E_2 and the value of ν are functions of the level of stresses and stress combinations. The concrete strength when subjected to biaxial stresses, σ_{ic} , is determined from the failure envelope given by Kupfer and Gerstle (1973). The values of E_1 and E_2 for a given stress ratio ($\alpha=\sigma_1/\sigma_2$) are found as the slopes of the σ_1 - ϵ_{1u} and σ_2 - ϵ_{2u} curves, respectively. The tangent modulus for the ascending branch, E_i , is given by:

$$E_i = \frac{d\sigma_i}{d\epsilon_{iu}} = \frac{E_0 \left(1 - \left(\frac{\epsilon_{iu}}{\epsilon_{ic}}\right)^2\right)}{\left[1 + \left(\frac{E_0}{E_{sc}} - 2\right) \left(\frac{\epsilon_{iu}}{\epsilon_{ic}}\right) + \left(\frac{\epsilon_{iu}}{\epsilon_{ic}}\right)^2\right]^2} \quad (3.14)$$

For the descending branch of compression zone (KC=5 and 6 in Fig. 3.2a), E_i is set with very small amount equal to 0.0001 to avoid computational problems associated with a negative and zero value for E_i .

3.4.2.2 Popovics' equation

The axial-stress versus strain curves for concrete up to a compressive strength of 80 MPa are shown in Fig. 3.2b. The shape of the ascending part of the stress-strain curve is more linear and steeper for high-strength concrete, and the strain at the maximum stress is slightly higher for high-strength concrete. High-strength concrete tends to behave in a more brittle manner in the descending portion of the curve and the stress drops off more rapidly than for the normal strength concrete. The slope of the descending part becomes steeper for high-strength concrete. Collins and Mitchell (1991) and Collins et. al. (1993) showed that the form of the stress-strain relationship first proposed by Popovics (1973) accompanied with some modification factors provides a good base for describing the behaviour of high-strength concrete. The following expression, with an alleined notation for NONLACS2 program, was proposed by Popovics (1973):

$$\frac{\sigma_i}{\sigma_{ic}} = \frac{\epsilon_{iu}}{\epsilon_{ic}} \frac{n_i}{n_i - 1 + (\epsilon_{iu} / \epsilon_{ic})^{n_i}} \quad (3.15)$$

where n_i is a curve fitting factor in the principal direction i , and as n_i becomes higher the ascending branch becomes more linear. Thorenfeldt et al. (1987) reported that although Popovics expression (Eq. 3.15) describes well the ascending branch of the stress-strain curve, it does not drop fast enough after the peak stress for high-strength concretes. The decay factor k_i was

proposed to increase the post-peak decay, so that Eq. 3.15 becomes:

$$\frac{\sigma_i}{\sigma_{ic}} = \frac{\epsilon_{iu}}{\epsilon_{ic}} \frac{n_i}{n_i - 1 + (\epsilon_{iu}/\epsilon_{ic})^{n_i k_i}} \quad (3.16)$$

where k_i is greater than 1.0 when $\epsilon_{iu}/\epsilon_{ic}$ exceeds 1.0, and k_i is equal to 1.0 when $\epsilon_{iu}/\epsilon_{ic}$ is less than 1.0. Collins and Porasz (1989) suggested that for $\epsilon_{iu}/\epsilon_{ic}$ greater than 1.0:

$$k_i = 0.67 + \frac{\sigma_{ic}}{62} \quad (MPa \text{ units})$$

$$k_i = 0.67 + \frac{\sigma_{ic}}{9000} \quad (psi \text{ units})$$
(3.17)

and the curve fitting factor, n_i , for normal-weight concrete can be obtained as:

$$n_i = 0.8 + \frac{f_c}{17} \quad (MPa \text{ units})$$

$$n_i = 0.8 + \frac{f_c}{2500} \quad (psi \text{ units})$$
(3.18)

As can be seen from Eq. 3.16, the relationship between σ_i and ϵ_{iu} is a function of four constants, k_i , n_i , σ_{ic} and ϵ_{ic} . In the NONLACS2 program, these four constants can be calculated using the strength of concrete, σ_{ic} , which is obtained from the failure envelope proposed by Kupfer and Gerstle (1973). One advantage of this equation is that the ultimate compressive strain of the concrete, ϵ_{cu} , is not required for prediction of the descending branch of the concrete stress-strain curve. If the initial concrete modulus of elasticity, E_0 , is known or it can be estimated, the strain, ϵ_{ic} , corresponding to the peak stress, σ_{ic} , can be obtained using:

$$\epsilon_{ic} = \frac{\sigma_{ic}}{E_0} \frac{n_i}{n_i - 1} \quad (3.19)$$

If the compressive strength and the unit weight of the concrete, w_c , are known, E_0 may be estimated from the equation recommended by the ACI Code (318-83)

$$E_0 = w_c^{1.5} 0.043 \sqrt{f_c} \quad (MPa \text{ units})$$

$$E_0 = w_c^{1.5} 33 \sqrt{f_c} \quad (psi \text{ units})$$
(3.20)

The modulus of elasticity based on Eq. 3.20 is the slope of a line passing through the stress-strain curve at $0.4f_c$. Carrasquillo et al. (1981) pointed out that Eq. 3.20 overestimates the modulus of

elasticity of concrete with strength greater than 6000 psi (41 MPa). The following expression was recommended for normal-weight concrete including the normal and the high-strength concrete:

$$\begin{aligned} E_0 &= 3320 \sqrt{f'_c} + 6900 && \text{(MPa units)} \\ E_0 &= 40,000 \sqrt{f'_c} + 1,000,000 && \text{(psi units)} \end{aligned} \quad (3.21)$$

The stress-strain curves that result from the Eq. 3.16 for 20 MPa, 40 MPa, and 80 MPa concretes are shown in Fig. 3.2b.

Popovics' equation was implemented in the HODA program by Shayanfar (1995) to accurately model the family of stress-strain curves for different strength concretes including the high strength concrete.

3.4.3 Crushing of Concrete

When the concrete compressive strain at any point (usually a Gauss integration point) in one or both of the principal directions reaches or exceeds the ultimate compressive strain, ϵ_{cu} , the concrete is assumed to crush. There will be a total loss of stiffness and the constitutive matrix will become zero.

$$[D] = 0 \quad (3.22)$$

This phenomenon causes some numerical difficulties after crushing of the concrete. In order to eliminate this drawback, a small amount of compressive stress as a fraction of compressive strength, $\gamma_c f'_c$, will be assigned (optional) at a high level of stress in the region with $KC=6$ (Fig. 3.2a), where parameter γ_c is the remaining compressive strength factor. El-Metwally (1994) used compressive stress-strain curve of confined concrete with $\gamma_c=0.2$, proposed by Kent and Park (1971), for instability analysis of R C beam-columns.

For determination of the concrete ultimate compressive strain, ϵ_{cu} , the following two equations which are suitable for high and normal-strength concretes are implemented into the NONLACS2 program.

1) Unconfined high and normal-strength concrete (Pastor 1986):

$$\epsilon_{cu} = 0.00364 - 4.086 \times 10^{-8} f'_c \quad f'_c \leq 12,000 \text{ psi} \quad (3.23)$$

2) Confined concrete (Scott et al. 1982):

$$\epsilon_{cu} = 0.004 + 0.9 \rho_s \left(\frac{f_{yh}}{300} \right) \quad (3.24)$$

where ρ_s is the ratio of volume of hoop reinforcement to the volume of the core measured to the outside of the hoops and f_{yh} is the yield strength of the hoop reinforcement (MPa). The value of ϵ_{cu} is calculated for each finite element using equations 3.23 and 3.24, or it can be introduced by the user.

3.4.4 Crack Modelling Techniques

Cracking of the concrete is one of the important aspects of material nonlinear behaviour of the concrete. Besides reducing the stiffness of the structure, cracks have resulted in redistribution of stresses to the reinforcing steel as well as increasing the bond stress at the steel-concrete interface. Intensive research effort has resulted in a large number of cracking models, which can be divided broadly into two categories, namely, discrete cracking models and smeared cracking models. The former approach was used in the early research studies, but the latter approach quickly replaced it, due to its greater ease of application. Furthermore, within each category, these models can be applied either with a strength-based, or fracture mechanics based crack propagation criterion (see Fig. 3.3). Table 3.2 summarizes the key features of each of the groups.

In the discrete cracking model, cracks are simulated by the separation of nodal points. It is normally implemented by disconnecting the displacement at the nodal points for the adjoining elements (Fig 3.4a). This procedure first was introduced by Ngo and Scordelis (1967) and then modified by Nilson (1968) in order to allow the finite element model to generate the location of the cracks. The discrete cracking model was further improved and partially automated by Mufti et al. (1972) who incorporated a predefined crack utilizing two nodes at one point connected by a linkage element. The main drawback of discrete cracking model is that redefining the structure topology after cracking results in an increased cost of solution and computational efforts.

In the smeared cracking model, introduced by Rashid (1968), the cracks are assumed to be smeared in a continuous manner with an infinite number of parallel cracks within the finite element as shown in Fig. 3.4b. There is no need to redefine the finite element topology after crack formation. The relatively simple strength based smeared crack model represents a good choice when the global behaviour of structure is to be studied and consequently, the most general purpose

finite element programs, including the NONLACS2 program, have adopted a smeared cracking option. In a strength based smeared cracking model, concrete is represented as an orthotropic material, and cracking is assumed to occur when the principal tensile stress at a point (usually a Gauss integration point) exceeds the tensile strength of concrete. After cracking, the axes of orthotropy are aligned parallel and orthogonal to the crack. The elastic modulus perpendicular to the crack direction is reduced to a very small value close to zero and the Poisson effect is ignored. The effect of the crack is smeared within the element by modifying the $[D]$ matrix. If σ_1 exceeds the tensile strength of concrete, f_t , the material stiffness matrix is defined as (one crack is opened):

$$[D] = \begin{bmatrix} 0 & 0 & 0 \\ 0 & E_2 & 0 \\ 0 & 0 & \beta G \end{bmatrix} \quad \text{where } 0 < \beta \leq 1.0 \quad (3.25)$$

Once one crack is formed, the principal directions are not allowed to rotate and a second crack can form only when $\sigma_2 > f_t$, in a direction perpendicular to the first crack. Then,

$$[D] = \begin{bmatrix} 0 & 0 & 0 \\ 0 & 0 & 0 \\ 0 & 0 & \beta G \end{bmatrix} \quad \text{where } 0 < \beta \leq 1.0 \quad (3.26)$$

The shear retention factor, β , with a value of less than unity, serves to eliminate the numerical difficulties that arise if the shear modulus is reduced to zero, and more importantly, it accounts for the fact that cracked concrete can still transfer shear forces through aggregate interlock and dowel action. While equations 3.25 and 3.26 represent the basic forms of the cracked concrete stiffness matrix, it is important to note that the various models differ in the definition of the reduced modulus of elasticity parallel to the crack direction and the variation of shear stiffness after cracking. The models of Hu and Schnobrich (1990), Balakrishnan and Murray (1988), Al-Manaseer and Phillips (1987), and Hanna and Mirza (1983) reflect these variations. Equations 3.25 and 3.26 do not represent the behaviour of the cracked concrete completely. The constitutive matrix needs to be modified so as to represent the post-cracking effects such as tension-stiffening and strength degradation parallel to the crack direction.

The smeared cracking models can be classified into three groups: (1) fixed crack models, (2) rotating (swinging) crack models, and (3) multiple non-orthogonal crack models. In a fixed crack model, the direction of the normal to the crack is fixed after initiation of the crack. This

model is suitable for concrete elements reinforced in only one direction, or in two directions with almost the same amounts of reinforcement. On the other hand, the rotating crack models as proposed originally by Cope et al. (1980), allow the normal to the crack to rotate during the fracture process. In principle, the normal to the crack can rotate with the axes of principal strain or with the axes of principal stress. Although the rotating crack concept has been utilized by many researchers (e.g., Gupta and Akbar 1984, Balakrishnan and Murray 1986, and Vecchio 1989), Bazant (1983) criticized this approach for not reflecting the physical nature of cracking. The multiple non-orthogonal crack models have been used only by a few investigators (e.g., Barzegar and Schnobrich 1986 and Rots 1988). This model is able to duplicate more than two non-orthogonal cracks at one point of the structure. For more information refer to ASCE (1991). Although the smeared cracking model is simple to apply and is widely accepted, it has the drawback of being dependent on the finite element mesh size. This deficiency has been eliminated from the program as explained in Chapter 4.

3.4.5 Proposed Models for Concrete in Tension

In R C structures generally a number of cracks will develop at early stages of loading. Due to the bond between the concrete and the steel reinforcement, a redistribution of the tensile stress from the concrete to the reinforcement will occur. In fact, the concrete is able to resist tension between the cracks in the direction normal to the crack. This phenomenon is termed tension-stiffening, because the response is stiffer than the response with a brittle fracture approach (sudden reduction in tensile stress to zero when crack initiates). The tension-stiffening is closely related to the tension-softening in plain concrete and the controversy between tension-stiffening and tension-softening approaches seems to have been exaggerated in the past (Balakrishnan et al. 1988). The term "tension-softening" is used to describe a concrete tensile stress-strain curve with a descending branch that is controlled by fracture consideration rather than by the presence of steel reinforcement. The use of both tension-stiffening and tension-softening in a finite element model help the numerical stability of the solution. Based on the results of the survey by Darwin (ASCE 1991), tension-stiffening is somewhat more popular than tension-softening.

Tension-stiffening effect is generally represented using two procedures. In the first method, which is more popular (Fig. 3.5a) and first introduced by Scanlon (1971), with a descending branch in the stress-strain curve. In fact, the post-cracking model is bounded on the one end by cracking strain, ϵ_{cr} , and with the ultimate tensile strain, ϵ_u , at the other end.

Table 3.2: Cracking models (Bello 1992)

Model	Base	Approach	Advantages	Disadvantages
<i>Discrete cracking model</i>	Fracture Mechanics	Based on energy release rate	<p>Bond effects are more accurately represented.</p> <p>Crack width computation is more accurate</p> <p>Problems of non-objectivity do not arise</p>	<p>Additional concrete properties required e.g. energy release rate, G_f, fracture toughness, K_{Ic}.</p> <p>Redefinition of structure topology after crack formation.</p> <p>Extensive remeshing is required where crack direction is not known <i>a priori</i>.</p>
	Strength based	Based on limiting tensile stress/strain	<p>More realistic when few cracks dominate behaviour.</p> <p>Can realistically represent aggregate interlock by use of linkage element.</p> <p>Useful in investigating stresses when crack location is predefined.</p>	<p>Same as above; but no additional concrete property is required.</p> <p>Often the predicted response is sensitive to the refinement of finite element mesh.</p>
<i>Smearred cracking model</i>	Fracture Mechanics	Based on energy release rate	<p>Problems of non-objectivity do not arise. Can handle problems involving few dominant cracks.</p> <p>In addition, it has the three advantages listed below for strength-based model.</p>	<p>Additional concrete properties required. eg. energy release rate, G_f, fracture toughness, K_{Ic}.</p>
	Strength based	Based on limiting tensile stress/strain	<p>Computational efficient; no need to redefine structure topology after cracking.</p> <p>Crack direction is not restricted to element boundaries.</p> <p>Adequate in problems in which precise crack location is not important.</p>	<p>Inadequate when precise crack location/geometry is important.</p> <p>Prone to non-objectivity; dependence of solution on grid size.</p> <p>Inadequate in problems involving few dominant cracks.</p>

In the second method, the steel stiffness is increased by modifying the stress-strain curve of steel (Gilbert and Warner 1978). Some researchers have suggested the following equation for calculation of the ultimate tensile strain:

$$\epsilon_{tu} = \alpha_1 \epsilon_{cr} \quad (3.27)$$

where α_1 is the tensile strain ratio. Lin (1973) used a value of about 5, but no justification for the use of this value was provided. Gilbert and Warner (1978) selected $\alpha_1=10$ and Abdel-Rahman (1982) set α_1 to 10-25. Hanna and Mirza (1983) figured out that the value of α_1 between 20 and 30 gives the good agreement with the experimental response. Extensive reviews of the tension-stiffening of cracked concrete models have been reported by Hanna (1983) and ASCE (1982, 1991). However, there is neither a general adopted value for α_1 , nor a certain rule for its determination. Therefore, a simple method of evaluating ϵ_m to idealize the tension-stiffening effect, and to remove the mesh dependency drawback is required.

In the present study, four different models, as shown in Fig. 3.5, have been suggested to approximate the tension-stiffening effects. One popular model proposed by Kabir (1976) is to assume that the response of concrete under tensile stresses is linear elastic until the cracking condition is reached, followed by the linear descending branch beyond the cracking point (Fig. 3.5a). This model uses Eq. 3.27 to evaluate the concrete ultimate tensile strain, ϵ_m , with either $\alpha_1=10$, or as an input value selected by the user.

The various analyses of R C beams and shear panel (Shayanfar et al. 1993 and Kheyroddin et al. 1994) indicate that the computed results including the failure load have been strongly influenced by the size of the finite element -termed the "finite element size effect" or "mesh size dependency". Comparison of the computed responses with the experimental results indicated that the length of the descending branch of the concrete tensile stress-strain curve defined by the value of the ultimate tensile strain, ϵ_m , has a significant effect on the computed results (Fig. 3.5b). If the value of ϵ_m is adjusted appropriately according to the finite element size, it can remove the mesh dependency drawback. For evaluation of an "appropriate" value of ϵ_m , a new model (Eq. 4.1), as a function of the element size, has been proposed. The crack band model, based on fracture mechanics, as a function of the fracture energy, element size and tensile strength of concrete (Eq. 4.3), is also used. More information in this regard along with implementation of these two models into the NONLACS2 program is presented in Chapter 4.

Another tension-stiffening model with discontinuous softening, as shown in Fig. 3.5c, was implemented in the HODA program (Shayanfar 1995). The model with discontinuous softening was first proposed by Cope et al. (1979) and then used by Al-Manaseer and Philips (1987) to

analyze R C deep beams. This model has also been adopted and implemented in the NONLACS2 program.

As can be seen from Fig. 3.5c, the model assumes that

$$\begin{aligned} \sigma &= E_c \epsilon & \text{for } \epsilon \leq \epsilon_{cr} \\ \sigma &= \frac{\alpha_2 f_t (\alpha_1 - \frac{\epsilon}{\epsilon_{cr}})}{(\alpha_1 - 1)} & \text{for } \epsilon_{cr} \leq \epsilon < \alpha_1 \epsilon_{cr} \\ \sigma &= 0.0 & \text{for } \epsilon \geq \alpha_1 \epsilon_{cr} \end{aligned} \quad (3.28)$$

where ϵ and σ are the strain and the stress normal to the crack directions, $\alpha_1 = \epsilon_w / \epsilon_{cr}$, and α_2 is dropping factor which is less than one. The parameters α_1 and α_2 are usually difficult to select in practice because of the lack of experimental data for calibration. An increasingly accepted view, for example, Rots et al. (1985), is that these parameters should be related to the fracture energy of the concrete. This at least reduces the dependency of the model on the mesh size. Al-Manaseer and Philips (1987) suggested $\alpha_1=10$ and $\alpha_2=0.6$, while Ueda and Kawai (1985) selected $\alpha_1=25$ and $\alpha_2=0.5$ in their studies.

The above models assume that when the concrete tensile strain at any point exceeds the ultimate tensile strain, ϵ_w , (region with KC=4 in Fig. 3.2a), there can be no tensile stress normal to the crack ($\sigma_t=0$). This phenomenon causes some numerical difficulties. In order to eliminate this drawback, a small amount of tensile stress as a fraction of tensile strength, $\gamma_t f_t$, is assigned to the point considered, where parameter γ_t is the remaining tensile strength factor as shown in Fig. 3.5d. For the elastic tension region, the tensile modulus of elasticity is assumed to be equal to the initial modulus of elasticity of concrete in compression, $E_i=E_0$, and for the descending branch of the tension zone (kc=3 and 4 in Fig. 3.2a), E_i is set to very small amount equal to 0.0001 to avoid computational difficulties associated with a negative and zero value for E_i .

3.4.6 Failure Criteria for Concrete

The behaviour of concrete under biaxial stress states, as reported by a number of investigators (including Kupfer et al. 1969, Liu et al. 1972 and Tasuji et al. 1978), is remarkably different from that under uniaxial conditions. It has been observed that under biaxial compression, concrete exhibits an increase in the compressive strength of about 20 percent over the uniaxial compressive strength. A constant strength has been reported under biaxial tension although Tasuji

et al. (1978) suggest that the tensile strength might increase slightly. The tensile strength is reduced under combined actions of tension and compression. It was found that the simple criterion of a constant tensile strength also works quite satisfactorily. Therefore, the biaxial strength envelope curve proposed by Kupfer and Gerstle (1973) is used in the NONLACS2 program, as shown in Fig. 3.6.

3.4.7 Constitutive Relationship for Steel Reinforcement

The response of steel is basically uniaxial and consequently modelling of its behaviour is relatively simple compared to that of the concrete. Two aspects of steel models are relevant here: the representation of steel in the finite element model and the constitutive relationship. As shown in Fig. 3.7, three most common methods used to represent reinforcing steel in finite element models (ASCE 1982) are: 1) Distributed (smeared), 2) Embedded, and 3) Discrete.

In the distributed representation, the steel is smeared over the concrete with a particular orientation angle θ and a perfect bond is assumed between the concrete and the steel (Fig. 3.7a). In the embedded representation, the reinforcing bars are considered to be a uniaxial member built into the concrete element, such that its nodal displacements are consistent with those of the concrete element. Again, perfect bond must be assumed between the concrete and the reinforcing steel. A discrete representation of the reinforcing bar, using one dimensional elements, has been widely used (Fig. 3.7c). Axial force members, or bar links, may be used and assumed to be pin connected with two degrees of freedom at the nodal points. A significant advantage of the discrete representation, in addition to its simplicity, is that it can account for possible displacement of the reinforcement with respect to the surrounding concrete.

The stress-strain behaviour of steel is usually represented by a bilinear or a trilinear idealization identical in tension and compression. An elastic-perfectly plastic, or an elastic-strain hardening model utilizes a bilinear curve, while an elastic-plastic strain-hardening model is represented by a trilinear curve. Figure 3.8 shows the typical idealizations.

In the NONLACS2 program, a bilinear elastic strain-hardening constitutive model is utilized for steel (Fig. 3.8b). The model is defined by four parameters; f_y , E_s , E_s^* , and ϵ_{su} , which are the yield strength, the modulus of elasticity, the strain-hardening modulus, and the ultimate strain of the steel, respectively. The reinforcing and prestressing bars can be modeled either as a smeared layer or as individual bars. In both cases, perfect bond is assumed between the steel and the concrete. The constitutive relationship for steel before yielding is given by:

$$\{\Delta\sigma\} = \begin{bmatrix} E_s & 0 & 0 \\ 0 & 0 & 0 \\ 0 & 0 & 0 \end{bmatrix} \{\Delta\epsilon\} \quad (3.29)$$

where E_s is the uniaxial elastic modulus, and the subscript s represents the direction parallel to the reinforcement. After the steel yields, the constitutive relationship is modified so that the initial elastic modulus, E_s , is replaced by strain-hardening modulus, E_s^* . For example, in an elastic-strain hardening model, the modification is as shown in Eq. 3.30.

$$\{\Delta\sigma\} = \begin{bmatrix} E_s^* & 0 & 0 \\ 0 & 0 & 0 \\ 0 & 0 & 0 \end{bmatrix} \{\Delta\epsilon\} \quad (3.30)$$

where E_s^* is the strain-hardening modulus (Fig. 3.8b).

3.5 THE NONLINEAR LAYERED FINITE ELEMENT FORMULATION

3.5.1 Displacement Based Formulation in Finite Element

There are two basic methods for structural analysis: the flexibility method (force method), and the displacement (stiffness) method. The first method treats the forces as unknowns, while in the second approach, the displacements are unknown. The displacement method is simpler, more systematic and convenient for computer implementation. An energy principle, such as the principle of virtual work can be used for establishing the stiffness matrix of the individual finite elements. The following basic steps are involved:

1) The displacements at any point within the element $\{u\}$ are expressed in terms of the nodal displacements of the specific points within, or on the boundary of element called "nodes", $\{U\}_n$, by shape function

$$\{u\} = [N]\{U\}_n \quad (3.31)$$

where $[N]$ is shape function matrix, $\{U\}$ is the displacement at any point and $\{U\}_n$ is the element nodal displacement vector in element local coordinate system.

2) The strains at any point of the element, $\{\epsilon\}$, are related to the element nodal displacements, $\{U\}_n$

$$\{\epsilon\} = [B]\{U\}_n \quad (3.32)$$

in which [B] is the strain-displacement matrix and can be obtained as:

$$[B] = [L][N] \quad (3.33)$$

where [L] is the linear-operator matrix and defined as

$$\{\epsilon\} = [L]\{u\} \quad (3.34)$$

3) Using an appropriate stress-strain relationship for linear elastic material

$$\{\sigma\} = [D](\{\epsilon\} - \{\epsilon_0\}) + \{\sigma_0\} \quad (3.35)$$

where [D] is the constitutive matrix, $\{\epsilon_0\}$ and $\{\sigma_0\}$ are the vectors of initial strains and stresses, respectively.

4) In considering the variation in the work done, δW_e , by the external forces, one must allow for the following possibilities: a body force, $\{b\}$ (per unit volume), a surface traction, $\{s\}$, and up to N point loads (external applied loads), $\{f_p\}$. The symbol $\{\delta u\}$ may be used represent either the variation of the displacements or the virtual displacement vector at any point of the element from the equilibrium condition, and can be defined in terms of the nodal displacements of the whole structure such that

$$\{\delta u\} = [N]\{\delta U\}_n \quad (3.36)$$

On the other hand, the internal virtual work can be obtained by

$$\delta W_i = \int_{V^e} \{\delta \epsilon\}^T \{\sigma\} dV \quad (3.37)$$

where the virtual strains at any point of the element, $\{\delta \epsilon\}$, is given by

$$\{\delta \epsilon\} = [B]\{\delta U\}_n \quad (3.38)$$

Based on the principle of virtual displacement for static and linear stress analysis, total internal work resulting from real stresses through the virtual strains must equal to the total external work due to the real external applied forces moving through the virtual displacements. This may be expressed as follows:

$$\sum_e \int_{V^e} \{\delta \epsilon\}^T \{\sigma\} dV = \sum_{p=1}^N \{\delta u\}^T \{f_p\} + \sum_e \int_{V^e} \{\delta u\}^T \{b\} dV + \sum_e \int_{S^e} \{\delta u\}^T \{s\} dS \quad (3.39)$$

where \sum_e is the summation over all elements, and V^e and S^e are volume and surface area of any element, respectively. Equation 3.39 is still quite general because a constitutive relationship has not been involved.

5) Substituting Eqs. 3.32, 3.35, 3.36, and 3.38 into Eq. 3.39, results in:

$$[K]\{U\} = \{F\} \quad (3.40)$$

where $[K]$ is the structure stiffness matrix, $\{U\}$ is the structure nodal displacement vector and $\{F\}$ is the equivalent nodal force vector of the structure, all in the global coordinate system. Once the element stiffness matrices have been calculated and transformed from local to global coordinates, the structure stiffness matrix $[K]$ is calculated by the systematic addition of element stiffnesses:

$$[K] = \sum_e [K]^e \quad (3.41)$$

in which $[K]^e$ is the element stiffness matrix and can be expressed as:

$$[K]^e = \int_{V^e} [B]^T [D] [B] dV \quad (3.42)$$

The equivalent nodal force vector $\{F\}$ is known and is given by

$$\{F\} = \{f_p\} + \{f_s\} + \{f_b\} + \{f_{\epsilon_0}\} + \{f_{\sigma_0}\} \quad (3.43)$$

where $\{f_p\}$ is the external applied nodal load vector; and $\{f_s\}$, $\{f_b\}$, $\{f_{\epsilon_0}\}$, and $\{f_{\sigma_0}\}$ are the equivalent nodal force vectors due to surface tractions, body forces, initial strains and initial stresses, respectively.

6) The solution of the Eq. 3.40 (equilibrium equation) yields the unknown nodal displacement vector. With the nodal point displacements known, the strains, $\{\epsilon\}$, and stresses, $\{\sigma\}$, at any point of the element are found using Eq. 3.35.

It can be noted that Eq. 3.40 can represent a system of linear equations when the stress-strain relationship given by Eq. 3.35 is linear, i.e. $[D]$ is independent of $\{\epsilon\}$. If the constitutive matrix $[D]$ is a function of $\{\epsilon\}$, the problem deals with material nonlinearity. On the other hand, obtaining Eq. 3.38 from Eq. 3.32 involves the assumption that the matrix $[B]$ is independent of $\{U\}$. If this assumption is not satisfied, the problem will be geometrically nonlinear (Ghoneim 1978).

3.5.2 Element Library

The program has an element library of membrane, plate bending, facet shell, one dimensional bar, boundary, and shear connector elements. Figure 3.9 shows some of the elements and their associated degrees of freedom. The two node, three degrees of freedom per node one dimensional bar element is used to model uniaxial truss members, unbonded prestressed tendons and shear connectors. The shear connector element is a specialized form of the standard bar element. This element is used to model the steel-concrete connection in composite construction.

There are two four node quadrilateral membrane elements RQUAD4 (Razapur and Nofal 1987) and QLC3 (Sisodiya et al. 1972) (see Fig. 3.9a). Both elements have three degrees of freedom per node (two in-plane translational, u and v , and one rotational degree of freedom, ω), but differ with respect to the assumed displacement fields (shape functions). The full development of the element RQUAD4, which uses a quadratic displacement field normal to the element side, together with the extensive performance tests, is given by Aziz (1988) and McNeal and Harder (1988). The element RQUAD4 is superior in its performance to the constant strain element and is comparable to the linear strain triangular element, but has fewer degrees of freedom than the latter. It also has the advantage of being easily connected to the standard beam elements when analyzing coupled shear walls or shear wall and frame interaction problems. Membrane element QLC3 has a cubic displacement field in one direction and a linear field in the orthogonal direction. The detailed derivation of QLC3 has been presented by Ghoneim (1978).

The library also contains two four node plate bending elements, the rectangular plate bending element, RBE (Zienkiewicz 1983), and the improved discrete Kirchhoff quadrilateral plate bending element, IDKQ (Chinniah 1985) (Fig. 3.9b). Both elements have three degrees of freedom per node (normal rotations θ_x and θ_y , and lateral displacement w). Element IDKQ does not account for the shear deformation through the plate thickness.

Two four node, six degree of freedoms per node, anisotropic facet shell elements are also available in the library (see Fig. 3.9d). These elements were obtained by combining the plate bending elements with the quadrilateral membrane elements. Since these elements are applied in problems involving material nonlinearities, the coupling between the membrane and bending actions is considered. In other words, the stiffness matrix $[k]$ of the shell element, with six degree of freedom per node shown in Fig. 3.9d, is given by

$$[k] = \begin{bmatrix} [k]_{pp} & [k]_{pb} \\ [k]_{bp} & [k]_{bb} \end{bmatrix} \quad (3.44)$$

where $[k]$ is a 24×24 stiffness matrix and the subscripts pp and bb denote the membrane and bending elements, respectively. The subscripts pb and bp signify the coupling effects between the membrane and bending actions. The coupling submatrices become null if the middle surface of the shell is an axis of material symmetry.

Shell element type I was obtained by combining the quadrilateral membrane element, QLC3, with the rectangular plate bending element, RBE. Shell element II (Quadrilateral Facet Shell Element, QFSE) was obtained by combining the quadrilateral membrane element, RQUAD4, with the discrete Kirchhoff quadrilateral plate bending element, IDKQ. The QFSE element includes the option to use a cubic field in both directions which is good for general behaviour, or a linear field in one and a cubic field in the other which best represent the beam behaviour problems. The type of element to be employed during an analysis normally depends on the behaviour of the structure under consideration. The type I shell element accurately models the behaviour of a beam and is suitable for spatial structures in which beam type behaviour is dominant, while the type II shell element is a more general element.

3.5.3 Layered Discretization

The program employs a layered finite element approach; the structure is idealized as an assemblage of thin constant thickness plate elements with each element subdivided into a number of imaginary layers as shown in Fig. 3.9d,e. The number of layers depends on the behaviour of the structure being analyzed; for shell and plate bending problems, five to eight layers might be needed to model the stress variation across the thickness, while for plane stress problems using more than one layer is not necessary. A layer can be either of concrete, smeared reinforcing steel or a continuous steel plate. Each layer is assumed to be in a state of plane stress, and can assume any state - uncracked, partially cracked, fully cracked, non-yielded, yielded, or crushed - depending on the stress level. These are indicated by indices $KC = 1, 2, 3, 4, 5,$ and 6 in Fig. 3.2a.

The reinforcing steel can be idealized as a smeared layer or as a bar element embedded in the concrete at the reference surface. Smeared steel representation is suitable for representing distributed reinforcement as in slabs and structural walls, while the bar representation is appropriate for isolated large reinforcing bars or tendons such as in beams with heavy longitudinal reinforcement. The stiffness is allowed to vary over the area of the element and from one layer to the other according to the associated stress variation. The element stiffness is obtained by adding the stiffness contributions of the various layers at each Gauss quadrature point.

3.5.4 Nonlinear Analysis Method

Analysis is performed using an incremental-iterative tangent stiffness approach. The change in the material stiffness matrix during loading necessitates an incremental solution procedure. Techniques have been developed (Desai and Abel 1972) for solution of nonlinear problems by the finite element method using piece-wise linearization. Three basic techniques are used presently: (1) Incremental or Stepwise procedures, (2) Iterative or Newtonian methods, and (3) Incremental-Iterative or Mixed procedures. The latter combines the advantages of both the incremental and the iterative methods and tends to minimize their disadvantages (for more information on the advantages and disadvantages of these methods, see Desai and Abel 1972).

As mentioned previously, the incremental-iterative procedure with a tangent stiffness scheme (see Fig. 3.10) has been adopted in the NONLACS2 program. This means that the tangent constitutive matrix $[D_i]$ after the i th iteration is employed in deriving the stiffness matrix to be used during the following iteration or load increment.

3.5.5 Unbalanced Forces

The unbalanced forces after each iteration are calculated using the initial stress method of Zienkiewicz et al. (1969). The method is based on a fact that a unique increment of stress corresponding to an increment of strain is available. After the iteration i , the unbalanced stress vector, $\{\bar{\sigma}_i\}$, is given by

$$\{\bar{\sigma}_i\} = \{\Delta\sigma_i\} - [D_{i-1}]\{\Delta\epsilon_i\} \quad (3.45)$$

where $[D_{i-1}]$ is the tangent constitutive matrix at the beginning of the iteration i , $\{\Delta\epsilon_i\}$ is the strain increment vector during the iteration i , and $\{\Delta\sigma_i\}$ is the "true" stress increment obtained from the stress-strain relationship.

The equivalent unbalanced forces, $\{\bar{F}_{i+1}\}$, to be applied in the next iteration are then given by

$$\{\bar{F}_{i+1}\} = -\sum_v \int [B]^T \{\bar{\sigma}_i\} dV^v \quad (3.46)$$

3.5.6 Convergence Criteria

Convergence criteria are utilized to stop the iterations in each load step as soon as a degree of accuracy has been reached. In the NONLACS2 program, two convergence criteria developed by Lin (1973) and Kabir (1976) are adopted. Lin used absolute values of input convergence/divergence data, but Kabir added convergence/divergence that uses input percentage factors to be multiplied by the solutions computed in the first iteration of each load step.

For any of these procedures, two possible convergence criteria are used:

- (1) How large are the unbalanced forces after the i th iteration $\{\bar{F}_{i+1}\}$? or

(2) How small are the displacement increments $\{\Delta\delta_i\}$?

The method based on criterion (1) is called the force convergence criterion and the one based on (2) is termed the displacement convergence criterion. In the NONLACS2 program, the convergence in iteration i , for example, is checked as follows:

(1) Evaluate the maximum absolute value of unbalanced force/displacement components in the six global directions at all nodes and establishes the norm vector $\{F_0\}^{(i)}_{6 \times 1}$.

(2) If all components of the norm vector $\{F_0\}$ are less than the tolerable convergence values, convergence is assumed to have occurred and no more iterations are performed. Otherwise another iteration is executed unless $i > n$ where n is the maximum number of iterations allowed per load step specified in the input data file. At the end of each load step (where either convergence criteria are satisfied, or $i > n$), the remaining unbalanced forces are added to the next load increment to avoid the accumulation of error over the load steps.

3.5.7 Divergence Criteria

As for the convergence criteria, two possible divergence criteria are available in the NONLACS2 program:

- 1) Displacement divergence criterion or,
- 2) Force divergence criterion.

If any of the norm vector components $\{F_0\}$ exceeds the corresponding maximum force/displacement values input as the divergence values, the solution will be terminated because of excessive unbalanced forces or displacements.

If during a load increment, displacement increments or unbalanced forces which do not decrease during the iterations are encountered, divergence is also said to have occurred indicating structural collapse. If this happens, zero values will appear on the main diagonal of the structural stiffness matrix, and the equilibrium equations will become singular and the execution will be stopped. A message stating " Zero on Diagonal of Stiffness Matrix, Solution is Stopped." will appear in the output file.

3.6 IMPLEMENTATION OF PROPOSED MODELS IN THE COMPUTER PROGRAM

The NONLACS2 program is based on nonlinear layered finite element approach and can be used as an ideal research-oriented tool to examine the nonlinear behaviour of reinforced normal and high-strength concrete structures. This program provides the following options for the user:

Mesh dependency analysis option

- 1 = No mesh dependency analysis
- 2 = Mesh dependency analysis based on the crack band model
- 3 = Mesh dependency analysis based on the proposed model

Tensile-softening branch option (dropping factor, α_2)

- 1.0 = No dropping
- 1.0-0.0 = Dropping after cracking including tension-stiffening
- 0.0 = Sudden drop to zero (no tension-stiffening)

Remaining tensile strength factor, γ_t , option

- 0.0 = Zero tensile stress when $\epsilon_t > \epsilon_{tu}$
- 0.01 - 0.1 = A small value to avoid numerical difficulties

Concrete compressive stress-strain curve option

- 1 = Saenz and Smith's equations
- 2 = Modified Popovics equation

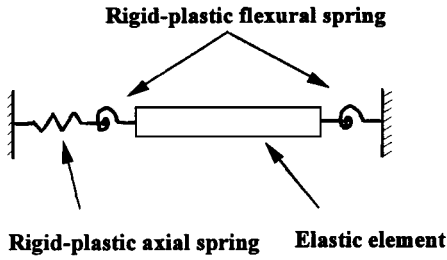
Concrete ultimate compressive strain, ϵ_{cu} , option

- 1 = As an input value by user
- 2 = Confined concrete (Scott et. al. 1982)
- 3 = Unconfined concrete (Pastor 1986)

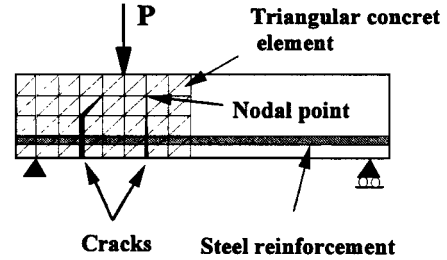
Remaining compressive strength factor, γ_c , option

- 0.0 = Zero compressive stress when $\epsilon_c > \epsilon_{cu}$
- 0.01 - 0.1 = A small value to avoid numerical difficulties

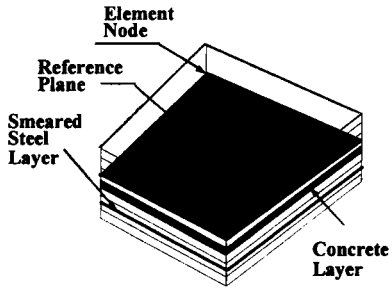
Although, it is attempted to verify the accuracy of new modifications into the NONLACS2 program in the rest of the present study, more analytical work is needed to investigate the effect of above new modifications on the computed response of R C structures. A flowchart for the NONLACS2 program is shown in Fig. 3.11. A detailed description of the input data required to run the program based on the latest modifications is presented in Appendix A.



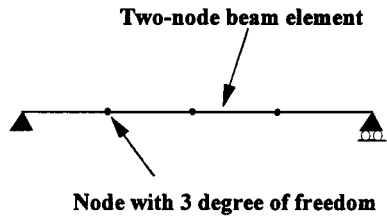
(a)



(b)

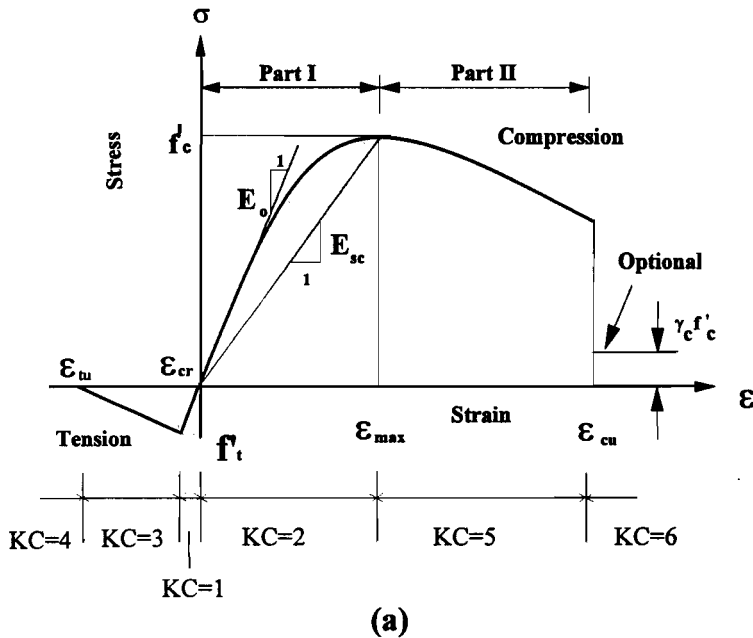


(c)

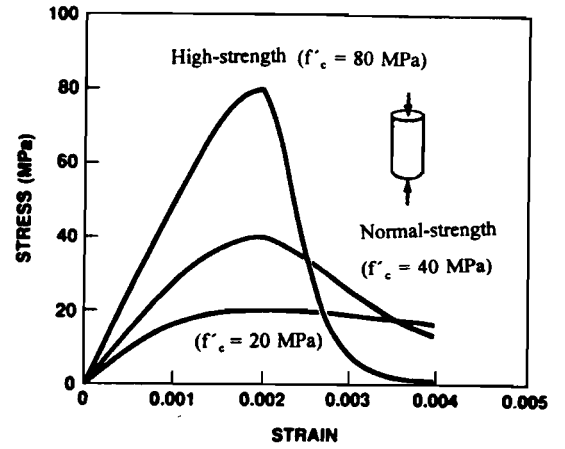


(d)

Figure 3.1: Nonlinear analysis methods: (a) lumped-plasticity approach (Riva 1988), (b) discrete model (Ngo and Scordelis 1967), (c) layered finite element, and (d) modified stiffness approach



(a)



(b)

Figure 3.2: Analytical uniaxial stress-strain curve for plain concrete: (a) Saenz and Smith equation, (b) modified Popovics equation (Collins and Porasz 1989)

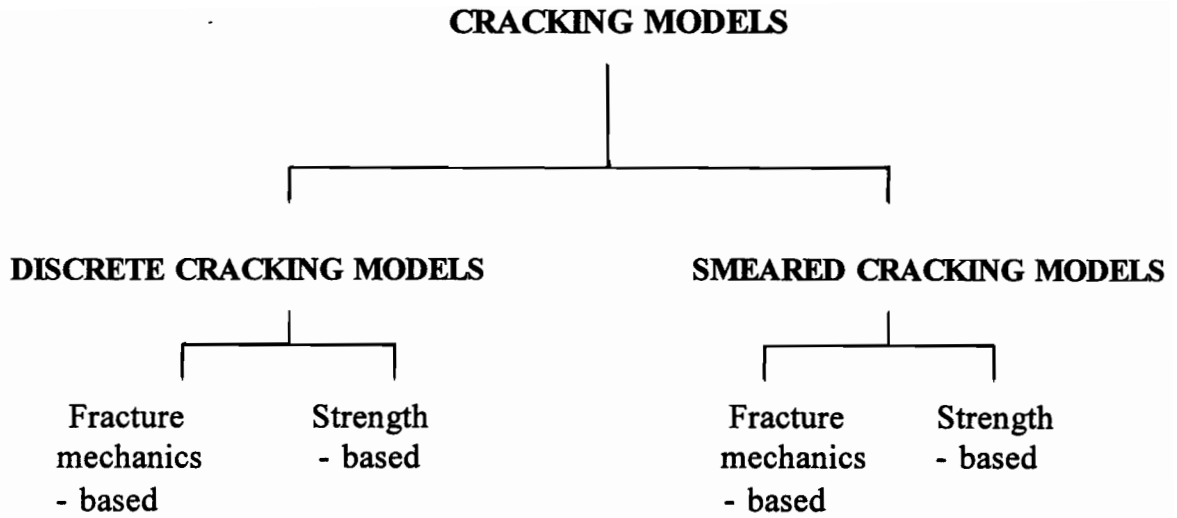


Figure 3.3: Classification of cracking models

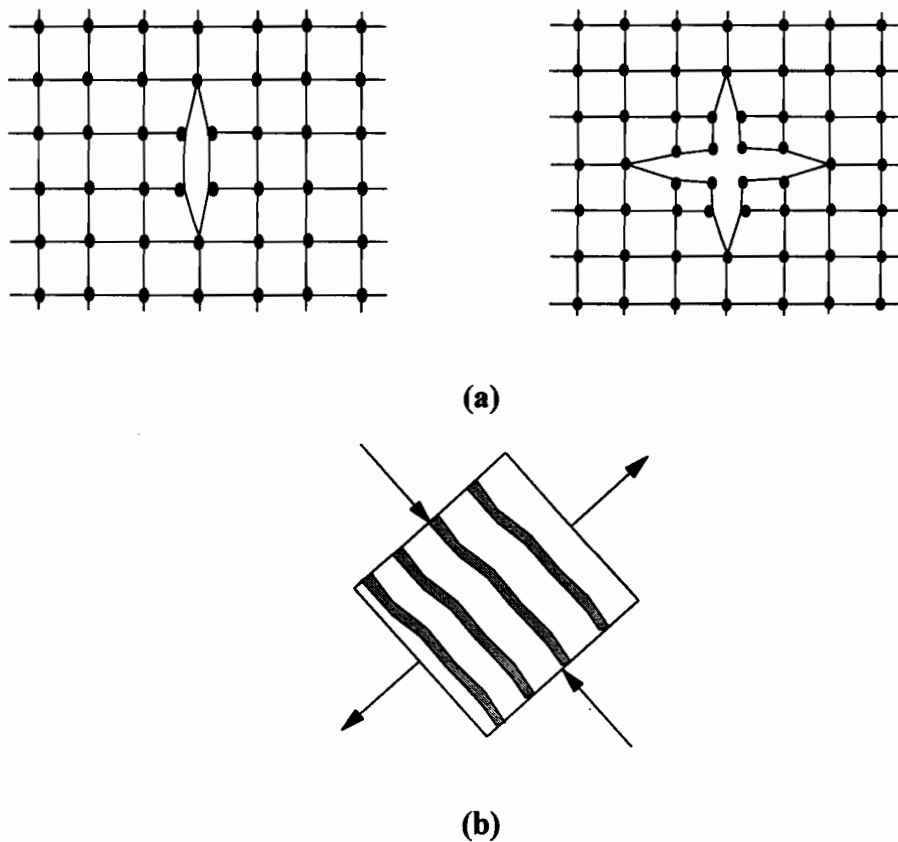


Figure 3.4: Idealization of Cracks: (a) nodal separation using two or four coincident nodes, (b) smeared crack (ASCE 1982)

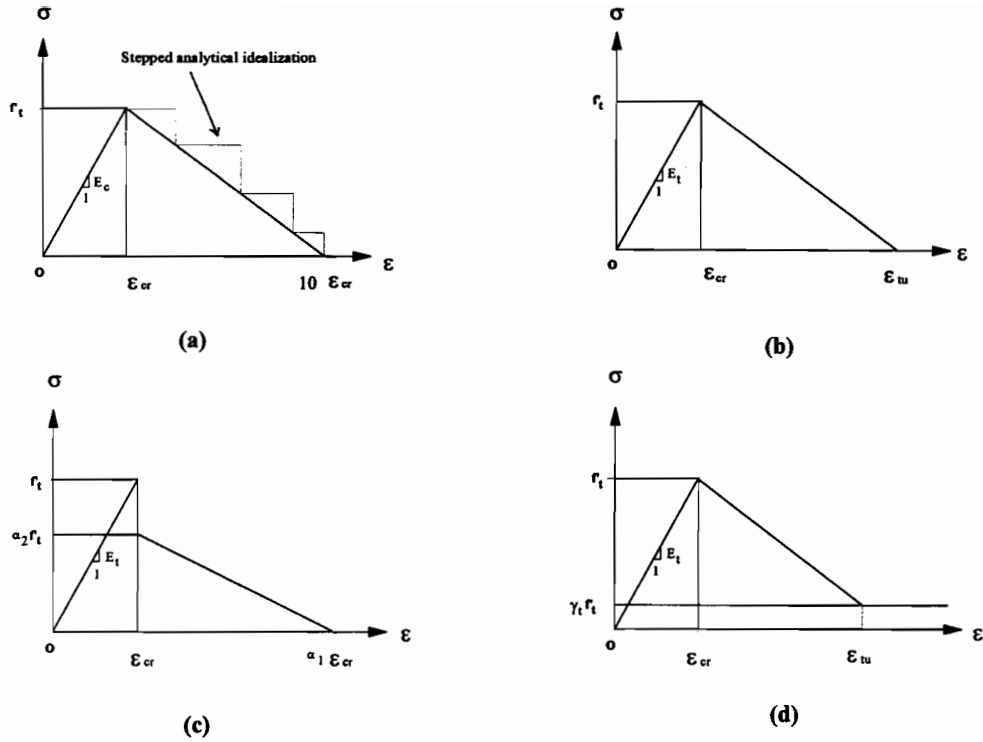


Figure 3.5: Different proposed models for concrete in tension: (a) linear softening, (b) proposed model, (c) discontinuous softening, and (d) small stress when $\epsilon_t > \epsilon_w$.

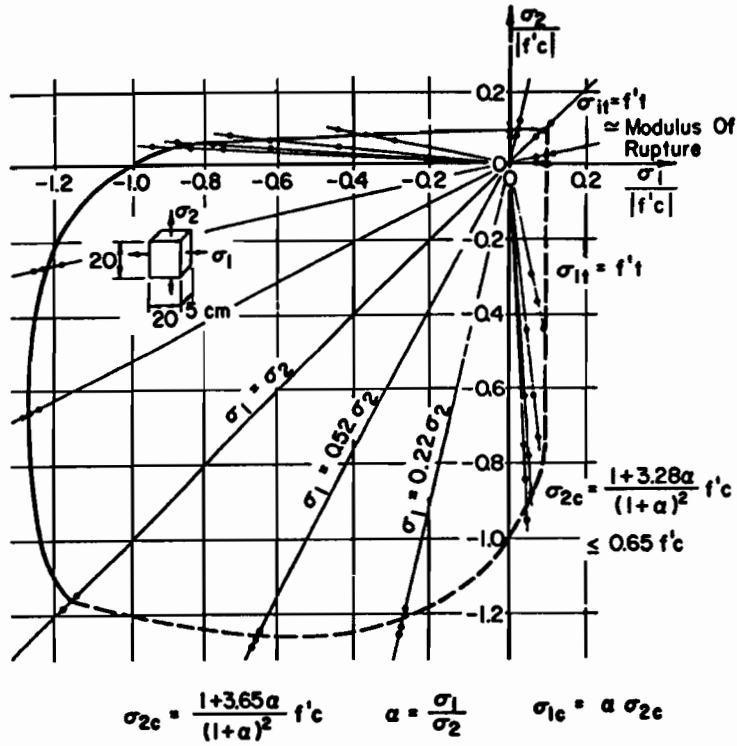


Figure 3.6: Typical biaxial failure envelope for concrete (Kupfer and Gerstle 1973)

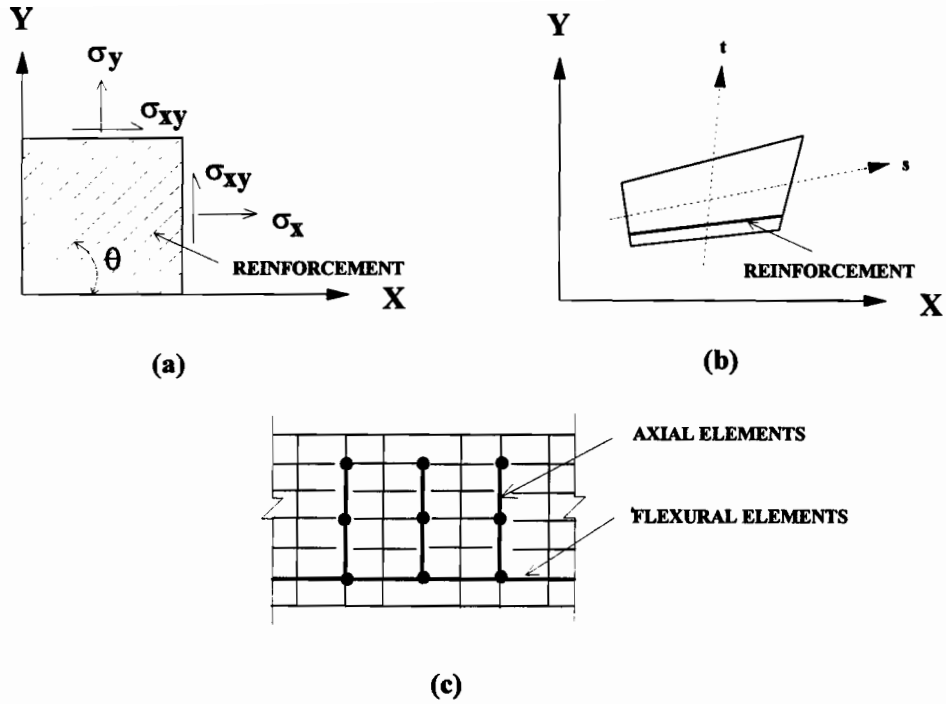


Figure 3.7: Typical steel representations in finite element models of concrete structures, (a) smeared, (b) embedded, and (c) discrete (ASCE 1982)

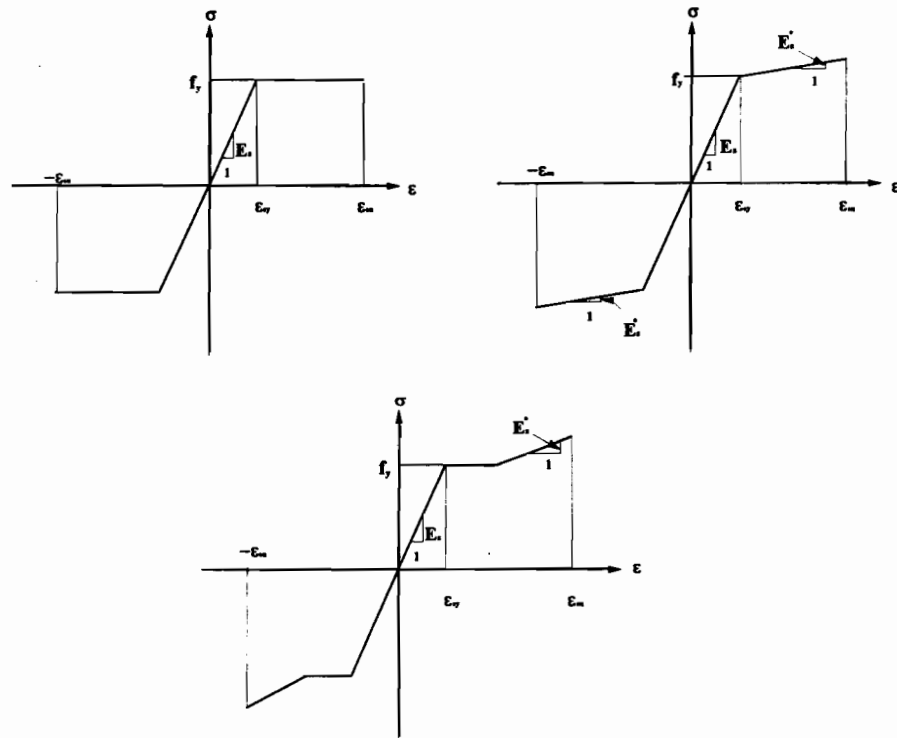


Figure 3.8: Idealized steel stress-strain curves: (a) elastic-perfectly plastic, (b) elastic-strain hardening, (c) elastic-plastic strain-hardening

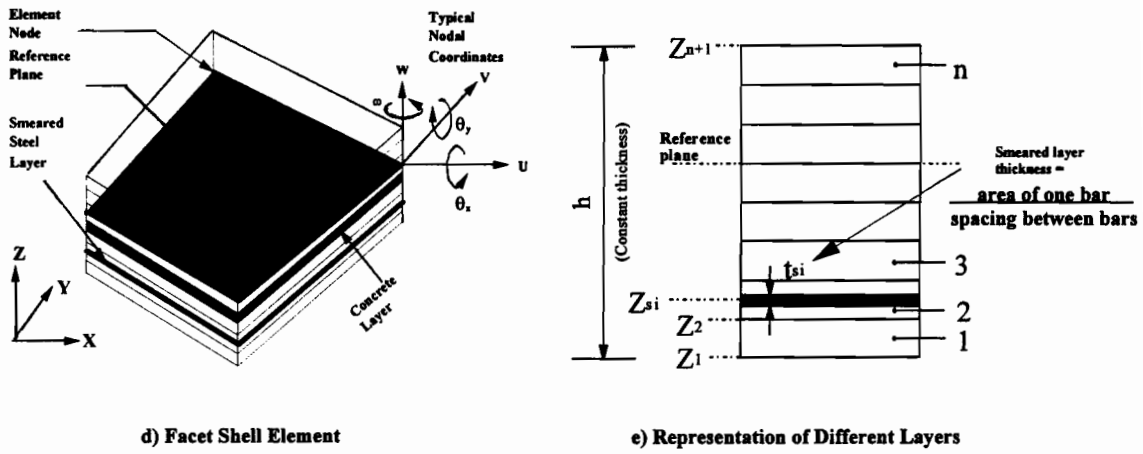
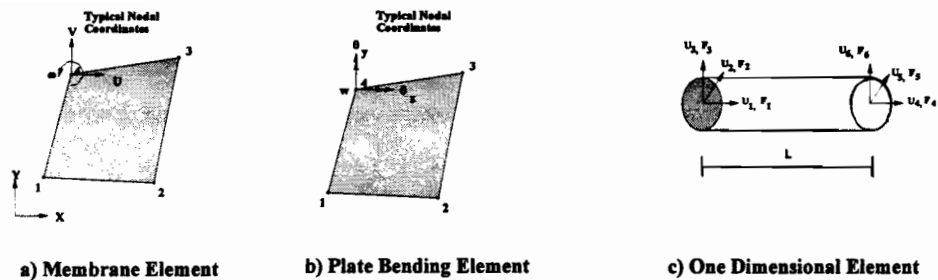


Figure 3.9: Some typical finite elements in the NONLACS2 program

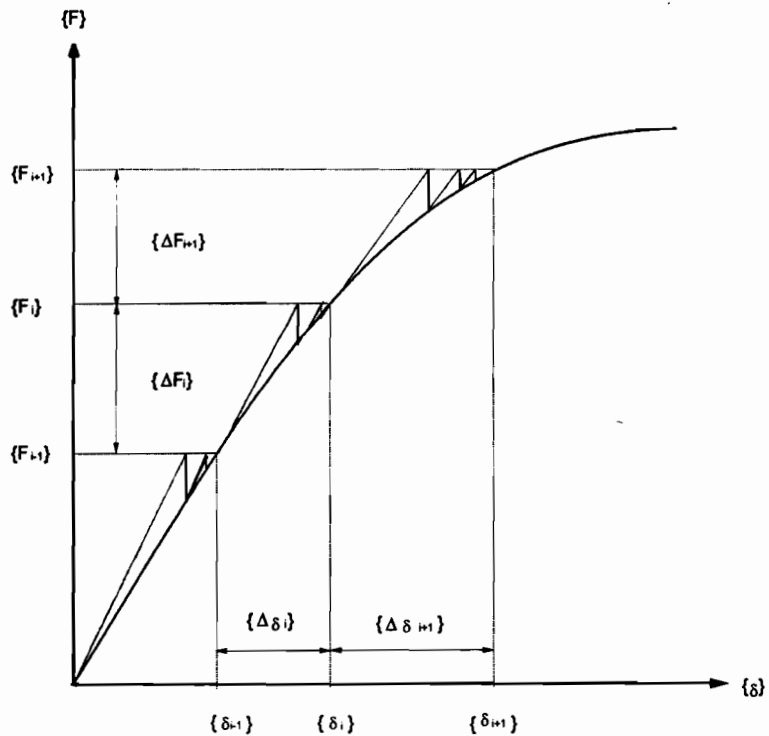


Figure 3.10: A schematic representation of the incremental-iterative tangent stiffness method

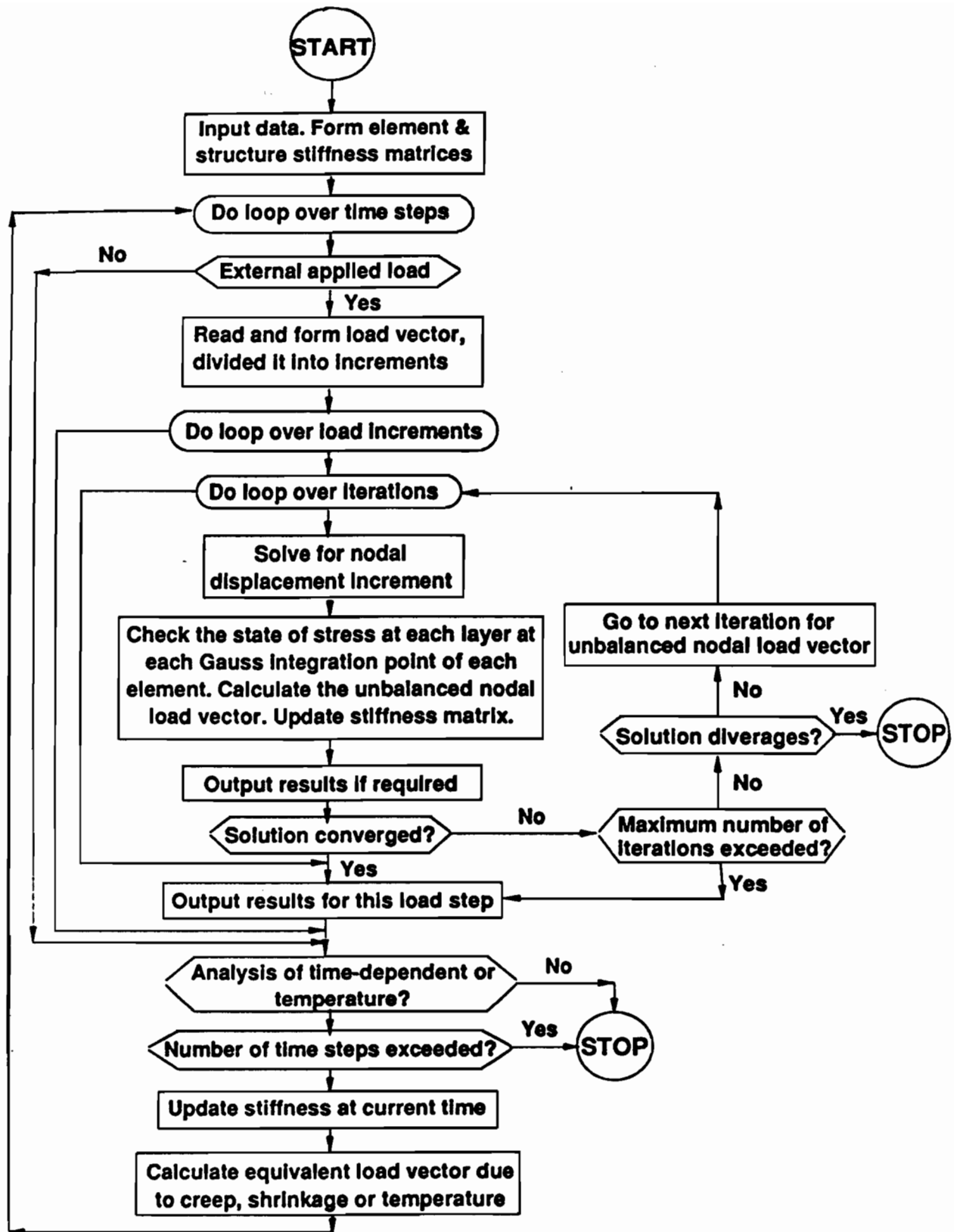


Figure 3.11: Flow chart of the NONLACS2 program (Ghoneim 1978).

CHAPTER 4

FINITE ELEMENT SIZE EFFECT PHENOMENON

Shayanfar, Kheyroddin and Mirza (1993) found from the analyses of two simply supported beams and a shear panel that the general computed response of selected reinforced concrete members was strongly influenced on the size of the finite element -termed the "mesh dependency phenomenon". This chapter reports the determination of the key parameters that can help to remove this drawback. The effect of finite element size on the different behavioural aspects of R C structures including the ultimate load, load-displacement and load-strain characteristics and crack pattern are discussed along with a comparison with the experimental data where available. A new formula, as a function of the element size, has been proposed for determination of the ultimate tensile strain of concrete, ϵ_{m} , and elimination of the mesh dependency phenomenon. The crack band model, based on the fracture mechanics concepts, as a function of fracture energy, element size and tensile strength of concrete is also used. The procedures employed for implementation of the crack band model and the new proposed model into the nonlinear finite element program, NONLACS2, are then presented. For further verification of the validity of the proposed model, the author investigated another five beams tested by Gaston et al. (1952) and the results are reported in this chapter. The analytical results obtained using the different models are compared; the new proposed model showed good agreement with the experimental results in the prediction of the ultimate load, load-deflection and concrete load-strain characteristics, and the concrete cracking pattern. The proposed model can be used effectively with meshes with relatively large size elements resulting in reasonably accurate results with much smaller computational effort compared with that required for finer meshes.

4.1 PARAMETERS INFLUENCING THE COMPUTED RESULTS

In nonlinear finite element analysis, the computed responses including the load-displacement and strain characteristics, cracking patterns and the ultimate loads are influenced by many parameters which the analyst incorporates into the model, or are specified during the analysis. Some of these are due to the numerical effects such as the element type, load step, convergence and divergence criteria, integration order and the finite element size. Some of the factors associated with the material model are cracking criterion, tension-stiffening, tension-softening, bond-slip, compression-hardening, compression-softening, compression ductility, variation of shear stiffness with cracking, multidirectional cracking, and multiaxial stress conditions. Balakrishnan and Murray (1986) studied the effect of many of these parameters on the predicted behaviour of R C beams. The effect of the shape of the descending branch of the tensile stress-strain curve, fracture energy, grid refinement and load-step size on the response of finite element models of plain concrete beams was also studied by Leibengood et al. (1986).

Cracking of the concrete is one of the important aspects of material nonlinear behaviour. Intensive research effort has resulted in a large number of cracking models, which can be divided broadly into two categories, namely, the discrete cracking models and the smeared cracking models. Furthermore, within each category, these models can be applied either with a strength-based, or fracture mechanics-based crack propagation criterion. The dependency of results on the finite element size arises basically from the use of the smeared, or the discrete cracking models based on the strength concept (Bazant and Cedolin 1979, Bazant 1992). As explained in Section 3.4.4, in the smeared cracking model, the tensile stress in a finite element is limited by the tensile strength of the material, f_t , and after reaching this strength limit, the stress in the finite element decreases. In the earlier research programs, the tensile stress was assumed to decrease abruptly to zero, with a vertical drop in the stress-strain curve at the maximum stress (Fig 4.1, curve OPC). However it was realized that improved and more realistic results are usually obtained if the tensile stress is reduced gradually, i.e., the material is assumed to exhibit strain-softening (Lin and Scordelis 1975) (Fig. 4.1, curve OPA). Experimental studies by Gopalaratnam and Shah (1985) showed that after cracking, the tensile strength of the concrete will not be lost suddenly. However, the concept of strain-softening proved to be a mixed blessing. After strain-softening had been implemented in large finite element analysis programs and widely applied, it was discovered that the computed results are not the same with regard to the element size used, i.e., the results change

significantly if the mesh is refined (Bazant 1976, Bazant and Cedolin 1979, 1980, 1983, Nilsson and Oldenburg 1982, Bazant and Oh 1983, Darwin 1985, Rots et al. 1985, Choi and Kwak 1990, Shayanfar et al. 1993, and Kheyroddin et al. 1994). Similar problems are encountered when cracking is idealized using the discrete cracking model, based on the strength concept (Bazant 1992). Gilbert and Warner (1978) analyzed the behaviour of R C slabs based on the variation of the slope of the descending branch of the stress-strain relationship of concrete. They were among the first to point out that the numerical analysis results of concrete structures are greatly dependent on the finite element mesh size used in modelling and are therefore affected by the tension stiffening effect in the concrete. Balakrishnan et al. (1988) also considered the size effect on the ultimate load for normal and deep beams.

The main focus of this chapter is the examination of the finite element size on the computed nonlinear response using the NONLACS2 program which is based on smeared cracking idealization for crack modelling. First, the existence of mesh dependency in the NONLACS2 program is demonstrated using two examples and then two analytical solutions are recommended for elimination of this drawback. The influence of the finite element size on the nonlinear analysis of R C frame structures is discussed in Chapter 8.

4.2 EFFECT OF FINITE ELEMENT SIZE ON COMPUTED RESPONSES

Two kinds of plane stress structural elements, i.e., beams and shear panel, are analyzed using different finite element meshes to study the effect of the element size. These structural elements were analyzed using the NONLACS2 program with no provision to account for the mesh size dependency. In this case the value of ϵ_u is given as an input value by the user and the computed results are influenced by the element size. For simplicity, this option is referred to as "no mesh dependency analysis" throughout the rest of this thesis. The experimental results for load-displacement and load-strain characteristics, cracking patterns and the ultimate loads are compared with the corresponding computed values. In each case, it is shown that the computed response and the ultimate load for these structures depend on the size and the number of elements.

4.2.1 Example 1: Reinforced Concrete Beams

Two simply supported R C beams with two concentrated third-point loads, tested by Gaston et al. (1952), are investigated. The geometry, reinforcement and loading of the beams are

shown in Fig. 4.2. The material properties and the dimensions of the beams are given in Table 4.1. The beam T2LA is under-reinforced, while the beam T5L is over-reinforced. The reinforcement is symmetrical with respect to the mid-span section for both beams.

In an attempt to study the influence of the element size and mesh refinement on the structures, six types of mesh configurations with 4, 20, 30, 80, 120, and 320 elements are used for idealizing beams T2LA and T5L, as shown in Fig. 4.3, and are analyzed using the NONLACS2 program. The element size varies from 1.5 in. (38.1 mm) to 18 in. (457.2 mm). Due to the symmetric configuration of the beam and the loading, only one-half of the beam is modeled for the finite element analyses.

Table 4.1: Dimensions and properties of Gaston's beams and Cervenka's shear panel

Dim. & Prop.	Beams								Shear Panel
	T2LA	T5L	T4LA	T1HB	C2W	C3YNA	C3YNB	C4XNB	W-2
A_s (in ²)	0.62	2.003	1.198	0.872	0.876	1.198	2.0035	1.198	0.11
A'_s (in ²)	0	0	0	0	0.3936	0.618	1.201	0.8765	-
f'_c (psi)	2120	2500	2380	5180	3940	3330	4860	2430	3650
E_o (psi)	262E4	288E4	280E4	415E4	361E4	332E4	331E4	280E4	290E4
ϵ_{cu} (*)	0.004	0.004	0.004	0.004	0.004	0.004	0.004	0.004	0.0035
f'_t (psi)	345	500	365	570	470	430	520	370	530
ν (*)	0.17	0.17	0.17	0.17	0.17	0.17	0.17	0.17	0.17
f_y (psi)	44000	40200	44100	52200	45400	45200	42100	46400	51200
E_s (psi)	275E5	288E5	322E5	300E5	300E5	322E5	288E5	322E5	273E5
E_s^* (psi)	106E4	822E3	161E4	150E4	150E4	161E4	822E3	161E4	251E3
ϵ_{su}	0.036	0.036	0.036	0.036	0.04	0.04	0.04	0.04	0.036

(*) *Assumed values*

Half of the total load is applied to the structure in 30 load steps varying from large to very small increments as the ultimate load is approached. The bending of these beams can be considered to be a plane stress problem, therefore, the concrete is modeled by one concrete layer.

The longitudinal reinforcements are lumped in a single bar at the reference surface as a bar element. The stirrups are modeled as smeared steel layers on the two sides of the beam. The concrete ultimate tensile strain, ϵ_m is assumed to be constant for all mesh sizes and equal to 0.0007.

The load-deflection curve for the under-reinforced beam T2LA is shown in Fig. 4.4, which presents the results for the models with five types of meshes. As can be seen from Fig. 4.3, the coarsest mesh (4 elements) overestimates the ultimate load (19,500 lb), while the finest mesh (320 elements) underestimates it (14000 lb), in comparison with the experimental ultimate load of 15,666 lb. When a coarse mesh is used, the structure is a little stiffer and behaves in a relatively more ductile manner. With a decrease in the size of the elements, the ultimate load also decreases and the structure exhibits a less ductile response. In fact, the deflection at the ultimate load decreases with a decrease in the element size. The experimental failure mode is flexural which agrees with the computed mode of failure.

Variation of the computed ultimate load with the number of elements is presented in Fig. 4.5, which shows that the ultimate load for the beam T2LA is dependent on the mesh used in the analysis. It can be noted that the ultimate load for this under-reinforced beam decreases with an increase in the number of finite elements.

Another important factor in the behaviour of concrete elements is the concrete load-strain curve. To show the effect of the element size on the predicted values of the concrete strain, for three mesh configurations with 4, 80, and 320 elements, the computed load-concrete strain curve at the beam midspan top is presented in Fig. 4.6. Once again the results are influenced by the element size and it emphasizes the sensitivity of the computed responses to the mesh characteristics.

For the beam T5L, which is over-reinforced, a similar analysis procedure is followed. The results show that the effect of element size on the ultimate load is not significant, i. e., the beam response is not dependent on the mesh characteristics.

Because of the high ratio of tensile reinforcement, cracking of the concrete does not have a significant effect on the material nonlinearity of the concrete. Also, as the value of ϵ_m was varied with all other parameters maintained constant, the ultimate load remained approximately constant and close to the experimental ultimate load (see Table 4.2).

Table 4.2: Effect of element size and ϵ_{tu} on the ultimate load of beam T5L.

Number of Elements	Size of Elements (in x in)	Finite Element Aspect Ratio	ϵ_{cr}	ϵ_{tu}	Ultimate Load (lb)	$P_{u,anl}/P_{u,exp}$
4	18 x 12	1.5	0.00013	0.001	17000	0.96
20	6 x 6	1.0	0.00013	0.001	17000	0.96
80	3 x 3	1.0	0.00013	0.001	16500	0.94
80	3 x 3	1.0	0.00013	0.0021	16500	0.94
80	3 x 3	1.0	0.00013	0.0031	16500	0.94
320	1.5 x 1.5	1.0	0.00013	0.001	16500	0.94
Experimental Result	-	-	-	-	17666	-

4.2.2 Example 2: Reinforced Concrete Shear Panel W-2

The shear panel W-2, tested by Cervenka (1970) under monotonically increasing load, is investigated in this example. The panel consisted of orthogonally reinforced square plates, 30 in. x 30 in. (762 mm x 762 mm) in size, and 3 in. (76.2 mm) in thickness. Two panels were combined to form one beam, like the specimen, shown in Fig. 4.7. The material properties and dimensions of the shear panel are summarized in Table 4.1. Because of symmetry, only one-half of the specimen is idealized for the finite element analysis. The total load is applied at the two points on the outer ribs as shown in Fig. 4.7.

The concentrated reinforcements in the ribs are modelled as embedded bar elements and the distributed reinforcement in the webs is idealized as smeared steel layers. These layers have the same configuration in the vertical direction, but are different along the horizontal alignment depending on the detailing configurations. The horizontal reinforcement is varied, so that more reinforcement is located in the bottom six inches of the panel than in the top twenty-four inches, as indicated in Fig. 4.7.

For the mesh size dependency study, three different meshes with 35, 120, and 460 elements have been examined. Figure 4.8 illustrates these mesh configurations for the shear panel. The ultimate tensile strain, ϵ_{tu} , is assumed to be constant and arbitrarily selected to be 0.002.

The load-deflection curve for this panel is plotted in Fig. 4.9. As in Example 1 (beam T2LA), it can be observed that the element size has a significant effect on the load-deflection characteristics. Once again, it was noted that with an increase in the number of finite elements idealizing the system, the ultimate load decreases. In each case, as expected, the deflection

response before cracking is identical, however, after cracking there are deviations from the experimental response and the deflection at the ultimate load decreases with a decrease in the element size. The mechanism of failure for all mesh configurations was of the flexural type, where the steel reinforcement yielded first, followed by the crushing of the concrete, which agreed well with the experimental mode of failure.

The effect of different mesh configurations on the analytical crack pattern at a certain load level ($P=24,000$ lb) for the shear panel is shown in Fig. 4.10. In this figure, the thick line is used to indicate the fully opened cracks ($\epsilon > \epsilon_w$), and the thin line shows the partially opened cracks ($\epsilon_{cr} < \epsilon < \epsilon_w$). According to Fig. 3.2a, in the ascending branch of tensile stress-strain curve with $KC=1$, the concrete is assumed to be uncracked; in the descending branch with $KC=3$, the concrete is assumed to crack, which is partially opened; and in the region with $KC=4$, the concrete is assumed to be cracked with the cracks fully open. It can be noted from Fig. 4.10 that the crack patterns are different and are influenced considerably by the element size. With a decrease in the element size, the progress of fully opened cracks increases resulting in wider crack patterns. It is also evident that the penetration of the fully opened cracks in a finer mesh configuration is greater than that for the coarse mesh and consequently it leads to a lower ultimate load and slightly softer response for the finer mesh.

4.3 PHYSICAL DESCRIPTION OF MESH SIZE DEPENDENCY

The influence of finite element size can be illustrated, for example, by qualitative consideration of the rectangular panel in Fig. 4.11 a and b, which is subjected to a uniform vertical displacement at the top boundary. A small region near the centre of the left side is assumed to have a slightly smaller strength than the rest of the panel, and consequently a smeared crack band starts growing from the left to the right. The solution is obtained by incremental loading with two finite element meshes of very different mesh sizes as shown. By stability checks, it is found that the cracking must always localize into a band of single element width at the cracking front (Fig.4.11 a,b). Typical qualitative results for this, and other responses such as load-deflection and energy released versus the number of elements are illustrated in Fig.4.11(c,d). In the load-deflection diagram (Fig. 4.11c), it is seen that the peak load as well as the post-peak softening is strongly dependent on the element size. In other words, with an increase in the element size, the ultimate load increases and the structure behaves in a stiffer manner compared with a model with

smaller size element. From a physical point of view, the magnitude of the tensile stress at the crack depends on the sharpness of the front of the crack band and the element width. The smaller is this width, the larger is the stress in the element just ahead of the crack front, and the smaller is the applied load that causes crack propagation. In the limit, if the element width decrease to zero, the stress in the element just ahead of the crack becomes infinite for any small value of load, which indicates that the crack would propagate at a very small load. Therefore, a finer element mesh increases the crack propagation rate, resulting in a decrease in the energy dissipation and an ultimate load smaller than the experimental load. The contrary is true when larger size elements are used, resulting in an overestimation of the ultimate load.

The energy which is dissipated due to cracking decreases with the refinement of the finite element mesh (solid line in Fig. 4.11d) and converges to zero as h tends to zero. The above dependence of the member response on finite element size is unacceptable. It is clear that the energy dissipation capacity of the structure must be independent of the element size and a new analytical solution is required to predict the same energy dissipation capacity regardless of the number of elements (dashed line in Fig. 4.11d).

4.4 ANALYTICAL SOLUTIONS FOR ELEMENT SIZE DEPENDENCY

As already mentioned, the problem of mesh sensitivity is encountered when cracking is idealized using the smeared or discrete cracking models based on the strength concept. The main objective of this chapter is to develop a solution to eliminate this drawback from the strength-based criterion with an appropriate adjustment of the value of the ultimate tensile strain, ϵ_m , as a function of only the element size, h . For the sake of comparison, the "crack band model" proposed by Bazant and Oh (1983) is also utilized in the present study and some key features of this model are presented in the following section.

4.4.1 The Proposed Model

Different elements such as the under-reinforced beam T2LA and the shear panel W-2 were analyzed using the NONLACS2 program with different mesh sizes. The various analyses using the program indicated that the length of the descending branch of the tensile stress-strain curve of the concrete defined by the value of the ultimate tensile strain, ϵ_m , has a significant effect on the computed results. If the value of ϵ_m is adjusted appropriately according to the element size,

it can eliminate the problems created by the mesh characteristics. In other words, as mentioned in Chapter 3, a detailed survey of the literature shows that there exist neither a universally accepted value for ϵ_{tu} , nor a suitable method for its determination. Therefore, a new method of evaluating ϵ_{tu} to idealize the tension stiffening effect and to remove the mesh dependency drawback is required.

For each mesh configuration, the value of ϵ_{tu} was adjusted so that the computed ultimate load was close to the experimental ultimate load. The results of analyses for beam T2LA and shear panel W-2 are presented in Tables 4.3 and 4.4, respectively. The best values of ϵ_{tu} for the beam and the shear panel for different mesh sizes are presented in Table 4.5. The results show that there is a unique value of ϵ_{tu} corresponding to each mesh size regardless of the type and detailing of the structure. After determining the best value of ϵ_{tu} for each mesh size (element width), h , the variation of ϵ_{tu} with respect to the element width is plotted in Fig. 4.12. Finally, based on regression analysis the following exponential equation is obtained:

$$\begin{aligned}\epsilon_{tu} &= 0.004 e^{-0.2 h} & (\epsilon_{tu} \geq \epsilon_{cr}) & \quad (psi \text{ units}) \\ \epsilon_{tu} &= 0.004 e^{-0.008 h} & (\epsilon_{tu} \geq \epsilon_{cr}) & \quad (MPa \text{ units})\end{aligned}\tag{4.1}$$

If ϵ_{tu} is smaller than ϵ_{cr} , then

$$\epsilon_{tu} = \epsilon_{cr}\tag{4.2}$$

where h is the width of the element (for the non-square elements: $h = \sqrt{A}$, where A is the element area), ϵ_{cr} is the cracking strain ($\epsilon_{cr} = f'_t / E$), and ϵ_{tu} is the concrete ultimate tensile strain.

This formula is empirical and is obtained by a trial and error procedure. Based on this formula, the value of ϵ_{tu} decreases with an increase in the value of h , and vice versa, so that the energy dissipation capacity and the ultimate load of the structure remain constant irrespective of the size of finite element used in the mathematical model. If the element size, h , is too large so that the ϵ_{tu} is less than ϵ_{cr} , then ϵ_{tu} is considered to be equal to ϵ_{cr} . This is because of the numerical difficulties in the snapback of the tensile stress-strain curve of concrete. It should be pointed out that using this formula, a coarse mesh with larger element sizes, which are often needed in practice for the analysis of large structures, can be selected for finite element idealization with an acceptable degree of confidence in the computed results and considerable saving in the computational effort. On the contrary, if a fine mesh is used, the formula gives a large value of ϵ_{tu} which increases the energy dissipation capacity of the structure and reduces the rate of crack progression within the element, and consequently it prevents failure of the structure at an early stage of loading.

Table 4.3: Effect of ϵ_{tu} on ultimate load for under-reinforced beam T2LA

Number of Elements	Size of Elements (in x in)	ϵ_{cr}	ϵ_{tu}	Ultimate Load (lb)	$P_{u,m1}/P_{u,exp}$
4	18 x 12	0.00013	0.0007	19500	1.24
4	18 x 12	0.00013	0.00018	16000	1.02
20	6 x 6	0.00013	0.0007	14000	0.90
20	6 x 6	0.00013	0.001	14500	0.93
20	6 x 6	0.00013	0.0013	15500	0.99
80	3 x 3	0.00013	0.0007	15000	0.96
80	3 x 3	0.00013	0.00013	13500	0.86
80	3 x 3	0.00013	0.0021	15500	0.99
80	3 x 3	0.00013	0.0028	16500	1.053
80	3 x 3	0.00013	0.005	17000	1.085
320	1.5 x 1.5	0.00013	0.0007	14000	0.90
320	1.5 x 1.5	0.00013	0.0031	15500	0.99
Experimental result	-	-	-	15666	-

Table 4.4: Effect of ϵ_{tu} on ultimate load of shear panel W-2

Number of Elements	Size of Elements (in x in)	ϵ_{cr}	ϵ_{tu}	Ultimate Load (lb)	$P_{u,m1}/P_{u,exp}$
35	6 x 6	0.00018	0.0002	26000	0.98
35	6 x 6	0.00018	0.0018	28500	1.08
35	6 x 6	0.00018	0.002	28700	1.083
35	6 x 6	0.00018	0.00125	26500	1.00
120	3 x 3	0.00018	0.0002	25500	0.96
120	3 x 3	0.00018	0.005	30500	1.15
120	3 x 3	0.00018	0.0006	25500	0.96
120	3 x 3	0.00018	0.0021	26250	0.991
460	1.5 x 1.5	0.00018	0.0002	24000	0.91
460	1.5 x 1.5	0.00018	0.002	24500	0.925
460	1.5 x 1.5	0.00018	0.0013	24500	0.925
460	1.5 x 1.5	0.00018	0.0031	26700	1.008
Experimental result	-	-	-	26500	-

Table 4.5: Optimum value of ϵ_{tu} for different mesh sizes for beam T2LA and shear panel W-2

Size of Element in inches	The Optimum Value of Ultimate Tensile Strain (ϵ_{tu})	
	Beam T2LA	Shear Panel
1.5 x 1.5	0.0031	0.0031
3 x 3	0.0021	0.0021
6 x 6	0.0013	0.00125
18 x 12	0.00018	--

It should be mentioned that the proposed formula is very simple and can be used for both square and non-square elements to predict the required value for ϵ_{tu} .

It should be pointed out that the proposed equation is not a general equation and is based on the regression analysis of only two R C beams and one shear panel. The same investigation is recommended in conjunction with other structural elements like slabs, shear walls, cores, etc. to examine the validity of the proposed formula or developing new formulas if needed.

4.4.2 Crack Band Model

Another alternative to eliminate the spurious dependence of the computed results on the finite element size is to use the crack band model proposed by Bazant and Oh (1983) based on fracture mechanics. The fracture mechanics concepts can be used to deal with propagation of cracks, and are based on the concept of energy dissipation in the structure undergoing the fracture process. It should be noted that if the computed response is to correlate with the experimental response, then the energy dissipated in the process should be independent of the type of mesh. This implies that irrespective of the finite element size selected, the area under the experimental and the computed load-deflection curves should be equal. Therefore, the energy release rate should be constant in both the experimental and the computer model, irrespective of the finite element size used (dashed line in Fig. 4.11d). This model involves using a fixed width, w_c , of the front of the strain-softening zone (crack band), which represents a material property. The imposition of constant w_c is required to avoid mesh sensitivity assuming that the energy dissipation due to fracture per unit length (and unit width) is constant and equal to the fracture energy of the material, G_f . Based on the crack band model, the ultimate tensile strain of the concrete can be

evaluated as:

$$\epsilon_m = \frac{2 G_f}{f_t' h} \quad (4.3)$$

where h is the element size, G_f is the fracture energy, and f_t' is the direct tensile strength of concrete. The fracture energy, G_f , is the energy consumed in the formation and opening of all microcracks per unit area of plane (x,y) which is equal to $G_f = 0.5 \epsilon_m f_t' w_c$. In other words, the fracture energy is the area under the tensile stress-strain curve of concrete times the crack band width, w_c . The values of fracture energy, G_f , vary between 50 N/m and 250 N/m. Balakrishnan and Murray found a value of 100 N/m (0.5 lb/in) to be effective for beam analysis (1986). Bazant and Oh (1983) suggested the following empirical formula for prediction of the fracture energy

$$G_f = (2.72 + 0.0214 f_t') f_t'^2 \frac{d_a}{E} \quad (4.4)$$

where d_a is maximum aggregate size, E is the concrete modulus of elasticity and f_t' is the direct tensile strength in psi. The existing methods for determination of fracture energy were reviewed by Iyengar et al. (1993). The width of the crack band front, w_c , can be assumed to be approximately three times the maximum aggregate size, d_a (i.e., $w_c = 3d_a$) (Bazant and Oh 1983).

The finite element size, $h = w_c$, required by the crack band model, may be too small in the case of very large structures. In this case, it is possible to enlarge the element size, provided that the softening branch of the stress-strain relationship is adjusted to obtain the same energy dissipation, G_f . The given stress-strain curve OPA in Fig. 4.1 for the strain-softening crack band needs to be replaced for increasing element size, h , by curves OPB, OPC, OPD, etc., such that when the areas under any of these curves is multiplied by h , the same fracture energy value, G_f , is obtained. One can also use elements with $h < w_c$, provided that the post-peak slope is decreased such that a constant fracture energy, G_f , is obtained, as shown in curve OPF.

As the element size is increased, the slope of the strain-softening branch gets steeper, until for a certain element size, h_0 , a vertical stress drop, as represented by the curve OPC is obtained. For a still larger element size, the diagram OPD would exhibit snapback, which would cause computational difficulties. The point of vertical drop is determined again from the condition that the area under the curve OHE must be the same as the area under the curve OPD. This consideration indicates that the equivalent tensile strength, f_{eq} , of the large finite element of size

$h > h_0$ is given by

$$f_{eq} = f_t' \sqrt{\frac{h_0}{h}} \quad (4.5)$$

in which $h_0 = (2EG_f/f_t'^2)$ is the element size for which a vertical stress drop is obtained.

It should be noted that if the "correct" ϵ_u is obtained using the crack band model for a specific element size, the fracture energy, G_f , is not affected by the variation of the direct tensile strength of the concrete, f_t' (Choi and Kwak 1993). It was also proved by Shayanfar et. al. (1993) that the value of f_t' does not have a considerable influence on the value of the ultimate load, as compared with the value of ϵ_u .

4.5 IMPLEMENTATION OF THE MODELS INTO THE NONLACS2 PROGRAM

The crack band and the proposed models have been implemented into the NONLACS2 program. The NONLACS2 program can use both square and non-square elements with different element sizes, h .

4.5.1 General Modifications

In the MAIN program, the values for MDEP and MUNIT are called from the input file, where:

MDEP= Mesh Dependency Analysis Factor

- 1 No Mesh Dependency Analysis
- 2 Mesh Dependency Analysis Based on the Crack Band Theory
- 3 Mesh Dependency Analysis Based on the Proposed Model

MUNIT= Unit System Option

- 1 Imperial Units
- 2 SI Units

In the subroutine INDATA, the parameters, GF(I) and AMAGR(I), are also given from the input data file. Here,

GF(I)= Fracture Energy for Concrete Type Number I

--Recommended Value of 0.5 lb/in (0.1 N/mm)

AMAGR(I)= Maximum Aggregate Size for Concrete System Type Number I

--Recommended Value of 1.0 in. (25.4 mm)

In the subroutine TDCOS, the size of each element is evaluated as \sqrt{A} (A is element surface area) and stored in the vector ASIZE. In the subroutines CYCMAT and TENSION, the basic formulation for evaluating an appropriate value of ϵ_u in accordance with both the crack band and the proposed models is imposed. The flow chart of the changes in these two subroutines is presented in Fig. 4.13. It should be mentioned that further modifications were carried out on the subroutines STIF1, CHECK and STRESS1.

4.5.2 The Proposed Model

As explained in Section 4.4.1, the following equation can be used to evaluate the concrete ultimate tensile strain, ϵ_u , corresponding to each element size, h :

$$\begin{aligned} \epsilon_u &= 0.004 e^{-0.2 h} & (\epsilon_u \geq \epsilon_{cr}) & \quad (psi \text{ units}) \\ \epsilon_u &= 0.004 e^{-0.008 h} & (\epsilon_u \geq \epsilon_{cr}) & \quad (MPa \text{ units}) \end{aligned} \quad (4.6)$$

where h is the element size. If h is large so that the Eq. 4.6 gives a value less than the cracking strain, ϵ_{cr} , to avoid numerical difficulties associated with a snapback portion on the tensile stress-strain curve, the value of ϵ_u is set equal to that of ϵ_{cr} .

4.5.3 Crack Band Model

The crack band model has been implemented in some large general purpose finite element programs (e.g. DIANA, TEMP-STRESS, NONSAP), including the NONLACS2 program. The algorithm using the crack band theory can be summarized for implementation into the NONLACS2 program as follows:

Case (1): If $h = w_c$, then the ultimate tensile strain of concrete is evaluated as (see curve OPA of Fig. 4.1)

$$\epsilon_u = \frac{2 G_f}{f_t' w_c} = \overline{OA} \quad (4.7)$$

where h is the element size, G_f is the fracture energy, w_c is the crack band width which is approximately three times the maximum aggregate size, d_a ($w_c \approx 3d_a$), and f_t' is the direct tensile strength, given by

$$f'_t = 4 \sqrt{f'_c} \quad (\text{psi units}) \quad (4.8)$$

$$f'_t = 0.33 \sqrt{f'_c} \quad (\text{MPa units})$$

Case (2): If $h < w_c$ then the ultimate tensile strains calculated using (see curve OPF of Fig. 4.1)

$$\epsilon_{tu} = \frac{2 G_f}{f'_t h} = \overline{OF} \quad (4.9)$$

Case (3): If $h > w_c$, then at first the element size, h_0 , is determined for the case for which a vertical drop in stress is encountered. From curve OPB of Fig. 4.1: $G_f = 1/2 \epsilon_{cr} f'_t(h_0) = 1/2 (f'_t/E_0) f'_t(h_0)$, then

$$h_0 = \frac{2 E_0 G_f}{f_t^2} \quad (4.10)$$

If $w_c < h < h_0$ then

$$\epsilon_{tu} = \frac{2 G_f}{f'_t h} = \overline{OB} \quad (4.11)$$

If $w_c < h > h_0$, to avoid a snapback part, OPD, an equivalent curve OHE is used by modifying the tensile strength of concrete, f_{eq} . Thus,

$$G_f = \frac{h_0 f_t^2}{2 E_0} = \frac{h f_{eq}^2}{2 E_0} \quad (4.12)$$

where f_{eq} is the equivalent tensile strength of concrete for large finite element size with $h > h_0$, and it is given by:

$$f_{eq} = f'_t \sqrt{\frac{h_0}{h}} \quad (4.13)$$

Finally, the ultimate tensile strain of concrete, ϵ_{tu} , is obtained as,

$$\epsilon_{tu} = \frac{f_{eq}}{E_0} = \overline{OE} \quad (4.14)$$

For more information on how this model and proposed model were implemented in the NONLACS2 program, refer to the flow chart in Fig. 4.13.

4.6 COMPARISON OF COMPUTED AND EXPERIMENTAL RESULTS

The crack band model and the proposed model have been implemented in the NONLACS2 program as previously discussed. With the imposed modifications, the NONLACS2 program can handle the nonlinear finite element analysis of the structures using three options: (a) no mesh dependency analysis (MDEP=1), (b) the crack band model (MDEP=2), and (c) the proposed model (MDEP=3). This program was used to analyze the Beams T2LA and the shear panel W-2, with different mesh configurations. For further verification of the computed results from the proposed model, a detailed analysis of five beams, T4LA, T1HB, C2W, C3YNA, and C3YNB, tested by Gaston et al. (1952), was also undertaken. The results of these analyses and their comparison with the experimental data are presented here.

4.6.1 Beam T2LA

Beam T2LA is examined using 4 and 320 elements for the computer models. The value of ϵ_u for the case of "no mesh dependency analysis" is assumed to be equal to 0.0007 for all beam idealizations. For the beam idealized using 4 elements, the results are shown in Fig. 4.14. The ultimate load computed using "no mesh dependency analysis" option is 19,500 lb which is 24% higher than experimental value of 15,666 lb. At load levels higher than 14,000 lb, the beam response is stiffer than the other models with yielding of steel reinforcement occurring at a load of 16,500 lb which is higher than the experimental yield load of 14,000 lb. The ultimate load obtained using the crack band model is 18,100 lb, which overestimates the ultimate load by 16%, while the value based on the proposed model is 16,100 lb, which is quite close to the experimental value with a discrepancy of only 2%. The yield load from both the crack band and the proposed models are the same as the experimental result of 14,000 lb. The load-deflection curve for these two models follow the same general pattern and are quite close to the experimental response. It is obvious that the proposed formulation can be used effectively with relatively large size finite elements. With this approach, the required computational time can be reduced considerably.

As can be seen from Fig. 4.15, the ultimate loads for the beam idealized using 320 elements obtained from both the crack band model and the proposed model are the same, 15,500 lb, and quite close to the experimental result. It shows that the application of these two models gives similar results with reasonably accurate prediction of the ultimate load. Use of the NONLACS2 program with MDEP=1 underestimates the value for the ultimate load at 14,000 lb

with an 11% discrepancy. A summary of the ultimate loads for the various mesh sizes computed for the different models for beam T2LA is presented in Table 4.6.

The values of the ultimate load obtained using the different finite element meshes are presented graphically in Fig. 4.16. Using "no mesh dependency analysis" option, without accounting for mesh dependency phenomenon, exhibits significantly different ultimate loads, while the crack band model and the proposed model show almost constant values close to the experimental findings. The crack band model gives good results for the finer meshes (approximately less than 3 in. or 76.2 mm), but for larger size meshes, it cannot simulate accurately the experimental behaviour of the structure. The proposed model showed that it does not have this drawback.

Table 4.6: Ultimate Load for the Beam T2LA and the Shear Panel W-2 for Different Models

Type of Structure	Number of Elements	Size of Elements (in x in)	Ultimate Tensile Strain (ϵ_w)	Ultimate Load (lb)			
				No Mesh Dependency Analysis	Crack Band Model	Proposed Model	Experimental Values
Beam T2LA	4	18 x 12	0.0007	19500	18100	16100	15666
	80	3 x 3	0.0007	15000	15000	15500	15666
	320	1.5 x 1.5	0.0007	14000	15500	15500	15666
Shear Panel W-2	35	6 x 6	0.002	28700	26700	26500	26500
	120	3 x 3	0.002	26500	25700	26500	26500
	460	1.5 x 1.5	0.002	24500	26700	26700	26500
	120	3 x 3	0.005	30500	25700	26500	26500

4.6.2 Shear Panel W-2

The shear panel W-2 is examined for the models with 35 and 120 elements to show the effect of fineness of the mesh on the computed results. The values of ϵ_w for the analysis with MDEP=1 are assumed to be equal to 0.002 and 0.005, respectively. The load-deflection curves for 35 element using the different models are shown in Fig. 4.17. The ultimate load obtained from the program with "no mesh dependency analysis" option is equal to 28,700 lb with a difference

of +8.3% from the experimental result of 26,500 lb. The load-deflection curves computed for the different models are quite close to the experimental response up to a load level of 12,000 lb. Beyond this load level, the NONLACS2 program with MDEP=1 exhibits a stiffer response compared with the experimental response. The load-deflection curves resulting from both the crack band model and the proposed model agree quite well with the experimental curve and predict the ultimate load quite accurately with a value of 26,700 lb which represents a deviation of only +0.7% from the experimental result.

The results for the shear panel idealized using 120 elements are presented in Fig. 4.18. The ultimate load resulting from the NONLACS2 program with "no mesh dependency analysis" gives a value of 30,500 lb, with a difference of 15% from the experimental value of 26,500 lb. The ultimate load for the crack band model is 25,700 lb, representing a discrepancy of -3%, while the ultimate load for the proposed model is 26,500 lb with no deviation at all from the experimental result. A summary of the ultimate loads for various mesh sizes computed for the different models for shear panel W-2 is presented in Tables 4.6. Excellent agreement between the computed values obtained using the proposed model and experimental values is obvious from a comparison of the last two columns.

4.6.3 Beams T4LA, T1HB, C2W, C3YNA, and C3YNB

As can be seen from Table 4.1, beams T4LA and T1HB are reinforced in tension, while beams C2W, C3YNA, and C3YNB are reinforced in both tension and compression, with varying amounts of reinforcement and material properties. The geometry, reinforcement and loading of these beams are shown in Fig. 4.2. These beams were analyzed with the NONLACS2 program using 80-element model. Idealization of the beam using 80 elements (size of the element is 3 in x 3 in) shows very good agreement with the experimental results and both the crack band model and the proposed model give similar values for ϵ_u in this model.

The load-deflection curves for beams T4LA and T1HB (singly reinforced), and C2W, C3YNA, and C3YNB (doubly reinforced) are shown in Figures 4.19, 4.20, 4.21, 4.22 and 4.23, respectively. The following stages can be noted in the analyses of these beams, which fail initially in tension: The concrete cracks in tension under a relatively small load (about 0.2-0.25 P_u). As the load is increased, the tension reinforcement yields and the beam shows a relatively large deflection with very little increase in the applied load. Subsequently, the concrete in the compression zone crushes. Until the tension steel yields, beams which are reinforced in both tension and

compression exhibit much the same behavior as the beams reinforced in tension only. Beams which are reinforced in tension and compression deflect much more before there is a substantial loss of load-carrying capacity than a comparable beam reinforced in tension only.

For beam T4LA, the analytical value of ultimate load obtained using the proposed model is 25,300 lb, with a difference of -0.7% from the experimental value of 25,490 lb. The ultimate load using "no mesh dependency analysis" option is equal to 24500 lb, representing a discrepancy of -4%.

As can be seen from Fig. 4.20, for doubly reinforced beam C3YNA, the computed ultimate load using proposed model is 31,000 lb, compared with the experimental result of 33,330 lb, representing a deviation of only about one percent. It should be pointed out that the ultimate load using "no mesh dependency analysis" option is 28,000 lb and results in a brittle behaviour as compared with the other models.

A summary of the ultimate loads computed for the different models for beams are listed in Table 4.7. The analytical results using the proposed model are quite close to the experimental findings. The results show that the simple proposed formula can be used with confidence for R C beams with different amounts of reinforcements and material properties. More details related to the cracking, yield and ultimate loads, load-deflection and load-strain curves, cracking patterns and failure modes can be found in the report by Kheyroddin and Mirza (1994).

Table 4.7: Ultimate load for singly and doubly reinforced beams tested by Gaston et. al.

Beams	Size of Element (in x in)	Ultimate Load (lb)				
		No Mesh Dependency Analysis (P_{Nmdep}) ($\epsilon_{tu} = 0.0007$)	Proposed Model (P_{Prop})	Experimental Value ($P_{u,exp}$)	$\frac{P_{Nmdep}}{P_{u,exp}}$	$\frac{P_{Prop}}{P_{u,exp}}$
T4LA	3 x 3	24500	25300	25490	0.95	0.993
T1HB	3 x 3	24500	27000	26670	0.92	1.01
C2W	3 x 3	21000	25000	27330	0.77	0.92
C3YNA	3 x 3	28000	31000	33330	0.84	0.93
C3YNB	3 x 3	42000	45000	49000	0.86	0.92

4.6.4 Crack Patterns

One of the most significant factors involved in the prediction of the behaviour of R C structures is the formation and propagation of cracks with increasing load. The cracks in the concrete are the major source of material nonlinearity. The ability of the different models to predict the crack propagation in concrete is examined in this section.

For this purpose, the crack pattern for only one mesh configuration of the beam T2LA and shear panel W-2 is presented with thick lines representing fully opened cracks ($\epsilon > \epsilon_{tu}$ or $KC=4$ in Fig. 3.2) and thin lines showing partially opened cracks ($\epsilon_{cr} < \epsilon < \epsilon_{tu}$ or $KC=3$ in Fig. 3.2). In Fig. 4.24, the crack patterns for the beam T2LA at a load level of 14000 lb are shown based on the different analytical models. Generally, the configuration of the cracks consists of the flexural cracks (vertical) forming around the mid-span and the shear-flexural cracks (inclined) near the supports. The rate of the crack propagation is controlled by the value of ϵ_{tu} , and the proposed model gives a smaller value for ϵ_{tu} (Eq. 4.1) and consequently wider crack pattern (more fully opened cracks) than the other models which seems to be more realistic.

The ability of the models to simulate the experimental cracking pattern for shear panel W-2 is demonstrated in Fig. 4.25. This figure compares the cracking patterns for the case of $MDEP=1$, the crack band model and the proposed model with the experimental cracking patterns at a load level of 25,500 lb. Comparison of the different configurations shows that the progress of fully opened cracks for both the crack band and the proposed models are wider than the case of "no mesh dependency analysis" option and it shows better agreement with the experimental crack pattern.

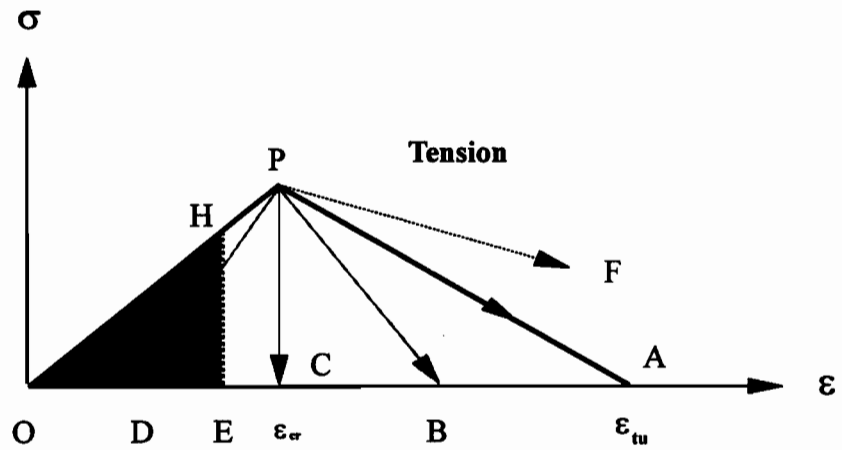
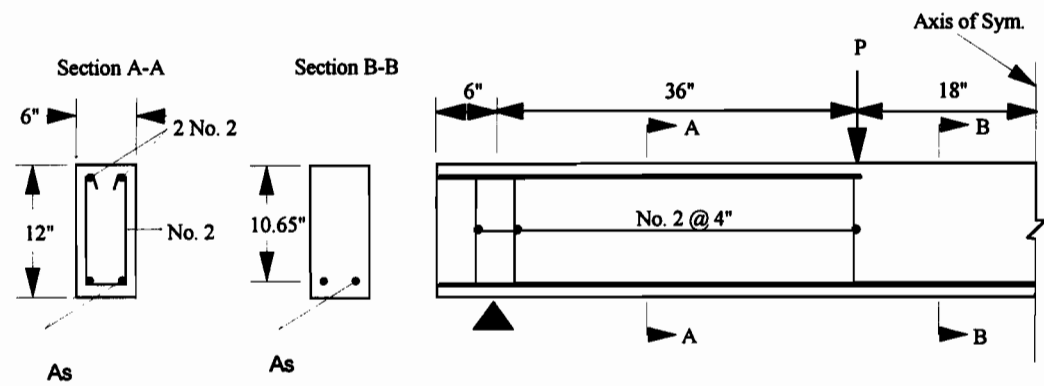
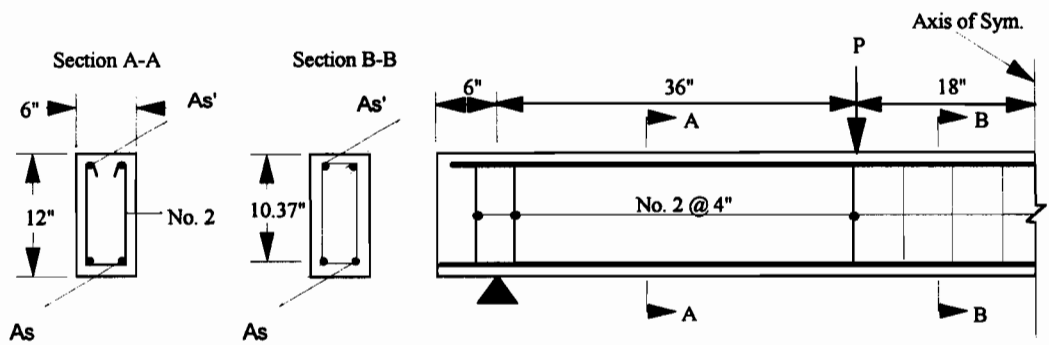


Figure 4.1: Effect of element size on post-peak softening



(a) Beams Reinforced in Tension Only



(b) Beams Reinforced in Tension and Compression

Figure 4.2: Geometry and reinforcement details of Gaston's beams (After Gaston et al. 1952)

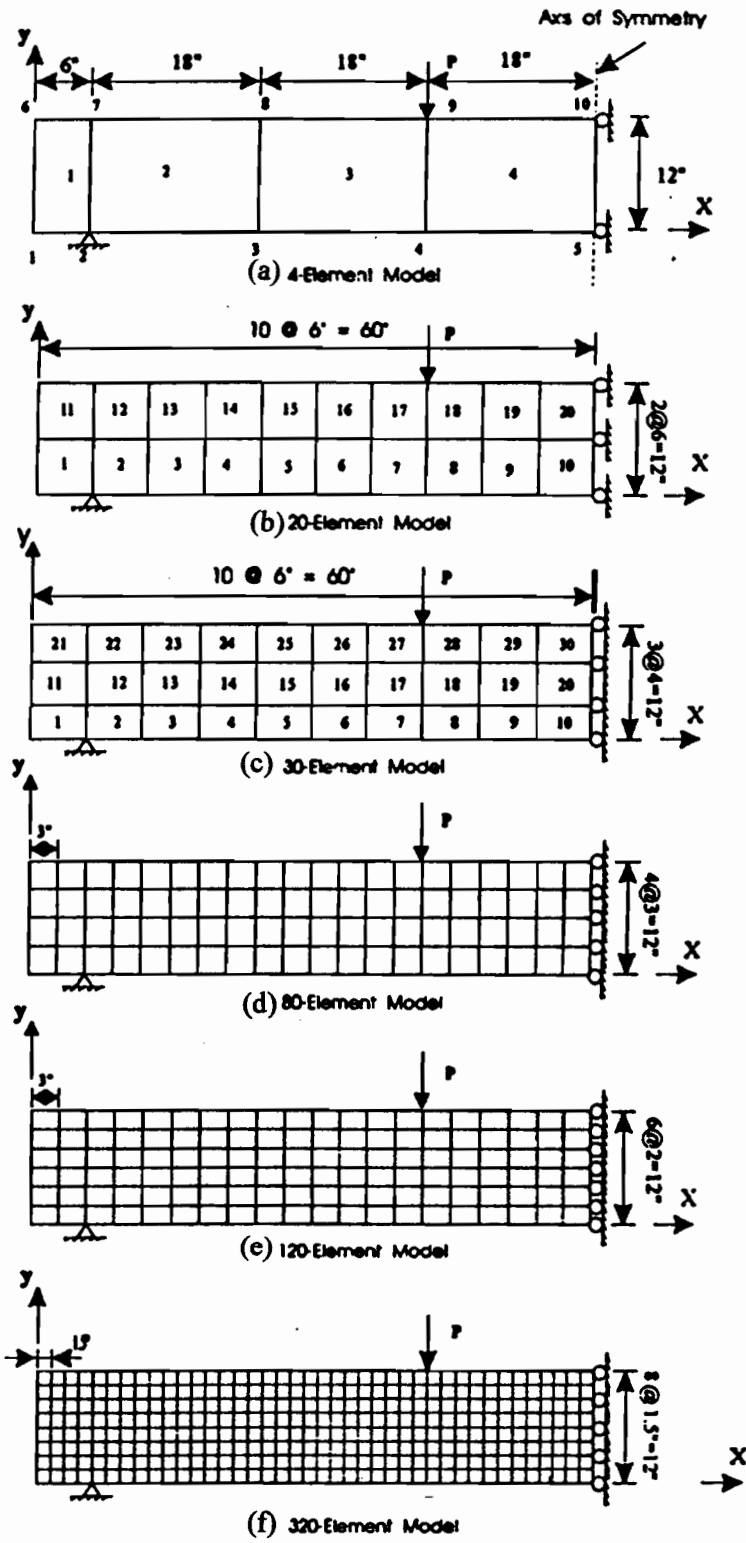


Figure 4.3: Mesh configurations for beams T2LA and T5L

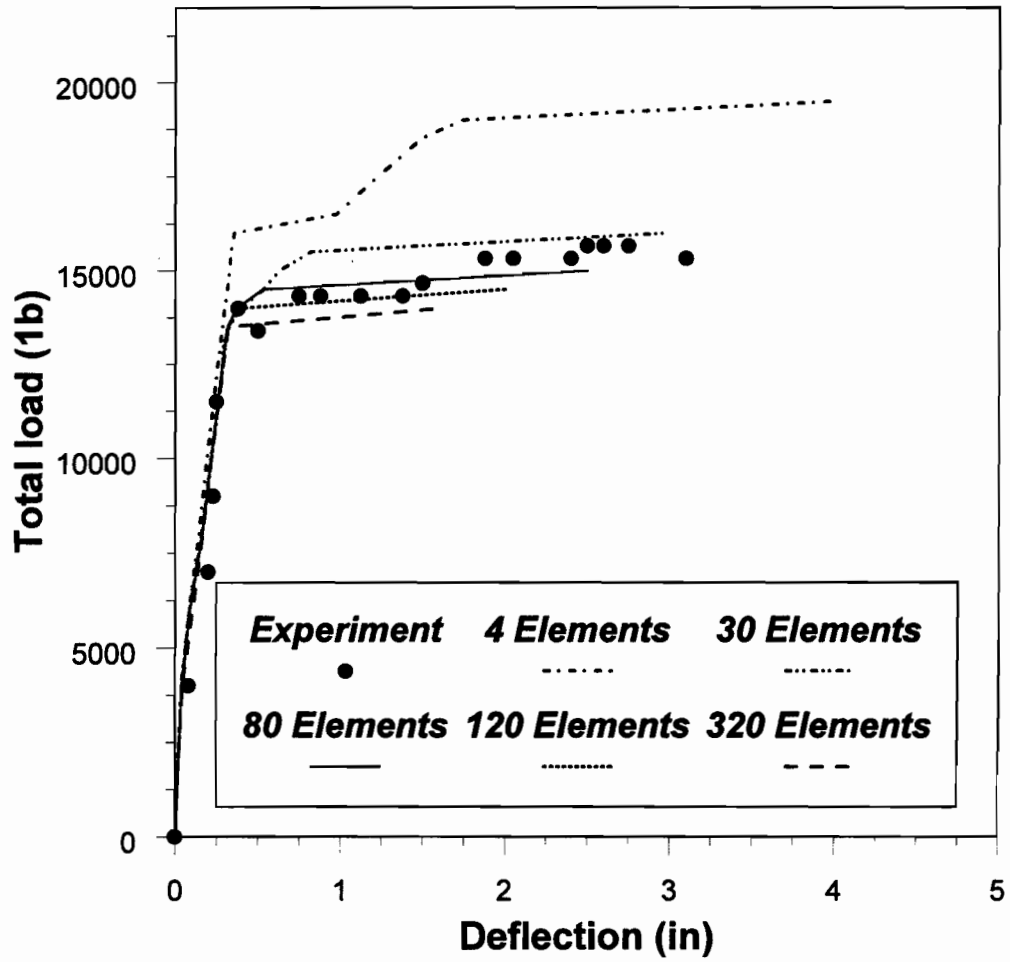


Figure 4.4: Load-deflection curve at mid-span for beam T2LA ($\epsilon_u = 0.0007$)

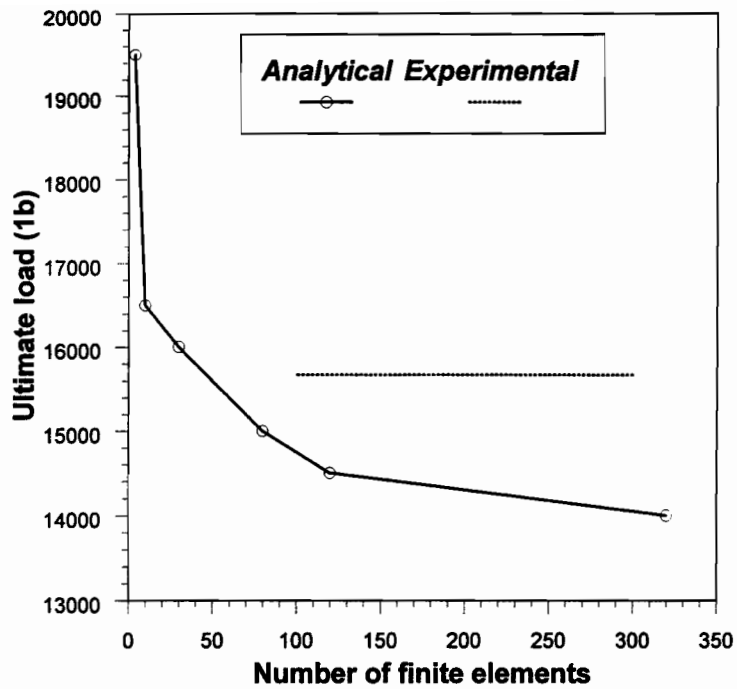


Figure 4.5: Effect of element size on computed ultimate load for beam T2LA ($\epsilon_w=0.0007$)

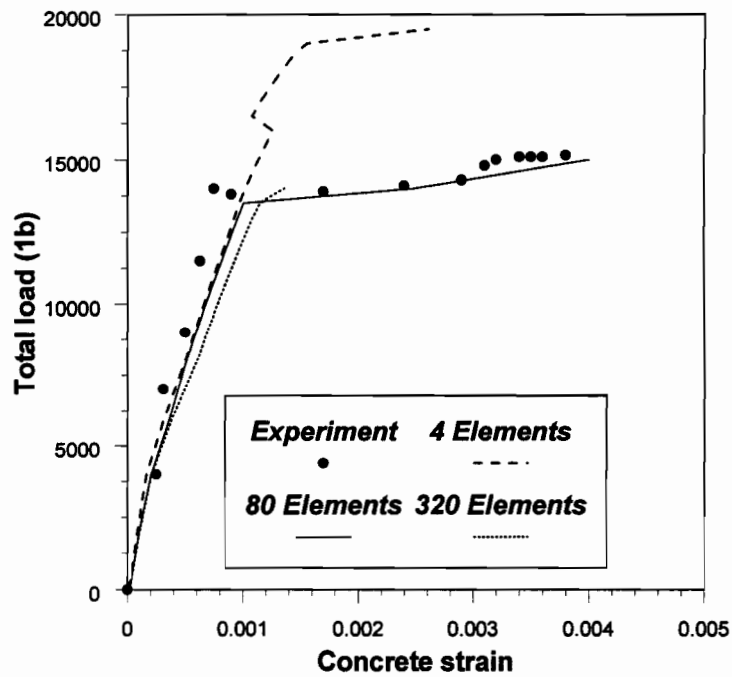
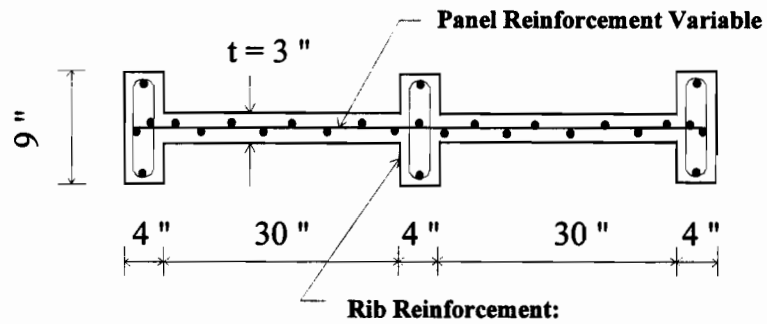
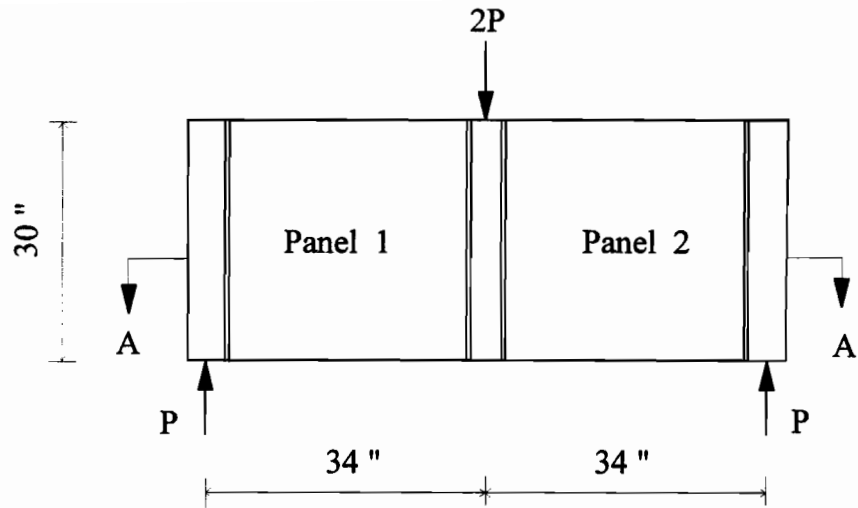


Figure 4.6: Load-concrete strain at mid-span top for beam T2LA ($\epsilon_w = 0.0007$)



Longitudinal 2 No. 3
Ties 4-9 Ga. at 4"

Cross Section A-A

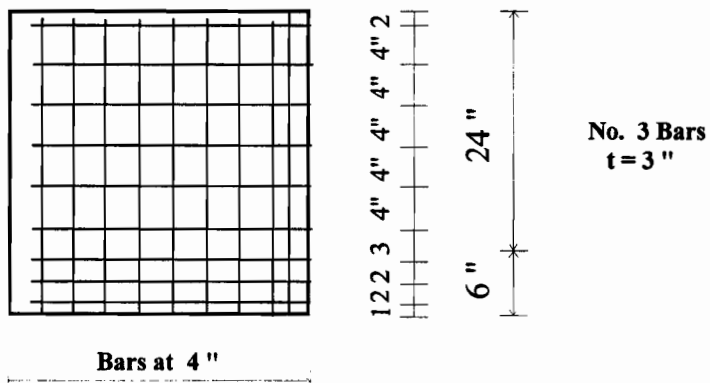


Figure 4.7: Details of reinforcement and geometry for shear panel W-2
(After Cervenka, 1970)

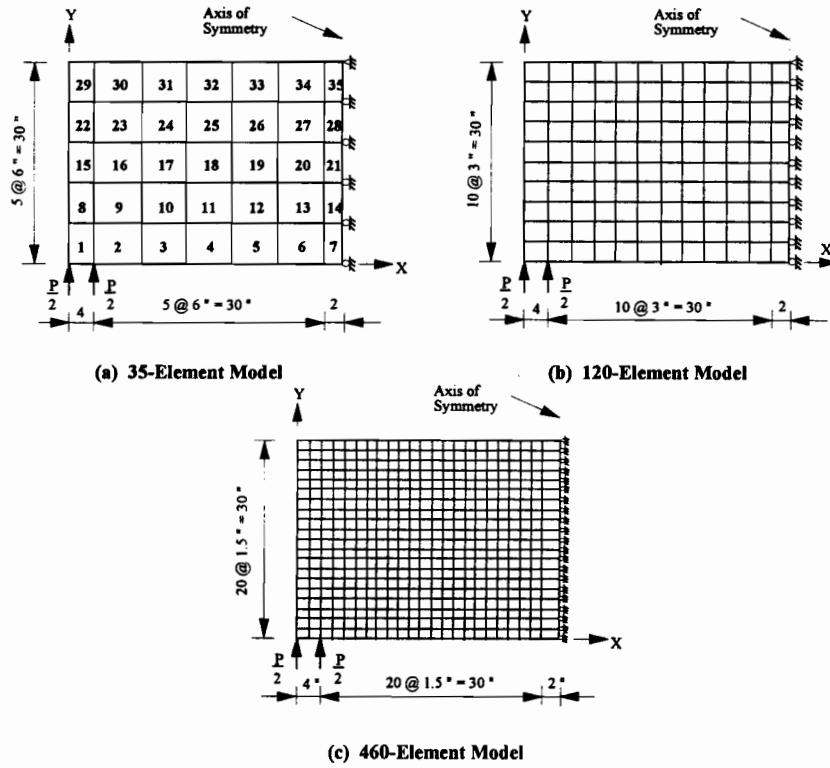


Figure 4.8: Mesh configurations for shear panel W-2

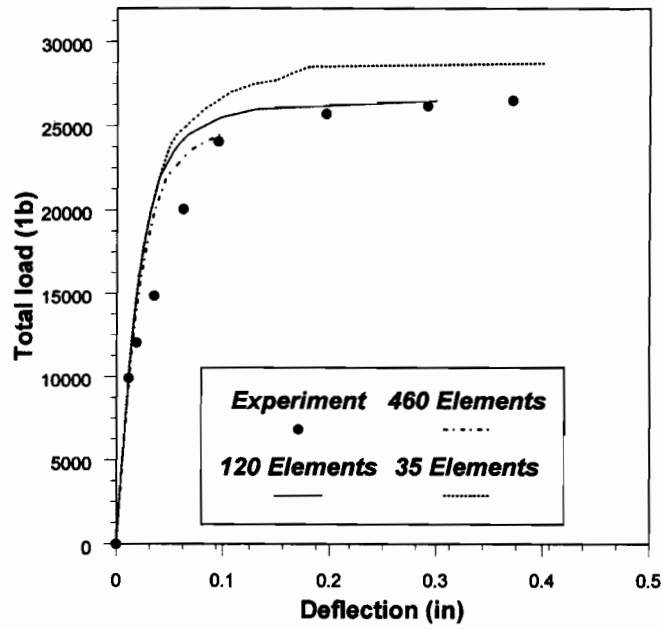
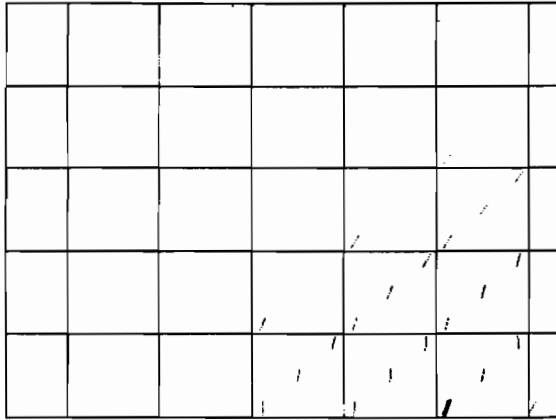
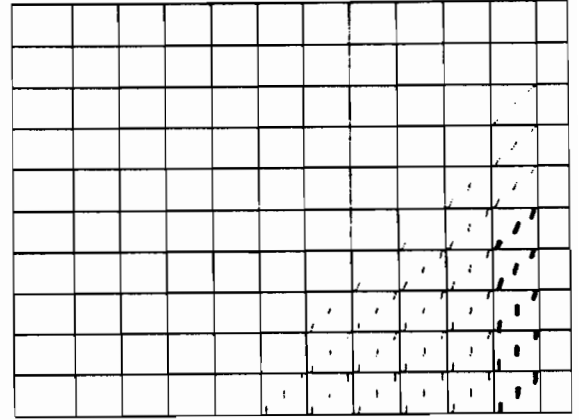


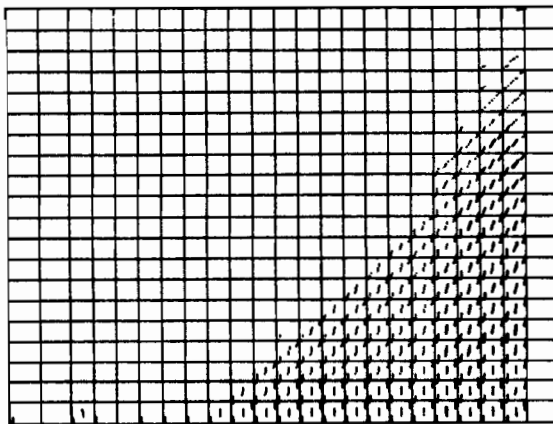
Figure 4.9: Load-deflection curve for shear panel W-2 ($\epsilon_u = 0.002$)



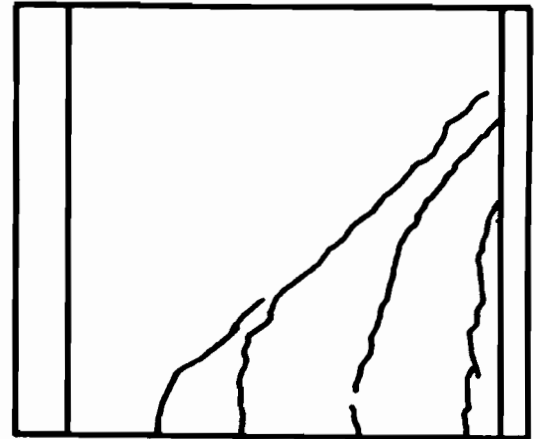
(a) 35-Element Model



(b) 120-Element Model

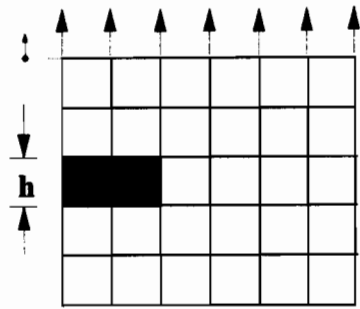


(c) 460-Element Model

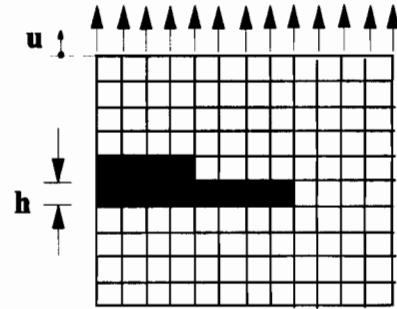


(d) Experiment

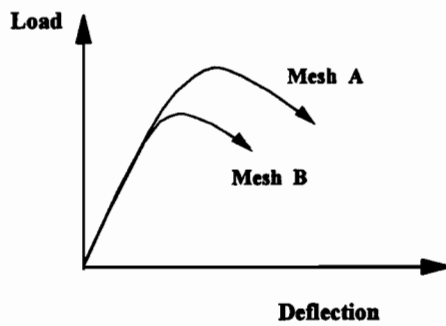
Figure 4.10: Effect of mesh size on crack pattern of shear panel W-2
($P=24,000$ lb, $\epsilon_w=0.002$)



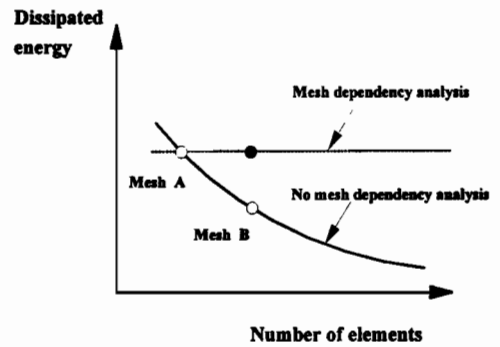
(a) Mesh A



(b) Mesh B



(c)



(d)

Figure 4.11: Qualitative influence of element size on the response of a tension member

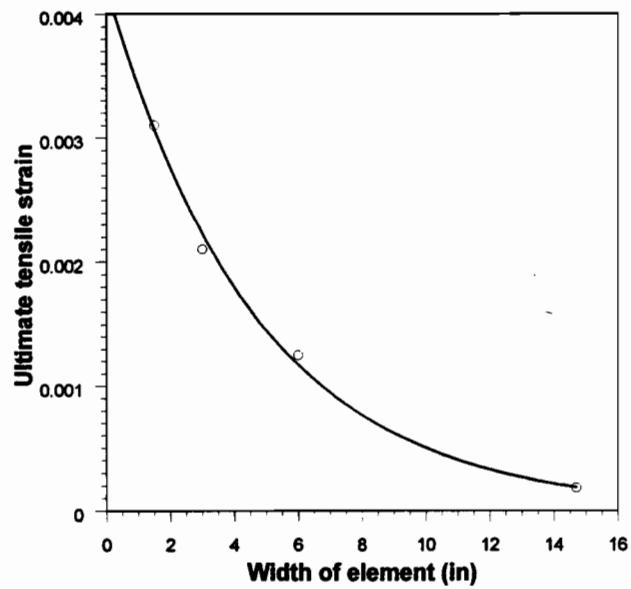


Figure 4.12: Ultimate tensile strain of concrete, ϵ_w , versus width of element, h

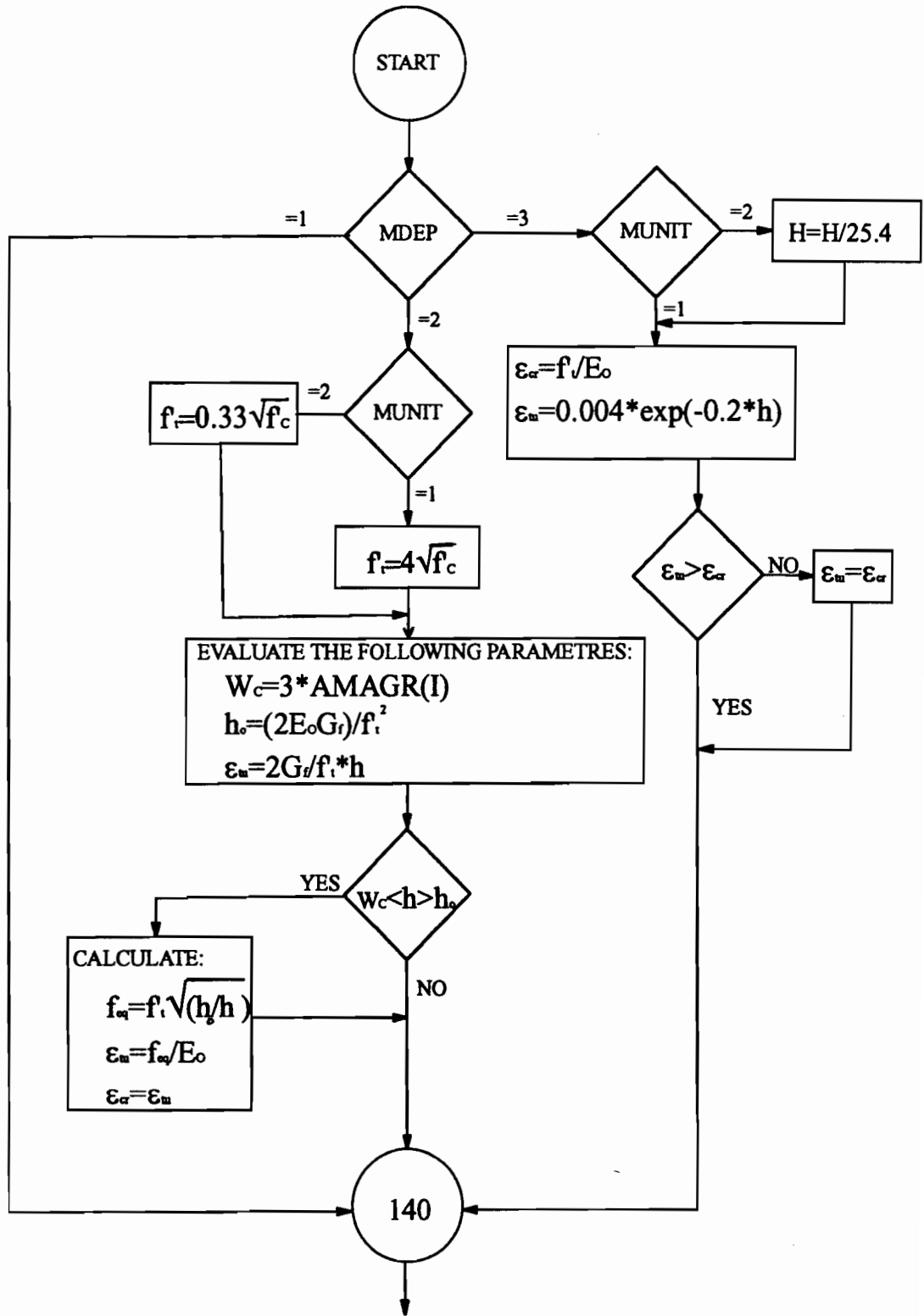


Figure 4.13: A flow chart for the changes on subroutines: TENSION and CYCMAT

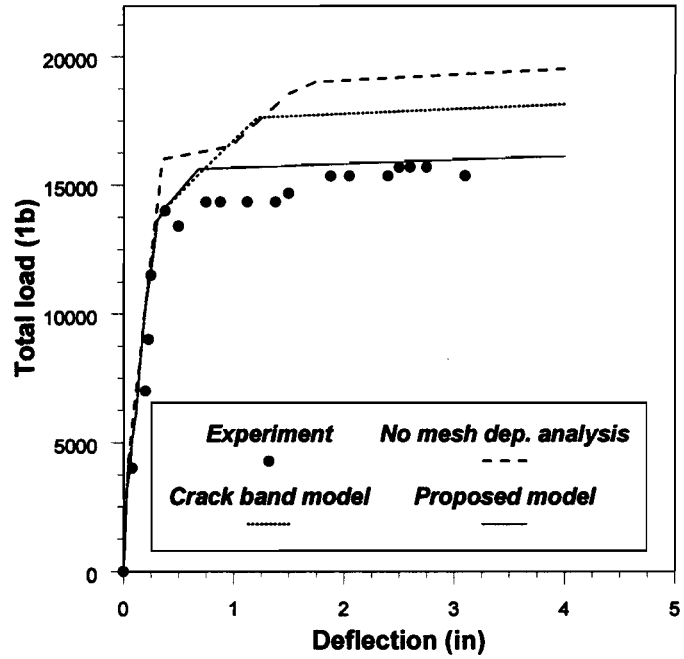


Figure 4.14: Load-deflection curves for beam T2LA idealized using 4 elements

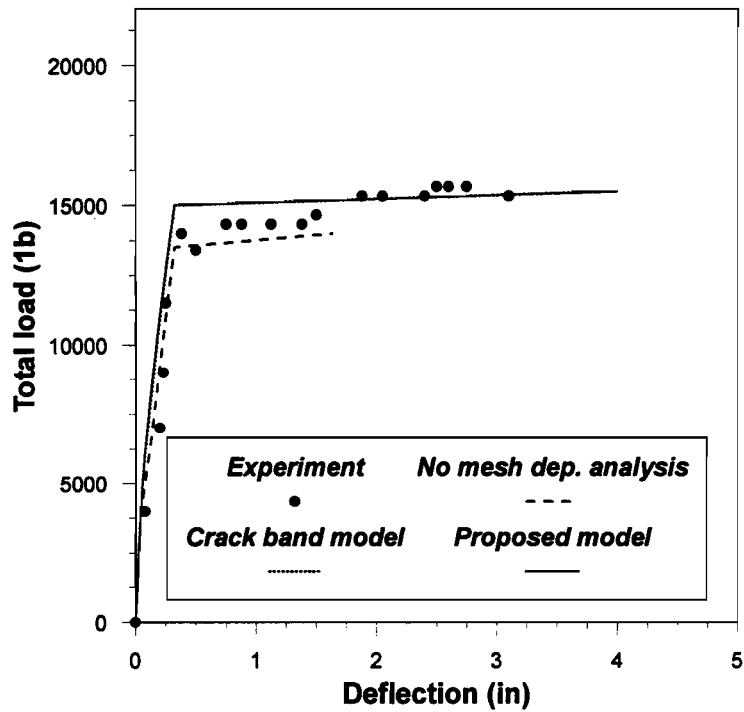


Figure 4.15: Load-deflection curves for beam T2LA idealized using 320 elements

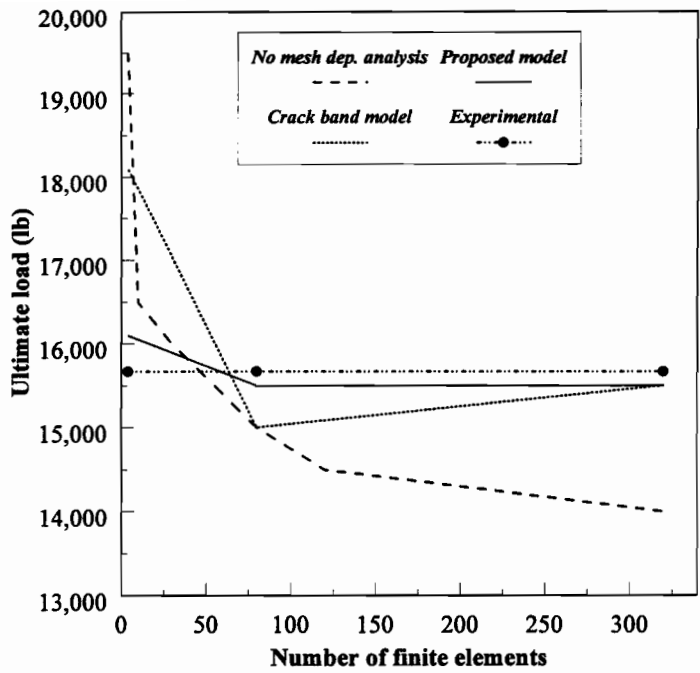


Figure 4.16: Comparison of ultimate loads computed using different models for beam T2LA

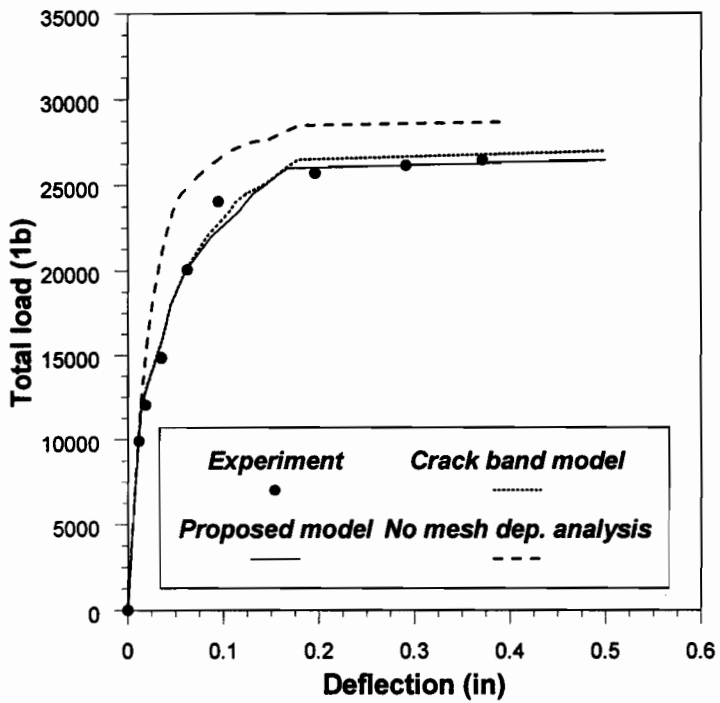


Figure 4.17: Load-deflection curves for shear panel W-2 using 35 elements

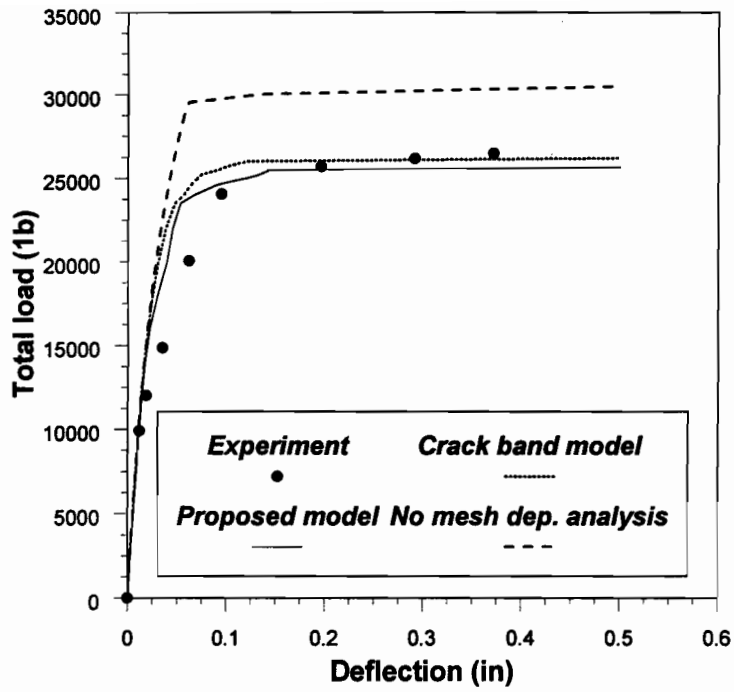


Figure 4.18: Load-deflection curves for shear panel W-2 using 120 elements

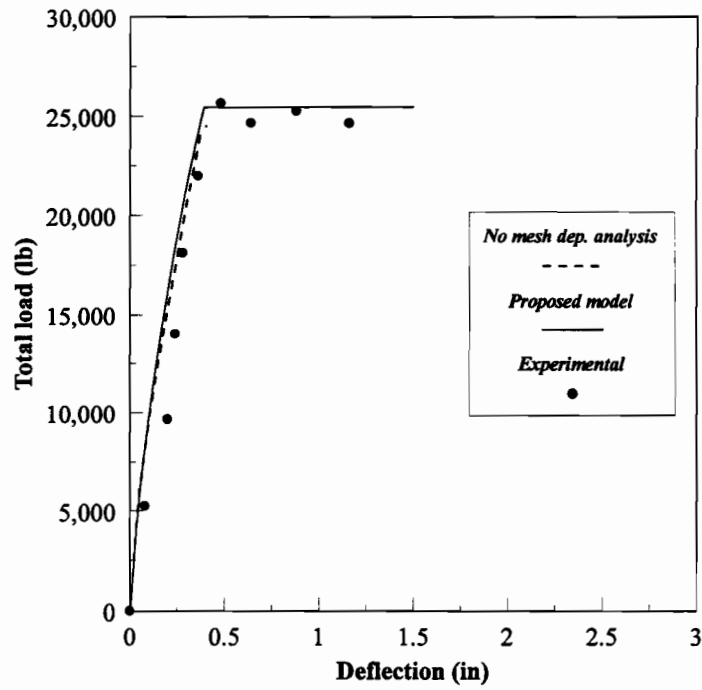


Figure 4.19: Load-deflection curve for beam T4LA idealized using 80 elements

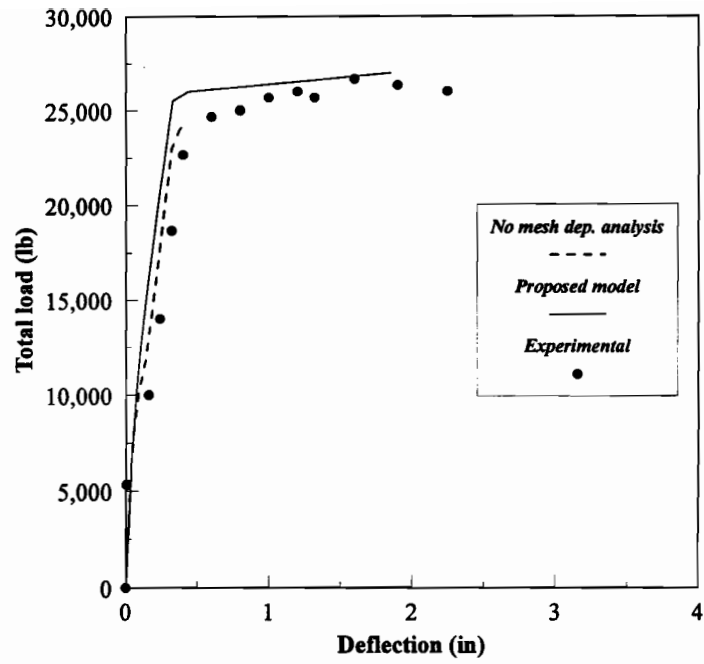


Figure 4.20: Load-deflection curve for beam T1HB idealized using 80 elements

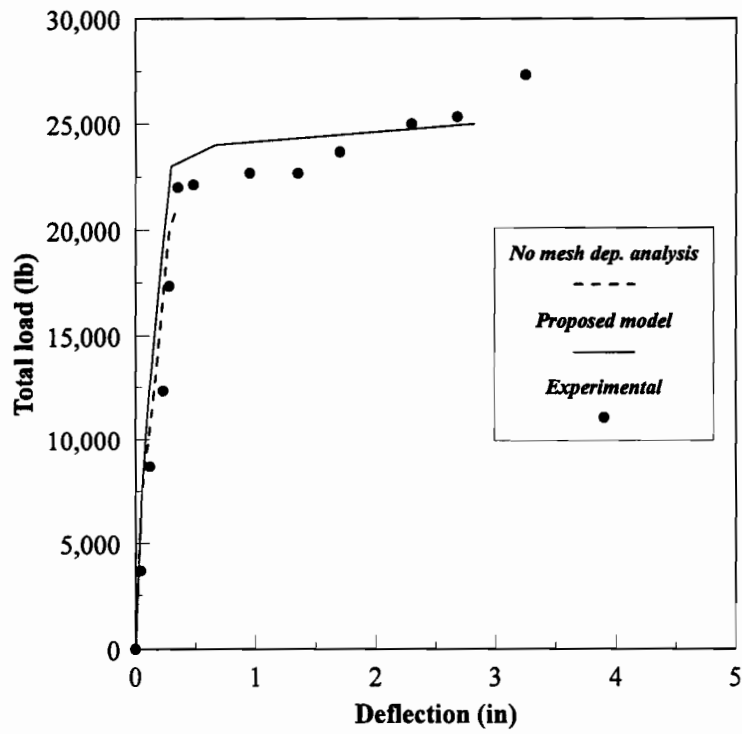


Figure 4.21: Load-deflection curve for beam C2W idealized using 80 elements

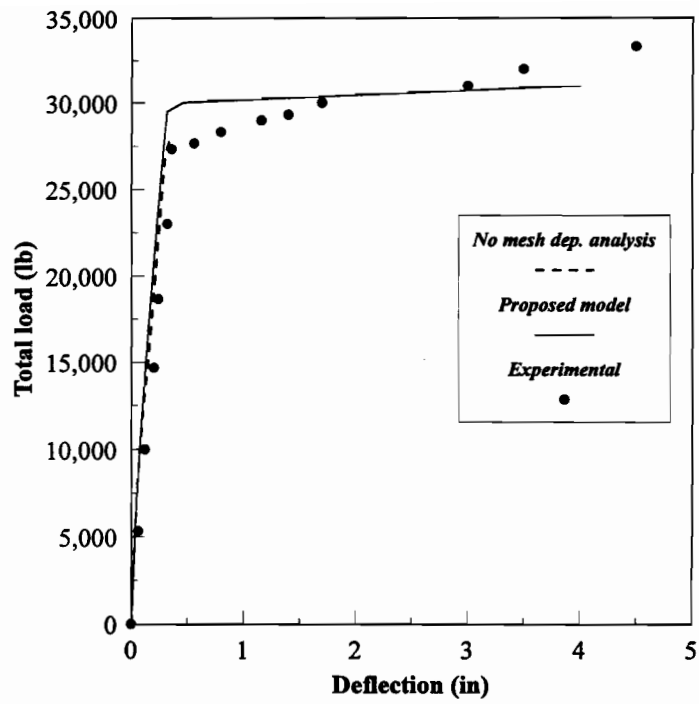


Figure 4.22: Load-deflection curve for beam C3YNA idealized using 80 elements

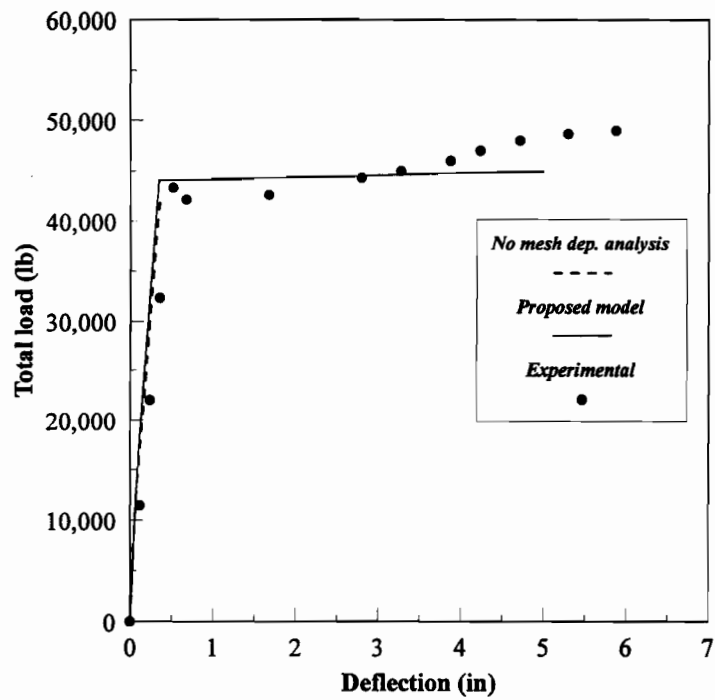
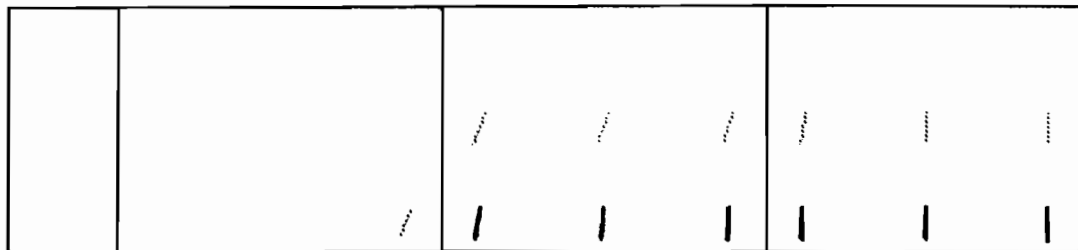
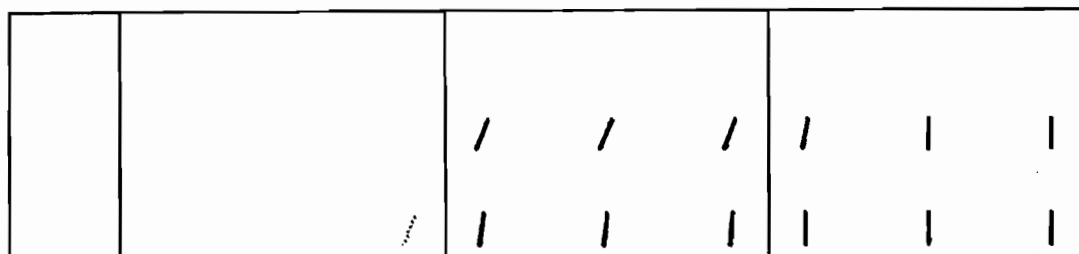


Figure 4.23: Load-deflection curve for beam C3YNB idealized using 80 elements

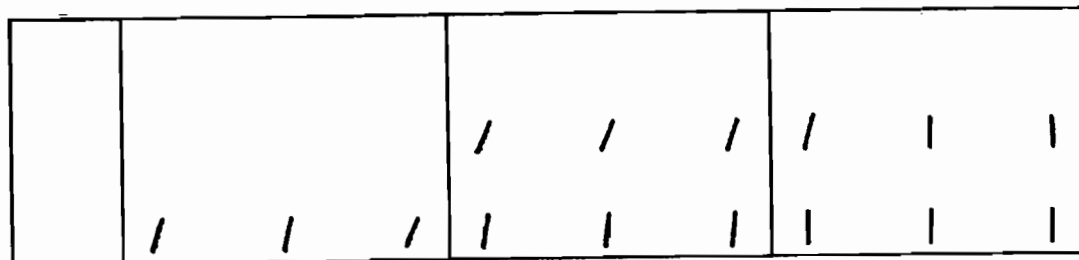


(a) No Mesh Dependency Analysis

($\epsilon_m=0.0007$)



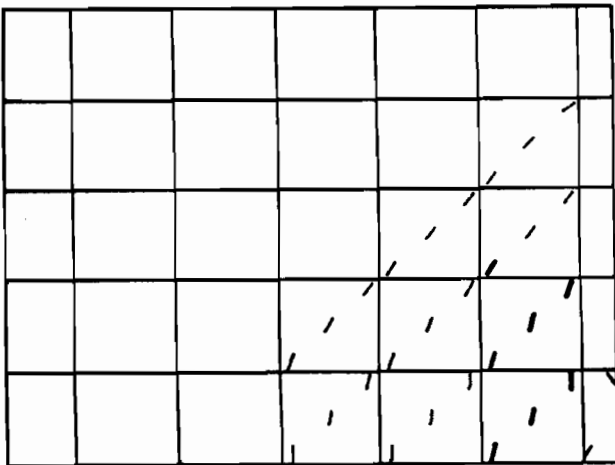
(b) Crack Band Model



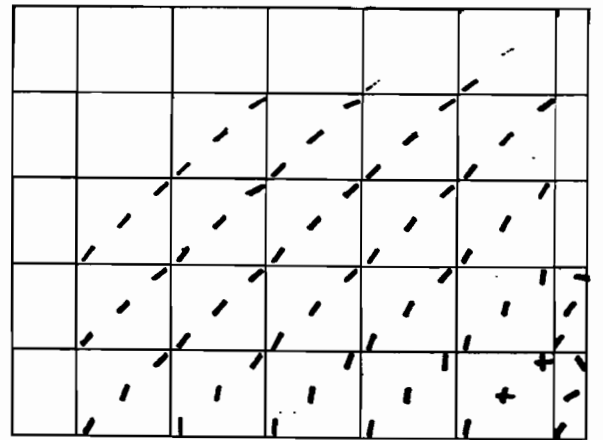
(c) Proposed Model

Figure 4.24: Comparison of analytical cracking patterns for beam T2LA

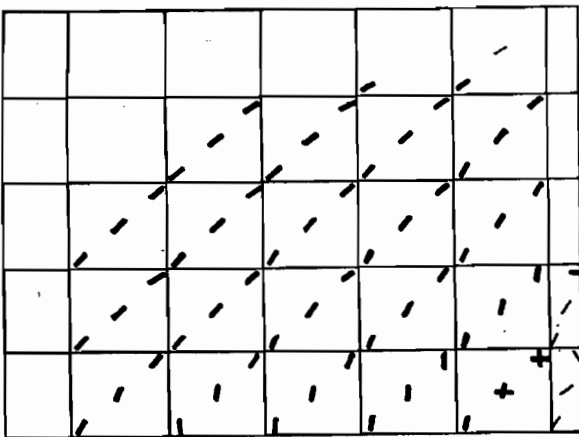
at load $P=0.9 P_{u,exp}=14000$ lb.



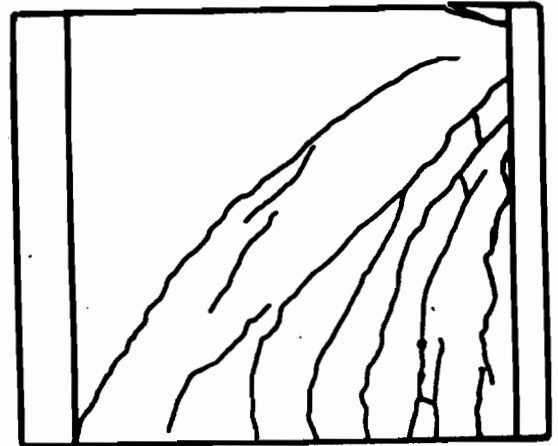
(a) No Mesh Dependency Analysis
 $(\epsilon_u=0.002)$



(b) Crack Band Model



(c) Proposed Model



(d) Experiment

Figure 4.24: Comparison of analytical and experimental cracking patterns for shear panel
 at load $P=0.96 P_{u,exp}=25,500$ lb.

CHAPTER 5

PARAMETRIC STUDY OF FLEXURAL BEHAVIOUR OF REINFORCED CONCRETE BEAMS

A parametric study is undertaken to examine the effects of tension and compression reinforcement ratios and steel yield strengths, loading types and stages, compressive strength of concrete, cracking and tension-stiffening using the nonlinear finite element analysis program, NONLACS2. The effects of the above parameters on different behavioral aspects including load-deflection and moment-curvature characteristics, failure load and the flexural rigidity, EI , of 56 reinforced concrete (R C) beams are reviewed along with a comparison with the experimental data where available. In this regard, the analytical responses of five simply supported beams tested by Gaston et al. (1952) and of one simply supported beam, C5, tested by Mattock (1964) are compared with the experimental data. New equations are proposed to calculate the analytical cracking moment, cracking flexural rigidity, tangent flexural rigidity and the deflection of R C beams at the serviceability limit state. The accuracy of the proposed models is also investigated along with a comparison with the analytical results obtained from the NONLACS2 program and the experimental data where available.

5.1 PROPOSED MODELS FOR CALCULATION OF FLEXURAL RIGIDITY, EI

The value of the tangent flexural rigidity (the slope of the moment-curvature curve) is computed using the following equation:

$$(EI)_{\tan} = \frac{(M_i - M_{i-1})}{(\Phi_i - \Phi_{i-1})} \quad (5.1)$$

where M_i and M_{i-1} are the moments, and ϕ_i and ϕ_{i-1} are the corresponding curvatures at the i th and $(i-1)$ th load steps, respectively, at the given section. Therefore, the moment-curvature relationship is required to calculate the flexural rigidity of the beam at different loading stages. In this study, a linear strain distribution is assumed across the depth of the cross section. Using the concrete and steel strains obtained from the NONLACS2 program, the value of curvature at a given section at different loading stages is determined (see Fig. 2.4). Several analytical and experimental tests on R C beams have borne out that linear strain distribution assumption is very nearly correct at all stages of loading up to flexural failure (Park and Paulay 1975, Kheyroddin and Mirza 1994). It is assumed that the sections are adequately reinforced for shear, and the mode of failure is flexural. The shear deformations are neglected.

The schematic variation of the analytical flexural rigidity at the midspan section with respect to the moment, M , is shown in Fig. 5.1. Generally, the curve has three stages: the elastic or pre-cracking ($M_a \leq M_{cr,ani}$), the post-cracking ($M_{cr,ani} \leq M_a \leq M_y$), and the post-yielding ($M_y \leq M_a \leq M_u$) stages. With an increase in the applied moment, the cracking of the concrete reduces the flexural rigidity of the section. The value of EI decreases with an increase in the bending moment, with a large EI value for low values of bending moment, followed by a sudden transition to a lower EI value for larger bending moment values. After yielding of the steel reinforcement, the flexural rigidity suddenly decreases and tends to zero with a small change in the load. As can be seen from Fig. 5.1, $(EI)_0$ is the initial flexural rigidity (the slope of $M-\phi$ curve at the beginning of the first load step) and $M_{cr,ani}$ and $(EI)_{cr}$ are defined as the analytical cracking moment and the cracking flexural rigidity corresponding to the cracking load, respectively.

The effective second moment of the area, I_e (Eq. 2.20) with a constant value of the concrete secant modulus of elasticity, E_c , is used to compute the flexural rigidity using the Branson's equation (ACI Building Code, 318-83). Both the second moment of the area of the uncracked gross section ignoring the reinforcement, I_g , and the second moment of area of uncracked transformed section, I_{ucr} , are used to calculate I_e . The results obtained from the NONLACS2 program and Branson's equation are referred as the "analytical results" and "Branson values", respectively, throughout the rest of this thesis.

Review of the various research results presented in Chapter 2 suggests a need for further modification of the EI equation for R C beams. New models are required to predict the flexural rigidity beyond the service load level at the various load stages up to the ultimate load. Two series of experimental tests are analyzed using the NONLACS2 program (modified to account for the

mesh size dependency) to investigate the flexural rigidity of R C beams.

5.1.1 Reinforced Concrete Beams Tested by Gaston

Five singly and doubly reinforced beams tested by Gaston et al. (1952), are analyzed to investigate the need of new formulation for EI in R C beams. As can be seen from Table 4.1, beams T2LA, T5L, and T4LA are reinforced in tension only, while beams C3YNA, and C4XNB are reinforced for both tension and compression. The material properties, details of geometry, reinforcement, loading pattern, and the finite element modelling of these beams are presented in Chapter 4. The mesh configuration with 80 elements (76.2×76.2 mm, Fig. 4.2c) using the proposed model (Eq. 4.1) for calculation of the concrete ultimate tensile strain, ϵ_{tu} , has been selected for these beams. As discussed in Chapter 4, this mesh configuration showed very good agreement with the experimental results for beams T2LA, T4LA, T1HB, C2W, C3YNA, and C3YNB.

To verify the effect of tension stiffening on the analytical response of R C beams, the beam T2LA is analyzed for two values of the concrete ultimate tensile strain, ϵ_{tu} . The load-deflection curve for the under-reinforced beam T2LA is shown in Fig. 5.2. For the model which considers the tension-stiffening effect ($\epsilon_{tu}=0.0021$, using the proposed model), the computed load corresponding to the initiation of cracks is 13.34 kN, and the ultimate load is 68.94 kN with only one percent deviation from the experimental result. The experimental values of loads for the yielding of the reinforcing steel and the crushing of the concrete are $P_y=62.27$ kN and $P_u=69.68$ kN, while the corresponding deflections are $\Delta_y=9.65$ mm and $\Delta_u=78.74$ mm, respectively. The analytical yielding and ultimate deflections are $\Delta_y=7.42$ mm and $\Delta_u=72.39$ mm, with a discrepancy of -23 percent and -8 percent from experimental results, respectively. If the tension-stiffening is neglected ($\epsilon_{tu}=\epsilon_{cr}=0.00013$), the ultimate load and the ultimate deflection are underestimated ($P_u=60.0$ kN and $\Delta_u=26$ mm). The mode of failure for beams T2LA, T4LA, C3YNA, and C4XNB is initially due to the yielding of the tension steel reinforcement, while the beam T5L fails in a compression failure mode i.e. the concrete crushes before the steel yields. A summary of the yielding and the ultimate loads for these beams are presented in Table 5.1.

The complete experimental load-concrete strain curve at the top of midspan and the load-steel strain curve for the bottom steel at midspan for beams T2LA are available (Gaston et al. 1952). Using these results, the curvature and consequently the flexural rigidity of midspan section are calculated (Eq. 5.1). The variation of flexural rigidity at the midspan section obtained using

the different methods versus the M_x/M_{cr} ratio for beam T2LA is shown in Fig. 5.3. It should be noted that despite its limited applicability at the service load level, Branson's equation has been used for comparison through the entire load range - from zero load until the ultimate load.

The analytical tangent flexural rigidity curve is quite close to the experimental response and has the same general pattern. Comparison of the analytical and the experimental results and the values obtained using the Branson's equation show that the values of both the analytical and the experimental tangent flexural rigidities are larger than the Branson values (using I_g), when the ratio of M_x/M_{cr} is less than 2.5, and then the Branson values tend to be constant, while the experimental and the analytical tangent flexural rigidities decrease with an increase in the M_x/M_{cr} ratio. This is because as the M_x/M_{cr} ratio becomes large, the value of the effective second moment of area, I_e , in the Branson's equation rapidly tends toward I_{cr} . For example, in the beam T2LA, in the usual working load range (M_x/M_{cr} =up to 3 to 4), a load equal to 44.48 kN ($P=0.63 P_u$), the experimental tangent flexural rigidity is 2.04×10^9 kN.mm², while the analytical flexural rigidity is 2.32×10^9 kN.mm², with a deviation of 13 percent from the experimental value. The use of Branson's equation results in a value of 3.21×10^9 kN.mm² with a 57 percent discrepancy from the experimental value (this deviation increases with an increase in the applied load). The use of the second moment of area of the uncracked transformed section, I_{ucr} , in Eq. 2.20 instead of I_g improves the estimate of $E_c I_e$ in the range of $M_x/M_{cr} < 2$. The principal effect of using I_{ucr} is in the calculation of an increased value of M_{cr} (Eq. 2.21, due to both I_{ucr} and y_t). In this range, the values of the analytical tangent flexural rigidity show good agreement with Branson values using the value of the second moment of area of the uncracked transformed section, I_{ucr} .

The effect of tension and compression reinforcement ratios, loading type and tension-stiffening on the flexural rigidity of beams T2LA, T4LA, T5L, C3YNA, and C4XNB is discussed later in this chapter. As can be seen from Table 5.1, the average value of the ratios of the analytical - to - experimental value of the ultimate load is found to be 0.978 with a standard deviation of 0.0255. This indicates excellent agreement between the analytical or computed values of the yield and ultimate loads and the corresponding experimental values. More details related to the cracking, yield and ultimate loads, load-deflection, moment-curvature and load-strain curves, failure modes and comparison of experimental and analytical flexural rigidities for these beams can be found in the report by Kheyroddin and Mirza (1995a).

Table 5.1: Comparison of experimental and analytical results, Gaston and Mattock beams.

Beams		Yielding Load, P_y (kN)		Ultimate Load, P_u (kN)		Comparison	
		Analytical ($P_{y,anl}$)	Experimental, ($P_{y,exp}$)	Analytical ($P_{u,anl}$)	Experimental ($P_{u,exp}$)	$P_{y,anl} / P_{y,exp}$	$P_{u,anl} / P_{u,exp}$
Gaston	T2LA	62.27	62.27	68.94	69.68	1.00	0.99
	T5L	155.68	157.16	155.68	157.16	0.99	0.99
	T4LA	112.10	114.18	113.38	114.18	0.98	0.993
	C3YNA	131.22	121.56	137.89	148.25	1.08	0.93
	C4XNB	134.33	126.90	138.56	142.78	1.05	0.97
Mattock	C5	115.65	115.29	121.43	121.79	1.003	0.997
Average Value						1.017	0.978
Standard Deviation						0.0391	0.0255

5.1.2 Reinforced Concrete Beam Tested by Mattock

One simply supported beam, C5, subjected to midspan-concentrated loading (termed concentrated loads) tested by Mattock (1964) is analyzed using the NONLACS2 program and a mesh with 88 elements (Fig. 5.4). This beam is also used for further parametric studies. The experimental material properties for concrete and reinforcing steel are presented in Table 5.2. The reinforcement and loading are symmetrical with respect to the mid-span. Due to the symmetric configuration of the beam and the loading on it, only one-half of the beam was modeled. Vertical loads are applied in 30 load steps with smaller increments of loads being applied just before the beam reaches its ultimate load stage. This would improve the rate of convergence of the solution and the accuracy in predicting the failure load. The details of geometry, reinforcement, loading pattern and finite element modelling of this beam are shown in Fig. 5.4.

As pointed out in Section 3.5.2, and Fig. 3.9, quadrilateral shell element (QLC3), inplane membrane element with 3 degrees of freedom per node (u , v , θ_z), and RBE, the rectangular bending element with 3 degrees of freedom per node (θ_x , θ_y , w) are used in this study. Integration order for these analyses is chosen to be 3 (i.e., nine Gauss quadrature points in each shell element). Plane stress conditions are assumed, and therefore, only one layer of concrete is sufficient. The longitudinal reinforcements are modelled using discrete bar elements and are lumped in single bars at the reference surfaces. The shear reinforcement in the shear spans is modeled as smeared steel layers on the two sides of the beam.

As can be seen from the load-deflection curve for beam C5 (Fig. 5.5), the analytical cracking load, considering tension-stiffening, is 14.23 kN, while the analytical values of loads for the yielding of the steel reinforcement and the crushing of the concrete are $P_y=115.65$ kN and $P_u=121.43$ kN, respectively. The experimental yielding and ultimate loads are $P_y=115.29$ kN and $P_u=121.79$ kN, while the corresponding deflections are $\Delta_y=11.38$ mm and $\Delta_u=46.74$ mm, respectively. The analytical load-deflection curve obtained from the NONLACS2 program, considering tension-stiffening, follow experimental curve quite closely. If tension stiffening is ignored, ($\epsilon_w=\epsilon_{cr}$), the ultimate load is underestimated ($P_u=113.42$ kN) and the structure is a little softer and behaves in a relatively less ductile manner.

Table 5.2: Dimensions and properties of Mattock's beam, C5.

A_s (mm ²)	A'_s (mm ²)	f'_c (MPa)	E_0 (MPa)	ϵ_{cu}	f'_t (MPa)	f_y (MPa)	E_s (MPa)	E_s^* (MPa)	ϵ_{su}
1135.5	142.0	23.4	23145	0.0078	3.0	328.2	195130	5515	0.05

Based on the experimental moment-curvature curve reported by Mattock (1964) and using Eq. 5.1, the experimental flexural rigidity is calculated. The variation of the flexural rigidity at the midspan section obtained using the different methods versus the $M_u/M_{cr,anl}$ ratio for beam C5 is shown in Fig. 5.6. The analytical curve obtained from the NONLACS2 program follows the variation of the experimental values very closely. The analytical response of the beam is stiffer than the experimental response, and therefore the analytical flexural rigidity is larger than the experimental values. For the same moment level, i.e., $M_u/M_{cr,anl}=3.7$, the experimental tangent flexural rigidity is 4.88×10^9 kN.mm², while the analytical flexural rigidity is 5.14×10^9 kN.mm², representing a deviation of 5 percent from the experimental value. The Branson values (using I_{ucr}) are very close to the experimental and the analytical results, when the ratio of $M_u/M_{cr,anl}$ is less than 2.0, and then the values obtained using Branson's equation tend to be constant. The difference between the experimental and the Branson values increases with an increase in the applied load (maximum deviation is 30 percent). As can be seen from Fig. 5.6, there is no reduction in the value of flexural rigidity when the Branson's equation (using I_g) is utilized. Because of the high ratio of tensile reinforcement for beam C5 ($\rho=0.0294$), the value of the cracked second moment of the area, $I_{cr}=2.71 \times 10^8$ mm⁴, is very close to the second moment of area of the uncracked gross

section ignoring the reinforcement, $I_g=2.77 \times 10^8 \text{ mm}^4$, and consequently the flexural rigidity for both the cracked and the uncracked sections are approximately the same. To eliminate this drawback, it is recommended to use the value of the uncracked transformed second moment of area, I_{ucr} in Eq. 2.20, especially for an over-reinforced section.

5.1.3 Parametric Study

A parametric study is conducted to examine the effects of the variables influencing the pre- and post-cracking behaviour of R C beams. For the parametric study, a $152.5 \times 280 \text{ mm}$ beam section (C5, Mattock 1964), with a tension reinforcement ratio of 0.0294 subjected to concentrated loads, is used (Fig. 5.4). In addition, the same beam is analyzed with five other assumed tension reinforcement ratios (0.044, 0.022, 0.0147, 0.011, and 0.0074) giving the entire range of under-reinforced to over-reinforced sections. For each reinforcement ratio, the parameters studied include the compression reinforcement ratio, ρ' , concrete compressive strength, f'_c , steel yield strength, f_y , and the three different loading types. Table 5.3 lists the parameters which are varied, together with their designations, cross sectional details, types of loading, concrete and steel strengths, for the 51 beams (9 Groups) investigated in this study. Each beam is designated as M_{ij} , where "i" is the group number and "j" indicates the rank of tension reinforcement ratio in an increasing order, commencing from the minimum tension reinforcement ratio.

A post-processing program is developed to extract the desired data from "NONLACS2" output file. This supplementary program provides the data such as the external nodal forces and displacements, principal and local stresses, the value of concrete strains at the integration points, curvature, internal moment and flexural rigidity at the section considered. The graphical part of this program can plot undeformed and deformed shapes of the structure and the crack pattern at a given load step.

5.1.4 Pre-cracking Stage ($M_a \leq M_{cr,anal}$)

5.1.4.1 Effect of influencing parameters on the I_{ucr}/I_g , $M_{cr,anal}$ and $(EI)_{cr}$

The sectional properties, cracking moments and flexural rigidities of the Mattock beams (Group No. 1) are presented in Table 5.4. The beam M16 with $\rho=0.0440$ is over-reinforced ($\rho > \rho_b=0.0337$), while the rest of beams have under-reinforced sections. The ratio of I_{ucr}/I_g changes from 1.18 to 1.60 when the tension reinforcement ratio, ρ , increases from 0.0074 to 0.0440.

Table 5.3: Details of Mattock beams used in parametric study.

Group No.	Beam	A_s (mm ²)	ρ	f'_c (MPa)	f_y (MPa)	A_s' (mm ²)	ρ'	Parameters Studied	Type of Loading
1	M16	1703.2	0.044	23.4	328.2	142	0.0037	ρ	Concentrated Loads
	M15	1135.5	0.0294						
	M14	851.6	0.022						
	M13	568	0.0147						
	M12	426	0.011						
	M11	284	0.0074						
2	M26	1703.2	0.044	23.4	328.2	426	0.011	ρ, ρ'	Concentrated Loads
	M25	1135.5	0.0294						
	M24	851.6	0.022						
	M23	568	0.0147						
	M22	426	0.011						
3	M36	1703.2	0.044	23.4	328.2	568	0.0147	ρ, ρ'	Concentrated Loads
	M35	1135.5	0.0294						
	M34	851.6	0.022						
	M33	568	0.0147						
4	M46	1703.2	0.044	35.1	328.2	142	0.0037	ρ, f'_c	Concentrated Loads
	M45	1135.5	0.0294						
	M44	851.6	0.022						
	M43	568	0.0147						
	M42	426	0.011						
	M41	284	0.0074						
5	M56	1703.2	0.044	35.1	328.2	142	0.0037	ρ, f'_c , Loading Type	Uniform Loads
	M55	1135.5	0.0294						
	M54	851.6	0.022						
	M53	568	0.0147						
	M52	426	0.011						
	M51	284	0.0074						

Table 5.3: (Cont'd) Details of Mattock beams used in parametric study.

Group No.	Beam	A_s (mm ²)	ρ	f'_c (MPa)	f_y (MPa)	A_s' (mm ²)	ρ'	Parameters Studied	Type of Loading
6	M66	1703.2	0.044	42.1	328.2	142	0.0037	ρ, f'_c	Concentrated Loads
	M65	1135.5	0.0294						
	M64	851.6	0.022						
	M63	568	0.0147						
	M62	426	0.011						
	M61	284	0.0074						
7	M76	1703.2	0.044	23.4	413.7	142	0.0037	ρ, f_y	Concentrated Loads
	M75	1135.5	0.0294						
	M74	851.6	0.022						
	M73	568	0.0147						
	M72	426	0.011						
	M71	284	0.0074						
8	M86	1703.2	0.044	23.4	328.2	142	0.0037	$\rho, \text{Loading Type}$	Uniform Loads
	M85	1135.5	0.0294						
	M84	851.6	0.022						
	M83	568	0.0147						
	M82	426	0.011						
	M81	284	0.0074						
9	M96	1703.2	0.044	23.4	328.2	142	0.0037	$\rho, \text{Loading Type}$	Third-Point Loadings
	M95	1135.5	0.0294						
	M94	851.6	0.022						
	M93	568	0.0147						
	M92	426	0.011						
	M91	284	0.0074						

Table 5.4: Sectional properties of Mattock beams, Group No. 1

Beam	$\rho =$ (A_s / bd)	I_{ucr} (10^8 mm^4)	I_{cr} (10^8 mm^4)	$M_{cr,lg}^*$ (kN.mm)	M_{cr^*+ucr} (kN.mm)	$M_{cr,anl}$ (kN.mm)	$E_c I_{ucr}$ (10^9 kN.mm^2)	$(EI)_{cr}$ (10^9 kN.mm^2)
M16	0.0440	4.44	3.42	5947	11674	12813	10.27	9.70
M15	0.0294	4.03	2.71	5947	9910	10830	9.33	8.92
M14	0.0220	3.80	2.26	5947	9004	9768	8.78	8.41
M13	0.0147	3.54	1.71	5947	8080	8653	8.21	7.75
M12	0.0110	3.40	1.39	5947	7611	8100	7.89	7.43
M11	0.0074	3.26	1.02	5947	7138	7600	7.55	7.20

* $M_{cr,lg} = f_r \times I_g / y,$ $I_g = 2.77 \times 10^8 \text{ mm}^4$ $E_c I_g = 6.40 \times 10^9 \text{ kN.mm}^2$

Since the effect of the reinforcement has been considered in the analytical models using the NONLACS2 program, the analytical moment at first cracking, $M_{cr,anl}$ is larger than M_{cr} using the value of I_g ($M_{cr,lg}$). The reinforcing steel causes an increase in the second moment of the area and a decrease in the distance from the centroidal axis to the extreme tension fibre, y_t , and consequently an increase in the moment at first cracking, M_{cr} ($M_{cr,lg} = f_r \times I_g / y$). The present study indicates that flexural cracks appear at loads between 15 and 20 percent of the ultimate load and consideration of the area of the reinforcement increases the calculated cracking moment based on the gross section ($M_{cr,lg}$) by about 25 to 80 percent. For example, for beam M14 with $\rho = 0.0220$, the analytical cracking moment is equal to 9768 kN.mm which is 64 percent more than the cracking moment based on the gross section ($M_{cr,lg} = 5947 \text{ kN.mm}$). For the beam M12 with the lower value of tension reinforcement ratio ($\rho = 0.011$), this increase is 36 percent.

The influence of the tension reinforcement ratio on the cracking flexural rigidity is presented in Table 5.4. Comparison of beams M11 and M13 with equal value of ρ' and different tension reinforcement ratios indicates that if the value of ρ increases by a factor of two, the cracking flexural rigidity, $(EI)_{cr}$ increases by about 7.5 percent. Similarly, a comparison of beams M12 and M22 with equal value of ρ' and different values of ρ' shows that if the value of ρ' increases by a factor of two, the $(EI)_{cr}$ value increases by about 17 percent.

An increase in the concrete compressive strength, f'_c , increases the values of the cracking moment and the flexural rigidity. Since, for higher concrete strengths, the initial slope of the

concrete compression stress-strain curve is steeper (higher value of the modulus of elasticity), an increase in f'_c results in higher values of the analytical cracking moment and the flexural rigidity. For example, in the over-reinforced beam with $\rho=0.044$, an increase in the value of f'_c by about 50 percent increases the analytical cracking moment by about 13 percent (beams M16 and M46 in Table 5.4). In under-reinforced beam with $\rho=0.011$, an increase in the value of f'_c by about 50 percent increases the analytical cracking moment by about 22 percent (beams M12 and M42).

To show the influence of f'_c on the $(EI)_{cr}$, beams M16 and M46 with $\rho=0.044$ and two different values of f'_c are compared. An increase in the value of f'_c by 50 percent results in an increase in the cracking flexural rigidity by about 20 percent. This effect is the same for the beams reinforced with different amount of reinforcements.

Since the analytical cracking moment and flexural rigidity, $M_{cr,anl}$ and $(EI)_{cr}$, are sectional properties, the value of f_y and the type of loading do not have any effect on these values.

5.1.4.2 Proposed model for analytical cracking moment, $M_{cr,anl}$

In order to derive the new equations, the normalized values of $M_{cr,anl}/M_{cr,Ig}$, $(EI)_{cr}/E_c I_g$ and $(EI)_{tan}/(EI)_{cr}$ are used. For regression analysis of analytical results obtained from the NONLACS2 program, a statistical and numerical program which is called SAS (1982) is utilized.

As mentioned previously, the analytical cracking moment is affected by the concrete compressive strength and the tension and compression reinforcement ratios. As shown in Fig. 5.7a, the value of $M_{cr,anl}/M_{cr,Ig}$ increases with an increase in the tension and compression reinforcement ratios. For example, for the beam with $\rho'=0.0037$, an increase in the value of ρ by about 50 percent will increase the value of the ratio $M_{cr,anl}/M_{cr,Ig}$ by about 18 percent (M15 and M16).

Comparison of beams M16 and M36 with equal tension reinforcement ratios and varying compression reinforcement ratios indicates that if the value of ρ' increases by a factor of about 4, the $M_{cr,anl}/M_{cr,Ig}$ increases by about 9 percent. An increase in the concrete compressive strength reduces the $M_{cr,anl}/M_{cr,Ig}$ values (Fig. 5.7b). For the beam with $\rho=0.044$, an increase in the value of f'_c by 50 percent (beams M16 and M46), the cracking moment ratio decreases by about 8.5 percent. This reduction is larger for heavily reinforced beams compared with the lightly reinforced sections. Since three parameters ρ , ρ' , and f'_c have considerable effect on the analytical cracking moment, based on a regression analysis of the analytical results for this multivariable problem, the following empirical equation is proposed:

$$\frac{M_{cr,anal}}{M_{cr,Ig}} = 1 + \beta (\rho + \rho') \quad (5.2)$$

where

$$\beta = 22 - \frac{f'_c - 27.6}{6.9} \quad (\text{for } f'_c \geq 27.6 \text{ MPa}) \quad (5.3)$$

The value of β is equal to 22 for $f'_c \leq 27.6$ MPa, and the value of β is reduced continuously by 1 for each 6.9 MPa increase in strength beyond 27.6 MPa. The average value and the standard deviation for the proposed - to - analytical cracking moment ratio are 0.982 and 0.0195, respectively. The value of correlation coefficient, r , is equal to 0.988 which is very close to 1.0. This indicates that a very high degree of correlation exists between the analytical results and the values obtained from the proposed model. Therefore, any prediction based on the regression equation would be quite accurate (see Fig. 5.7).

5.1.4.3 Proposed model for cracking flexural rigidity, $(EI)_{cr}$

Figure 5.8a shows the effect of tension and compression reinforcement ratios on the cracking flexural rigidity ratio. Comparison of beams M11 and M13 with equal value of ρ' and different tension reinforcement ratios indicates that if the value of ρ increases by a factor of two, the $(EI)_{cr}/E_c I_g$ ratio increases by about 7 percent. Similarly, a comparison of beams M12 and M22 with equal value of ρ and different values of ρ' shows that if the value of ρ' increases by a factor of two, the $(EI)_{cr}/E_c I_g$ value increases by about 17 percent. Therefore, the effect of the compression reinforcement ratio on the cracking flexural rigidity ratio is about 2.5 times more than that the tension reinforcement ratio. When the amount of compression reinforcement increases, the neutral axis depth, c , decreases and consequently, the transformed second moment of area and the cracking flexural rigidity increases.

It can be seen from Fig. 5.8b that the value of the ratio $(EI)_{cr}/E_c I_g$ decreases by a small amount with an increase in the concrete compressive strength. For the beam with $\rho=0.044$, the reduction of cracking flexural rigidity ratio is about 2 percent when the value of f'_c increases about 50 percent. Analysis of the results using the SAS software (1982) shows that the ratio of $(EI)_{cr}/E_c I_g$ is generally independent of the concrete and the steel strengths. Based on the analysis results, the following equation is suggested:

$$\frac{(EI)_{cr}}{E_c I_g} = 1 + 8(\rho + 3\rho') \quad (5.4)$$

The results obtained using Eq. 5.4 show good agreement with the analytical results obtained from the NONLACS2 program with a maximum deviation of 7 percent. The average value and standard deviation for the proposed - to - analytical cracking flexural rigidity ratio are 0.975 and 0.024, respectively. The correlation coefficient for this data set is equal to 0.955 which exhibits the accuracy of proposed equation 5.4 (see Fig. 5.8).

Before the concrete cracks, the analytical flexural rigidity decreases with an increase in the M_a/M_{cr} ratio (see Figures 5.9 and 5.10), while Branson's equation gives a constant value equal to $E_c I_g$. The following empirical equation was proposed (Kheyroddin and Mirza 1994) for evaluating the analytical pre-cracking flexural rigidity

$$EI = \left(1 - 0.06 \frac{M_a}{M_{cr,ani}}\right) (EI)_0 \quad \text{where } M_a \leq M_{cr,ani} \quad (5.5)$$

where $M_{cr,ani}$ is the analytical cracking moment and $(EI)_0$ is the initial analytical flexural rigidity.

The cracking flexural rigidity is the value of EI corresponding to the cracking point ($M_a = M_{cr,ani}$) and based on Eq. 5.5, it is given by

$$EI = (EI)_{cr} = 0.94 (EI)_0 \quad \text{when } M_a = M_{cr,ani} \quad (5.6)$$

For simplicity, the analytical flexural rigidity in the pre-cracking stage can be assumed to be constant and equal to $(EI)_{cr}$.

5.1.5 Post-Cracking Stage ($M_{cr} < M_a < M_y$)

5.1.5.1 Effect of tension reinforcement ratio on EI

The effect of tension reinforcement ratio, ρ , on the flexural rigidity, EI, of R C beams is discussed in this section. A plot of the analytical flexural rigidity at the midspan section versus the M_a/M_{cr} ratio for beams with approximately equal concrete strengths and varying percentages of tension reinforcement (T2LA, T4LA, and T5L) are shown in Fig. 5.9, which shows that, the heavily reinforced section has a significantly higher EI value compared with that for the lightly reinforced section. For the same moment level, i.e., $M_a/M_{cr} = 3.25$, a larger value of EI equal to 5.88×10^9 kN.mm² is obtained for the over-reinforced beam, T5L, compared with a value of

4.91×10^9 kN.mm² and 2.70×10^9 kN.mm² for the under-reinforced beams T4LA and T2LA, respectively, giving differences of about 20 percent and 218 percent, respectively. The reduction of the flexural rigidity due to cracking is greater for the lightly reinforced sections than for the heavily reinforced sections.

Figure 5.10 shows the variation of the flexural rigidity ratio, $(EI)_{\text{un}}/(EI)_{\text{cr}}$ with the moment ratio, $(M_a/M_{\text{cr,an}})$ for the Mattock beams (Group No. 1) subjected to concentrated loads. Like Gaston beams, an increase in the tension reinforcement ratio results in an increase in the flexural rigidity ratio. Generally, the differences between the "high" values (corresponding to cracking point) and "low" values (corresponding to the yielding of steel) of EI are larger for lightly reinforced beams compared with heavily reinforced section (Fig. 5.10). For the beam M11 with $\rho=0.0074$, the flexural rigidity, EI, is 5.62×10^9 kN.mm², while for the beam M13 with $\rho=0.0147$, this value is 4.82×10^9 kN.mm². It can be concluded that the stiffness of a beam with a low value of steel would vary more with respect to moment than for a beam with a high percentage of steel.

For over-reinforced beam M16 with $\rho=0.044$, there is a reduction in the flexural rigidity at five load steps before failure (critical zone), as shown in Fig. 5.10. At higher load levels, the response of the concrete elements in compression governs the overall behaviour and the response of the concrete and when the concrete strain in compression zone exceeds the compressive strain corresponding to f'_c , the curvature increases suddenly and consequently the flexural rigidity decreases. In under-reinforced beams, the response of the concrete element in tension governs the overall behaviour and there is a gradual increase of the compressive strain of the concrete.

The variation of EI values for the differently reinforced beams may be explained by the difference in the cracked length, L_{cr} (L_{cr} , the beam segment over which the maximum moment exceeds the analytical cracking moment, $M_{\text{cr,an}}$). In the present study, the value of L_{cr} has been calculated using the NONLACS2 program. It is the distance between the locations where the concrete tensile strain, ϵ_t , exceeds the concrete cracking strain, ϵ_{cr} . Variation of the cracked length ratio, L_{cr}/L , with the moment ratio, $M_a/M_{\text{cr,an}}$ is shown in Fig. 5.11. This figure reveals that, at the same moment ratio, $M_a/M_{\text{cr,an}}=3.3$, the cracked length of the heavily reinforced beam, M16, with $\rho=0.044$ is equal to 1118 mm which is 61 percent less than that for the lightly reinforced beam, M11 with $\rho=0.0074$, hence leading to a greater flexural rigidity.

5.1.5.2 Influence of compression reinforcement ratio on EI

The flexural rigidity of the Gaston beams T4LA with $\rho=0.019$ and C4XNB with $\rho=0.019$

and $\rho' = 0.014$ with approximately equal concrete strengths are shown in Fig. 5.12. The addition of compression reinforcement results in a decrease in depth of the neutral axis, and consequently a decrease in the curvature and an increase in the EI values. The reduction in the flexural rigidity is greater for the singly reinforced beam (T4LA) than for the doubly reinforced beam (C4XNB). At $M_a/M_{cr} = 4$, the value of flexural rigidity for beam C4XNB is 6.03×10^9 kN.mm² which is 40 percent more than the value of 4.3×10^9 kN.mm² for the beam T4LA. After cracking, the beam with the compression reinforcement behaves in a stiffer manner but the EI values for both beams decrease rapidly.

As can be seen from Fig. 5.12, the analytical results and the values obtained using Branson's equation show a considerable difference, especially when the value of I_g is used to determine the effective second moment of the area, I_e . At $M_a/M_{cr} = 6$, the difference between the analytical and the Branson values for beams T4LA and C4XNB is 60 and 15 percent, respectively.

The effect of the compression reinforcement ratio on the flexural rigidity of Mattock beams with two different tension reinforcement ratios of 0.044 and 0.022 are shown in Figures 5.13 and 5.14, respectively. For each tension reinforcement ratio, the effects of the three values of compression reinforcement ratios are investigated (Group Nos. 1, 2, and 3). With a decrease in the compression reinforcement ratios, the EI values decrease. As can be seen from Fig. 5.13, for heavily reinforced beam M36, at $M_a/M_{cr,anal} = 4.93$, the value of EI for $\rho' = 0.0147$ is 7.60×10^9 kN.mm² which is 37 percent greater than the EI value of 5.54×10^9 kN.mm² for the beam M16 with $\rho' = 0.0037$. Figure 5.14 reveals that the influence of ρ' on the EI values for under-reinforced beam with $\rho = 0.022$ is less than that for the beam with $\rho = 0.044$. The above findings show that the compression reinforcement ratio has a significant effect on the EI values for the heavily reinforced beams and this effect decreases with a decrease in the tension reinforcement ratio.

Figure 5.15 reveals that at the same level of moment ratio and for the same value of ρ , the flexural rigidity ratio is approximately the same for different amounts of compression reinforcement ratio, ρ' . Thus, the flexural rigidity ratio, $(EI)_{tan}/(EI)_{cr}$ is independent of the compression reinforcement ratio.

5.1.5.3 Effect of concrete compressive strength on EI

In order to study the effect of the concrete compressive strength, f'_c , and the tension reinforcement ratio on the overall behaviour of R C beams, the Mattock beams are analyzed with three different values of f'_c , loaded at midspan (Group Nos. 1, 4, and 6). Plots of the variation

of the analytical flexural rigidity at the midspan section versus the $M_a/M_{cr,anal}$ ratio with the different concrete compressive strengths for beams with tension reinforcement ratios of 0.044 and 0.022 are shown in Figures 5.16 and 5.17, respectively. The use of the concrete with higher value of f'_c with its higher modulus of elasticity results in a higher stiffness and a higher flexural rigidity. For example, in Fig. 5.16 for beam M11 with $\rho=0.044$, an increase in the value of f'_c by about 50 percent increases the flexural rigidity by about 19 percent. Based on Fig. 5.17, the increase in the EI values for beam M14 with $\rho=0.022$ is 8 percent, when the value of f'_c increases by about 50 percent.

Thus, the effect of the compressive strength of the concrete on the EI values in the post-cracking stage decreases with a decrease in the tension reinforcement ratio. In the over-reinforced section, because of the high ratio of tensile reinforcement, the cracking of the concrete does not have a significant effect on the overall response and the concrete elements in compression govern the overall behaviour of beam. In this case, the value of f'_c have a significant effect on the response. On the other hand, in under-reinforced sections, the flexural rigidity depends primarily on the stress and strain in the tension reinforcement and the neutral axis depth, c . The value of f'_c only influences the value of c , which is small for small reinforcement ratios.

Various analyses (Kheyroddin and Mirza 1995a) indicate that the concrete compressive strength has the same effect on the value of EI for differently loaded beams.

5.1.5.4 Effect of yield strength of steel on EI

To investigate the influence of the yield strength of steel, f_y , on the response of R C beams, Mattock beams with two different values of f_y (Group No. 1 with $f_y=328.2$ MPa and Group No. 7 with $f_y=413.7$ MPa) subjected to concentrated loads have been analyzed. The results show that, as expected, the value of f_y does not have a significant effect on the behaviour of beam before yielding of tension reinforcement.

5.1.5.5 Influence of tension-stiffening

Figure 5.18 shows the analytical flexural rigidity of the models with and without tension-stiffening for beam C5. The model which considers the tension-stiffening effect ($\epsilon_{tu}=0.0023$) behaves in a stiffer manner and results in a higher value of EI at the same load level. For example, at $M_a/M_{cr,anal}=3.0$, the flexural rigidity of the model with tension stiffening is 7.0×10^9 kN.mm², while the model which ignores tension stiffening after ϵ_{cr} ($\epsilon_{tu}=\epsilon_{cr}=0.00013$), gives a

value of EI equal to 5.85×10^9 kN.mm². It is clear that the pre-cracking flexural rigidities for the two models at the same moment ratios are exactly the same.

Branson's equation considers the tension-stiffening effect empirically, but it predicts EI values which are smaller than the analytical flexural rigidity obtained from the model with tension stiffening. At $M_a/M_{cr,anl}=3.0$, the deviation of EI value using Branson's equation is about 13 percent from the analytical flexural rigidity obtained from the model with tension stiffening. The effect of tension stiffening decreases as the bending moment increases. As can be seen from Fig. 3.5, after cracking of the concrete, the tensile stress in the concrete decreases ($\epsilon_{cr} \leq \epsilon \leq \epsilon_u$) and when the strain of concrete exceeds the ultimate tensile strain, ϵ_u , the stiffness across the cracks is assumed to be zero.

5.1.5.6 Effect of loading type on EI

In an attempt to study the influence of the loading type on the section flexural rigidity for beam C3YNA, the values of the flexural rigidity versus the $M_a/M_{cr,anl}$ ratio at midspan for the three types of loading (midspan-concentrated loading, third-point loading, and uniformly distributed loading) are shown in Fig. 5.19. The results indicate that, at the same level of internal moment in the post-cracking stage, the flexural rigidity is affected by the type of loading. For the same moment level, i.e., $M_a/M_{cr,anl}=2.7$, larger values of EI are obtained for the beam subjected to a central load compared with that for the beam loaded at third-points or with a uniform load, with differences of about 8 percent and 18 percent, respectively.

The variation of EI values for the beams subjected to different loading types can be explained by the difference in the bending moment diagram and the cracked length, L_{cr} , for each type of loading. Figure 5.20 reveals that, at the same $M_a/M_{cr,anl}$ ratio, the cracked length ratio of the beam under central load is less than that under uniform or third-point load, leading to a greater beam flexural stiffness and therefore a larger section flexural rigidity. It is clear that the beam with a larger length with cracks naturally behaves in a more flexible manner and deflects a greater amount.

Branson's equation cannot take into account the effect of the loading type and it predicts the same value of EI for the three different loading types. As mentioned in Chapter 2, the only load parameter included in Branson's equation is the maximum moment M_a at which I_e is estimated. This means that the effective moment of inertia is the same for all identical beams loaded to the same level of moment, regardless of the type of loading applied.

To study the effect of the loading type and the tension reinforcement on the overall behaviour of R C beams, the Mattock beams with six different values of tension reinforcement ratios were subjected to three different types of loading: midspan-concentrated loading, third-point loading, and uniformly distributed loading (Group Nos. 1, 8, and 9). Figure 5.21 shows the effect of the different loading types on the flexural rigidity of the under-reinforced beam with tension reinforcement ratio of 0.0074. Like beam C3YNA, the beam M11 loaded at midspan gives a stiffer response with a higher value of flexural rigidity and a lower value of the L_{cr}/L compared with that for the beams M81 and M91 subjected to uniform and third-point loadings, respectively. At $M_a/M_{cr,ani}=2.0$, a larger value of EI equal to 3.10×10^9 kN.mm² is obtained for the beam loaded at midspan, M11, compared with a value of 2.50×10^9 kN.mm² and 2.44×10^9 kN.mm² for the beam M91 loaded at third-points, or the beam M81 loaded with a uniform load (M81), giving differences of about 24 percent and 27 percent, respectively. At this level of moment, the cracked length ratio for the beam M11 is 0.50, which is 76 percent and 71 percent less than for the beams M91 and M81, respectively.

As can be seen from Figure 5.22, in over-reinforced beam with $\rho=0.0440$ the analytical curves for three different loading types are very close to each other and the effect of loading types on the EI values is negligible. Comparison of Figures 5.21 and 5.22 indicates that the effect of loading type on the flexural rigidity of heavily reinforced beams is not as significant as for the lightly reinforced beams. From the above discussions, it can be concluded that both the type and level of loading influence the value of the flexural rigidity of cracked reinforced beams.

5.1.5.7 Proposed equations for post-cracking stage ($M_{cr,ani} \leq M_a \leq M_y$)

For the post-cracking stage, the various analyses indicated that the variation of $((EI)_{tan}/(EI)_{cr})$ with respect to $(M_a/M_{cr,ani})$ can be represented by the equation:

$$\frac{(EI)_{tan}}{(EI)_{cr}} = \left(\frac{M_{cr,ani}}{M_a} \right)^n \quad \text{when } M_a \geq M_{cr,ani} \quad (5.7)$$

The value of the power n in Eq. 5.7 is evaluated as

$$n = \frac{\log (EI)_{tan} - \log (EI)_{cr}}{\log M_{cr,ani} - \log M_a} \quad (5.8)$$

For each beam, the value of n is calculated so that the analytical results using the Eq. 5.7 converge to the results obtained from the NONLACS2 program. The variation of the power n with

respect to the tension reinforcement ratio, ρ , for different groups is plotted in Fig. 5.23. This figure shows that for a ρ value greater than about 3 percent, the reduction in the value of the power n is very small. The effect of f'_c on the value of the power n for a heavily reinforced beam such as M16 with $\rho=0.044$ is more than that for the lightly reinforced beam like M13 with $\rho=0.0147$. Statistical analysis of the results indicate that the tangent flexural rigidity ratio, $(EI)_{tan}/(EI)_{cr}$, and the value of the power n is independent of the compression reinforcement ratio, and the yield strength of the reinforcing steel. On the other hand, the power n is a function of ρ and f'_c (Figures 5.10 and 5.23). Finally, based on the results of the regression analysis for the beams subjected to concentrated loads, the following equation is proposed:

$$n_{conc.} = 0.10 + 0.0018 \frac{\sqrt{f'_c}}{\rho} \quad (MPa \text{ units}) \quad (5.9)$$

Based on this formula, as the value of tension reinforcement ratio decreases, the value of the power n increases, and consequently the analytical flexural rigidity decreases. The average value of the ratios of the proposed - to - analytical value of the power n is found to be 1.008 with a standard deviation of 0.122. The value of correlation coefficient, r , is equal to 0.982 and indicates that the proposed model predictions are in good agreement with the analytical results obtained from the NONLACS2 program.

The effect of the different loading types on the value of the power n is presented in Table 5.5. As mentioned before, the beam loaded at midspan gives a stiffer response with a higher value of the flexural rigidity and a lower value of the coefficient n compared with that for a beam subjected to uniform and third-point loadings. As can be seen from Table 5.5, the value of the coefficient n for a beam subjected to uniform and third-point loading is approximately the same (maximum difference is 4.5 percent). For simplicity, the value of n for a beam loaded at third-point loads or uniform loads is assumed to be the same. The following definition can be suggested for relationship between the three different loading types:

$$n_{unif., third.} = \alpha n_{conc.} \quad (5.10)$$

where α is the loading type factor and it is a function of the tension reinforcement ratio (Fig. 5.24). The difference in the value of n and α for beams with different type of loading increases with a decrease in the tension reinforcement ratio. For example, the difference in the value of n for beams M12 and M82 ($\rho=0.011$) is 20 percent, while this difference for the beams M14 and

M84 ($\rho=0.022$) is 6 percent. The following equation is suggested for the value of α

$$\alpha = 1.25 - 8 \rho \geq 1.0 \quad (5.11)$$

As can be seen from Table 5.5, the average value and standard deviation of the ratios of the proposed model predictions to the analytical results are 0.995 and 0.0097, respectively. This indicates that the proposed equation predictions are in excellent agreement with the analytical results.

The proposed equations (5.2 through 5.11) permit a quick estimate of the flexural rigidity without the need to compute the cracked second moment of area, I_{cr} . The analyst need only know the maximum moment at the section, M_s , the value of f'_c , the size of the structural member, and the cross-sectional areas of tension and compression reinforcements.

Table 5.5: Variation of n for Mattock beam under different loading types

Tension Reinforcement Ratio, ρ	Values of power "n" ($f'_c=23.4$, $f_y=328.2$ MPa, $\rho'=0.0037$)			$\alpha_{ani} = n_{(unif.)}/n_{(conc.)}$	α_p (Proposed Eq. 5.11)	α_p/α_{ani}
	Concentrated Loads	Third-Point Loading	Uniform Loads			
0.0440	0.425	0.420	0.425	1.00	1.00	1.00
0.0294	0.456	0.460	0.466	1.015	1.015	1.00
0.0220	0.473	0.501	0.502	1.060	1.070	1.009
0.0147	0.628	0.730	0.698	1.140	1.132	0.993
0.0110	0.802	0.940	0.963	1.180	1.162	0.985
0.0074	1.189	1.428	1.440	1.210	1.191	0.984
Average Value						0.995
Standard Deviation						0.0097

The analytical cracking moment, $M_{cr,ani}$, and the analytical cracking flexural rigidity, $(EI)_{cr}$, can be calculated using Equations 5.2 and 5.4, respectively. Then, Equations 5.9, 5.10 and 5.11 can be utilized to predict the value of the power n for beam under different types of loading. Finally, the flexural rigidity can be determined by Eq. 5.7. Since the values of $M_{cr,lg}$ and $E_c I_g$ can be computed easily, the task for the computation of flexural rigidity is considerably simplified.

With the development of the tangent flexural rigidity equation, the modified stiffness approach can be utilized in the nonlinear finite element analysis of R C structures which will save the required computational time considerably.

5.1.6 Post-Yielding Stage ($M_y \leq M_u \leq M_u$)

After yielding of the steel reinforcement, the flexural rigidity suddenly decreases significantly and tends to zero with a small change in the load. A number of investigations show that there is a considerable reduction in the flexural rigidity of R C members near the ultimate load stage. Figure 5.25 shows the variation of ultimate moments for Mattock beams for different amounts of tension and compression reinforcement ratios and concrete compressive strengths.

With an increase in the tension reinforcement ratio, the yield and ultimate moments increase (Fig. 5.25a). Comparison of beams M12 and M14 shows that if the value of ρ increases by a factor of two, the yield and ultimate moments increase by about 73 percent and 65 percent, respectively.

When $\rho > \rho_b$, a beam fails in a brittle manner due to the crushing of the compression zone before the steel yields (compression failure). When enough compression steel is added to a beam, the compression zone is strengthened sufficiently to allow the tension steel to yield before the concrete crushes (tension failure). The analytical results show that the effect of the compression reinforcement on the yield and ultimate moments is not as significant as the tension reinforcement ratio. For example, an increase in the value of ρ' by about 34 percent results in an increase of only about 2 percent in the yield and ultimate moments (beams M24 and M34).

With an increase in the value of f'_c , the amount of balanced reinforcement ratio, ρ_b , increases and the mode of failure changes from compression to tension. In fact, with the same amount of tension reinforcement ratio, the beam with a higher value of f'_c , fails in tension. For example, when $f'_c=23.4$ MPa, the beam M16 with $\rho=0.0440$ is an over-reinforced beam ($0.044 > \rho_b=0.0337$), while when $f'_c=35.1$ MPa, this beam (M46) would be an under-reinforced beam ($0.044 < \rho_b=0.047$). It can be noted that the effect of f'_c on the value of M_y and M_u is considerable for heavily reinforced sections and this effect decreases with a decrease in the tension reinforcement ratio (Fig. 5.25b). For example, in beams M16 and M46 with $\rho=0.044$, an increase in the value of f'_c by about 50 percent results in an increase of about 25 percent in the yielding and ultimate moments. This percentage for under-reinforced beams M11 and M41 with $\rho=0.0074$ is only 4 percent. The reason is that the flexural strength of R C beams with a small amount of

tension reinforcement is affected little by the concrete compressive strength. In such beams, the flexural strength depends primarily on the force in the tension reinforcement and the neutral axis depth, c . The concrete compressive strength influences only the value of the neutral axis depth, c , which for a small value of ρ is very small in comparison with the effective depth, d . Therefore, significant variation of the concrete strength results in only a small variation of the internal lever arm, and of the flexural strength.

With an increase in the value of f_y , the amount of balanced reinforcement ratio, ρ_b , decreases and the mode of failure changes from tension to compression. In fact, with the same amount of tension reinforcement ratio, the beam with a higher f_y , fails in brittle manner. For example, when $f_y=328.2$ MPa, the beam M15 with $\rho=0.0294$ is an under-reinforced beam ($0.0294 < \rho_b=0.0337$), while when $f_y=413.7$ MPa, this beam (M75) would be an over-reinforced beam ($0.0294 > \rho_b=0.0238$). This causes the yielding and ultimate moments to increase with an increase in the value of f_y . The yield and ultimate moments increase by about 10 to 25 percent when the value of f_y increases by about 26 percent. The effect of f_y on the yield and ultimate moments increases with an increase in the tension reinforcement ratio.

Various analyses reported by Kheyroddin and Mirza (1995a) indicate that the effect of loading type is not considerable on the yielding and ultimate moments of simply supported R C beam.

5.1.7 Comparison of Results

To evaluate the accuracy of the proposed models, the proposed equations are used to calculate the value of EI for Gaston and Mattock beams. A comparison of the results indicate that the proposed model can be used to estimate the EI value with reasonable accuracy. Because of space, only the results of two beams, T2LA and C5, are presented here.

The variation of the flexural rigidity at the midspan section versus the $M_a/M_{cr,anl}$ ratio for the beam T2LA is shown in Fig. 5.26. The flexural rigidity curve obtained from NONLACS2 and the proposed model are quite close to the experimental response and have the same general pattern. For example, at the same level of moment, $M_a/M_{cr,anl}=3.32$, the experimental flexural rigidity is 2.04×10^9 kN.mm², while the analytical flexural rigidity is 2.32×10^9 kN.mm², which represents a deviation of 13 percent from the experimental value. The use of the proposed model (Eq. 5.7) results in a value of 2.15×10^9 kN.mm² with a 5 percent discrepancy from the experimental value. The average value of the ratio $(EI)_p/(EI)_{tan,anl}$ was found to be 0.94 with a

standard deviation of 0.066, which indicates the capability and accuracy of proposed model.

The accuracy of the proposed model is also investigated for the Mattock beam, C5. The variation of flexural rigidity at the midspan section obtained using the different methods versus the $M_u/M_{cr,ani}$ ratio for the under-reinforced beam C5 is shown in Fig. 5.27. The proposed model predicts the value of the flexural rigidity quite accurately with a maximum deviation of 10 and 7 percent from the experimental and analytical results, respectively. Comparison of the values obtained using the NONLACS2 program, the proposed model and the experimental values show that the values of both the analytical and proposed flexural rigidities are a little higher than the experimental findings, when the value of $M_u/M_{cr,ani}$ ratio is greater than 2.0.

5.1.8 Predicting Short-Term Deflections

Many methods have been proposed to estimate the short-term deflections of R C beams. Extensive review of deflection of R C beams has been discussed in Chapter 2.

For the cases where the deflection computations may become necessary, the proposed equations (Eq. 5.2 through 5.11) can be utilized to estimate the value of EI which is used in Eq. 2.1. A computer program has been written to compute short-term deflection of R C beams. This program was written in Quick Basic and runs on IBM compatible personal computers. This program calculates the deflection based on proposed model and Branson's equation.

The accuracy of the proposed models is also investigated using the test results available in the literature. In Table 5.6, the details of test beams from five investigations are presented. For calculation of the cracking moment, $M_{cr,lg}$, the concrete modulus of rupture, f_r , is determined according to the ACI Code as: $f_r = 0.62 \sqrt{f'_c}$ (MPa units).

The test results are reproduced in Table 5.7, along with the relevant computed results using the proposed model and Branson's equation. The maximum difference between the experimental and computed deflection is 18 percent, while this difference for Branson's equation is 31 percent. The average value and the standard deviation for the Branson values - to - experimental ratio are 0.866 and 0.135, respectively. The ratios of the computed (using the proposed model) to the experimental deflections in Table 5.7 vary from 0.841 to 1.18 with an average value of 0.971 and a standard deviation of 0.088. The value of correlation coefficient, r , is equal to 0.943. This indicates that there is good correlation between the computed and the experimental results. The experimental deflection values obtained from the reported test results are plotted in Fig. 5.28 against the computed values, using Eq. 5.7. As can be seen, 90 percent

of the data points lie within the ± 15 percent limits, indicating the acceptable accuracy of the proposed model.

Comparison of the results obtained from the Branson's equation and the proposed model show that the proposed models are reasonably accurate, especially for the beam with third-point loading (see Table 5.7, Gaston and Abrishami's beams). For the beams subjected to uniform loads, the maximum difference between the experimental results and the values obtained from the proposed model and Branson's equation are 16 and 11 percent, respectively. In Branson's equation (Eq. 2.20), calculation of the cracking second moment of area, I_{cr} , is the most time-consuming operation, especially for flanged members, while the proposed model is independent of I_{cr} . According to the ACI Committee 435 (1972), using deflection criteria of ACI 318-71 (Branson's equation), there is approximately a 90 percent chance that deflection of a particular beam is within the range of 20 percent less than to 30 percent more than the calculated value. However, several investigators have shown that the Branson's equation is the best practice-oriented tool to calculate deflections in concrete beams (Mirza and Sabnis 1971, and Al-Shaikh and Al-Zaid 1993).

Based on the above discussions, it can be concluded that the proposed equations take into account the effect of tension and compression reinforcement ratios, the compressive strength of concrete and the type of loading. This model is simple and can be used to estimate the values of the flexural rigidity and deflection of R C beams with reasonable accuracy. Because of space, several figures and tables are not presented. These results can be found in the reports by Kheyroddin and Mirza (1994, 1995a, 1995b).

Table 5.6: Details of test beams for comparison of test and calculated short-term deflections

Reference	Beam Designation	Loading Type	Concrete Compressive Strength, f_c (MPa)	Steel Yield Strength, f_y (MPa)	Span L (mm)	Section Details			
						b (mm)	t (mm)	ρ	ρ'
Al-Shaikh and Al-Zaid (1993)	B-H-13	Concentrated loads	33.0	413.7	2500	200	240	0.02	0.002
	B-N-12		33.0	413.7	2500	200	240	0.014	0.002
	B-L-11		33.0	413.7	2500	200	240	0.008	0.002
Al-Zaid et al. (1991)	B3-C, B4-C	Concentrated loads	38.2	413.7	2500	200	240	0.0124	0.002
	B1-U, B2-U	Uniform loads	38.2	413.7	2500	200	200	0.0124	0.002
	B5-T, B6-T	Third-point loads	38.2	413.7	2500	200	200	0.0124	0.002
Abrishami et al. (1995)	UCB	Two-point loads	32.0	440.0	4500	200	400	0.0088	0
Mattock (1964)	C5	Concentrated loads	23.4	328.2	2800	152.5	280	0.0294	0.0037
Gaston et al. (1952)	T1LB	Third-point loading	17.38	317.2	2740	152.5	305	0.0034	0
	T2LA		14.62	303.4	2740	152.5	305	0.0096	0
	T1MB		32.75	295.8	2740	152.5	305	0.0137	0
	T1HA		40.54	304.8	2740	152.5	305	0.0137	0
	T1HB		35.72	360.0	2740	152.5	305	0.0137	0
	T4LA		16.41	304.1	2740	152.5	305	0.019	0
	T5L		17.24	277.2	2740	152.5	305	0.032	0
	C2W		27.17	313.0	2740	152.5	305	0.0137	0.0062
	C2XM		28.1	367.5	2740	152.5	305	0.0137	0.0062
	C3YNA		22.96	311.7	2740	152.5	305	0.019	0.0098
	C4XNA		16.90	313.7	2740	152.5	305	0.019	0.0098
	C4XNB		16.75	320.0	2740	152.5	305	0.019	0.014

Table 5.7: Comparison of experimental and calculated short-term deflections

Reference	Beam Designation	Maximum Moment (M_u , kN.mm)	Experimental Deflection (mm)	ACI Code (Branson's Eq., Using I_{ucr})		Present Study (Proposed Equation)	
				Deflection (mm)	Ratio *	Deflection (mm)	Ratio *
Al-Shaikh and Al-Zaid (1993)	B-H-13	34830	5.69	6.65	1.170	5.33	0.938
	B-N-12	35870	7.62	8.81	1.157	8.00	1.050
	B-L-11	22040	7.62	7.42	0.973	6.45	0.850
Al-Zaid et al. (1991)	B3-C, B4-C	22065	8.46	8.92	1.054	8.38	0.991
	B1-U, B2-U	18388	10.06	8.99	0.894	8.46	0.841
	B5-T, B6-T	18795	9.91	9.45	0.954	9.14	0.924
Abrishami et al. (1995)	UCB	51850	13.67	10.67	0.78	12.52	0.916
Mattock (1964)	C5	48338	5.59	4.90	0.877	6.60	1.180
Gaston et al. (1952)	T1LB	13558	4.45	3.86	0.870	4.83	1.085
	T2LA	19297	5.84	4.42	0.760	5.94	1.017
	T1MB	27115	5.72	4.60	0.80	5.23	0.92
	T1HA	27115	5.00	4.24	0.85	4.65	0.93
	T1HB	29420	6.10	4.83	0.792	5.84	0.958
	T4LA	28470	6.10	4.32	0.710	5.77	0.946
	T5L	40673	6.35	4.98	0.784	5.89	0.928
	C2W	311.94	7.11	5.74	0.81	7.47	1.05
	C2XM	45240	6.30	4.80	0.762	5.51	0.875
	C3YNA	37970	6.10	4.67	0.770	5.79	0.950
	C4XNA	33894	5.03	4.32	0.86	5.64	1.12
C4XNB	40673	7.11	4.90	0.69	6.76	0.95	
Average Value					0.866		0.971
Standard Deviation					0.135		0.088

* Ratio of computed to measured deflections.

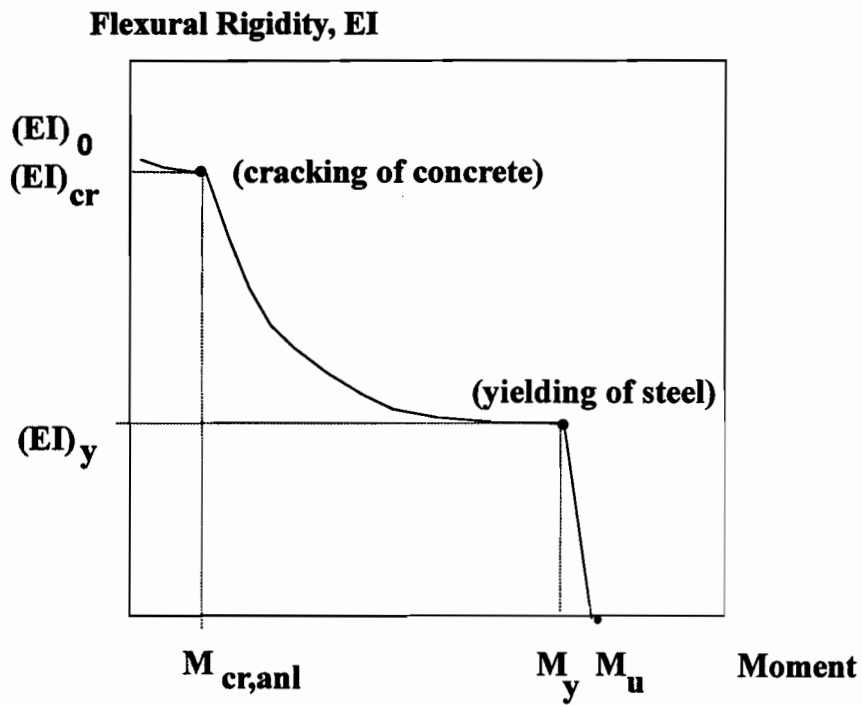


Figure 5.1: Schematic variation of flexural rigidity versus moment, M

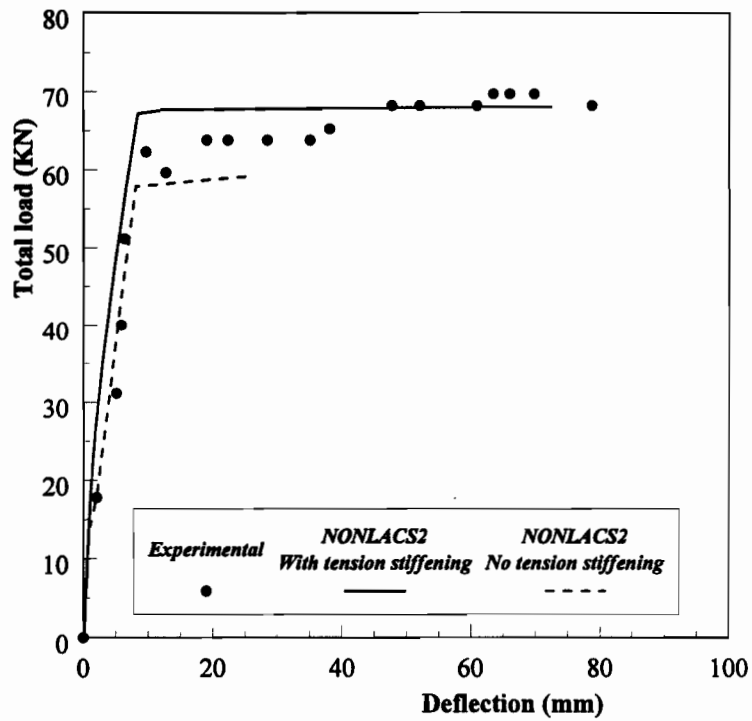


Figure 5.2: Comparison of analytical and experimental load-deflection response of beam T2LA

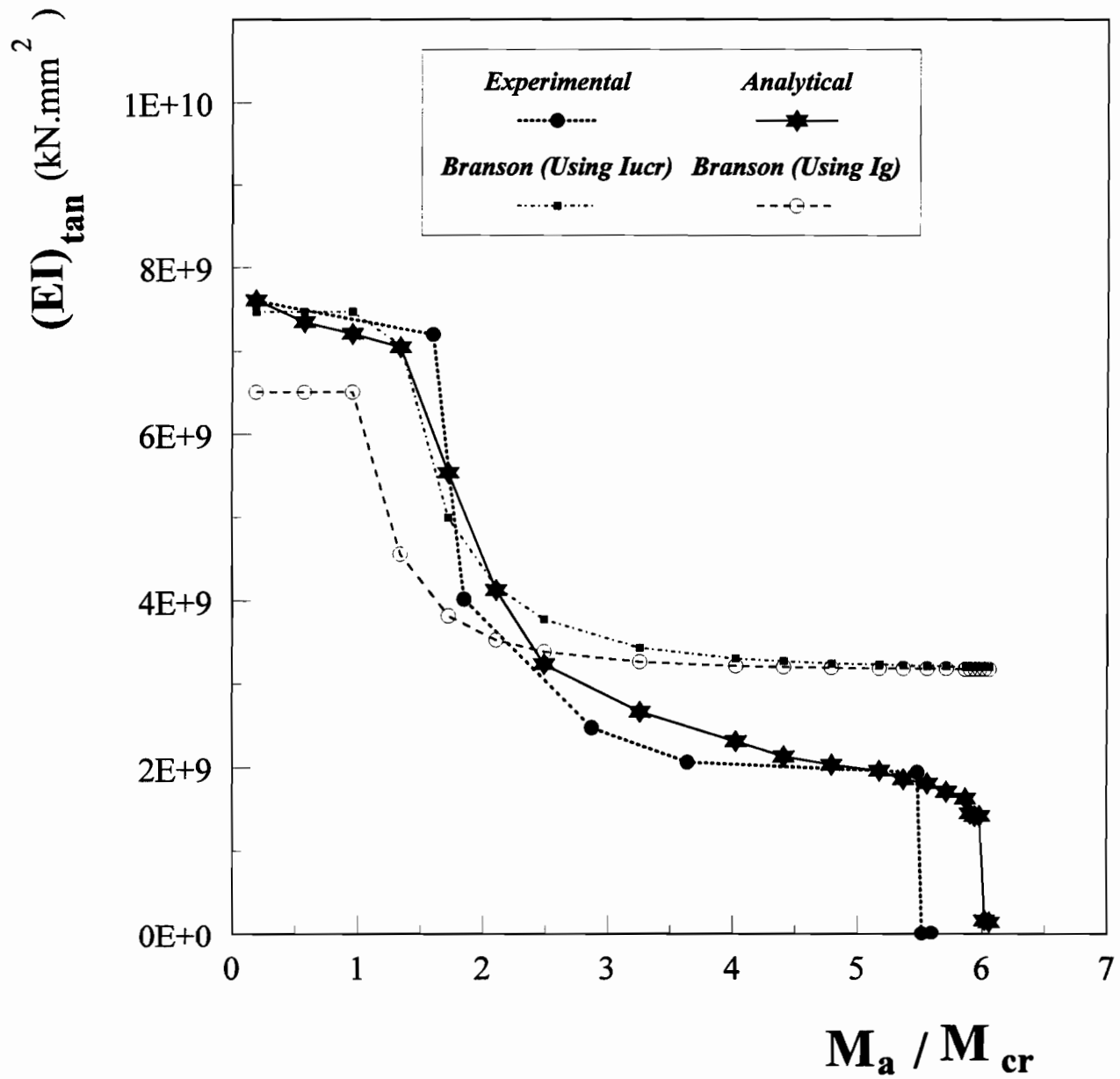
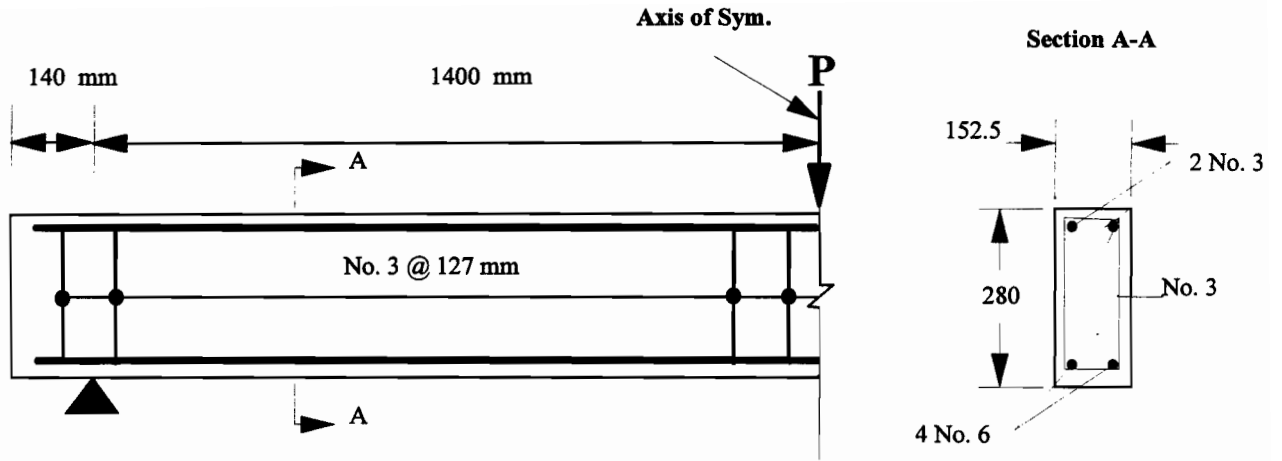
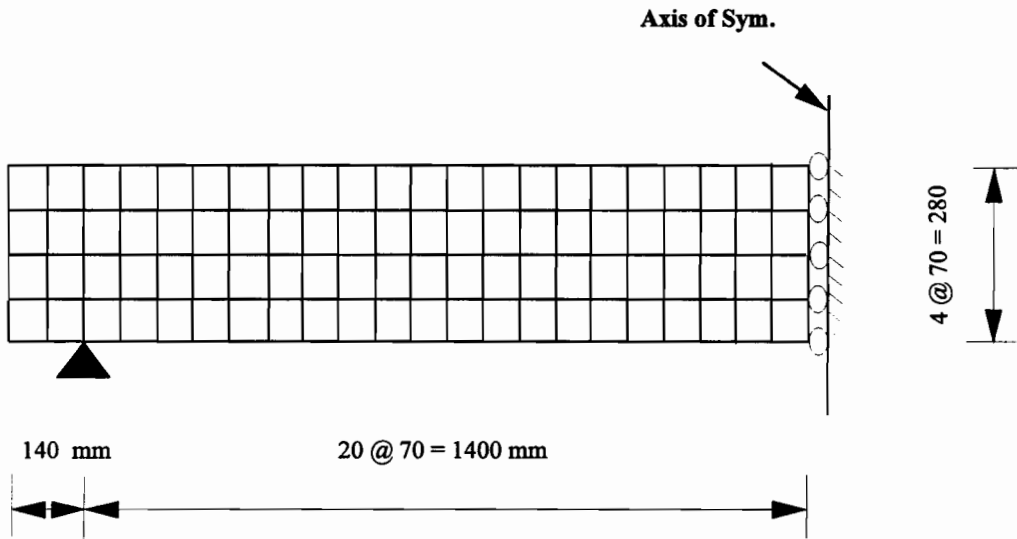


Figure 5.3: Variation of flexural rigidity versus M_a/M_{cr} ratio for beam T2LA



(a) Beam Details



(b) 88-Element mesh Configuration

Figure 5.4: Geometry, reinforcement details and mesh configuration for beam C5

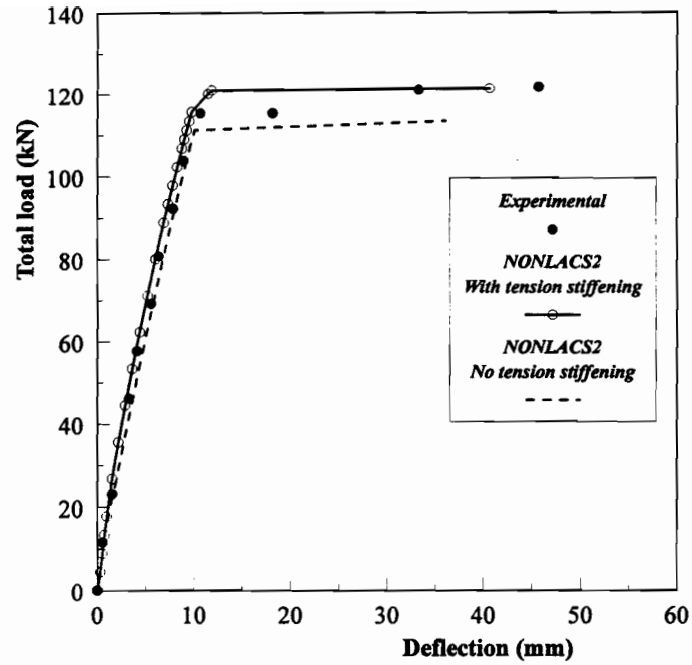


Figure 5.5: Comparison of analytical and experimental load-deflection response of beam C5

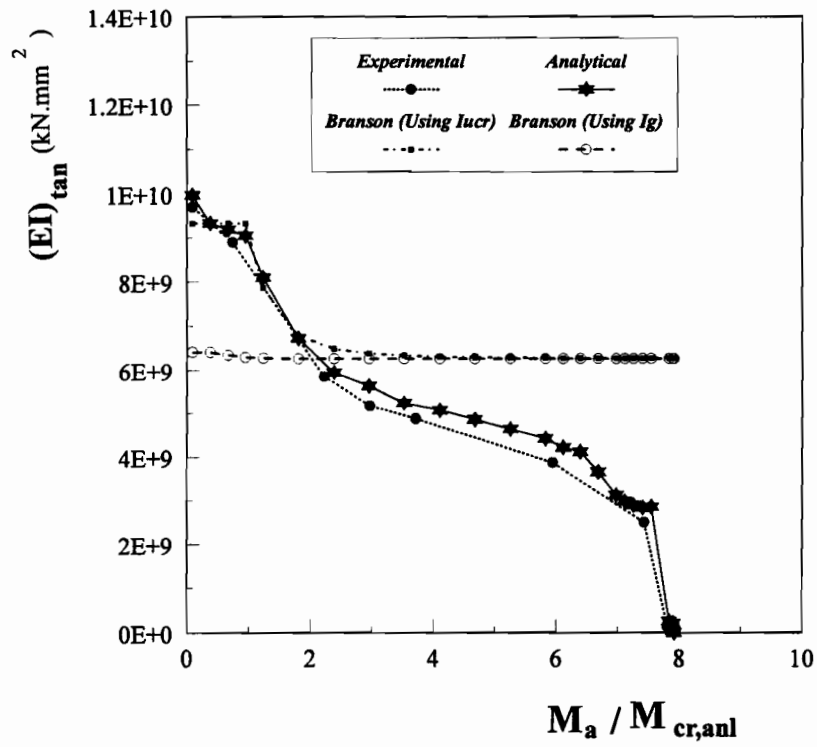
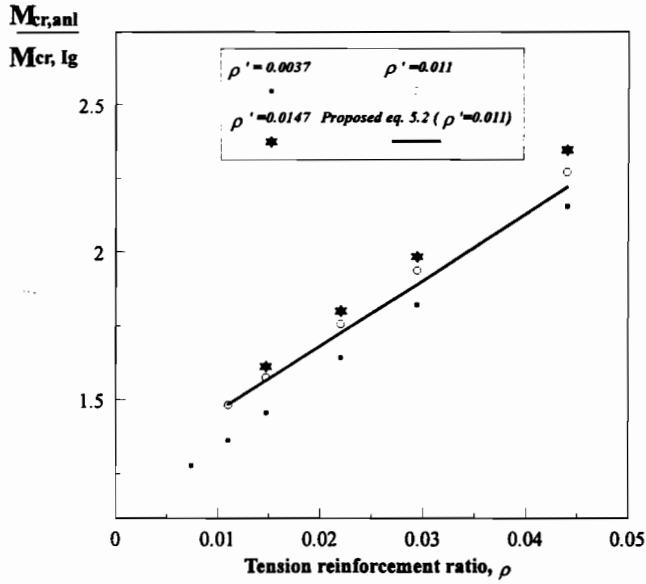
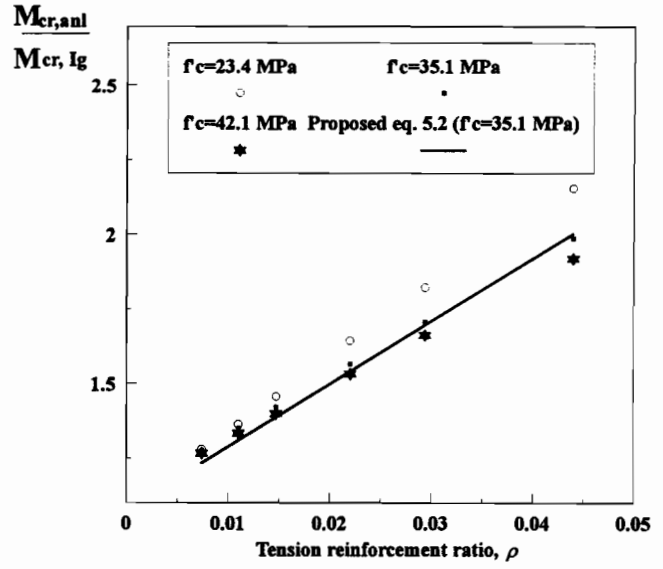


Figure 5.6: Variation of flexural rigidity versus $M_a/M_{cr,anl}$ ratio for beam C5

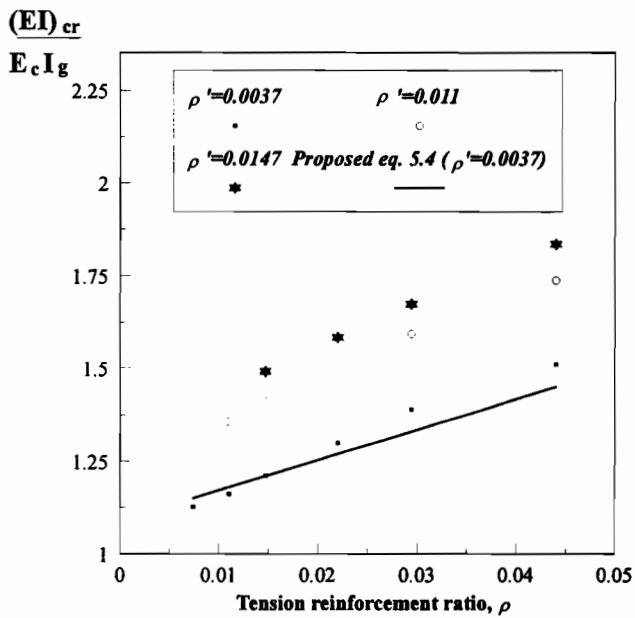


(a)

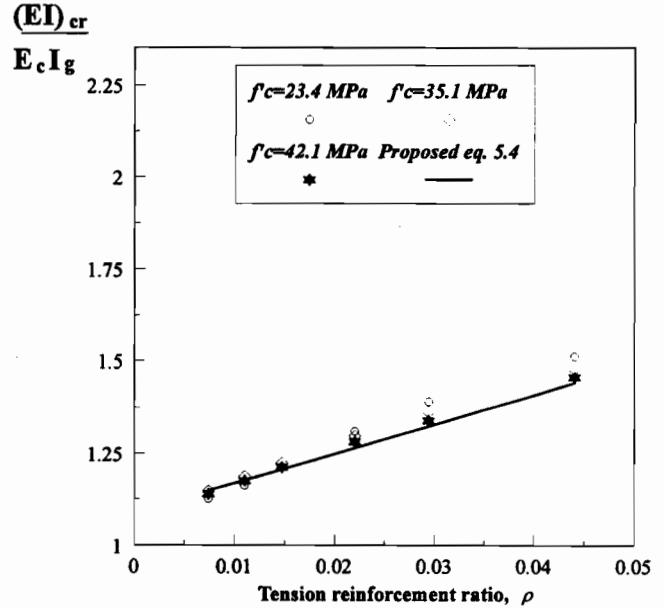


(b)

Figure 5.7: Effect of compression reinforcement and compressive strength of concrete on analytical cracking moment, $M_{cr,anal}$.



(a)



(b)

Figure 5.8: Effect of compression reinforcement and compressive strength of concrete on cracking flexural rigidity, $(EI)_{cr}$.

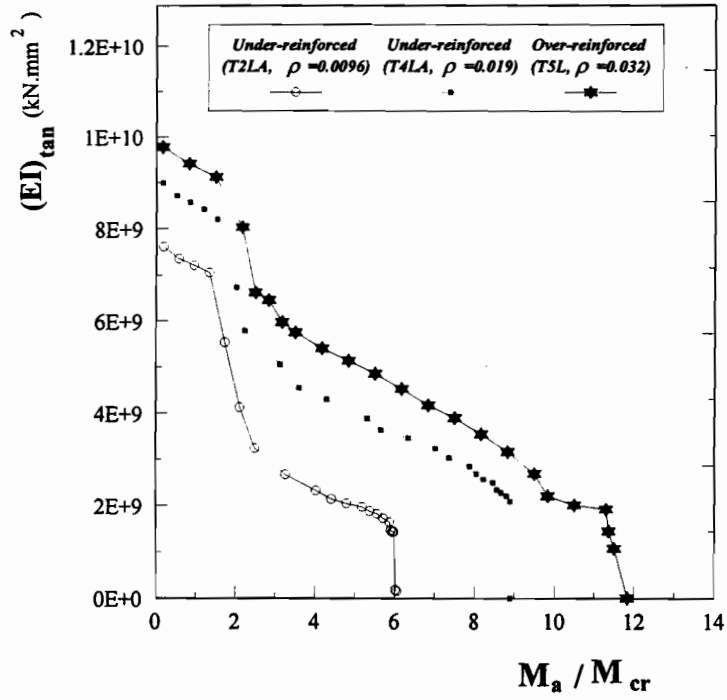


Figure 5.9: Effect of tension reinforcement on flexural rigidity of Gaston beams

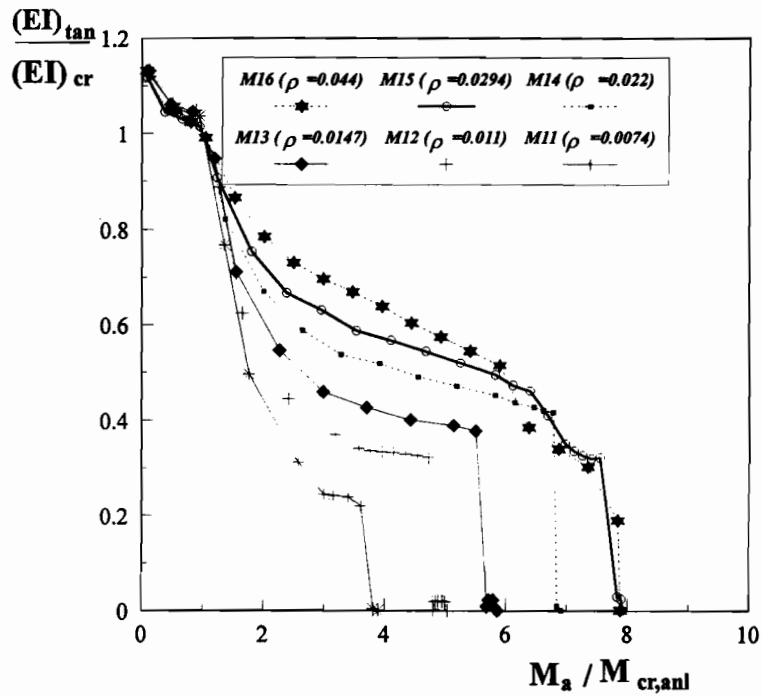


Figure 5.10: Theoretical variation of the flexural rigidity ratio with the level of loading (Mattock beams, Group No. 1)

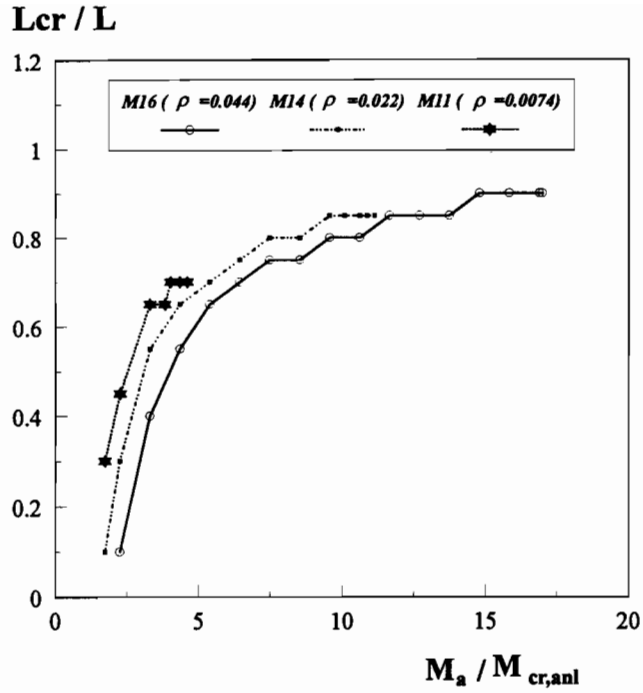


Figure 5.11: Variation of the cracked length ratio with level of loading (Group No.1)

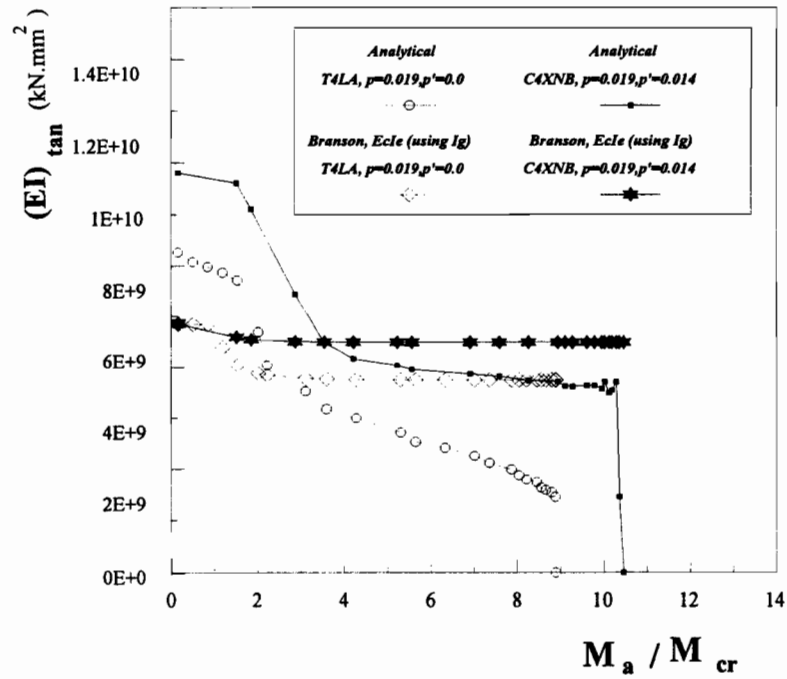


Figure 5.12: Effect of compression reinforcement on flexural rigidity of Gaston beams

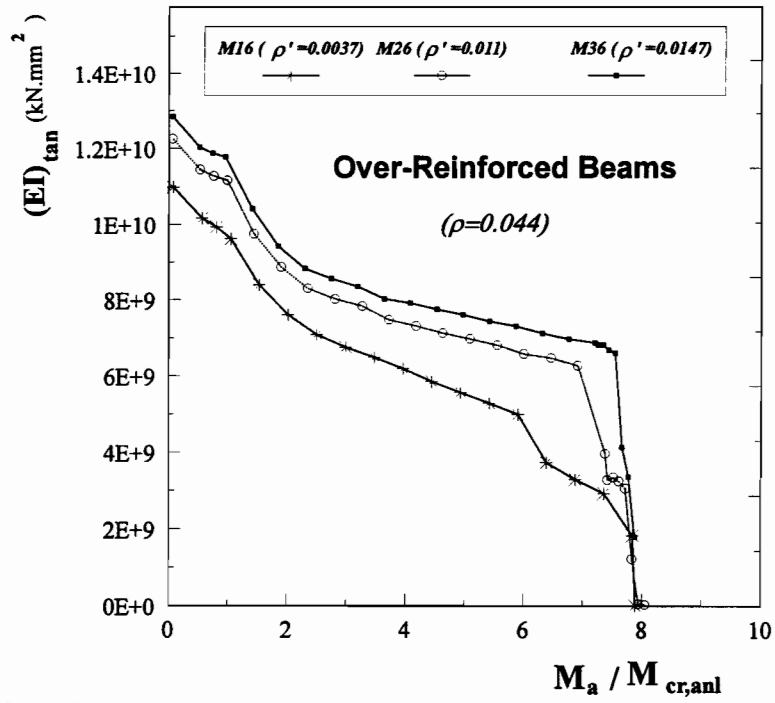


Figure 5.13: Effect of compression reinforcement on flexural rigidity of over-reinforced beams

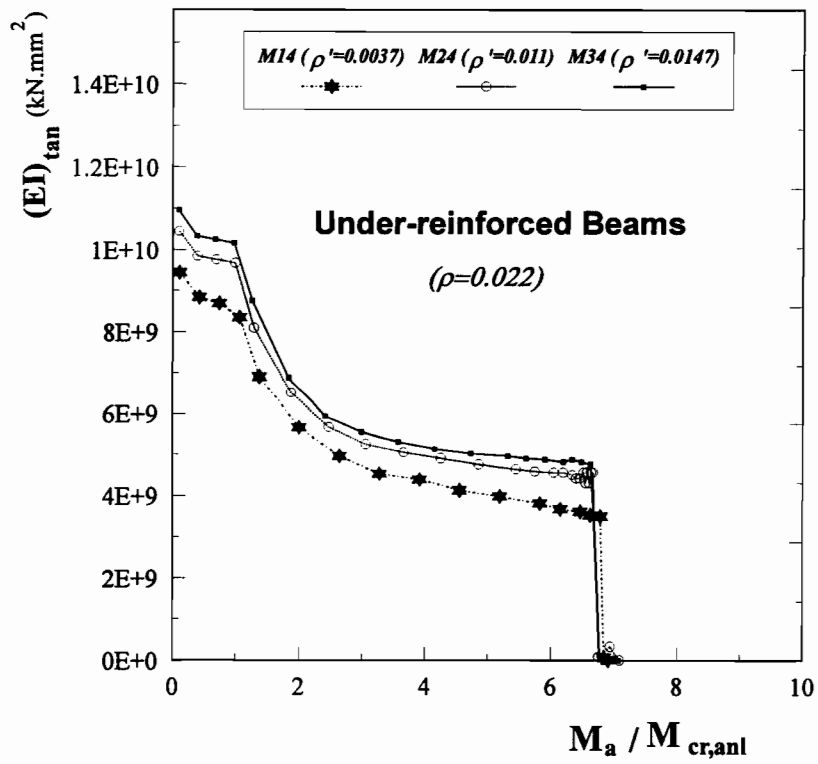


Figure 5.14: Effect of compression reinforcement on flexural rigidity of under-reinforced beams

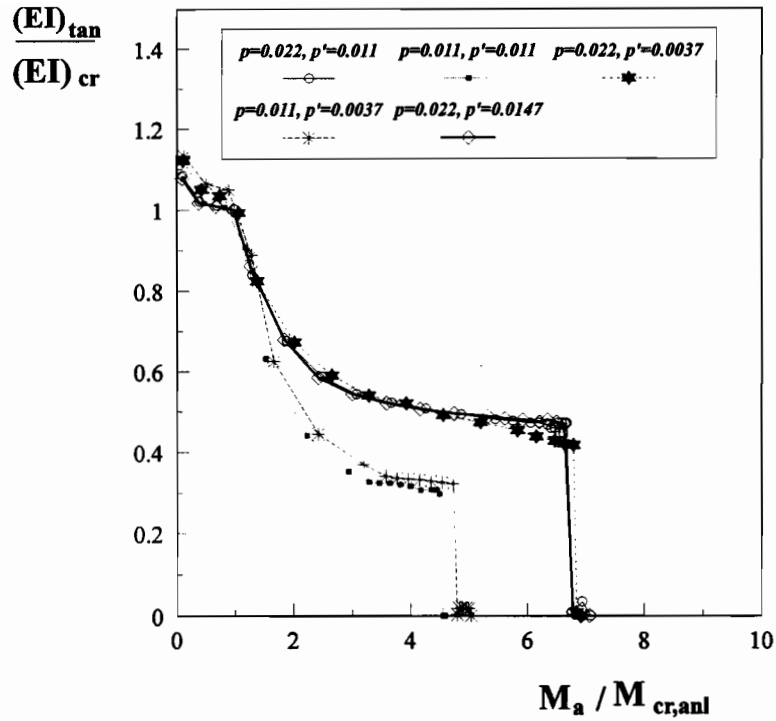


Figure 5.15: Effect of compression reinforcement ratio on the flexural rigidity ratio (Mattock beams, concentrated loads)

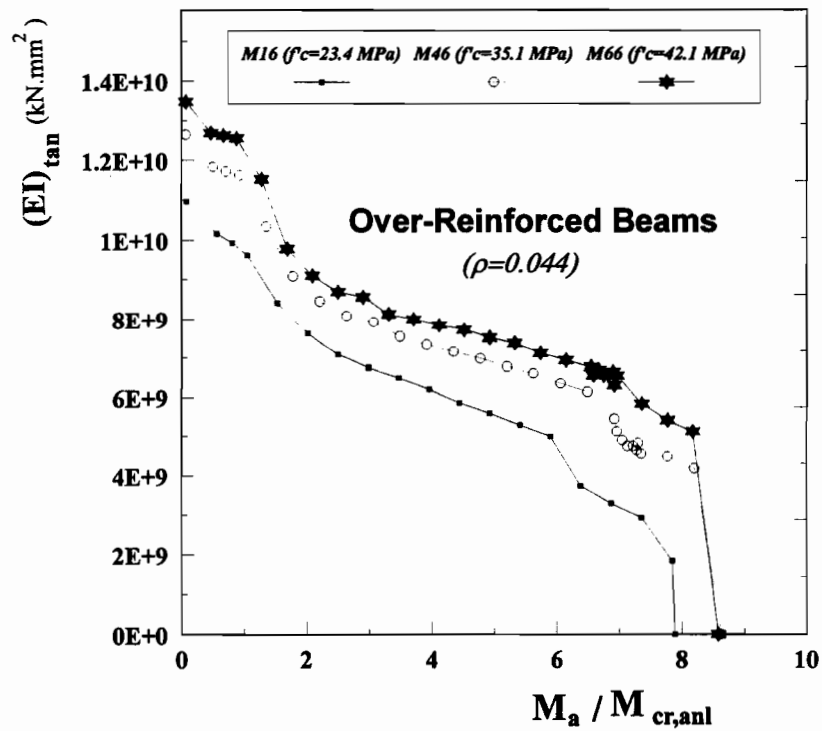


Figure 5.16: Effect of concrete compressive strength on flexural rigidity of over-reinforced beams

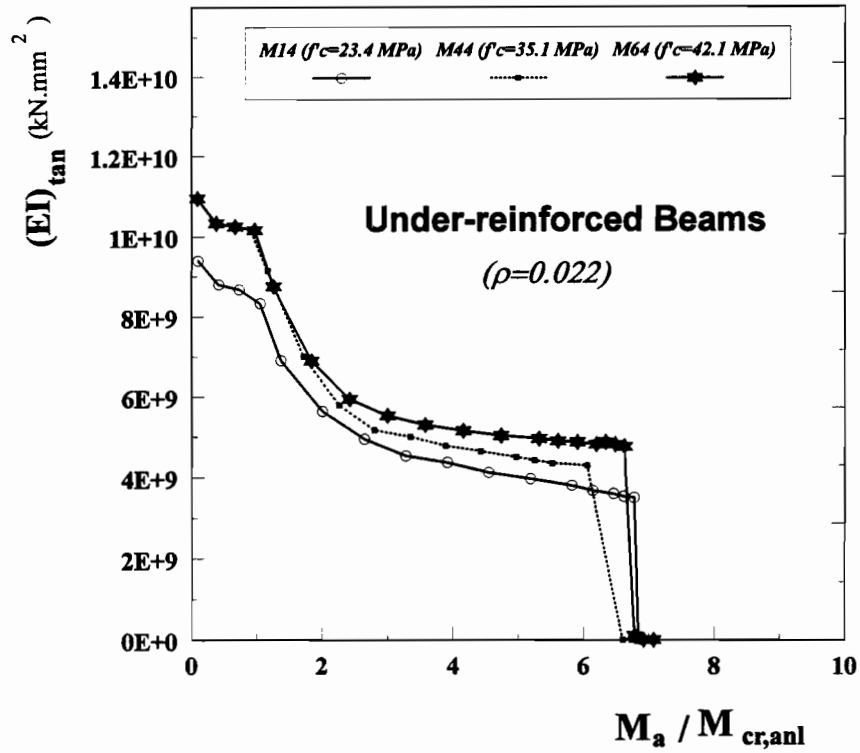


Figure 5.17: Effect of concrete compressive strength on flexural rigidity of under-reinforced beams

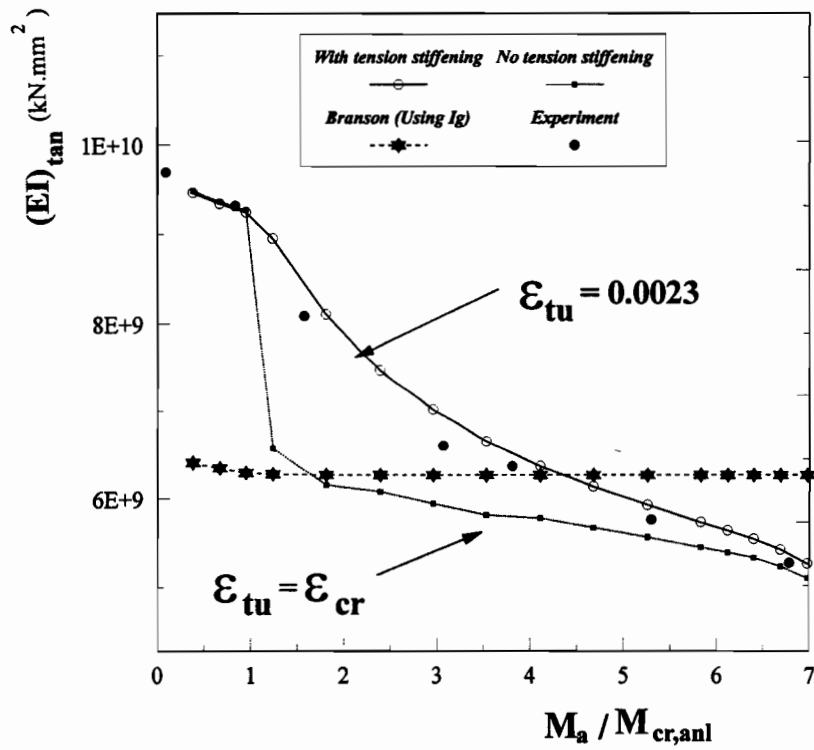


Figure 5.18: Effect of tension stiffening on flexural rigidity of beam C5

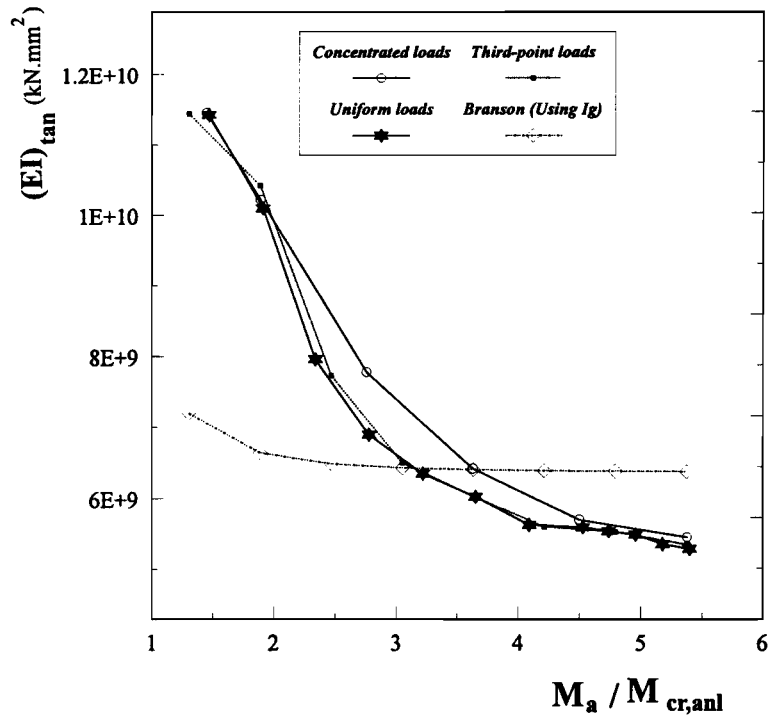


Figure 5.19: Effect of loading type on post-cracking flexural rigidity of beam C3YNA

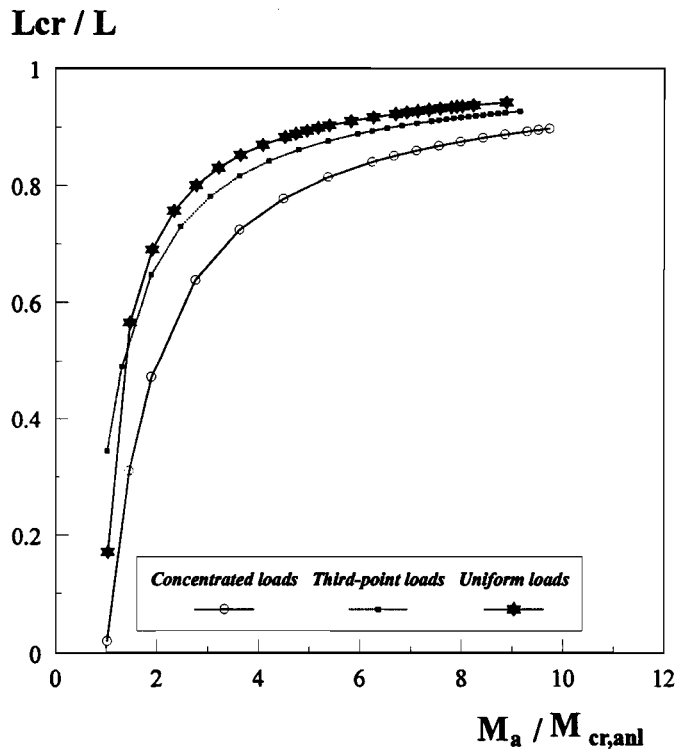


Figure 5.20: Variation of the cracked length ratio with the type of loading, beam C3YNA

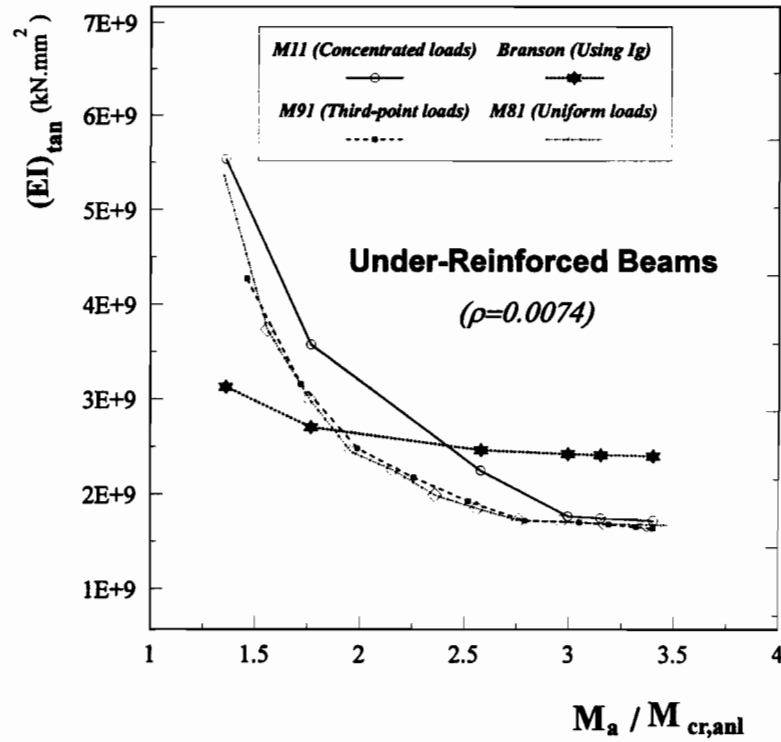


Figure 5.21: Effect of different loading types on flexural rigidity of under-reinforced beams

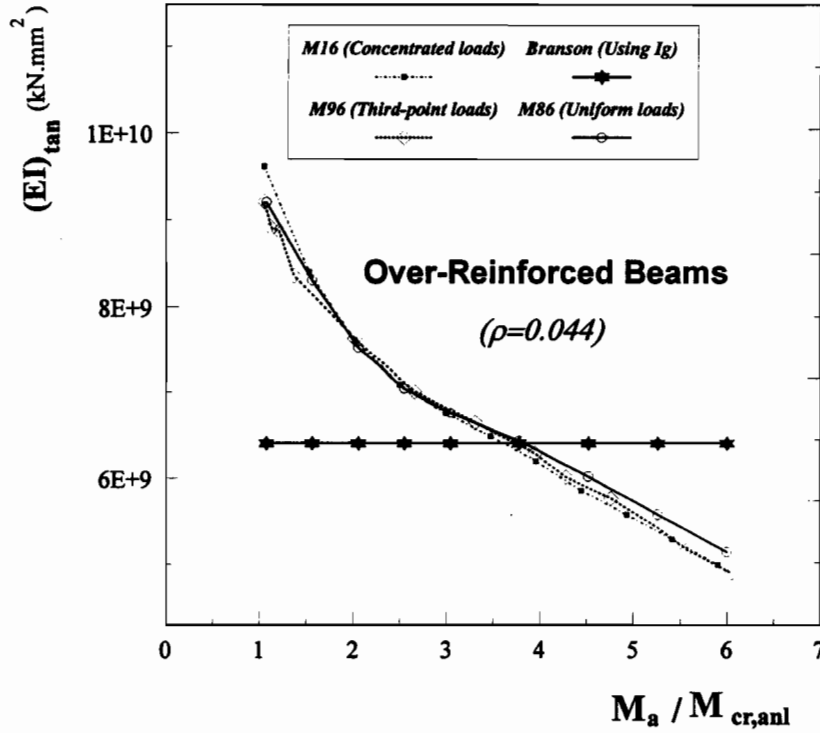


Figure 5.22: Effect of different loading types on flexural rigidity of over-reinforced beams

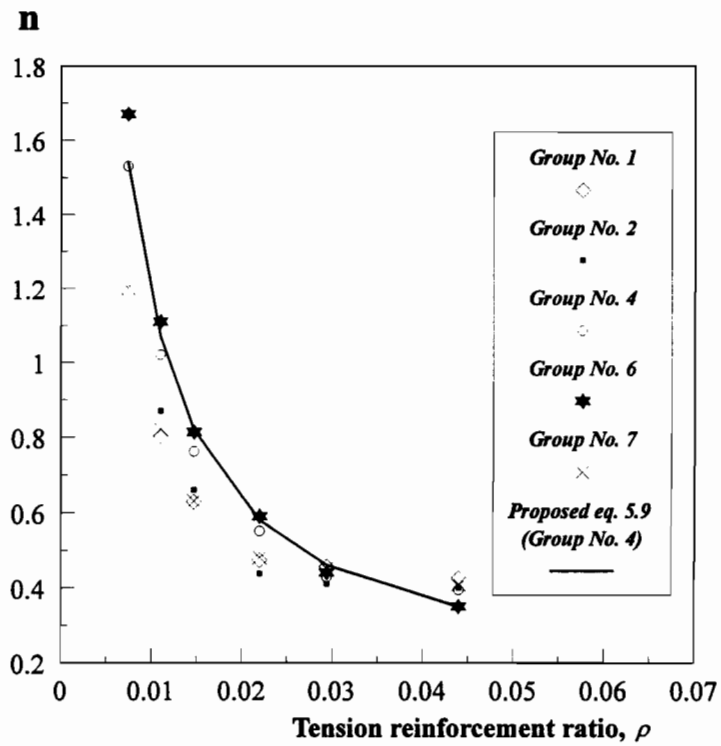


Figure 5.23: Effect of different parameters on the value of "n" for proposed equation

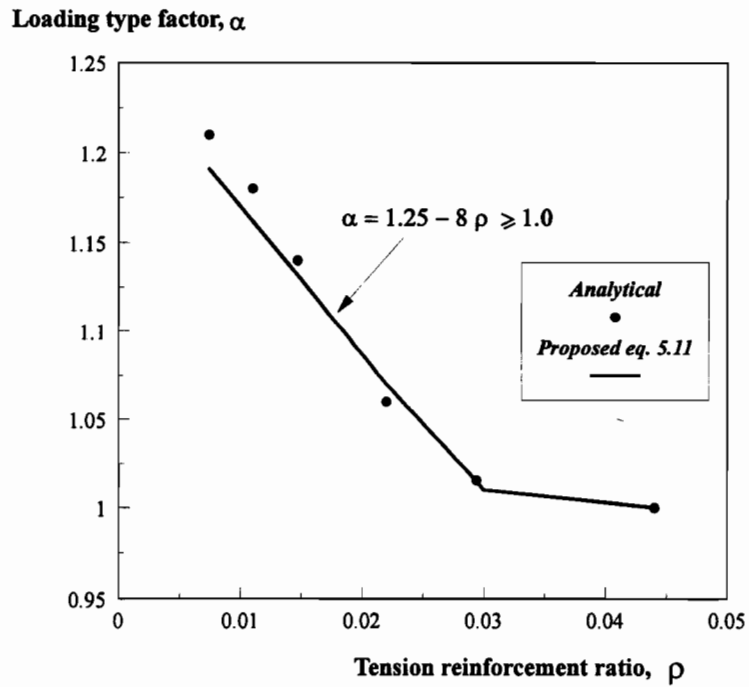
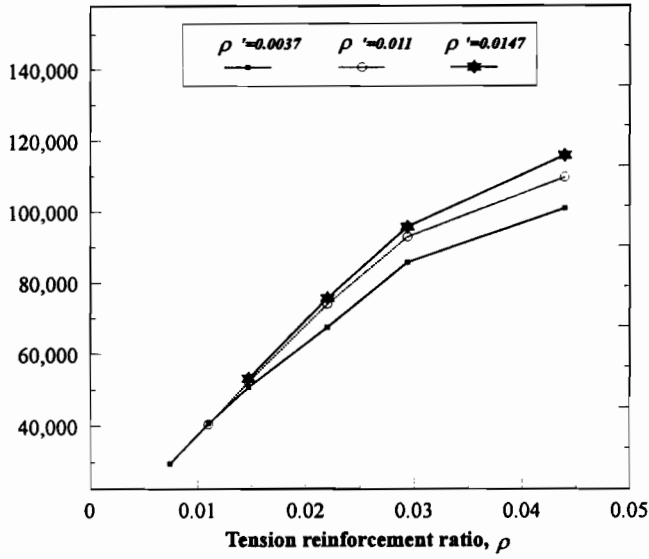
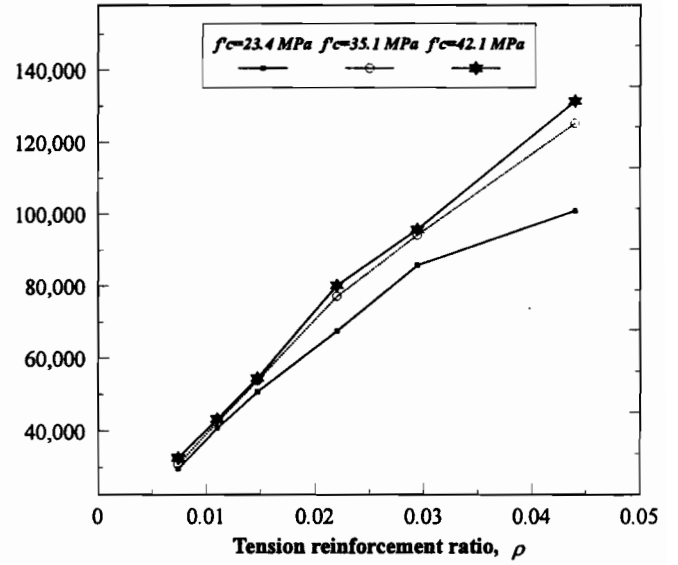


Figure 5.24: Effect of tension reinforcement ratio on the value of "α" for proposed equation

Ultimate moment, M_u (kN.mm)



Ultimate moment, M_u (kN.mm)



(a)

(b)

Figure 5.25: Effect of reinforcement ratios and compressive strength of concrete on ultimate moment for Mattock beams

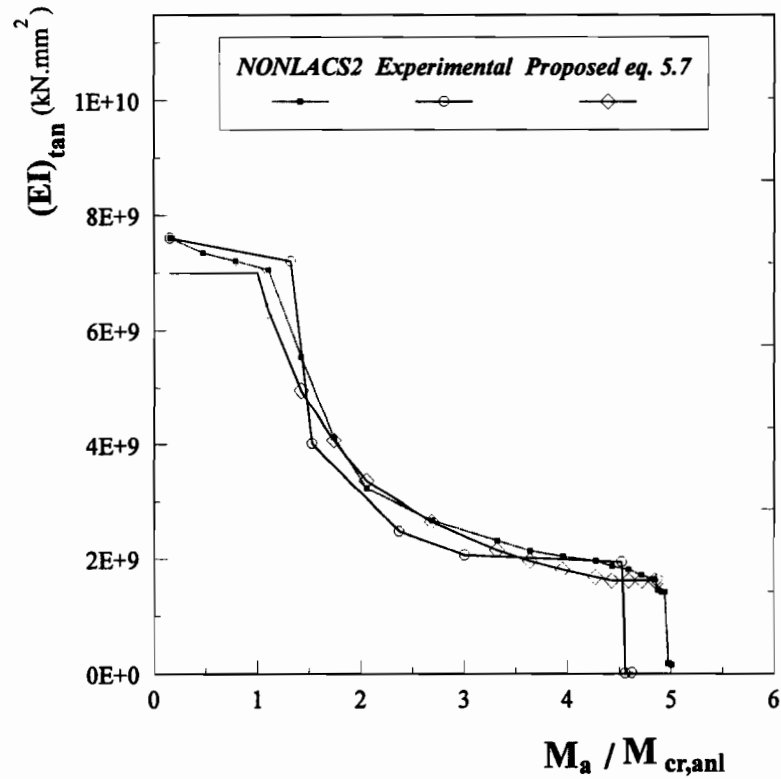


Figure 5.26: Comparison of experimental, analytical, and proposed flexural rigidity for beam T2LA

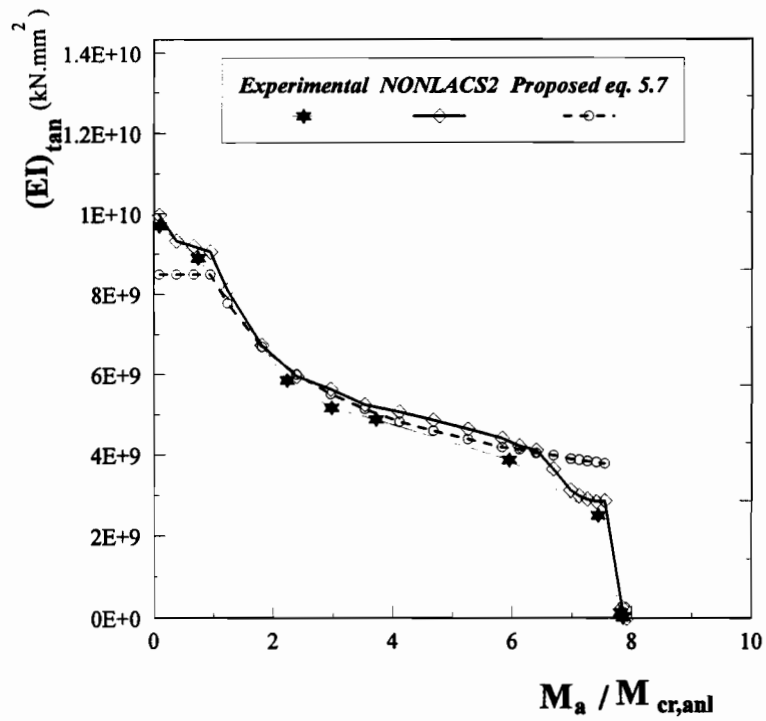


Figure 5.27: Comparison of experimental, analytical, and proposed flexural rigidity for beam C5

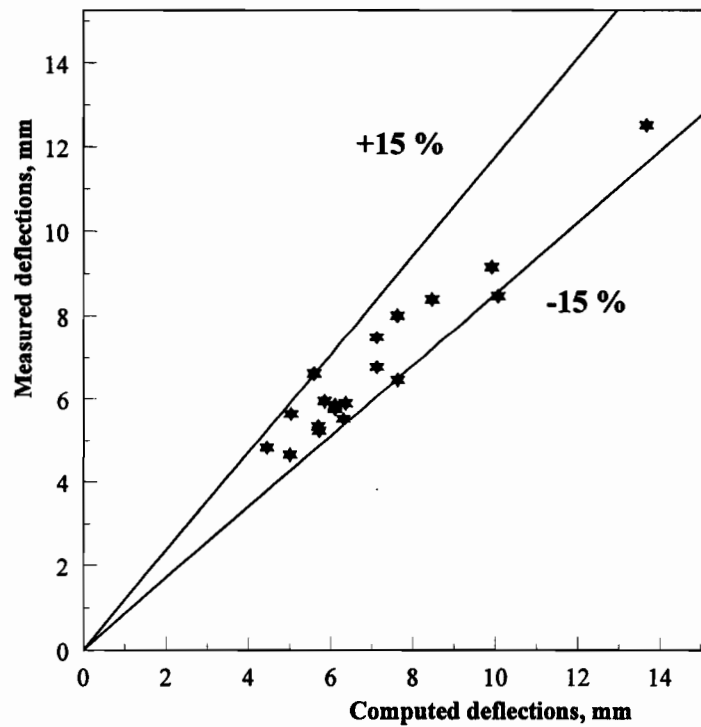


Figure 5.28: Comparison of experimental and computed (proposed model) short-term deflections

CHAPTER 6

ANALYTICAL INVESTIGATION OF PLASTIC HINGE ROTATION CAPACITY

The parameters which influence ductility, plastic hinge rotation and length of R C beams were discussed in Chapter 2. Several investigations concerning this problem have been reported, however, individual authors seem to differ even on the basic definition of what is to be taken as plastic rotation capacity. Some of these contradictions among the various researchers are partly due to the definition of the ultimate limit state, and the different test conditions such as the specimen dimensions, loading plate, and the method of application and type of loads on the beam. The nature and complexities of the problems discussed in Chapter 2 are such that further research is needed to clarify the influence of the different parameters on the plastic hinge rotation, θ_p . A parametric study is performed to assess the influence of tension reinforcement index, ($\omega = \rho f / f_c$), and bending moment distribution (loading type) on the ultimate deformation characteristics of R C beams. The analytical results of 15 simply supported beams with different amounts of tension reinforcement ratio under three different loading conditions are presented and compared with the predictions of the formulations and the experimental data, where available. Based on the analytical results obtained from the NONLACS2 program, new simple equations as a function of the tension reinforcement index, ω , and the loading type are proposed. Attention is focussed on the plastic rotation capacity at the ultimate limit state only.

6.1 FINITE ELEMENT MODELLING, BEAM C5

One simply supported beam, C5, tested by Mattock (1964) is used for the parametric study

(Fig. 5.4a). In order to determine accurate values of yielding length and plastic rotations near the critical section (midspan), a fine mesh configuration with 172 elements is utilized (Fig. 6.1). In other words, nonlinear finite element analysis of selected beams have been carried out using the NONLACS2 program using small elements (35×35 mm) in the neighbourhood of critical section, and progressively increasing to 70×70 mm elements in the neighbourhood of the zero moment location at the support. To evaluate the accuracy of the new model (172-element model), beam C5 is analyzed using the NONLACS2 program. The load-deflection and moment-curvature curves obtained from the program are compared with the experimental findings in Fig. 6.2. Idealization of the beam using 172 elements shows excellent agreement with the experimental results. In this model, the load corresponding to the initiation of crack in the structure is 14.23 kN, when the first crack occurs in the beam. The experimental values of loads for yielding of steel reinforcement and crushing of the concrete at the ultimate load are $P_y=115.29$ kN and $P_u=121.79$ kN, while the analytical yielding and ultimate loads are 118.76 kN and 119.2 kN, with discrepancies of +3 and -2 percent from experimental results, respectively, showing excellent agreement with the experimental results. The analytical yielding and ultimate deflection are 10.95 mm and 40.64 mm with a deviation of -4 and -13 percent from the experimental values of $\Delta_y=11.38$ mm and $\Delta_u=46.74$ mm, respectively. As can be seen from Fig. 6.2b, the analytical moment-curvature curve follows the same general pattern and is quite close to the experimental response. The analytical and experimental yielding and ultimate curvatures for this beam are compared in the following sections.

6.2 INFLUENCE OF TENSION REINFORCEMENT INDEX, ω

For the parametric study, Group Nos. 1, 8, and 9 from Table 5.3 are used. In each group, five under-reinforced beams with tension reinforcement ratios of 0.0294, 0.022, 0.0147, 0.011, and 0.0074 are studied. The corresponding values of tension reinforcement indices, ω , for these beams vary from 0.412 to 0.103 as presented in Table 6.1. Each beam is designated as MijF, where "i" is the group number, "j" indicates the rank of the tension reinforcement ratio in increasing order, and "F" represents the use of fine mesh with 172 elements.

The load-deflection curves obtained from the NONLACS2 program for the beams in Group No. 1, are shown in Fig. 6.3, which presents the results of five under-reinforced beams with different values of ω . The analytical results including the yielding and ultimate deflections and

curvatures, and ductility ratios for these beams are also presented in Table 6.1. The failure mode is flexural for all of the beams, i.e., steel yields first at the bottom at midspan and then the concrete crushes at the top of the beam at midspan. The cracking, yielding and the ultimate loads increase with ω . The yielding deflection increases with an increase in the tension reinforcement index. An increase in ω by about 50 percent increases the yielding deflection by about 18 percent. The ultimate deflection and the deflection ductility ratio, $\mu_{\Delta}=\Delta_u/\Delta_y$, decrease with an increase in the tension reinforcement index. The ultimate deflection for beam M11F with $\omega=0.103$ is 84.3 mm which is 79 percent higher than that the beam M14F with $\omega=0.309$. The deflection ductility ratio varies between 3.71 to 15.1, as ω changes from 0.412 to 0.103.

Table 6.1: Analytical results obtained using the NONLACS2 program (Group No. 1).

Beam	$\rho=\frac{A_s}{bd}$	$\omega=\frac{\rho f_y}{f_c}$	Δ_y (mm)	Δ_u (mm)	$\mu_{\Delta}=\frac{\Delta_u}{\Delta_y}$	ϕ_y (10^{-5} rad/mm)	ϕ_u (10^{-5} rad/mm)	$\mu_{\phi}=\frac{\phi_u}{\phi_y}$	c (mm)	θ_p (rad)	l_y (mm)	l_p (mm)
M15F	0.0294	0.412	10.95	40.64	3.71	1.70	8.27	4.88	102.87	0.013	314.5	197.6
M14F	0.022	0.309	8.84	47.0	5.32	1.54	9.84	6.41	85.1	0.0148	332.7	178.1
M13F	0.0147	0.206	7.49	62.23	8.30	1.30	12.9	9.92	65.53	0.020	349.3	172.7
M12F	0.011	0.154	6.43	69.3	10.8	1.18	16.7	13.83	50.30	0.026	393.7	167.1
M11F	0.0074	0.103	5.59	84.3	15.1	1.02	22.4	21.9	37.08	0.034	402.6	158.8

6.2.1 Yielding Curvature

In reinforced concrete sections, the yielding curvature, ϕ_y , is well defined as a curvature when the tension reinforcement first reaches the yield strength, f_y . Most researchers (e.g. Park and Paulay 1975) used a linear distribution of concrete stress and strain at the yielding stages (see Fig. 6.4). In a more accurate model, a nonlinear (curved) stress distribution should be used at the yielding stage, especially when the concrete compressive stress is high. As can be seen from Fig. 6.4, the value of neutral axis depth, c, calculated assuming a linear distribution of concrete stress is smaller than the "actual" value of the c if the concrete stress distribution is nonlinear, which will lead to an underestimation of the curvature at first yield, ϕ_y , and an overestimation of the curvature ductility ratio, $\mu_{\phi}=\phi_u/\phi_y$. Since the NONLACS2 program considers the nonlinear concrete stress distribution, the yielding curvatures obtained from the program are about 9 to 35 percent

greater than that the model assuming the linear stress distribution. For beam C5 (M15F) with $\omega=0.412$, the analytical yielding curvature is 1.7×10^{-5} rad/mm which is very close to experimental value of 1.57×10^{-5} rad/mm with an 8 percent discrepancy, while the model with a linear stress distribution underestimates the yielding curvature by about 20 percent ($\phi_y=1.26 \times 10^{-5}$ rad/mm). As the tension reinforcement index is increased, the yielding curvature increases and the difference between two models (linear and nonlinear stress distributions) increases.

6.2.2 Ultimate Curvature and Curvature Ductility Ratio

Various definitions of the ultimate limit state adopted by the building codes and the researchers were discussed in Chapter 2 (Section 2.2.4). The ultimate limit state in ACI 318-83 Building Code is based on the assumption of a limiting strain for concrete ($\epsilon_{cu}=0.003$), while in the CEB Model Code it is based on both the steel and concrete ultimate strains ($\epsilon_{cu}=0.0035$, and $\epsilon_{su}=0.01$). The most common definition adopted in the literature is that the ultimate limit state corresponds to the maximum moment capacity of the section (i.e. $\partial M/\partial \phi=0$). In the present study, the ultimate limit state is defined by the failure of structure when the ultimate load capacity of the structure is reached (computational failure of structure). In the NONLACS2 program, two reasons cause a failure in the structure: (1) if any of the norm vector components $\{F_0\}$ exceeds the corresponding maximum force/displacement values input as the divergence values, the solution will be terminated because of excessive unbalanced forces or displacements, and (2) if during a load increment, zero values appear on the main diagonal of the structural stiffness matrix, the equilibrium equations will become singular and the execution will be stopped. No limiting strain is assumed for the concrete in compression and for the steel in tension.

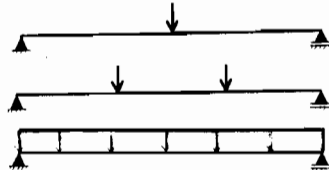

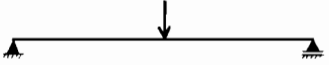


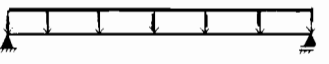

Based on the experimental data reported by Mattock (1964), the concrete ultimate compressive strain, ϵ_{cu} , is selected equal to 0.0078 (as an input value for NONLACS2 program). The most widely used ϵ_{cu} formulations available in the literature are presented in Table 6.2. The values of $\epsilon_{cu}=0.0057$, $\epsilon_{cu}=0.012$, $\epsilon_{cu}=0.00645$, and $\epsilon_{cu}=0.015$ have been adopted from the works of Baker and Amarakone (Table 6.2), Mattock (Table 6.2), Corley (Table 6.2), and Scott et al. (Eq. 2.38).

Figure 6.5 shows the variation of analytical ultimate compressive concrete strain, ϵ_{cu} , at the top and the ultimate tensile steel strain, ϵ_{su} , at the bottom at midspan with respect to ω for beams in Group No. 1. The ultimate compressive strain of concrete is larger than 0.0082 and can be as high as 0.0085. The values of ϵ_{cu} and ϵ_{su} decrease with an increase in the value of ω . It

must be emphasized that the ϵ_{cu} value depends on the various parameters such as transverse and compression reinforcements which are constant in this investigation. Riva and Cohn (1990) arrived at a similar conclusion from their analyses. As can be seen from Baker and Amarakone's equation (Table 6.2), with an increase in tension reinforcement index, the neutral axis depth, c , increases and consequently the value of ϵ_{cu} decreases. All other equations for ϵ_{cu} estimate constant values of ϵ_{cu} regardless of the amount of tension reinforcement index. The ultimate steel tensile strain at the bottom of the beams at midspan, as shown in Fig. 6.5, varies from 0.0115 to 0.049, as the tension reinforcement index changes from 0.412 to 0.103.

The neutral axis depth, c , is determined from the compatibility of the strains at the section. The ultimate curvature is then calculated as the ratio of ultimate concrete compressive strain at the top of beam to the neutral axis depth when the failure of structure occurs, i.e. $\phi_u = \epsilon_{cu}/c$. The influence of the tension reinforcement index on the ultimate curvature and curvature ductility ratio, $\mu_\phi = \phi_u/\phi_y$, for Group No. 1 are shown in Figures 6.6 and 6.7, respectively. For comparison, the ultimate curvatures obtained using NONLACS2 program, Mattock's equation (Table 6.2), Corley's equation (Table 6.2) and ACI method are presented. The neutral axis depth for each method is calculated based on its own assumptions. For a given z/d ratio, the ultimate curvature decreases with an increase in the tension reinforcement index. According to equation 2.35, the curvature is inversely proportional to the depth of the neutral axis, c , which varies directly as the tension reinforcement index at the ultimate limit state. The analytical results are about 2.35, 1.31, and 0.84 times the values obtained from ACI, Corley's, and Mattock's methods, respectively. The ACI 318-83 Building Code predicts the ultimate curvature very conservatively as compared with the other methods. Although the ultimate concrete compressive strain value, $\epsilon_{cu}=0.003$, is satisfactory for ultimate strength design, it is very conservative for deformation analysis. Mattock's method overestimates the ultimate curvature compared with the analytical results, because the concrete ultimate compressive strain determined by Mattock's equation (Table 6.2) is about 54 percent greater than the analytical concrete compressive strain value. The analytical curve shows good agreement with the curve obtained using Corley's method. For beam C5 (M15F), the value of ϕ_u using NONLACS2 program is equal to 8.3×10^{-5} rad/mm, while the ACI, Corley's, and Mattock's methods result the values of 2.4×10^{-5} rad/mm, 5.5×10^{-5} rad/mm, and 9.3×10^{-5} rad/mm, respectively. The experimental value of the ultimate curvature for this beam as reported by Mattock (1964) is equal to 11.8×10^{-5} rad/mm, respectively.

Table 6.2: Comparison of existing ϵ_{cu} and θ_p formulations (θ_p is the plastic rotation on one side of section).

Author	Loading type	Expression for θ_p
Present study (Kheyroddin and Mirza)		$\theta_p = \int_0^{l_p} [\Phi(x) - \Phi_y] dx$
Baker and Amarakone (1964)		$\theta_p = 0.8 (\epsilon_{cu} - \epsilon_{cy}) k_1 k_3 \left(\frac{z}{d}\right) \quad (k_1 k_3 = 0.5)$ $\epsilon_{cu} = 0.0015 [1 + 150 \rho_s + (0.7 - 10 \rho_s) \frac{d}{c}]$
Mattock (1964)		$\theta_p = (\phi_u - \phi_y \frac{M_u}{M_y}) (1 + (1.14 \sqrt{\frac{z}{d}} - 1) (1 - (\frac{\omega - \omega'}{\omega_b}) \sqrt{\frac{d}{16.2}})) \frac{d}{2}$ $\epsilon_{cu} = 0.003 + \frac{0.5}{z}$
Corley (1966)		$\theta_p = (\phi_u - \phi_y \frac{M_u}{M_y}) (1 + \frac{0.4}{\sqrt{d}} \frac{z}{d}) (\frac{d}{2})$ $\epsilon_{cu} = 0.003 + 0.02 \frac{b}{z} + (\frac{\rho_s f_y}{20})^2$
Riva and Cohn (1990)		For $\frac{\phi_{pu}}{\phi_{py}} \leq 7.0$: $\theta_p = (0.39 - \frac{7.0}{800 \omega}) (\frac{\phi_{pu}}{\phi_{py}})^{-0.9} \phi_{pu} z$ For $\frac{\phi_{pu}}{\phi_{py}} > 7.0$: $\theta_p = (\frac{5.4}{100}) \phi_{pu} z$
		For $\frac{\phi_{pu}}{\phi_{py}} \leq 7.0$: $\theta_p = (0.58 - \frac{3.0}{800 \omega}) (\frac{\phi_{pu}}{\phi_{py}})^{-0.9} \phi_{pu} z$ For $\frac{\phi_{pu}}{\phi_{py}} > 7.0$: $\theta_p = (\frac{5.0}{100} + \frac{6.5}{1000} \frac{\phi_{pu}}{\phi_{py}}) \phi_{pu} z$
CEB-FIP MC90 (1991)		Figure 3.7.2 from CEB-FIP Model Code 1990 (No. 203)

As can be seen from Fig. 6.7, the curvature ductility ratio varies from 4.88 to 21.9, when the value of ω changes from 0.412 to 0.1. This figure shows that the curvature ductility ratios for the various methods are distributed in the same manner as the ultimate curvatures calculated using the same methods. This was expected because the yield curvature is about the same for all of the methods. The ACI Code underestimates the curvature ductility ratio (up to 2.5 times) compared with the analytical results. For beam C5 (M15F), the analytical, ACI, Corley's, and Mattock's methods have discrepancies of -36, -75, 44, and -5 percent from the experimental value of $\mu_\phi=7.65$.

6.2.3 Plastic Hinge Rotation and Length

A survey of the literature shows that most researchers first calculate the equivalent plastic hinge length, l_p , and then the plastic rotation, θ_p , is determined using equation 2.32. But in the present study, at first the plastic rotation is determined and then the equivalent plastic hinge length is derived only for comparison. The advantage of the present study is that the yielding length and the "exact" value of plastic rotation (shaded area in Fig. 6.8b) can be determined without using the idea of equivalent plastic hinge length. Figure 6.8 illustrates how to determine the analytical plastic rotation and the equivalent plastic hinge length for beam M13F. First, the curvature along the beam is obtained from the concrete strain in the compression zone and from the steel strain in tension zone at the ultimate state. Then, the plastic rotation, θ_p , is obtained by integration, along the yielding length, l_y (where the curvature in the section is higher than its yielding curvature, ϕ_y), of the difference between the ultimate curvature and the yielding curvature (Table 6.2). Here, θ_p refers to the plastic hinge rotation on one side of the critical section. Finally, the equivalent plastic hinge length, l_p , can be calculated as shown in Fig. 6.8b.

The failure mechanism of beam M13F including cracking of the concrete (solid lines) and its crushing (small circles) is shown in Fig. 6.8a. The crushing of the concrete is concentrated at the top near the midspan or the critical section where the spread of inelasticity starts. The curvature increases linearly from the support to the yielding point and then the curvature suddenly increases and in the crushing region, it is very close to the ultimate curvature.

The variation of the curvature along the length of beam for two different values of ω (beams M12F and M15F) is compared in Fig. 6.9. Generally, in the elastic region (before yielding), the beam with a lower value of ω has a smaller curvature, and in the yielding zone, the curvatures in the beam with lower value of ω are larger than that for the beam with higher values

of ω . The spread of plasticity (yielding length), ultimate curvature and consequently the plastic rotation for the lightly reinforced beam (M12F) are greater than that for heavily reinforced beam (M15F). Comparison of the beams M12F and M15F indicates that an increase in ω by about 2.68 times decreases the yielding length and the plastic rotation by about 20 percent and 50 percent, respectively (Table 6.1).

A comparison of the analytical plastic rotation obtained from the NONLACS2 program with some models available in the literature is made here. The most widely used θ_p formulations in Europe and North America along with the formula used in the present study are presented in Table 6.2. The plastic rotations for the beams in Group No. 1 with $z/d=5.5$ using the NONLACS2, CEB-FIP MC90, Baker and Amarakone's, Corley's, Mattock's and Riva and Cohn's methods are plotted in Fig. 6.10. Since the CEB, Corley, Mattock and Baker and Amarakone expressions in Table 6.2 are based on experiments mostly characterized by $z/d \approx 5.0$, and Riva and Cohn expression is valid for any z/d values, therefore a comparison among these models is reasonable. It is noted that the plastic hinge rotation obtained from Riva and Cohn's model (Table 6.2) is the total inelastic rotation from the onset of inelastic behaviour i.e. cracking of concrete. This method is useful especially for prestressed concrete structures. For all of the other methods including the present study, the plastic hinge rotation is defined as the rotation between the yielding and ultimate states. The parameters ϕ_{pu} and ϕ_{py} in Riva and Cohn's formula are measured from the onset of cracking (ϕ_{cr}) and are determined using the NONLACS2 results. Compared with CEB-FIP MC90, the analytical results and Corley's theory are found to give safe values except in one case ($\omega=0.1$) and yet they are not as conservative as Baker and Amarakone's and Riva and Cohn's formulations. For ω values greater than 0.15, the analytical results are close to the values obtained from CEB-FIP MC 90. The first branch of the CEB-FIP MC90 curve with a positive slope represents the failure of the tension reinforcement, and the second branch, with negative slope, indicates failure through the crushing of the concrete. The plastic rotation capacity predicted by the formula given by Riva and Cohn appear to represent a fairly safe estimate of the actual rotation capacities available up to the maximum load. Mattock's equation give much higher values of plastic rotation compared with any other models considered. This indicates that the expression given by Mattock for calculation of ϵ_{cu} tends to overestimate the deformability of R C sections. For beam C5 (M15F), the experimental plastic hinge rotation is 0.0249 rad, while the present study results in a value of 0.013 rad. The CEB, Baker and Amarakone's, Corley's, Mattock's and Riva and Cohn's methods predict plastic hinge rotation values of 0.0072 rad, 0.0035 rad, 0.0092

rad, 0.017 rad, and 0.0098 rad, respectively.

The above comparison indicates that the experimental value is much higher than any other models considered. The experimental plastic rotation as reported by Mattock (1964) was obtained from the measured inelastic deflection, δ_p , at midspan. The plastic rotation was assumed to be concentrated at the point of the maximum moment, and was equal to $\tan^{-1} (\delta_p/z)$. In fact, this assumption overestimated the plastic rotation and is independent of the shape of the bending moment diagram. In other words, if it were to be assumed that the behaviour at the critical section is representative of the behaviour of the member as a whole, this would overestimate the ultimate deformations. Comparison of Mattock's experimental results with the experimental work of other researchers as shown in Fig. 2.7 (Siviero 1974) corroborates the finding that Mattock's method results in much higher plastic rotations. The scatter of the results may be explained mainly by the fact that the various authors measured the plastic rotation of the specimen in different ways.

After calculation of the plastic hinge rotation, the analytical equivalent plastic length, l_p , on one side of critical section can be determined. As mentioned earlier, this value is obtained only for comparison with other available methods. As can be seen from Table 6.1 and Fig. 6.11, the analytical value of l_p is not constant for the different values of the tension reinforcement indices. It increases linearly from 158.8 mm to 197.6 mm, as the value of ω changes from 0.103 to 0.412. The average value of the analytical plastic hinge length l_p is 174.9 mm, which is 69 percent of effective depth (0.69 d). Baker's previous method (Eq. 2.39) gives a constant value of l_p equal to 194.5 mm (0.77 d) for different amounts of ω , while in the new equation proposed by Baker and Amarakone (Eq. 2.40), l_p increases linearly with the c/d ratio. Riva and Cohn's formulation result in the lowest values of plastic hinge length and approximately the same pattern as the analytical curve (Fig. 6.11). The Corley's, Mattock's, and Sawyer's theories give a constant plastic hinge length regardless the reinforcement index, of 215.4 mm (0.85 d), 196.9 mm (0.78 d), and 168.2 mm (0.66 d), respectively. Based on the above discussion, it can be concluded that the rotation capacity of the plastic hinges in R C beams can be predicted using NONLACS2 program with sufficient accuracy.

6.3 INFLUENCE OF BENDING MOMENT DISTRIBUTION (LOADING TYPE)

In order to study the effect of the loading type, three loading conditions are considered: (1) concentrated load at midspan (linear moment distribution) to achieve a rapid moment variation

as is observed at the supports in continuous beams, (2) third-point loading (linear moment distribution from support to location of the load and a constant moment between two loads), and (3) uniformly distributed loading (nonlinear moment distribution). The influence of the bending moment distribution on the plastic rotation for Group Nos. 1, 8, and 9 is shown in Fig. 6.12. For these groups, all of the variables are the same, and the only difference is in the type of loading. The plastic rotation increases going from the concentrated load, to the third-point loading, and it is a maximum for the case of uniform load. The plastic hinge rotation for beams subjected to uniform loads are always greater than that for the same beams under third-point loadings or concentrated load.

As can be seen from Fig. 6.12, θ_p values for the beam subjected to third-point loading are larger than that for the beam loaded at midspan, when the value of ω is less than 0.38. Beyond $\omega=0.38$, the value of θ_p for third-point loaded beam tends to be slightly less than the corresponding values for the beam loaded at midspan. In fact, the plastic rotation for the third-point loading depends on the length of constant moment region and localization of the plastic zone and crushing of the concrete within a narrow area. This phenomenon will be explained latter. Bosco et al. (1990) compared the plastic hinge rotations of simply supported beams under two different loading conditions: (1) three loads applied symmetrically with respect to the midspan, and (2) midspan concentrated load. They arrived at the same conclusion as in the present study. The plastic hinge rotations of lightly reinforced beams under three point loads were higher than that the beams loaded under central loads, while in the heavily reinforced beams, the plastic hinge of concentrated loaded beams were greater.

For two extreme values of ω , the effect of loading type is discussed. For beam with $\omega=0.103$, uniformly distributed loads on a simply supported beam lead to θ_p values varying from 1.90 to 1.35 times as high as those corresponding to the beams loaded with a midspan concentrated load or a third-point loading on the same beam, respectively. These ratios for the heavily reinforced beam with $\omega=0.412$ are 1.59 and 0.88. Thus it can be concluded that the effect of the loading type on the plastic rotation capacity of heavily reinforced beams is not as significant as for the lightly reinforced beams. For beam M81F ($\omega=0.412$), Riva and Cohn's formula (Table 6.2, for uniform loads) predicts the plastic hinge rotation equal to 0.064 rad, which is very close to the analytical value of 0.070 rad.

The variation of θ_p values for the differently loaded beams can be explained by the differences in the bending moment diagram and the yielding length, l_y , for each type of loading.

Figure 6.13 shows that, with the same tension reinforcement index, the yielding length of the beam under a central load is less than that under a uniform or third-point loads, leading to a smaller plastic rotation. Beams under uniform load show a considerable increase in the yielding length and the zone of plasticity. This is due to the smaller moment gradient (nonlinear moment distribution) in the neighbourhood of the critical section.

On the other hand, the bending moment distribution will also influence the distribution of curvature along the length of the beam. Figure 6.14 shows the variation of curvature over half length of beams with $\omega=0.412$ subjected to different loading types. Although the yielding length for the beam subjected to third-point loading is higher than that for the beams subjected to uniform and concentrated loads, localization of the plastic zone and the crushing of concrete, cause a smaller value of θ_p even less than that the beam subjected to concentrated load. Figure 6.15 shows the effect of loading type on the failure mechanism of the beam with $\omega=0.412$. As can be seen from Figures 6.14 and 6.15c, in the beam M95F under third-point loadings, plasticization and crushing of concrete occur over a small length and do not spread along the length of the constant moment region. In fact, at some sections (usually in tests it is under one of loading points but ideally it should be at midspan), additional cracking and crushing of concrete take place and the plastic zone get concentrated in this region. The spread of plasticity (larger difference between the ultimate and the yielding curvatures) increases with a decrease in the tension reinforcement index, and it leads to a greater value of plastic hinge rotation. With the same amount of compression reinforcement for different beams, the ratio of ρ'/ρ is larger for the lightly reinforced beam. Therefore, the confinement due to compression reinforcement is higher for the lightly reinforced beam, which stabilizes the inelastic deformation and permits its to spread along a longer region or the entire zone of constant moment, rather than allowing the damage to be localized within a narrow area.

Bertero and Felippa (1964) figured out that in the case of beams (subjected to third-point loadings) without transverse and compression reinforcement, inelastic rotation was concentrated in one small region where the length was smaller than the effective depth. When the transverse and compression reinforcements were used, the inelastic deformations spread over the longer length and with an increase in the confinement of the concrete, the plastic hinge zone spread over whole region subjected to constant moment.

Figure 6.15 reveals that the crack patterns and crushing of the concrete are different for the different loading types and are influenced considerably by the loading pattern. With the same

value of ω , the concrete crushing zone in neighbourhood of critical section is larger for the beam subjected to uniform loads, while the beam loaded at midspan has the shortest crushing zone. The progress of cracks along the length of the beam and the crushing zone of the concrete is higher for the beam subjected to uniform load, leading to a larger plastic hinge rotation.

The variation of the analytical equivalent plastic hinge length for Group Nos 1, 8, and 9 with the tension reinforcement index, ω , are plotted in Fig. 6.16. The beams in Group No. 8 (subjected to uniform loads) have much higher plastic hinge lengths with an average value of 310.3 mm (1.22 d). The plastic hinge length for beams in Group No. 9 (third-point loadings) decreases as tension reinforcement index increases. The average value of plastic hinge length for this group is 208.1 (0.82 d), which is 19 percent higher than for the Group No. 1 (concentrated loaded beams) and 33 percent smaller than that the Group No. 8 (uniformly loaded beams). Although it has become common practice to use the terms "plastic hinge" and "critical section" or concentration of plastic rotations in critical sections, the properties of the plastic hinge are not the properties of individual critical sections. As shown here, the loading type has a significant effect on the plastic hinge rotation and length, and the assumption of a constant plastic hinge length implies that the effects of the structural layout, magnitude and the type of load on the inelastic rotation have been neglected.

6.3.1 Proposed Equations

The relationship between three different loading types at the ultimate load stage can be defined as:

$$\alpha_{u(Unif.)} = \frac{\theta_{p(Unif.)}}{\theta_{p(Conc.)}} = \frac{l_{p(Unif.)}}{l_{p(Conc.)}} \quad (6.1)$$

$$\alpha_{u(Thrd.)} = \frac{\theta_{p(Thrd.)}}{\theta_{p(Conc.)}} = \frac{l_{p(Thrd.)}}{l_{p(Conc.)}}$$

where α_u is the loading type factor at the ultimate load stage. Variation of α_u with respect to the tension reinforcement index is shown in Fig. 6.17. Regression analysis of the results of the parametric study shows that the loading type factor can be expressed in term of the tension reinforcement index:

For uniform loads:

$$\alpha_{u(Unif.)} = (2.0 - \omega) \quad (6.2)$$

For third-point loadings:

$$\alpha_u (Thrd.) = 1.5 (1 - \omega) \quad (6.3)$$

The analytical values of the plastic hinge rotations obtained from NONLACS2 program, $\theta_p (anl.)$, and the values estimated using equations 6.2 and 6.3, $\theta_p (est.)$, are compared in Table 6.3. The comparison is based on the relative error which is defined as:

$$ERR = \frac{\theta_p (est.) - \theta_p (anl.)}{\theta_p (anl.)} \quad (6.4)$$

The maximum error between analytical and estimated values is 9.76 percent. The average value of the ratios of the proposed - to - analytical value of plastic rotations for beam subjected to uniform loads is found to be 0.991 with a standard deviation of 0.0486. The average value and the standard deviation for the proposed - to - analytical plastic rotations ratio for beam under third-point loadings are 0.965 and 0.0485, respectively. This indicates that the proposed equation predictions are in good agreement with the analytical results as shown in Fig. 6.17. As a final remark, it is worth nothing that the reinforcement index and the type of loading are important factors to be considered in evaluating the rotation capacity of plastic hinges. The proposed equations can be used in any limit design method to evaluate the plastic hinge rotations and other deformation characteristics at the ultimate load when the statically indeterminate just becomes a collapse mechanism.

Table 6.3: Analytical and estimated values of plastic rotation, θ_p (rad), for different loading types.

$\omega = \rho f_y / f_c$	Group No. 1 (Concentrated loads)	Group No. 8 (Uniform loads)			Group No. 9 (Third-point loadings)		
	NONLACS2	NONLACS2	Estimated (Eq. 6.2)	ERR %	NONLACS2	Estimated (Eq. 6.3)	ERR %
0.412	0.013	0.021	0.0206	-1.90	0.011	0.0114	3.63
0.309	0.0148	0.0245	0.025	2.04	0.017	0.0153	-9.76
0.206	0.020	0.034	0.0359	5.59	0.025	0.024	-4.0
0.154	0.026	0.0494	0.048	-2.83	0.034	0.033	-2.9
0.103	0.034	0.070	0.065	-7.14	0.048	0.046	-4.17

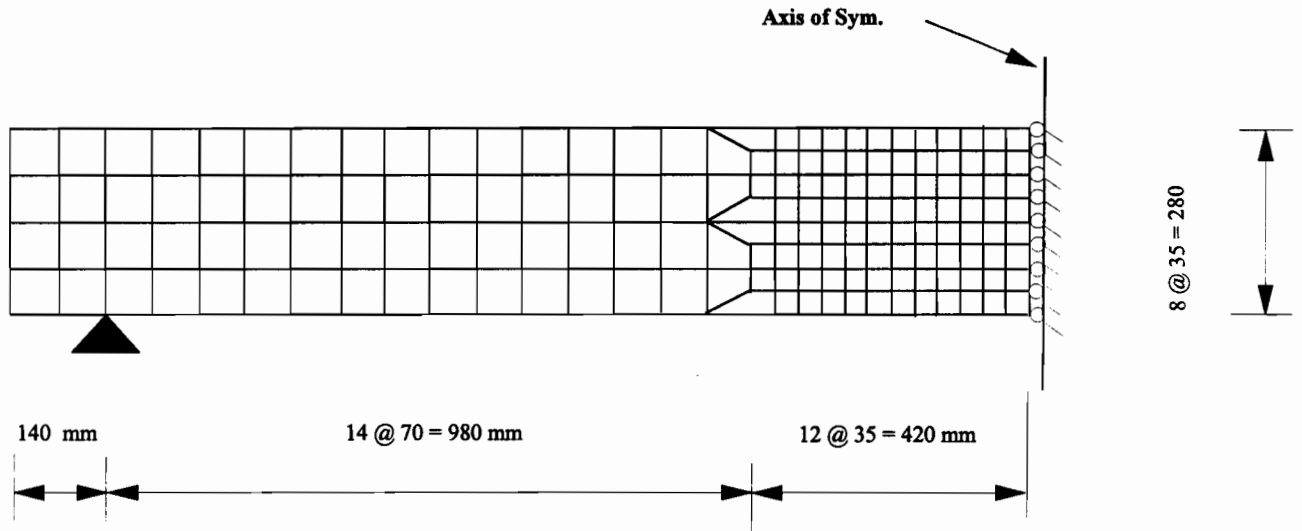


Figure 6.1: 172-element mesh configuration for beam C5

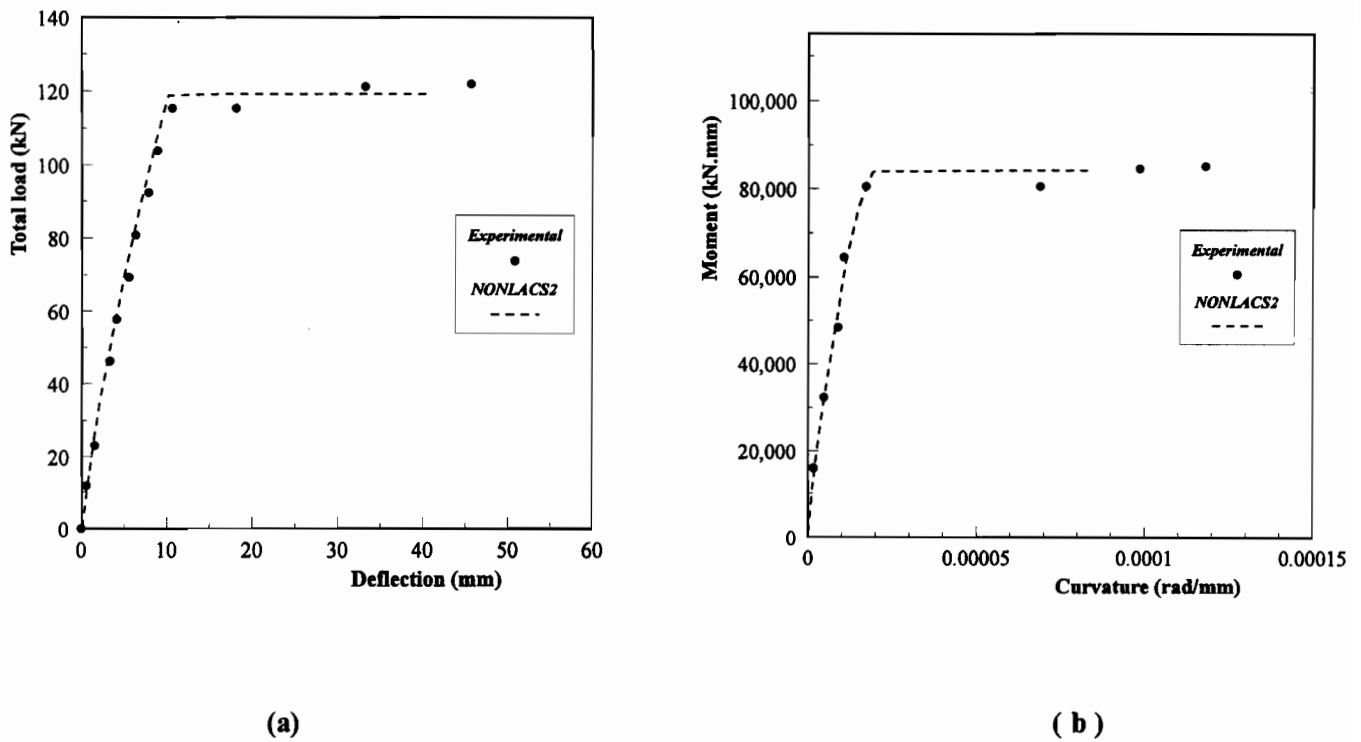


Figure 6.2: Comparison of experimental and analytical results for beam C5: (a) load-deflection curve, (b) moment-curvature curve

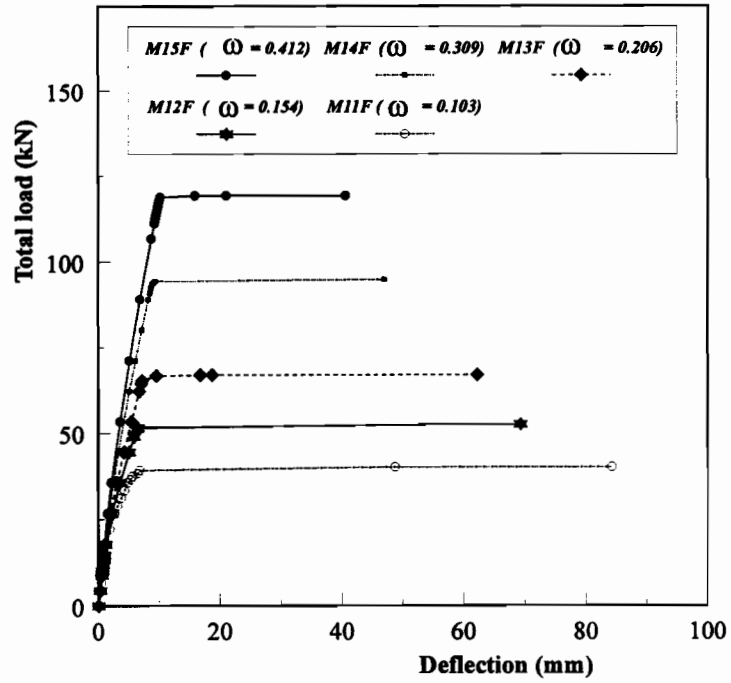


Figure 6.3: Load-deflection curves at mid-span for beams with different reinforcement index (Group No. 1)

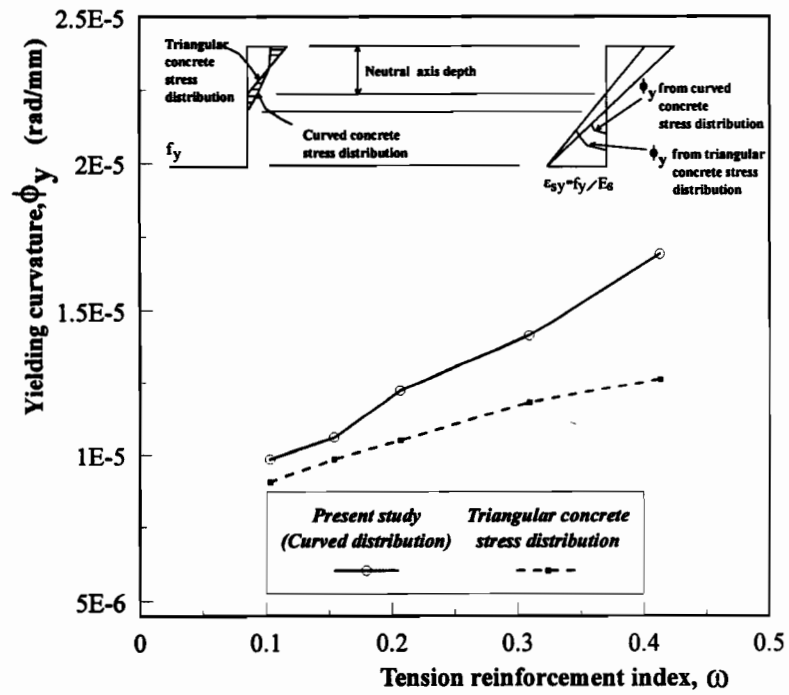


Figure 6.4: Variation of yielding curvature with tension reinforcement index, ω

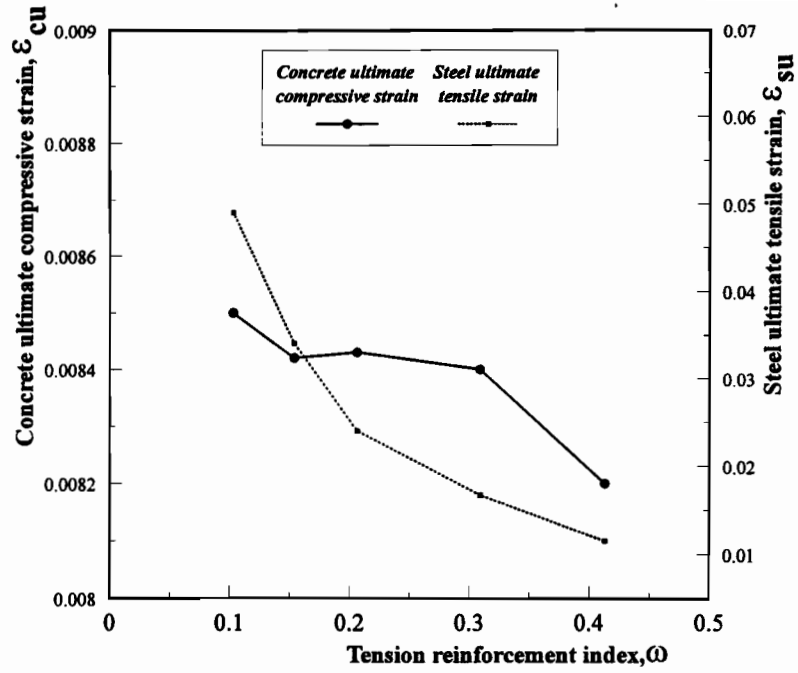


Figure 6.5: Effect of ω on ultimate concrete and reinforcing steel strains (Group No. 1)

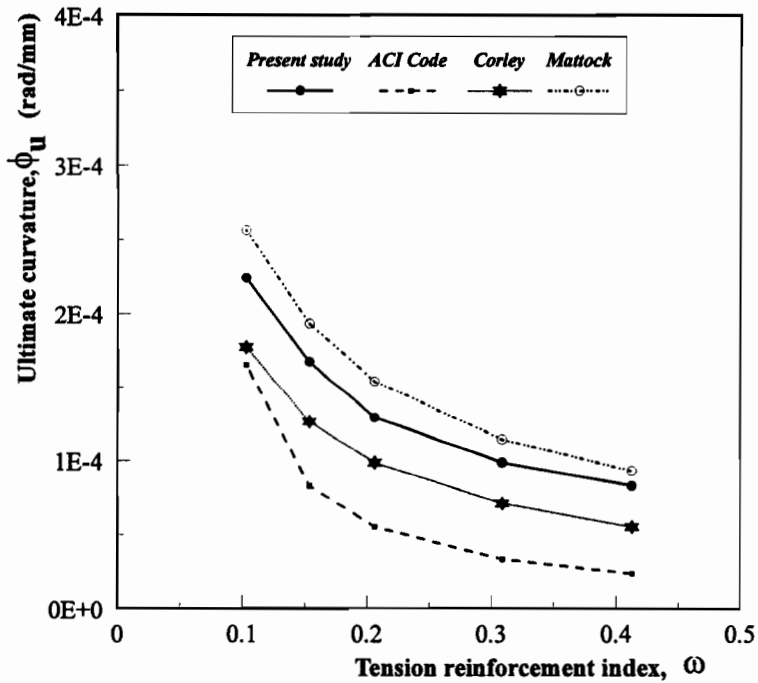


Figure 6.6: Variation of ultimate curvature with respect to tension reinforcement index, ω (Group No. 1)

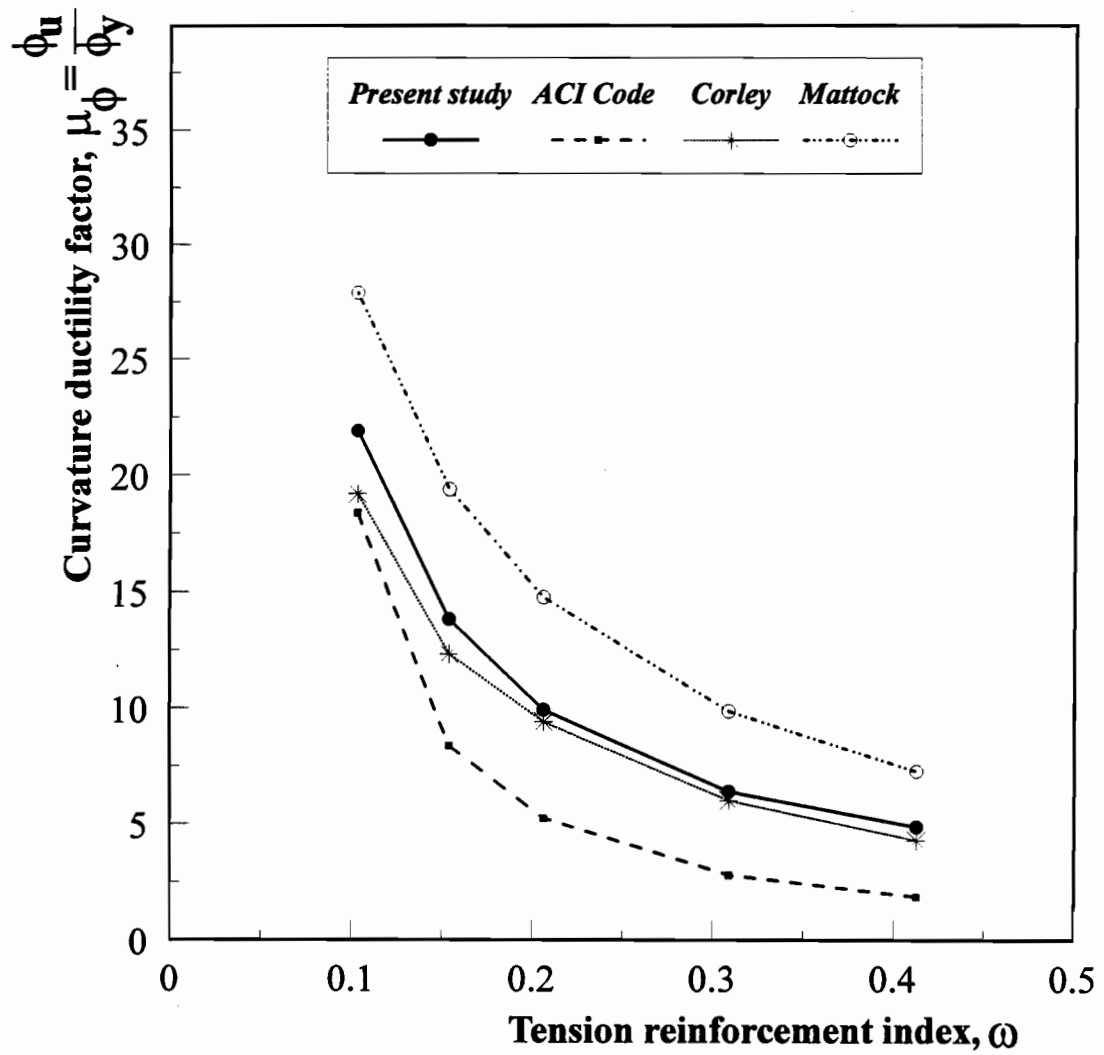


Figure 6.7: Effect of tension reinforcement index, ω , on the ductility factor (Group No. 1)

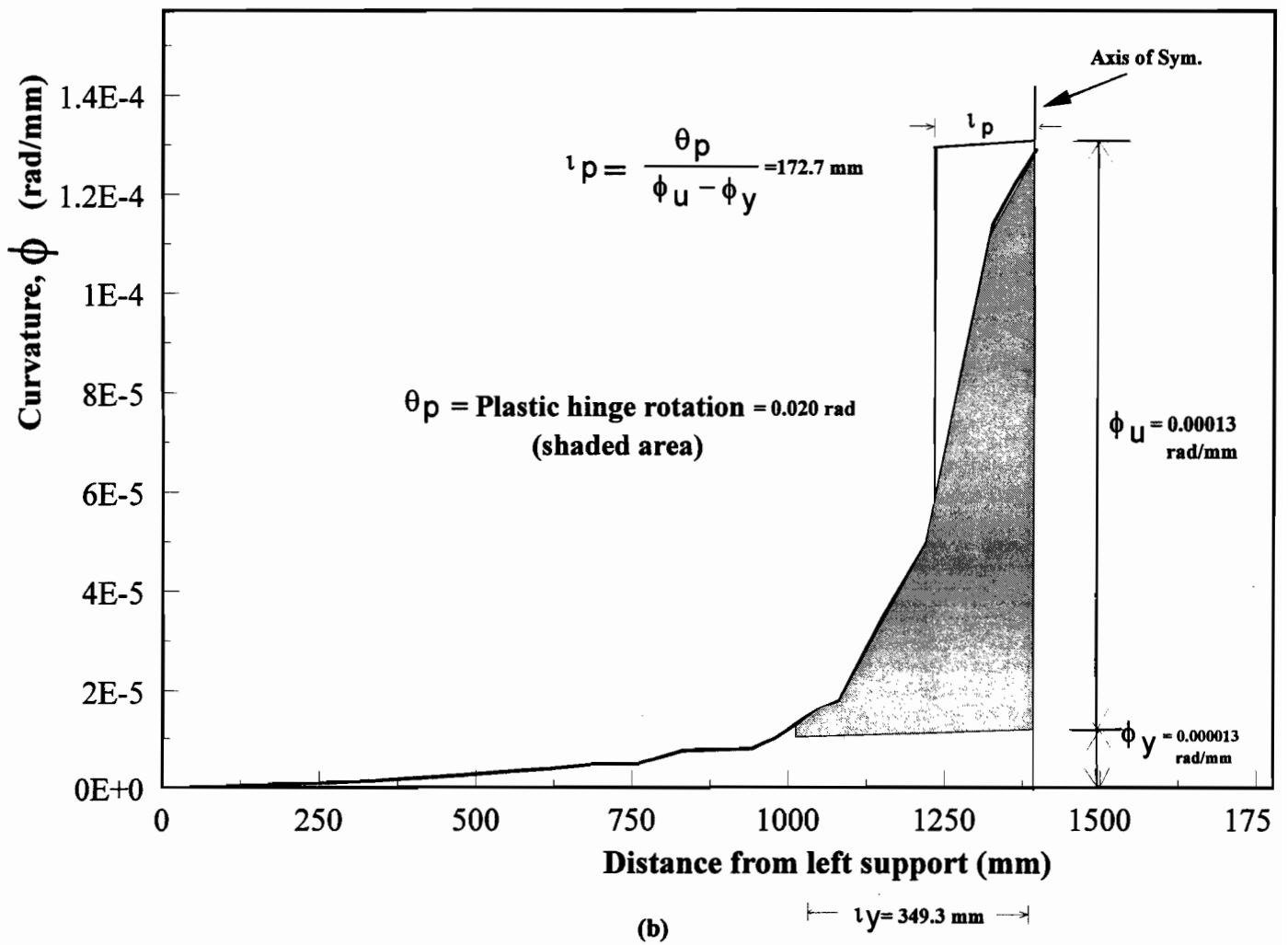
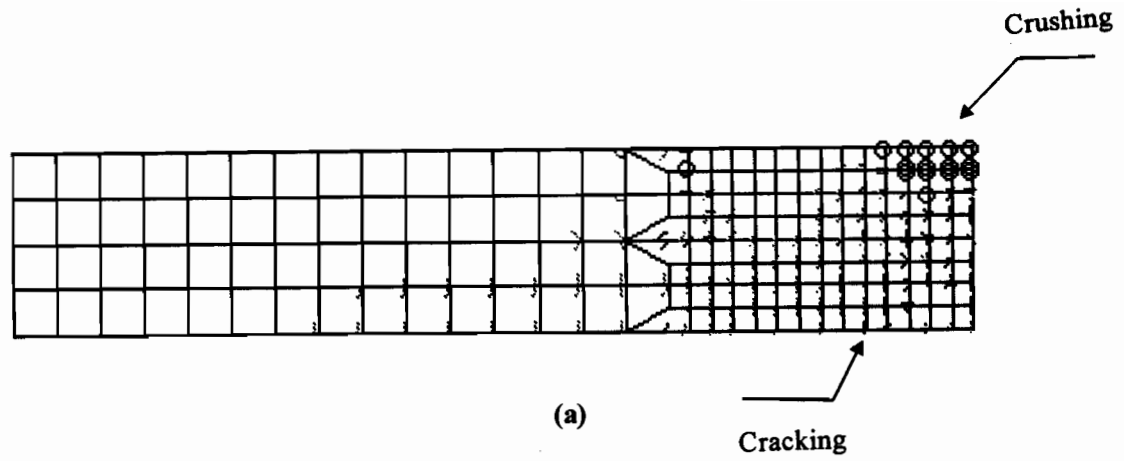


Figure 6.8: Calculation of plastic rotation for beam M13F ($\omega=0.206$) at ultimate stage: (a) crack pattern and crushing of concrete, (b) plastic hinge rotation

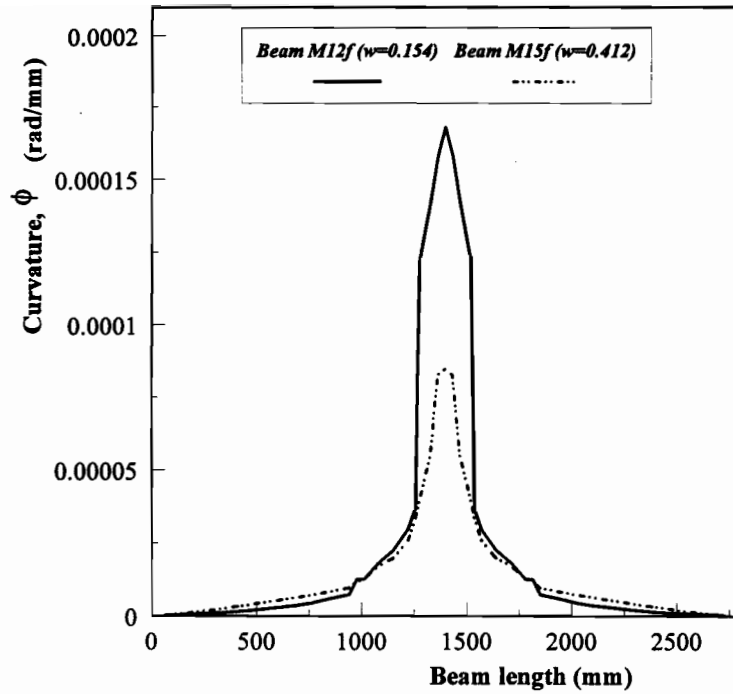


Figure 6.9: Variation of curvature along the length of beam for two different values of ω

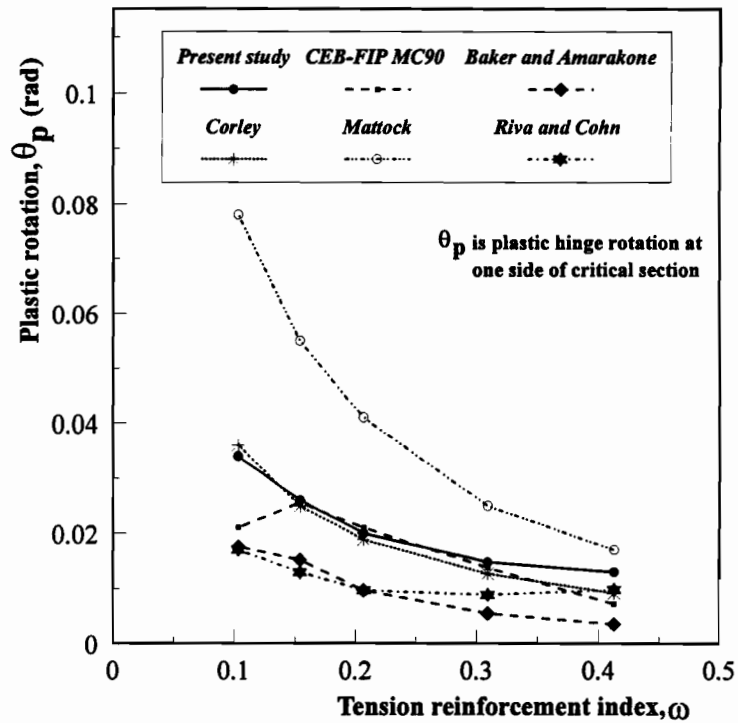


Figure 6.10: Comparison of existing plastic hinge rotation formulations for simply supported beams subjected to concentrated load at midspan ($z/d=5.5$)

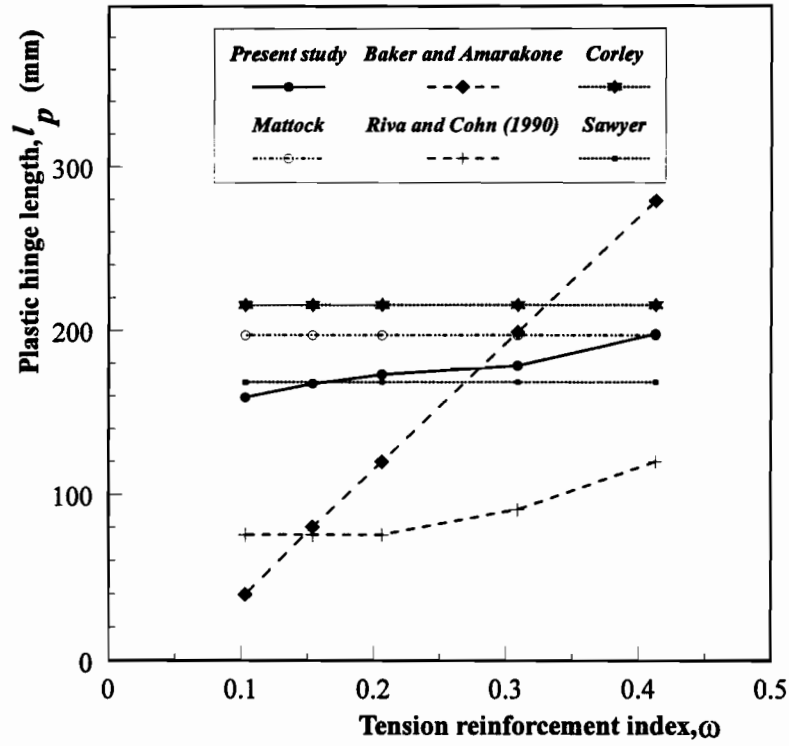


Figure 6.11: Comparison of existing plastic hinge length equations (Group No. 1, $z/d=5.5$)

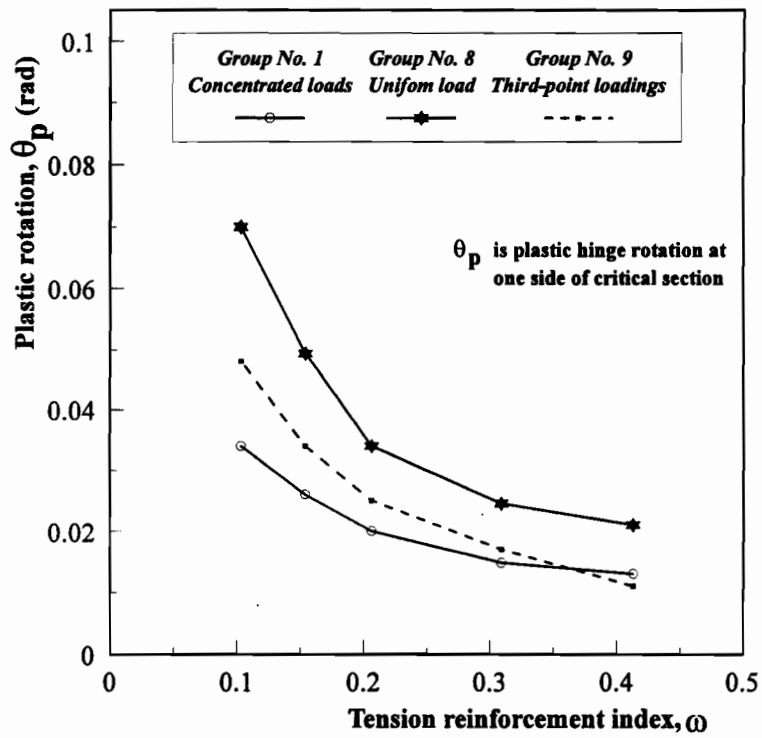
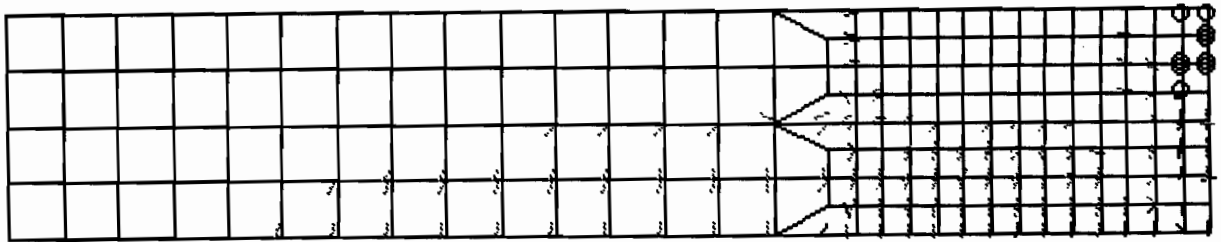
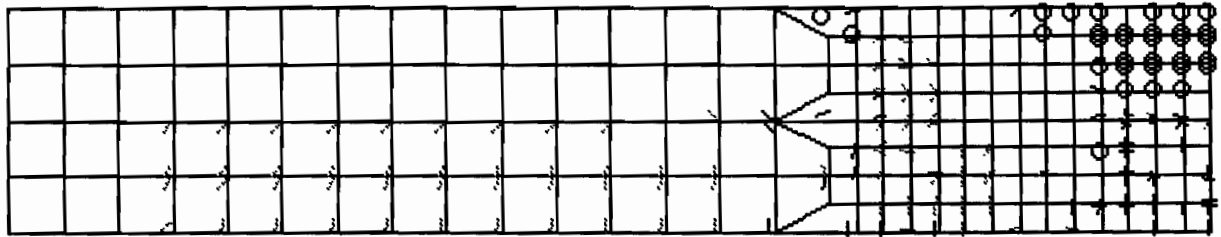


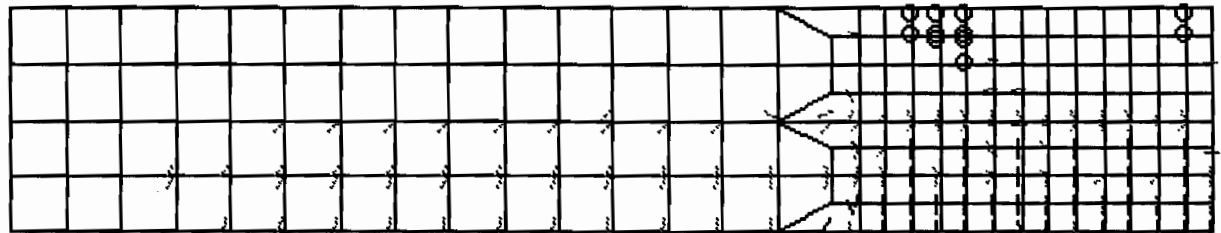
Figure 6.12: Influence of different loading types on the plastic rotation



(a) Beam M15F (Concentrated loads)



(b) Beam M85F (Uniform loads)



(c) Beam M95F (Third-point loading)

Figure 6.15: Effect of loading type on the failure mechanism of beams with $\omega=0.412$

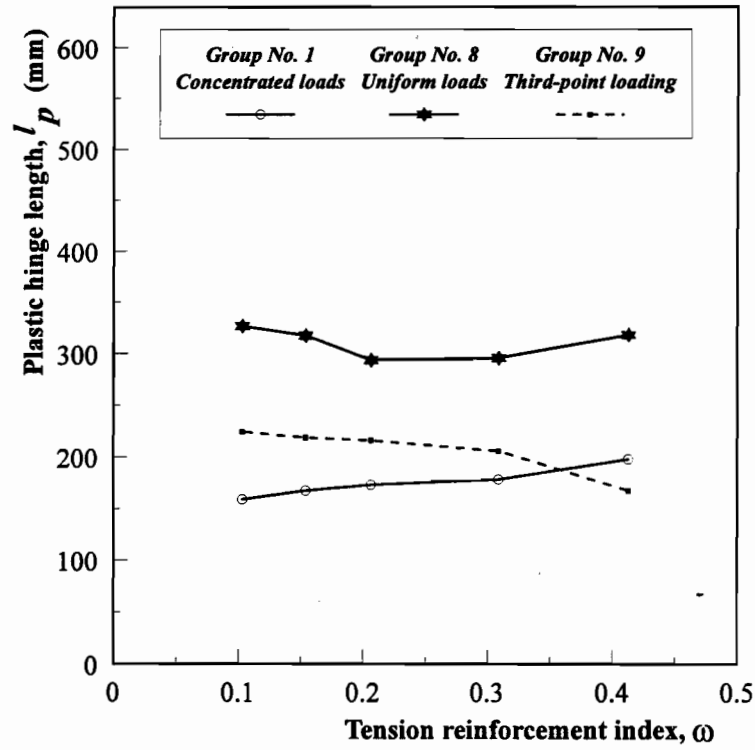


Figure 6.16: Influence of different loading types on the equivalent plastic hinge length

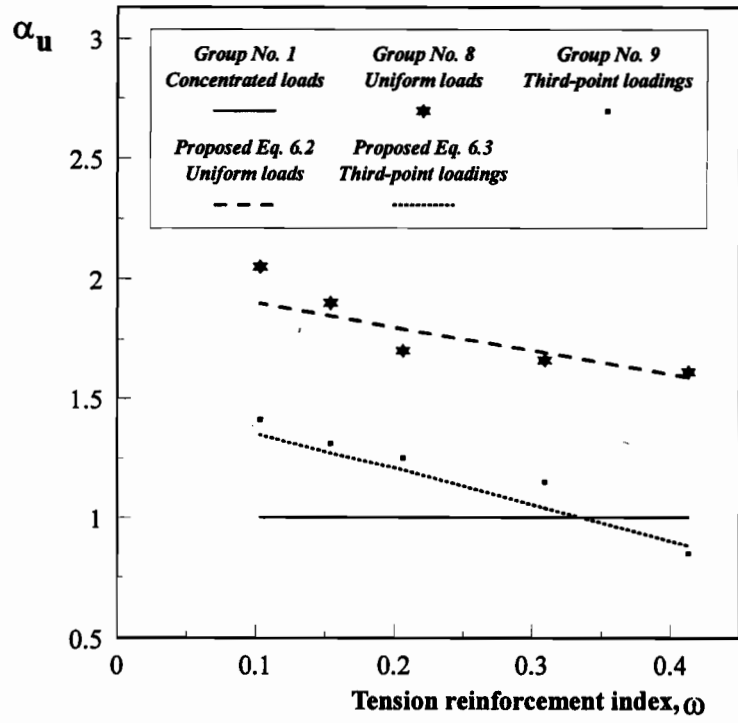


Figure 6.17: Analytical and estimated values of plastic rotations

CHAPTER 7

NONLINEAR ANALYSIS OF HIGH-STRENGTH CONCRETE BEAMS

The development of a finite element model suitable for nonlinear analysis of high-strength concrete members is needed because of its continually increasing applications. High-strength concrete has been defined as one having a compressive strength greater than 42 MPa (6000 psi). In order to study the effect of different material modelling techniques on the response of high-strength concrete beams, the HODA program developed by Shayanfar (1995) was used to perform a parametric study at the early stages of this part of the investigation. For the parametric study, beam LS1 tested by Leslie et al. (1976) was used. The material modelling techniques available in the HODA program which were studied are: Darwin's constitutive matrix and proposed constitutive matrix utilizing the transformation of equivalent uniaxial strains during the subsequent iteration, tension-compression failure criteria (Kupfer and Gerstle, and Vecchio and Collins), fixed crack and rotating crack models, Saenz and Smith's and Popovics' models for concrete stress-strain curves, horizontal and secant unloadings, and softening branch parameter.

Based on the analytical results of the above parametric study, it was found that the different techniques did not have a significant effect on the computed response of high-strength concrete beam, LS1, except for the softening branch parameter which improved the computed response considerably.

The tension-stiffening model with discontinuous softening is implemented in the NONLACS2 program and the accuracy and capability of the program is verified through analyses of three high-strength concrete beams, Specimens: 9.0-1 (LS1) and 9.0-2 (LS2) tested by Leslie et al. (1976), and the beam HUCB tested by Abrishami et al. (1995). Influence of the concrete tensile strength and the tensile softening branch factor, α_2 , on the computed response of high-strength concrete beams including the cracking behaviour, yielding, ductility and failure

mechanism is studied. Comparison of normal and high-strength concrete beams is made using the analysis of beams, UCB and HUCB, tested by Abrishami et al. (1995).

7.1 DESCRIPTION OF THE BEAMS ANALYZED

Recently, six normal and high-strength concrete beams were tested by Abrishami et al. (1995) at McGill University to examine the effect of epoxy-coated reinforcement on the flexural behaviour of normal and high-strength concrete beams. In the present study, the normal-strength concrete beam UCB and the high-strength concrete beam HUCB with no epoxy coating on the reinforcement are analyzed using NONLACS2 program. As shown in Fig. 7.1, both beams are 400 mm deep, 200 mm wide, 4500 mm clear span, simply supported, singly reinforced (with $\rho=0.0088$) and without shear reinforcement. Two monotonically increasing concentrated loads are applied to the beams. The detailing, geometry and loading of the beams are shown in Fig. 7.1. The material properties and sectional details of these beams are given in Table 7.1. The only difference between UCB and HUCB is in the ultimate uniaxial compressive strength of concrete (UCB with $f'_c=32$ MPa and HUCB with $f'_c=90$ MPa) .

Table 7.1: Sectional details and material properties of beams analyzed

Dimension and Material Property	Beams Tested by Leslie et al. (1976)		Beams Tested by Abrishami et al. (1995)	
	(9.0-1) LS1	(9.0-2) LS2	HUCB	UCB
d (mm)	270	267	340	340
A_s (mm ²)	568	1050	600	600
A_s' (mm ²)	142.6	142.6	0	0
ρ	0.01	0.019	0.0088	0.0088
ρ'	0.0023	0.0023	0	0
f'_c (MPa)	73.2	81.2	90.0	32.0
E_o (MPa)	35,300	36,800	34,150	25,680
ϵ_{cu}	0.004	0.004	0.0034	0.004
f_y (MPa)	415	461	440	440
E_s (MPa)	200,000	200,000	200,000	200,000
ϵ_{su}	0.06	0.06	0.075	0.075

* Assumed values

In addition, two simply supported high-strength reinforced concrete (R C) beams, "9.0-1" (designated as LS1 in the present study), and "9.0-2" (LS2), subjected to third-point loading tested by Leslie et al. (1976) are investigated. The beams are 305 mm in height, 200 mm in width and a clear span of 2130 mm. The details of reinforcement layout and the geometry of the beams are shown in Fig. 7.2. The material properties and the sectional details are given in Table 7.1. Both beams have the same compression and shear reinforcements, and approximately equal concrete strengths, and the only difference between them is the tension reinforcement ratio (i.e. LS1 with $\rho=0.01$ and LS2 with $\rho=0.019$).

7.2 FINITE ELEMENT IDEALIZATION

Because of the symmetry of loading and geometry, only half of the beams are modelled. The mesh configuration with 80 elements (Fig. 4.3d) is used for finite element analysis. For beams, UCB and HUCB, the size of each finite element is 100×125 mm, while for beams LS1 and LS2, each element is 77.5×59.2 mm. Shell element type I (facet shell element which is a combination of inplane membrane element, QLC3, and the rectangular bending element, RBE) is quite suitable for beam behaviour problems, therefore, it is used in this study. Also, half of the total load is applied to the structure in 30 load steps. Because of the plane stress conditions, the concrete is modelled by one concrete layer. The longitudinal reinforcements are lumped at the reference surface as a single bar element. The stirrups are modelled as smeared steel layers on the two sides of the beam. The proposed model (Eq. 4.1) is used to determine the value of concrete ultimate tensile strain, ϵ_m , and Popovics' equation is utilized to represent the concrete uniaxial compressive stress-strain curve during the analyses in this chapter.

7.3 INFLUENCE OF CONCRETE TENSILE STRENGTH

The concrete tensile strength governs the cracking behaviour and influences other response aspects such as stiffness and bond between reinforcement and concrete. Since the direct tensile strength of concrete is difficult to evaluate experimentally, it is generally determined by indirect tension tests, namely the cylinder splitting tests (splitting tensile strength, f_{ct}), while the flexural tensile strength is determined using beam flexure tests. In the direct tension test, the specimen is pulled apart in pure tension. In the splitting test, a cylinder is loaded in compression at the two ends of a selected diameter, and the specimen fails in tension on the plane between the loaded

points. In the beam flexure test, a rectangular beam is loaded at third points and it fails in bending with a linear strain distribution across the cross-section.

Depending on the type of the strain distribution, one of the above tensile strengths is used. For example, the direct tensile strength, f'_t , is recommended for cylinder concrete tank subjected to internal pressure, where the concrete wall has a uniform strain distribution across its section. The splitting tensile strength, f_{ct} , is utilized for studying web-shear cracking in prestressed concrete members or for structures with shear mode of failure, while the modulus of rupture is used for structures with flexural mode of failure (linear strain distribution), such as R C beams and slabs in bending and concrete pavements. In estimating the cracking load for a flexural member, the modulus of rupture will in fact lead to a more accurate prediction because of the strain gradient in the flexural member and the modulus of rupture test specimen. The tensile strength of the concrete is often taken as a constant times $\sqrt{f'_c}$ for design purposes. For normal weight concrete, the ACI 318 Building Code (1983) recommends the following equations:

Direct tensile strength, f'_t :

$$\begin{aligned} f'_t &= 0.33 \sqrt{f'_c} && \text{(MPa units)} \\ f'_t &= 4 \sqrt{f'_c} && \text{(psi units)} \end{aligned} \quad (7.1)$$

Splitting tensile strength, f_{ct} :

$$\begin{aligned} f_{ct} &= 0.56 \sqrt{f'_c} && \text{(MPa units)} \\ f_{ct} &= 6.7 \sqrt{f'_c} && \text{(psi units)} \end{aligned} \quad (7.2)$$

Modulus of rupture, f_r :

$$\begin{aligned} f_r &= 0.62 \sqrt{f'_c} && \text{(MPa units)} \\ f_r &= 7.5 \sqrt{f'_c} && \text{(psi units)} \end{aligned} \quad (7.3)$$

The ACI Committee 363 (State-of-the-Art Report on High Strength Concrete, 1992) reports that for normal weight concrete the modulus of rupture may be taken as

$$\begin{aligned} f_r &= 0.94 \sqrt{f'_c} && \text{when } 21 \leq f'_c \leq 83 \text{ MPa} \\ f_r &= 11.7 \sqrt{f'_c} && \text{when } 3000 \leq f'_c \leq 12000 \text{ psi} \end{aligned} \quad (7.4)$$

Some more proposed empirical equations for prediction of tensile strength of concrete are reported by Shah and Ahmad (1994).

The selection of the concrete tensile strength in the finite element analysis of R C structures always presents a problem because of the size effect between the standard beam used in the flexure test and the real structure, and because microcracking might already exist due to nonstructural cracking caused by shrinkage, etc. The effect of different values of the tensile strength of concrete on the computed response of high-strength R C beams tested by Leslie et al. and Abrishami et al. are studied and finally recommendation is made about which value of the modulus of rupture is more appropriate for use in the finite element analysis.

7.3.1 Computed Response of Beam HUCB

In order to verify which value of f_t can predict the response more accurately, the beam HUCB is analyzed with three different values of the modulus of rupture (4.3 MPa, 5.9 MPa, and 8.9 MPa) using the NONLACS2 Program. The values of 5.9 MPa and 8.9 MPa are obtained using the ACI 318 (Eq. 7.3) and ACI 363 (Eq. 7.4), respectively. The tensile strength is also taken as 4.3 MPa so that the initial cracking in the analysis corresponds with that adopted from the experimental data. This value is approximately the average of the direct tensile strength (Eq. 7.1) and the modulus of rupture (Eq. 7.3). The effect of the different values of the concrete tensile strength on the analytical load-deflection curves of beam HUCB are shown in Fig. 7.3. Table 7.2 presents the analytical and experimental results at the cracking load for beam HUCB with different values of f_t .

Table 7.2: Effect of concrete tensile strength on the cracking behaviour of beams HUCB and UCB

Beam		Modulus of Rupture, f_t (MPa)	Equation	Cracking Strain, $\epsilon_{cr} = f_t / E_c$	Cracking Moment, $M_{cr,lg}$ (kN.m)	Analytical Cracking Moment, $M_{cr,anl}$	Experimental Cracking Moment	Ratio *
High strength	HUCB	4.30	Experimental	0.00013	23.0	26.3	23.0	0.88
	HUCB	5.90	$0.62\sqrt{f'_c}$	0.00017	31.5	35.1	23.0	0.66
	HUCB	8.90	$0.94\sqrt{f'_c}$	0.00026	46.9	53.1	23.0	0.43
Normal strength	UCB	3.20	Experimental	0.000125	17.2	19.52	17.2	0.88
	UCB	3.50	$0.62\sqrt{f'_c}$	0.000136	18.67	21.0	17.2	0.82

* Ratio of experimental to analytical cracking moments.

As can be seen from Fig. 7.3, the concrete tensile strength has a significant effect on the value of the cracking moment, the stiffness of structure and the cracking pattern. An increase in the value of f_t , the cracking moment value increases and the structure behaves in a stiffer manner. The predicted load-deflection curve for $f_t=4.30$ MPa shows excellent agreement with the experimental load-deflection curve. The agreement between the experimental and computed load-deflection curves for $f_t=5.90$ MPa is also good, however, the computed model is stiffer than that for $f_t=4.30$ MPa which is just slightly stiffer than the experimental load-deflection curve. The value of the modulus of rupture equal to 8.9 MPa ($0.94\sqrt{f_c}$) recommended by ACI 363 predicts a 57 percent higher cracking moment besides a much stiffer response (Fig. 7.3).

Figure 7.4 presents the cracking pattern of beam HUCB at a load level of 30 kN (cracking load for beam with $f_t=8.9$ MPa) for three different values of f_t . It should be noted that if the principal strain of concrete at each of the nine Guass quadrature points exceeds the cracking strain, ϵ_{cr} , the NONLACS2 program output indicates cracking at the corresponding Gauss quadrature point. The crack patterns show that, as expected, cracks initiate first at the outermost tension edges of the beam, which spread progressively toward the compression zone with an increase in the applied load. As can be seen from Fig. 7.4, there is considerable difference in the cracking patterns for the three different values of the modulus of rupture, f_t . Since the value of ϵ_u ($\epsilon_u=0.0016$), softening branch factor ($\alpha_2=0.2$), and the modulus of elasticity are the same for these analyses, however, with an increase in the value of f_t , the cracking strain, $\epsilon_{cr}=f_t/E_c$, increases. This causes the initiation of the cracks in the beam to be delayed with a higher value of f_t . With an increase in the value of f_t , the energy dissipation capacity (area under concrete tensile stress-strain curve) increases and the crack propagation of the structure decreases. Therefore, there is a maximum dissipation of energy with $f_t=8.9$ MPa, while it is a minimum for $f_t=4.3$ MPa, which indicates why with $f_t=4.3$, the number of cracks is a maximum. Unfortunately, the experimental cracking pattern is not available, and a comparison of the computed and the experimental crack patterns is not possible.

A summary of the computed responses of the beams analyzed including the yielding and ultimate loads and the corresponding mid-span deflections, ductility factors and the predicted mode of failures are given in Table 7.3. The decrease in the concrete tensile strength does not seem to decrease the failure load very significantly. It should be pointed out that by decreasing the value of modulus of rupture, the deflection ductility factor, μ_Δ , decreases and for the value of $f_t=8.9$ MPa (ACI 363), it does not match with the experimental findings. In the model with $f_t=5.9$ MPa (ACI 318), the analytical values of loads for the yielding and ultimate stages are $P_y=46.8$ kN and $P_u=49$ kN, with a maximum deviation of +5 percent and -3.5 percent from experimental findings,

respectively. In this case, the ductility factor of 3.42 is very close to the experimental value of 3.44 with a deviation of only 1 percent.

7.3.2 Computed Response of Beams Tested by Leslie et al.

The beam LS1 is analyzed with two different values of f_r using equations 7.3 and 7.4. The value of the ultimate tensile strain and the softening branch factor are assumed to be constant for these analyses ($\epsilon_w=0.002$ and $\alpha_2=0.2$). The analytical and experimental load-deflection curves for this beam is shown in Fig. 7.5. The model using ACI 318 equation ($f_r=5.1$ MPa) gives a relatively softer response closer to the experimental results but it underestimates the ultimate load of the structure by 8 percent.

Table 7.3: Summary of analytical results at yielding and ultimate of beams HUCB, LS1, and LS2.

Beam	Modulus of Rupture, f_r (MPa)	Yielding		Ultimate		Ductility $\mu_\Delta = \Delta_u / \Delta_y$
		P_y (kN)	Δ_y (mm)	P_u (kN)	Δ_u (mm)	
HUCB	4.30	46.2	18.96	49	56.81	3.0
	5.90	46.8	18.11	49	62	3.42
	8.90	48.4	17.25	50	75	4.35
	Experimental	44.5	21.0	50.8	72.3	3.44
LS1	5.10	170	5.88	184	30	5.10
	8.0	170	5.28	197	36.2	6.86
	Experimental	152	6.2	200	33.4	5.38
LS2	5.40	310	7.29	320	22.5	3.09
	8.47	320	7.24	330	25.95	3.58
	Experimental	313.5	10	352	28.2	2.82

The model with $f_r=7.6$ MPa (ACI 363), exhibits very stiff response, but it predicts the ultimate load of the beam quite accurately with a difference of 1.5 percent from experimental value.

Figure 7.6 shows the effect of different values of modulus of rupture on the analytical cracking pattern at failure for beam LS1. It can be noted that the crack patterns are different and are influenced considerably by the value of modulus of rupture. With a decrease in the value of modulus of rupture, the progress of cracks increases resulting in softer load-deflection response.

In the experimental program, shear failure was prevented by use of heavy stirrups in the shear span, as shown in Fig. 7.2. This caused the mode of failure for both beams LS1 and LS2 to be flexural, thus the steel reinforcement yielded first, followed by the crushing of the concrete. The analytical mode of failure is similar to the experimental findings. Unfortunately, the experimental cracking pattern is not available to make a comparison.

Figure 7.7 reveals that different values of f_t ($f_t=5.4$ MPa and $f_t=8.47$ MPa) result in approximately the same load-deflection responses for beam LS2. The model with $f_t=8.47$ MPa gives a little stiffer response and the ultimate load in this case is 330 kN, which is 6.25 percent smaller than the experimental value of 352 kN. The analytical predictions are in good agreement with the experimental results when a value of $f_t=5.4$ MPa, recommended by the ACI Committee 318, is assumed for the concrete tensile strength. The analytical yielding and ultimate loads and ductility factor are very close to the experimental findings with a deviation of -1.1, -9 and +9.5 percent, respectively.

Comparison of Figures 7.5 and 7.7 shows that the effect of f_t on the response of heavily reinforced high-strength concrete beams is less than on that of lightly reinforced beams. Because of the high ratio of tensile reinforcement, the concrete in compression governs the overall behaviour and the characteristics of concrete in tension do not have significant effect on the stiffness and the ultimate load capacity of the beam.

7.3.3 Recommended Value of f_t for Finite Element Analysis

It appears that the ACI 318 value of $f_t=0.62\sqrt{f'_c}$ is low compared with the value of $0.94\sqrt{f'_c}$ reported by ACI 363. However, for curing conditions such as seven days moist curing, followed by air drying, a value of $0.62\sqrt{f'_c}$ is probably fairly close for the full strength range. It may, therefore, be recommended with no change (ACI 363, 1992). The average modulus of rupture, measured by Abrishami et al. on $100\times 100\times 400$ mm plain concrete beams subjected to third-point loading were 4.1 MPa and 9.8 MPa for the normal and high-strength concrete beams, respectively. Generally the tensile strength measured by the modulus of rupture in the laboratory (Abrishami et al. 1995 and Carrasquillo et al. 1981) was generally higher than the ACI Building Code values. Some investigators (e.g. Carrasquillo et al. 1981) have reported that the tensile strength of high strength concrete gets reduced significantly because of drying shrinkage. The large difference between the measured modulus of rupture on the standard beam in flexure test ($100 \times 100 \times 400$ mm) with $f_t=9.8$ MPa and the specimen HUCB with $f_t=4.3$ MPa can also be explained by the

phenomenon of size effect. Mirza (1967) pointed out from his experimental results that with an increase in the size of the specimen, the modulus of rupture decreases. Bazant and Li (1995) showed that the ratio of modulus of rupture to the direct tensile strength, f_r/f_c , is inversely proportional to the beam depth, i.e. with increasing the depth of beam, the modulus of rupture decreases.

The assumption of a modulus of rupture lower than the actual value for a flexural member simply results in an inaccurate prediction of the cracking load. This will result in an inaccurate estimation of the elastic deflections. However, for prediction of deflections, ACI 363 recommended that a value of $0.62\sqrt{f_c}$ may be used to calculate the flexural cracking moment of the beam.

Several investigators have used different values of the concrete tensile strength for finite element analysis. For example, Marzouk and Chen (1993) used a value of f_r equal to 5 percent of f_c for finite element analysis of high-strength concrete slabs. Ghoneim and Ghali (1982), Hu and Schnobrich (1991), Al-Manaseer and Philips (1987), Bazant and Oh (1983), Razaqpur and Nofal (1990), Shayanfar et al. (1993), Kheyroddin and Mirza (1994, 1995) used the modulus of rupture obtained using $f_r=0.62\sqrt{f_c}$ recommended by the ACI Committee 318. The concrete tensile strength was estimated to be $0.33\sqrt{f_c}$ by Chung and Ahmad (1994) for finite element analysis of shear critical high-strength concrete beams as recommended by Vecchio (1989 and 1990).

Based on the analytical results in this section, it can be concluded that the model using the modulus of rupture recommended by ACI 318 ($f_r=0.62\sqrt{f_c}$) can be used for finite element analysis of high-strength concrete flexural beams with reasonable accuracy. If the experimental cracking moment is available, the modulus of rupture can be obtained using $f_r = M_{cr} \times I_g / y$.

7.4 TENSION-STIFFENING MODEL WITH DISCONTINUOUS SOFTENING

The different tension-stiffening models in the NONLACS2 program were discussed in Chapter 3. Generally, high-strength concrete in tension behaves in a much more brittle manner than normal-strength concrete and it seems realistic to allow some rapid partial loss of stress after fracture, since the experimental evidence does seem to indicate that this happens (e.g., Scanlon et. al 1986). Here the performance of tension-stiffening model with a sudden drop of stress after cracking (Fig. 3.5c) is shown. The predictions of the model are compared with the available experimental data, and the comparisons show good agreement.

7.4.1 Response of High-Strength Concrete Beam HUCB

In an attempt to study the influence of the softening branch factor, α_2 , on the flexural response of high-strength concrete beams, beam HUCB is analyzed with four different values of α_2 . The modulus of rupture for these analyses is constant and equal to 4.3 MPa. The analytical load-deflection curves for different values of α_2 equal to 0.0, 0.2, 0.4, and 1.0 are compared with experimental load-deflection curve in Fig. 7.8. Incorporating a sudden drop of stress after the initiation of crack has a strong effect on the stiffness but less significant effect on the ultimate load. The load-deflection curves are closer to the experimental results when a smaller values of α_2 are used. A summary of the yielding and ultimate loads, corresponding deflections, ductility factors and mode of failure for different values of α_2 for beam HUCB are presented in Table 7.4. The model with $\alpha_2=1.0$ (no stress drop at cracking point) exhibits a very stiff response but results in an accurate value for the beam ultimate load with a deviation of only +0.4 percent from the experimental value of 50.8 kN. The ultimate load for the case of $\alpha_2=0.4$ is 50 kN, which decreases only slightly when compared with the case of $\alpha_2=1.0$. From Table 7.4, it can be observed that the yielding and the ultimate loads and the ductility factor increase as the value of α_2 increases. In fact, with an increase in the value of α_2 , the energy dissipation capacity of the beam, and consequently the yielding and the ultimate loads and the ductility factor increase. Figure 7.8 and Table 7.4 indicate that a value of α_2 equal to 0.2 is acceptable. For α_2 less than 0.2, the analytical results do not match with the experimental findings. However, the ultimate loads do not appear to change significantly. The model with $\alpha_2=0.0$ (no tension-stiffening) underestimates the ultimate load by about 11.4 percent and gives a softer response than that the experimental one at an early stage of loading.

Variation of the applied load with respect to the concrete compressive strain at the top of the beam and the steel tensile strain at the bottom of the beam HUCB at mid-span section for the two extreme values of α_2 equal to 0.0 and 1.0 are plotted in Figures 7.9 and 7.10, respectively. The figures show that the steel reinforcement first yields and at failure the concrete strain in compression zone does not exceed the ultimate compressive strain, ϵ_{cu} (i.e. there is no crushing of concrete at midspan). Failure of the structure occurs when the concrete crushes under the loading point at the top of beam. For the model with $\alpha_2=0.0$, a sudden brittle failure occurs when the yielding of reinforcing bar is reached at the last load step, resulting in a ductility factor of $\mu_\Delta=1.0$. Since the tensile stress is assumed to decrease suddenly to zero, there is a considerable increase in steel tensile strain and the concrete compressive strain at the cracking load for the

model with $\alpha_2=0.0$. Figure 7.11 presents the cracking patterns of beam HUCB for the models with α_2 equal to 0.0, 0.2, 0.4, and 1.0 at the initiation of cracking. The factor, α_2 , has a significant effect on the cracking pattern, so that with an increase in the value of α_2 the dissipation of energy increases and progress of cracks reduces. The number of cracks for model with $\alpha_2=1.0$ is a minimum, while it is a maximum with $\alpha_2=0.0$, with intermediate values for $\alpha_2=0.2$ and 0.4.

Table 7.4: Summary of analytical results at yielding and ultimate of beam HUCB.

Beam	Tensile Softening Branch factor, α_2	Yielding		Ultimate		Ductility $\mu_\Delta = \Delta_u / \Delta_y$
		P_y (kN)	Δ_y (mm)	P_u (kN)	Δ_u (mm)	
HUCB (High-strength)	Experimental	44.5	21.0	50.8	72.3	3.44
	0.0	45.0	18.77	45	18.77	1.0
	0.2	46.2	18.96	49	56.81	3.0
	0.4	47.4	19.16	50	63	3.29
	1.0	50.6	19.22	51	68	3.54
UCB (Normal-strength)	Experimental	42.2	24.7	48.5	83.4	3.37
	0.4	45.0	20.73	46	68	3.28

7.4.2 Response of High-Strength Concrete Beam LS1

To verify the effect of the softening branch factor, α_2 , on the analytical response of high-strength R C beams with shear reinforcement, the beam LS1 is analyzed for two values of α_2 . The modulus of rupture is assumed to be constant and equal to 5.1 MPa. Comparison of the experimental and the analytical load-deflection curves is shown in Fig. 7.12. The model with $\alpha_2=1.0$ (no stress drop after cracking) behaves in a stiffer manner and results in a higher value of the ultimate deflection. Considering a sudden drop of the tensile stress ($\alpha_2=0.2$) has a strong effect on the load-deflection curve but less significant effect on the ultimate load. The ultimate loads for the models with $\alpha_2=1.0$ and 0.2 are 188 kN and 184 kN, with a deviation of -6 percent and -8 percent from the experimental ultimate load values. The analytical predictions for the beam stiffness, strength and the ductility factor are in good agreement with the experimental results when a value of $\alpha_2=0.2$ is assumed.

The crack patterns at a selected load level of $P=180$ kN for models with $\alpha_2=1.0$ and 0.2 are plotted in Fig. 7.13. Different values of α_2 can lead to different crack patterns. Like the beam

HUCB, it is clear that the number of cracks is less for the value of $\alpha_2=1.0$ compared with the model with $\alpha_2=0.0$.

7.5 COMPARISON OF NORMAL AND HIGH-STRENGTH CONCRETE BEAMS

To study the influence of the compressive strength of the concrete, f'_c , on the computed response of R C beams, the beams UCB and HUCB are analyzed using the NONLACS2 program. The value of α_2 is assumed to be constant and equal to 0.4 for both beams. Two values of the modulus of rupture are considered for beams UCB and HUCB: 4.3 MPa and 3.2 MPa (obtained from the experimental cracking moments), respectively. The analytical and experimental load-deflection characteristics for beams UCB and HUCB are compared in Fig. 7.14. The analytical load-deflection curves obtained from NONLACS2 program follow the same general pattern and are quite close to the experimental responses. As expected, the high-strength concrete beam has higher stiffness, cracking moment, yielding and ultimate loads than the normal-strength concrete beam (Tables 7.2 and 7.4). With an increase in the value of f'_c by a factor of about 2.8, the analytical cracking moment, yielding and ultimate loads increase by about 34 percent, 5.3 percent and 8.7 percent, respectively. An examination of the under-reinforced beams UCB and HUCB ($\rho=0.0088$) shows that, as expected, the ultimate load capacity is not very sensitive to the value of f'_c . Although the high-strength concrete beam has a greater value of lever arm, variation in f'_c makes little difference to the lever arm for both beams.

The analytical displacement ductility factors for beams UCB and HUCB are 3.28 and 3.29, respectively. These values are very close to the experimental findings of 3.37 and 3.44. Although the high-strength concrete is more brittle, and has a lower value of the ultimate concrete compressive strain, ϵ_{cu} , compared with the normal-strength concrete, the curvature and deflection ductility ratios may be the same or greater for the high-strength concrete. This is because the ultimate curvature is inversely related to neutral axis depth, c , which is inversely related to f'_c . It means the high-strength concrete has lower value of c and consequently a higher value of ϕ_u and ductility factor. This was also confirmed by a number of experimental tests conducted at Cornell and McGill Universities.

In the normal-strength concrete beam UCB, after significant flexural cracking and yielding of reinforcing bars, diagonal cracks formed with flexural failure of the beam occurring by the crushing of concrete in the compression zone. As observed in the experimental program, although the beam HUCB reaches flexural yielding, it fails due to diagonal tension and bond splitting failure (lack of shear reinforcement). The presence of shear reinforcement would help to control the diagonal tension cracks and the splitting-bond failure.

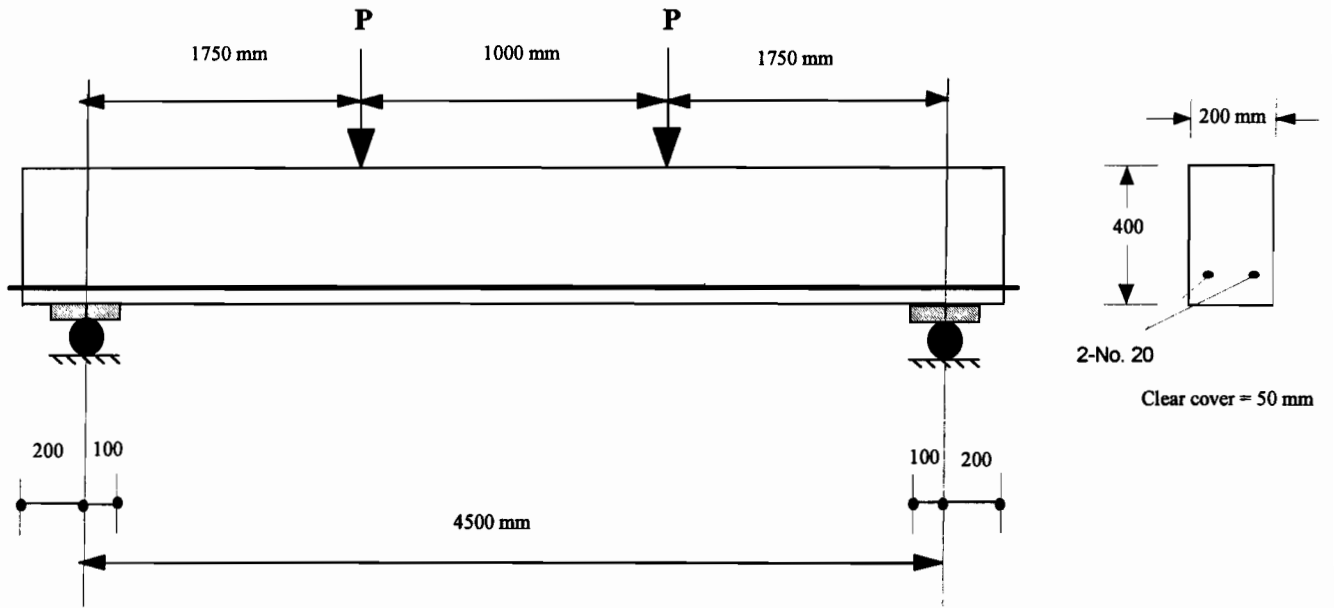


Figure 7.1: Geometry and reinforcement details of beams tested by Abrishami et al. (1995)

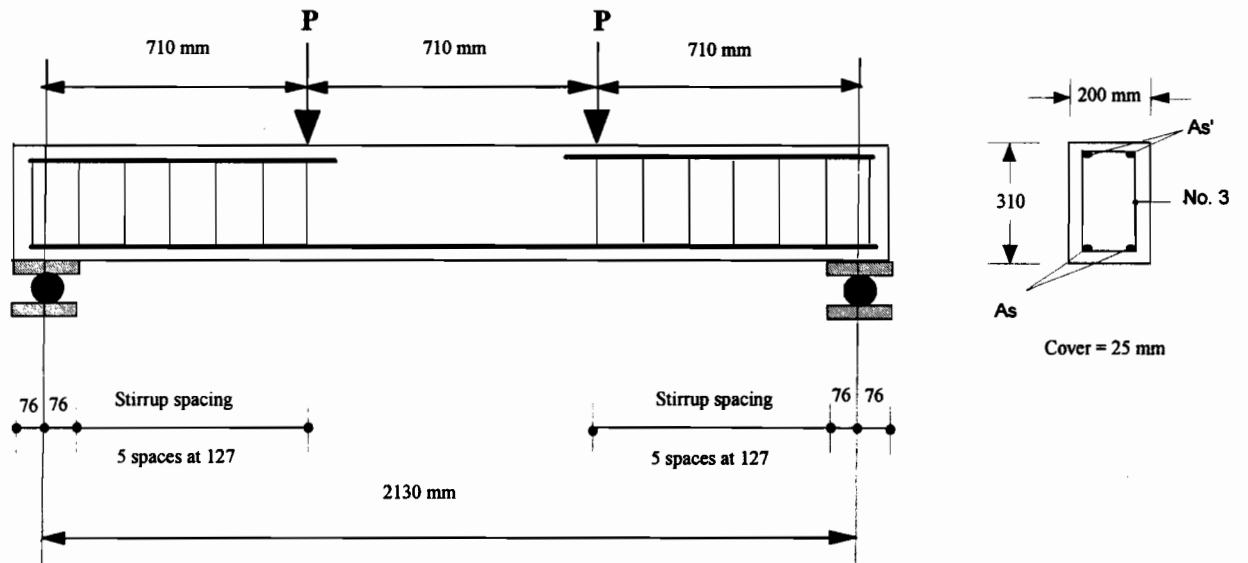


Figure 7.2: Geometry and reinforcement details of beams tested by Leslie et al. (1976).

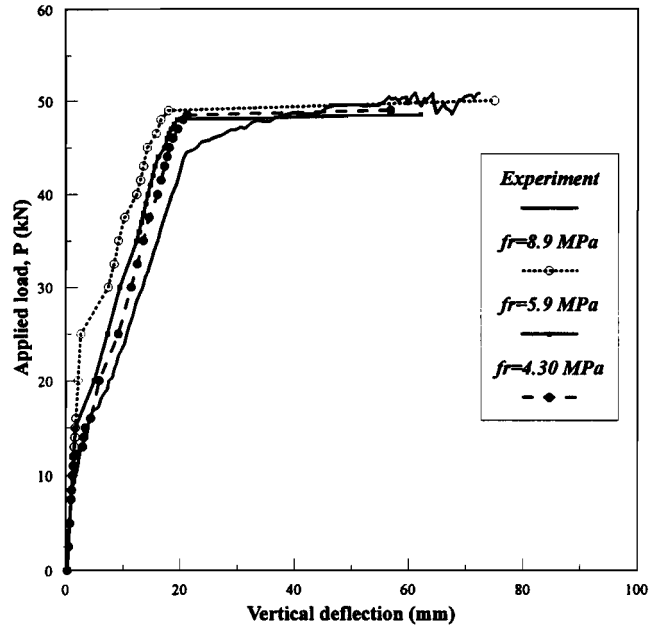
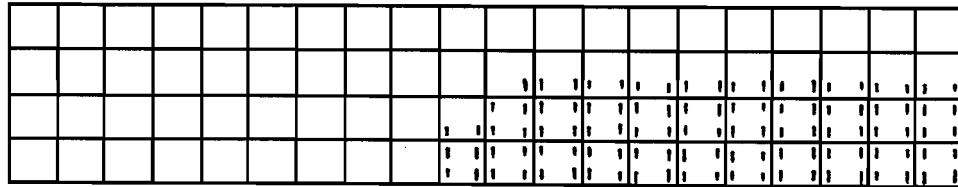
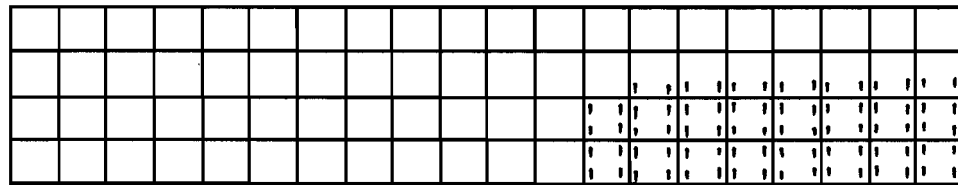


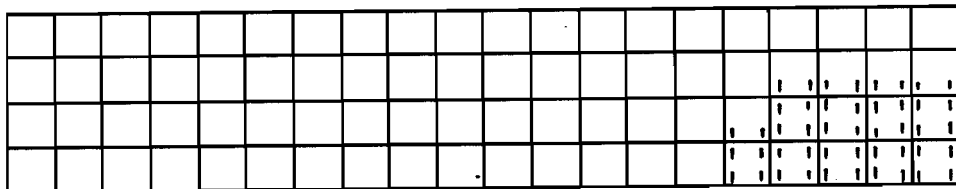
Figure 7.3: Effect of concrete tensile strength on the load-deflection response of beam HUCB



(a) $f_t=4.30$ MPa



(b) $f_t=5.9$ MPa



(c) $f_t=8.9$ MPa

Figure 7.4: Crack patterns for beam HUCB at load $P=30$ kN using different values of f_t

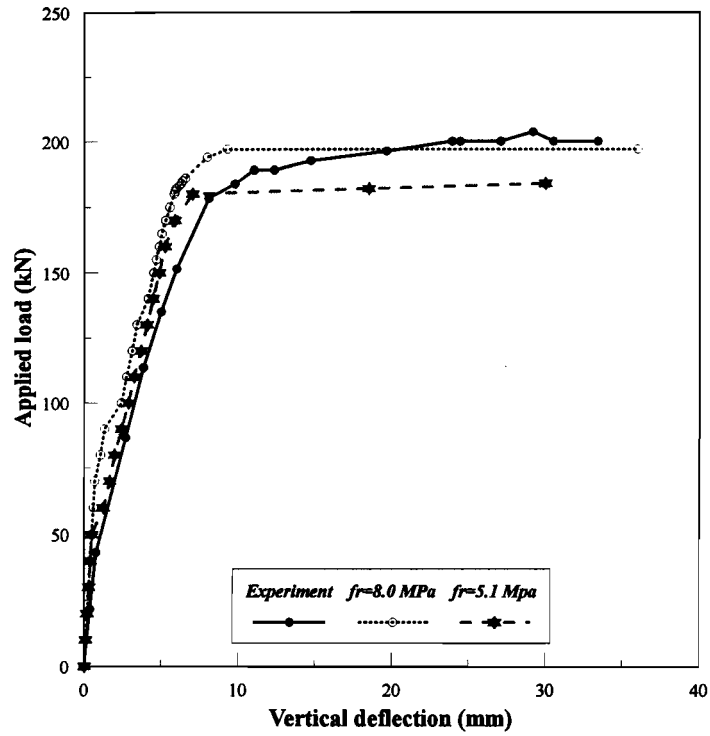
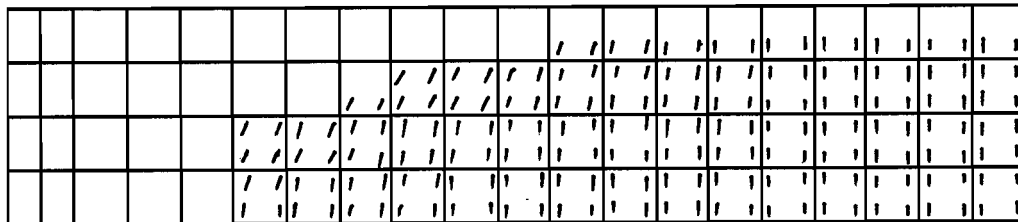
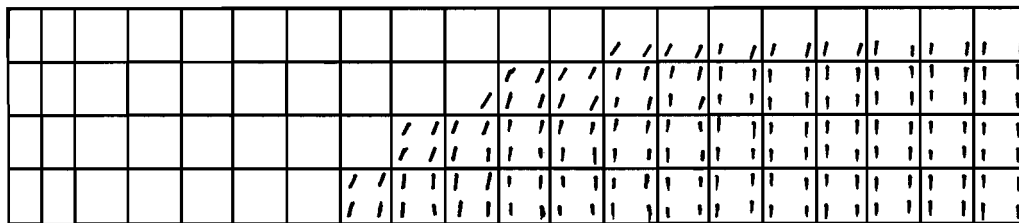


Figure 7.5: Effect of concrete tensile strength on load-deflection response of beam LS1



(a) $f_r=5.1$ MPa



(b) $f_r=8.0$ MPa

Figure 7.6: Crack patterns for beam LS1 at failure using different values of f_r

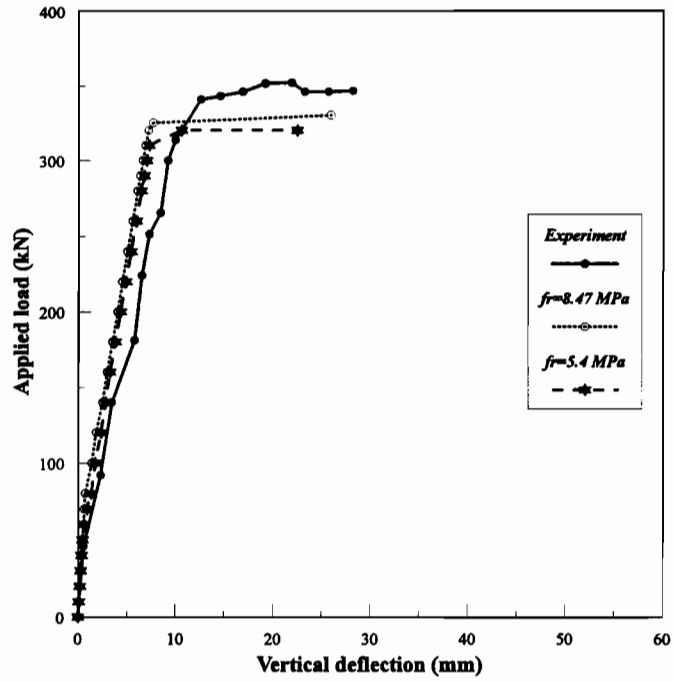


Figure 7.7: Effect of concrete tensile strength on the load-deflection response of the LS2

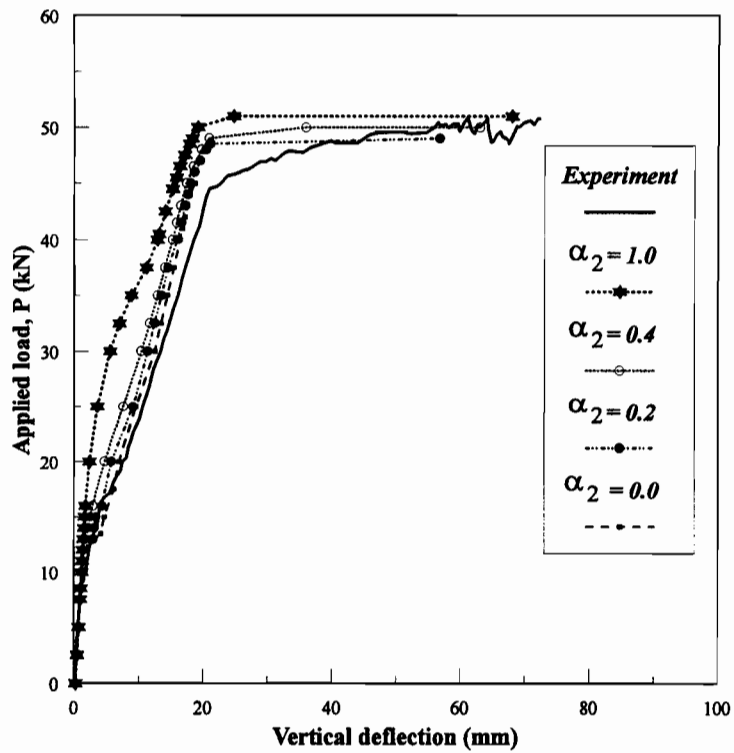


Figure 7.8: Effect of tensile softening branch factor, α_2 , on the response of beam HUCB

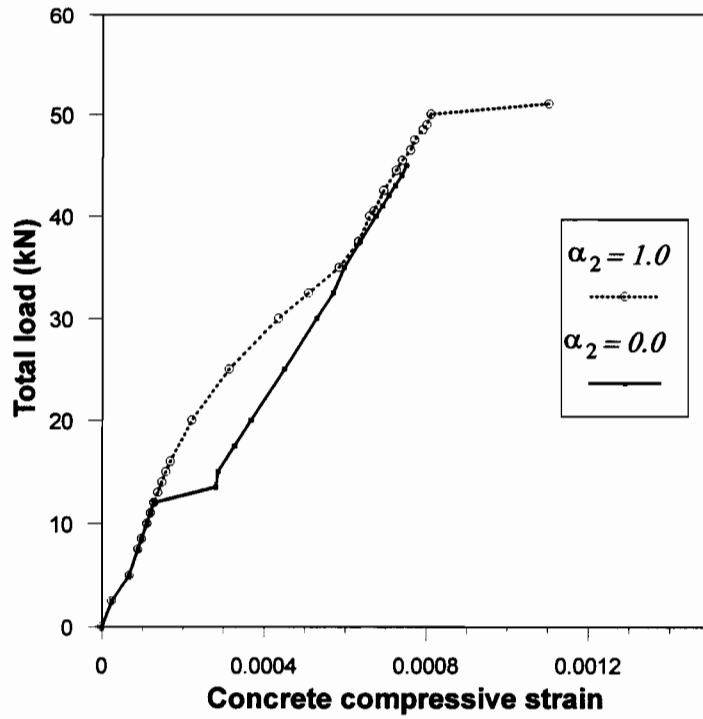


Figure 7.9: Load-concrete compressive strain curve at the top of beam HUCB at midspan

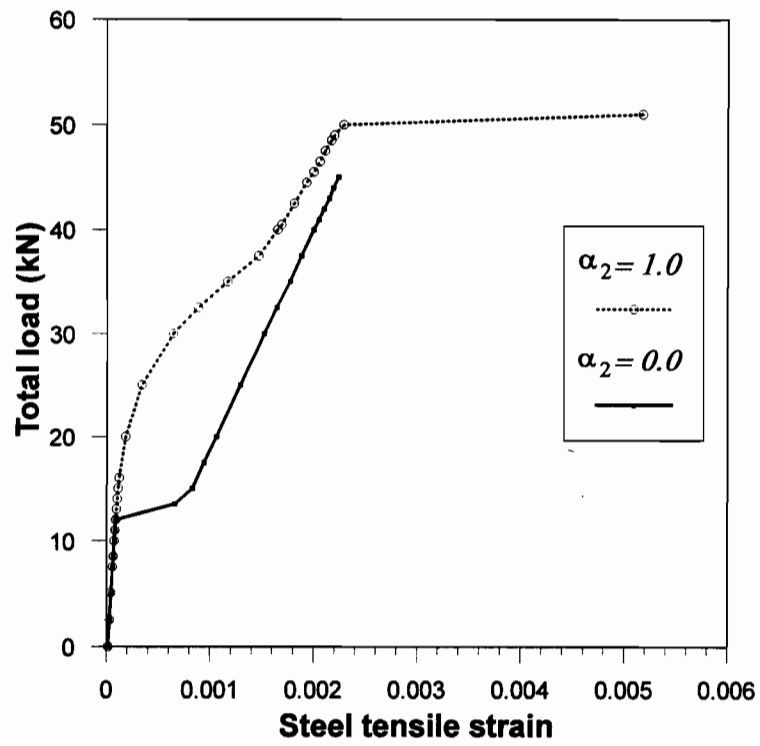
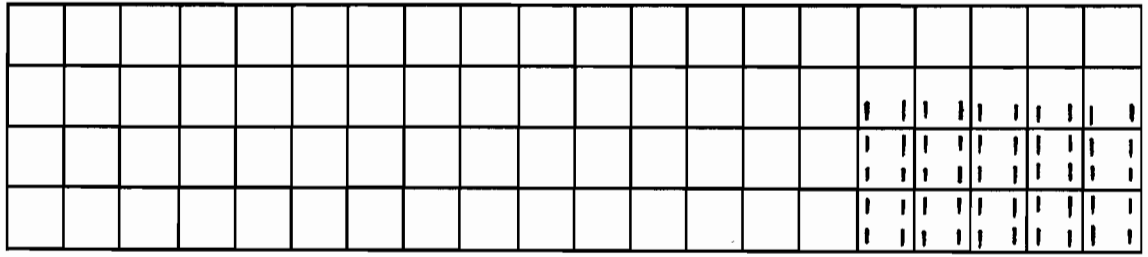
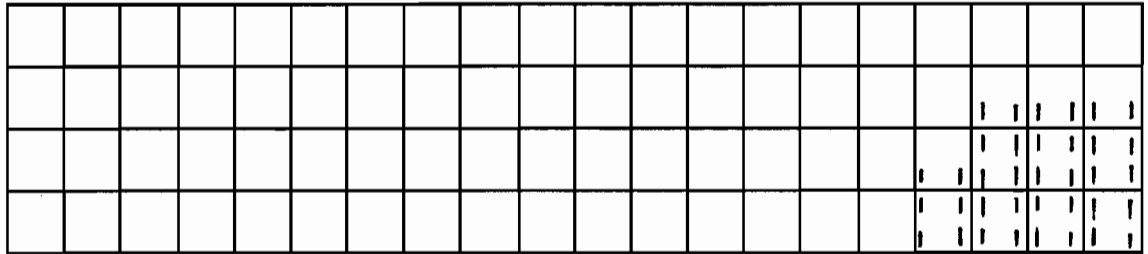


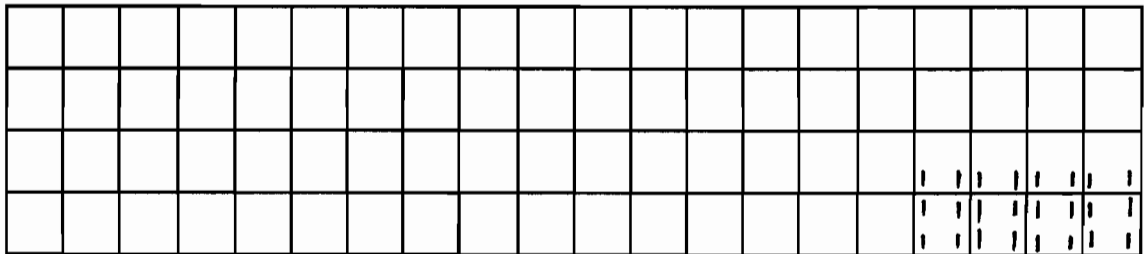
Figure 7.10: Load-steel tensile strain curve at the bottom of beam HUCB at midspan



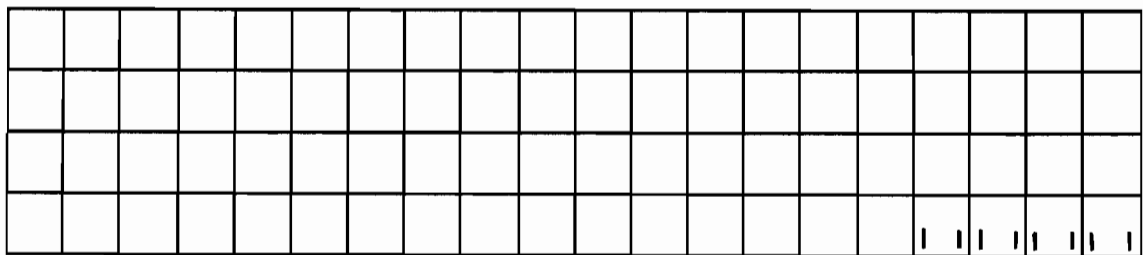
(a) $\alpha_2=0.0$



(b) $\alpha_2=0.2$



(c) $\alpha_2=0.4$



(d) $\alpha_2=1.0$

Figure 7.11: Crack patterns for beam HUCB at initial cracking using different values of α_2

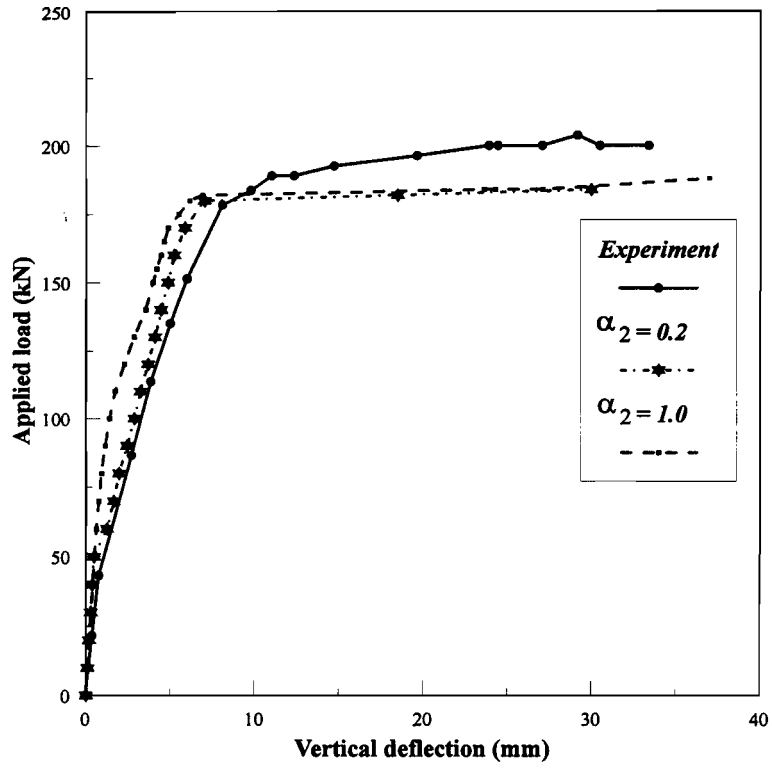
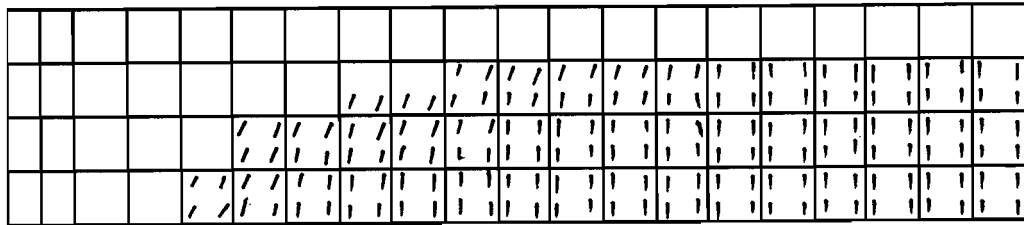
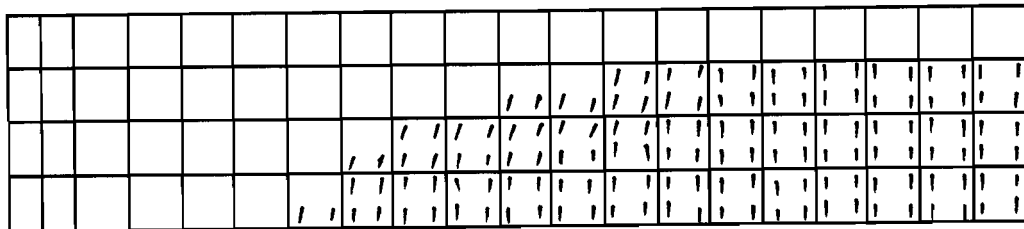


Figure 7.12: Effect of tensile softening branch factor, α_2 , on response of beam LS1



(a) $\alpha_2=0.2$



(b) $\alpha_2=1.0$

Figure 7.13: Crack patterns for beam LS1 at load level of $P=180$ kN using different values of α_2

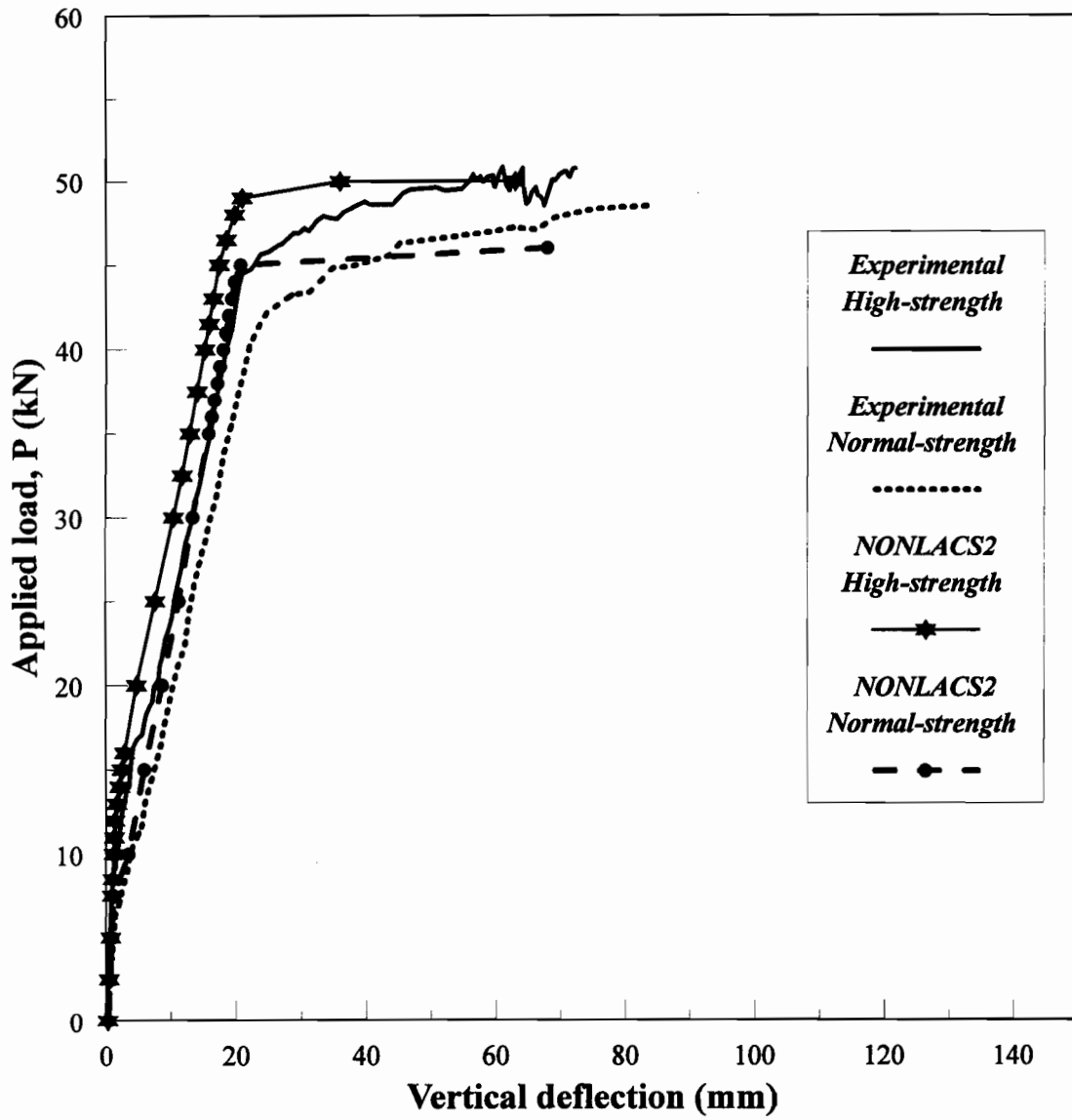


Figure 7.14: Comparison of normal and high-strength concrete beams, UCB and HUCB

CHAPTER 8

FINITE ELEMENT ANALYSIS OF REINFORCED CONCRETE FRAMES

This chapter investigates the nonlinear behaviour of a reinforced concrete (R C) single-bay portal frame, FP4, tested by Cranston and Cracknell (1969) under monotonically increasing vertical and lateral loads. The capability and accuracy of the finite element program, NONLACS2, in predicting the nonlinear response of R C frame structures is verified along with a comparison between the analytical and the corresponding experimental results. The effects of finite element size, concrete ultimate tensile strain, and tension-stiffening on the response of the R C frame, FP4, are also investigated in this chapter. In addition, the program is used to carry out a "plastic" analysis of the frame to define the mechanism of failure, the plastic hinge rotations, and their yielding and equivalent lengths. The location and the sequence of formation of hinges and the final collapse mechanism for the frame FP4 are also discussed. The different frame behavioural aspects including the cracking, yielding and ultimate load, load-displacement curve, load-strain curves for concrete and reinforcement, crack patterns, and the plastic hinge deformations are studied.

8.1 PREVIOUS STUDIES

The extensive experimental investigations carried out to study the nonlinear behaviour of R C frames structures can now be advantageously supplemented, or partially replaced by detailed nonlinear finite element analyses of their behaviour. It is now becoming possible, at a comparatively low cost and effort, to obtain a complete survey of the deformations of the concrete and the reinforcing steel along the frame structure, to detect their causes, and to study the effect of different variables at all stages of loading until the ultimate load.

Glanville and Thomas (1935) tested a series of R C frames, which were pin-ended single bay portals, and reinforced to obtain different types of failure. This was followed by considerable work in this area by Baker (1962), Cranston (1965), Becker (1967), Sader (1967), Cranston and Cracknell (1969), Shaikh et al. (1971), Adenot (1970), Wang (1970), Ernst et al. (1973), Lazaro and Richards (1973), Gunnin et al. (1977), Krishnamoorthy and Panneerselvam (1978), Darvall (1984) and others. Extensive reviews of analytical and experimental investigations on nonlinear behaviour of R C frames have been reported by Hsu (1974) and Ahmad (1996). Here, only some of the recent developments in nonlinear finite element analysis of concrete frames are briefly reviewed.

Pulmano et al. (1987) developed a simplified method for the analysis of R C frames subjected to sustained service loads. Modified stiffness approach along with Branson's equation were used to model the material nonlinearity of the concrete. The full-range of behaviour of frames up to the failure load cannot be predicted by this method.

The nonlinear behaviour of R C frames including the geometric and material nonlinearities together with the joint flexibility was investigated by El-Metwally and Chen (1989). They examined two frames tested by Ernst et al. (1973) subjected to vertical and lateral loads. Material nonlinearity was found to be the most influential factor on the behaviour of frames. Geometric nonlinearity played a more significant role in the case of lateral loads.

Kim and Lee (1992) used the displacement control method and the combined layered and modified stiffness approach to investigate the nonlinear behaviour of R C frames up to collapse. The spurious sensitivity to the chosen element size in the result of analysis by the finite element method for materials with strain-softening can be overcome by modifying the rigidities and the curvatures for each element based on the concept of concentrated inelastic rotations at a plastic hinge.

Mo (1992) investigated the material and geometric nonlinearities of R C frame structures. A formulation was devised to develop trilinear moment-curvature curves for the entire loading history, and an appropriate curve was selected for the critical section of the R C frame. It was noted that the ultimate curvatures at the critical sections were reduced by the presence of axial loads. When a plastic hinge formed in a column, the buckling strength of the column was reduced. The analytical results based upon these assumptions were in good agreement with the experimental results.

Sun et al. (1994) have developed a layered finite element model for nonlinear analysis of

R C frame structures. To account for both material and geometrical nonlinearities, the algorithms can analyze concrete frames up to the mechanism of failure. Comparison with the experimental results demonstrates that behaviour over the entire loading range until failure can be traced in a very reliable manner.

Rasheed and Dinno (1994) developed a numerical method for the analysis of R C plane frames. Economic and exact formulations for section analysis and the frame element modelling together with a suitable solution strategy and technique were adopted to construct an accurate and efficient analysis algorithm.

A survey of the literature shows that more analytical work is needed to investigate the yielding and equivalent plastic hinge lengths and rotations in R C portal frames. The present study is an extension of the previous studies carried out to examine the effect of monotonically increasing loading, plastic hinge formation and load-deflection relationships.

8.2 CCA SPECIMENS

Cranston and Cracknell (1969) tested seven R C portal frames at the Cement and Concrete Association, England, with fixed column supports, subjected to different loading conditions. It should be noted, however, that in all of these tests, the ultimate strength of the section and the plastic deformation were governed by the yielding of the reinforcing steel alone.

Three frames, FP4, FP3, and FP2 are analyzed using the NONLACS2 program in the present research program. The analytical results of frame FP4 are presented in this chapter and the results of frames FP3 and FP2 are discussed in detail in Chapter 9, where the layered finite element method and modified stiffness approach are compared with the experimental data. The dimensions of the frames and details of the loading are shown in Fig. 8.1. Each frame has two fixed supports; the beam span is 3050 mm (120 in), and the column height is 1524 mm (60 in), while the cross-section of the frame is constant throughout at 153 mm (6 in) deep by 102 mm (4 in) wide. The frame footing has a cross-section 102 mm (4 in) wide, 229 mm (9 in) deep, and 1270 mm (50 in) long. Provision was made for the application of both vertical (W_1) and lateral (W_2) loads, with a constant ratio W_2/W_1 , with the vertical load W_1 being applied as two equal concentrated loads placed symmetrically about the centre-line of the frame.

The details of reinforcement layout for the frames FP4, FP3, and FP2 are shown in Figures 8.2, 8.3 and 8.4, respectively. The major variables are the percentage and layout of the

longitudinal reinforcement. The beam and the corner sections of frame FP4 were reinforced with 2.8% of tension reinforcement and 1.9% of compression reinforcement, while for frame FP3, the beam and the corner sections were reinforced with 3.7% of tension reinforcement and 1.9% of compression reinforcement. The midspan of beam and the corner sections of frame FP2 were markedly over-reinforced, having 6.0% of tension reinforcement and 2.0% of compression reinforcement. The concrete and the steel material properties used in the analysis are summarized in Table 8.1.

Table 8.1: Material properties used in the analysis of frames

Frame	f'_c (MPa)	E_c (MPa)	f'_t (MPa)	ϵ_{cr}	ϵ_{cu}^*	ν^*
FP4	25.5	22,160	3.10	0.00014	0.007	0.17
FP3	28.5	25,275	3.30	0.00013	0.007	0.17
FP2	18.9	18,980	2.70	0.00014	0.007	0.17

Frame	f_y (MPa)	E_s (MPa)	E'_s (MPa)	ϵ_{su}^*	ϵ_{sy}	$f_{y(stirrups)}$ (MPa)
FP4	440	200,000	6,200	0.15	0.0022	310
FP3	440	200,000	6,200	0.15	0.0022	310
FP2	440	200,000	6,200	0.15	0.0022	310

* Assumed values

8.3 EFFECT OF FINITE ELEMENT SIZE

In an attempt to investigate the influence of mesh size on the results of the finite element analysis of the frame structure, three types of mesh configurations with 89, 212 and 700 elements are used to analyze the frame FP4, as shown in Fig 8.5. The frames with these meshes are analyzed using the NONLACS2 program with no provision to account for the mesh size dependency (MDEP=1 or "no mesh dependency analysis"). In this case the value of ϵ_m is given as an input value by the user and the computed results are influenced by the element size. Here,

the ultimate tensile strain, ϵ_u , is assumed to be constant and equal to 0.0021 for all mesh sizes. Due to the unsymmetric loading on the frame, the entire frame is modeled for the finite element analysis. Since both the size of element and load increments have significant effect on the computed results, the same load steps are used for the different mesh configurations. The analytical results are used only for the preliminary analysis. The total load is applied to the structure in 30 load steps. The experimental results for the load-displacement curves and the ultimate loads are compared with the corresponding computed values. In each case, it is shown that the computed response and the ultimate load for these structures depend on the size and the number of elements.

As pointed out earlier, shell element type I is quite suitable for studying flexural behaviour problems, therefore, it is used to analyze the frame. The bending of these frames can be considered to be a plane stress problem, therefore, the concrete is modeled using one layer only. The longitudinal reinforcing bars are lumped in a single bar at the reference surface as a bar element. The stirrups are modeled as smeared steel layers and they are placed at their respective distances from the element reference surface.

The load-sidesway deflection curve for the frame FP4 is shown in Fig. 8.6, which presents the results for the models with three types of meshes. The coarser mesh of 89-element (152 mm x 152 mm) gives an ultimate load value of 49 kN, which is very close to the experimental ultimate load of 48 kN, while the medium size mesh of 212-element (76 mm x 76 mm) results in an ultimate load 39.4 kN, and the finer mesh of 700-element (38 mm x 38 mm) underestimates the ultimate load (35.6 kN). When a coarse mesh is used, the structure exhibits a stiffer behaviour compared with the experimental response. As can be seen in Fig. 8.6, with an increase in the number of elements, the structure is slightly more flexible than for the case for the coarse mesh idealization, and the frame tends to be less ductile. The pre-cracking behaviour and the cracking load is the same and equal to 6.67 kN for the different mesh configurations.

The yielding and the ultimate loads for the different mesh configurations are compared with the experimental values in Table 8.2. This table shows that the ultimate load for the frame FP4 is dependent on the mesh configuration used in the analysis.

It can be noted that the ultimate load for this frame decreases with an increase in the number of finite elements, as observed for beams and shear panel in Chapter 4. The computed results are influenced by the element size and it emphasizes the sensitivity of the computed responses to the mesh characteristics.

Table 8.2: The yielding and ultimate loads of frame FP4 for different meshes

Number of Elements	Size of Element (mm x mm)	Cracking Load (kN)	Yielding Load (kN)	Ultimate Load (kN)	$P_u (Anl.) / P_u (Exp.)$
89	152 x 152	6.67	47.3	49	1.02
212	76 x 76	6.67	39.25	39.4	0.82
700	38 x 38	6.67	31.5	35.6	0.74
Experiment	---	---	44.2	48	---

This behaviour can be attributed to the fact that the energy dissipated during cracking decreases with the refinement of the finite element mesh. The problems of mesh dependency in using the NONLACS2 program have been discussed in Chapter 4. The sensitivity of the mesh size makes it difficult to decide on the critical mesh that will predict the "correct" response. Since the mesh configuration with 700 elements grossly under-estimated the response of the frame and needs large storage requirements and computational time, it was decided not to use it further in this study.

8.4 EFFECT OF CONCRETE ULTIMATE TENSILE STRAIN

The frame idealized using 89-elements (with element size equal to 152 mm x 152 mm) is analyzed with three different values of ϵ_{tu} . Two values of ϵ_{tu} are assumed ($\epsilon_{tu}=0.0007$ and 0.0021), and one value of $\epsilon_{tu}=0.001$ is calculated using the proposed equation 4.1. The magnitude of the cracking, yielding and ultimate loads for the different values of ϵ_{tu} are summarized in Table 8.3. Figure 8.7 shows the load-sidesway deflection curves at the top of the frame FP4 for 89-element model for different values of ϵ_{tu} . As can be seen from these curves, the change in the value of ϵ_{tu} does not have a large influence on the shape of the curves. With an increase in the value of the ϵ_{tu} , the effect of tension stiffening does not increase the ultimate load value significantly (refer to Table 8.3). The frame tends to be more flexible due to the lower value of the ultimate tensile strain, ϵ_{tu} . Also, it is evident that the proposed equation (Eq. 4.1) does not increase the ultimate load significantly.

Table 8.3: Summary of cracking, yielding and ultimate loads for different values of ϵ_{tu}

Number of Elements	Size of Element (mm x mm)	ϵ_{tu}	Cracking Load (kN)	Yielding Load (kN)	Ultimate Load (kN)	P_{Non} / P_{Exp}
89	152 x 152	0.0021	6.67	47.87	50	1.04
89	152 x 152	0.001 (Eq. 4.1)	6.67	46.75	47.8	0.99
89	152 x 152	0.0007	6.67	46.0	47	0.97
Experiment	---	---	---	44.2	48	---

The results of this investigation have shown that the change of the concrete ultimate tensile strain does not appear to have a significant effect on the load-deflection characteristics of the frame. Although the proposed model gives reasonable results for 89 and 212-element models, however, more analytical work is needed for frame with a very fine mesh configuration.

8.5 RESPONSE OF REINFORCED CONCRETE FRAME FP4

To achieve closer agreement between the computed results and the experimental values, smaller load increments are used in the analysis for the medium-size mesh configuration with 212 elements. The results include the load-deflection, load-concrete compressive strain, load-tensile steel strain curves and the crack patterns. The ultimate deformation characteristics such as plastic hinge length and rotations for this model are also discussed.

8.5.1 Load-Deflection Curve

Frame FP4 with 212-element model is analyzed to study the influence of tension-stiffening. Very small load increments are used near the critical loading stages such as cracking, yielding and the ultimate load. The experimental and the analytical (212 elements mesh) load-deflection curves for the frame FP4 are shown in Fig. 8.8. In the model without tension-stiffening, once a crack occurs, the concrete is unable to carry any forces between the cracks that results in a rapid deterioration of a frame stiffness as indicated by the change in slope of the load deflection curve. For the case where the concrete tension-stiffening is ignored, the analytical ultimate load is underestimated (40.34 kN) which is 16% lower than the experimental value. However, the model without tension-stiffening ($\epsilon_{tu} = \epsilon_{cr}$) exhibits softer response than the experimental finding.

In this case, the mode of failure is brittle without any deflection after yielding of reinforcement. When the tension-stiffening of the concrete is considered ($\epsilon_m=0.0021$, using proposed equation 4.1), the ultimate load increases to 43.6 kN which is about 9.2% lower than the experimental value of 48 kN and 7.7% higher than for the case when the tension-stiffening is ignored. In addition, the predicted load-deflection response is close to the experimental response until the first yielding of the steel reinforcement at 39.4 kN, which is 10% lower than the experimental yield load of 44.2 kN. The analytical value of the first cracking load is 6.67 kN. As shown in Fig 8.8, the deflection value at the failure stage is 122.7 mm which is 16% lower than the experimental value of 146.3 mm. The load-deflection curves (Fig. 8.8) also show that irrespective of the tension stiffening, the two models show initial cracking at the same load of 6.67 kN. However, the two loads-deflection curves deviate from each other immediately after the cracking load (Fig. 8.8). With further increase in load, yielding of the reinforcement occurs. The yield loads of the two models are approximately the same and equal to 39.4 kN). The difference in the deflection values between the two models is significant at the ultimate stage. This difference of the deflection values between the two models at the failure stage shows the importance of considering the tension stiffening in the analysis, in increasing the ductility of the structure. The following discussions are based on the analytical results for the 212-element model with tension-stiffening.

8.5.2 Load -Strain Curves for Concrete and Steel

Figure 8.9a illustrates the load-strain curve for the compression zone at the top of the mid-span of the beam in the frame. The initial crack forms in the concrete frame at the bottom of the mid-span section of the beam at a load level of 6.67 kN. At this stage, the neutral axis shifts from the mid-height of the section toward the compressive zone near the top. As the neutral axis approaches the compressive zone, the steel strain increases at a faster rate than the concrete strain. The concrete strain continues to increase at a constant rate until the initial yielding of the reinforcing steel occurs. This is when the first hinge forms at the top right hand of the column in the frame FP4. Increase in the concrete strain under constant load accompanies the formation of the second hinge at the right foot of the frame. This is indicated at the end of the plateau as shown in the Fig. 8.9a. Because of the tension- stiffening, the concrete is capable of resisting more loads. However, increasing the load further results in yielding of the steel reinforcement around the mid-span of the beam. This leads to the formation of the third hinge under the left concentrated load on the beam. The last hinge is formed at the left foot of the frame at the load

of 43.6 kN with a corresponding concrete strain value of 0.007. At this stage, the concrete at the critical sections becomes fully crushed with a considerable loss in stiffness and complete yielding of the reinforcing steel, leading to collapse of the frame.

The response of the longitudinal reinforcing steel is shown in Fig 8.9b, where the steel strain versus the load is plotted for the bottom of the mid-span of the beam in frame FP4. The reinforcing steel shows elastic behaviour with an increase in the load until the reinforcing steel starts to yield at a load of 39.4 kN. This is the stage where the first hinge is formed at the top right hand of the column in the frame FP4. The response then exhibits a short yield plateau (i.e, a horizontal portion of the curve where strain continues to increase at constant load). The end of this plateau is the stage at which the second hinge is formed at the right foot of the frame. An increase in the applied load results in an increase in the steel strain though at a slower rate until a load of 43.37 kN. This is the stage at which the third hinge is formed under the left vertical load. Therefore, the strain increases considerably with the load remaining constant until the frame fails as the last hinge is formed at the left foot of the frame.

8.5.3 Cracking Pattern and Formation Sequence of Plastic Hinges

In this section, the ability of the one mesh configuration (212-elements) to reproduce the crack propagation is presented. The cracking patterns for the other meshes have a similar trend. The propagation of the cracks along with the crushing of concrete and the sequence of plastic hinge formations are presented in Figures 8.10, 8.11, 8.12, and 8.13. In the following figures, the cracking of concrete is indicated by solid lines (KC=3 or 4 in Fig. 3.2a) and the crushing of concrete is represented by small circles (KC=6 in Fig. 3.2a). Because of computational time and storage requirements, only the output results are presented for integration points 3 and 9. Unfortunately, the experimental crack patterns are not available, to compare with the computed crack patterns.

Generally, the configuration of the cracks consists of flexural cracks (normal to the member axis) and flexural shear cracks (inclined cracks), at a load level of 6.67 kN as shown in Fig 8.10. The first crack appears with a slight inclination, forming around the bottom mid-span of the beam and the outer tension fibres of the right corner of the frame (beam and column). Further loading causes the cracking to spread at an increased inclination toward the compression zone at the left and the right corners of the frame due to the redistribution of the moments and forces, as shown in Fig 8.11. The initial yielding of the steel at the beam top near the right beam-column junction at a load of 39.4 kN is accompanied by crushing of the concrete at bottom face of the beam and inside the beam-column connection near the inside right corner, leading to the formation of the first hinge. The

location of the first hinge agrees quite well with the experimental results. With further increase in load, more elements crack, while other elements experience crushing at the right foot (outside of the column) of the frame until the second yielding of the steel occurs at 41.15 kN, leading to the formation of the second hinge (Fig 8.12). Increasing the load leads to the extension of the flexural crack at the mid-span of the beam which is indicated by the inclined crack. The third hinge forms at a load level of 42.25 kN under the left vertical load by the yielding of the tensile reinforcement, followed by crushing of concrete at the top. This phenomenon can be observed clearly from the crack patterns (Fig 8.13). At this point, most of the concrete around the critical section crushes at the three locations where the plastic hinges have been formed previously. At this stage, the steel enters the strain hardening zone, the steel strain increases until the ultimate load is reached at a load level of 43.37 kN. The fourth hinge forms at the left foot of the frame as shown in Fig. 8.14. Since the frame has a degree of indeterminacy equal to three, at this stage the frame loses its stability, when the ultimate load reaches a level of 43.37 kN, and failure occurs. The deformed shape of frame FP4 at ultimate stage is shown in Fig. 8.15.

8.5.4 Available Plastic Hinge Rotations

The different types of collapse mechanisms in a single bay frame loaded to failure have been discussed by Ahmad (1996). The alternate mechanisms are assumed by considering the action of the separate loads as their actions cause deformations at the various hinges. The hinge at the critical section could develop either in the beam and /or in the column, or at the points of application of loads, depending on the relative ultimate moment capacity of the hinged section.

Figure 8.16 shows the distribution of the yield and ultimate curvatures, yielding length and equivalent plastic hinge length at the critical points of the frame. The values of the tensile steel strain and the concrete compressive strain at each section and at the same load step are used to derive the yield and ultimate curvatures. Then the area under curvature-yielding length gives the plastic hinge rotation θ_p . Finally using Eq. 2.44, the equivalent plastic hinge length, l_p , is computed. For example, for the right corner of frame, the yield length, l_y , extends from the edge of the corner frame over a 533 mm length (Fig 8.16). The yield and the ultimate curvature values at the right hand corner of the frame are $\phi_y=3.15 \times 10^{-5}$ rad/mm and $\phi_u=7.48 \times 10^{-4}$ rad/mm, respectively. The ultimate curvature is located at the edge of the right corner of the frame. Integration of the curvature diagram area either at the top of column or at the corner of beam provides the analytical plastic rotation $\theta_p=0.125$ rad, while the experimental plastic rotation for this region is $\theta_p=0.113$ rad. The equivalent plastic hinge length in this region is 174 mm (1.2d).

This value is within the limits noted in the literature ($0.4d < l_p < 2.4d$). Unfortunately there are no experimental values in this region to compare the accuracy of the values of the computed yielding and the equivalent plastic hinge lengths. The same procedure is used for calculating the plastic hinge length at the other critical sections.

The plastic hinges rotation calculated using the NONLACS2 program are compared with the experimental values in Table 8.4. Although the analytical results are slightly lower than the experimental values, the agreement between the two sets of results is very good. The maximum deviation between the analytical and the experimental values of the plastic hinge rotations is approximately 13%, while the minimum deviation is 4%. Therefore, the above method of calculation for the plastic hinge rotation gives good correlation with the experimental values. Figure 8.16 and Table 8.4 indicates the ability of NONLACS2 program to predict the plastic rotation, equivalent plastic hinge and yielding length which is difficult to obtain even in the experimental tests.

Figure 8.17 shows a comparison between the position of the plastic hinges obtained in the experimental and the analytical work using the NONLACS2 program. The location of the analytical plastic hinges are exactly the same as in the experimental findings. The failure mechanism obtained experimentally shown in Fig. 8.17 is in good agreement with the results obtained from the NONLACS2 program. In the case of R C members in which the strength varies with the curtailment of reinforcement, it is possible for hinges to occur at other points along the length of members. It had been noted in the tests that the plastic hinge did not in fact, develop directly under the loads, or in locations immediately adjacent to joints. For this reason, it was decided to locate the hinges 76 mm (3 in) away from the theoretical point of maximum moment (Cranston and Cracknell, 1969).

Table 8.4: Comparison of experimental and analytical plastic hinge rotations

Sequence and Location of Plastic Hinge		Plastic Hinge Rotation, θ_p (rad)		θ_p (Anl) / θ_p (Exp)
Sequence	Location	Experimental	NONLACS2	
First Hinge	Right Corner	0.13	0.125	0.96
Second Hinge	Right Foot	0.13	0.113	0.87
Third Hinge	Left Vertical Point Load	0.09	0.0945	1.05
Last Hinge	Left Foot	0.08	0.0754	0.94

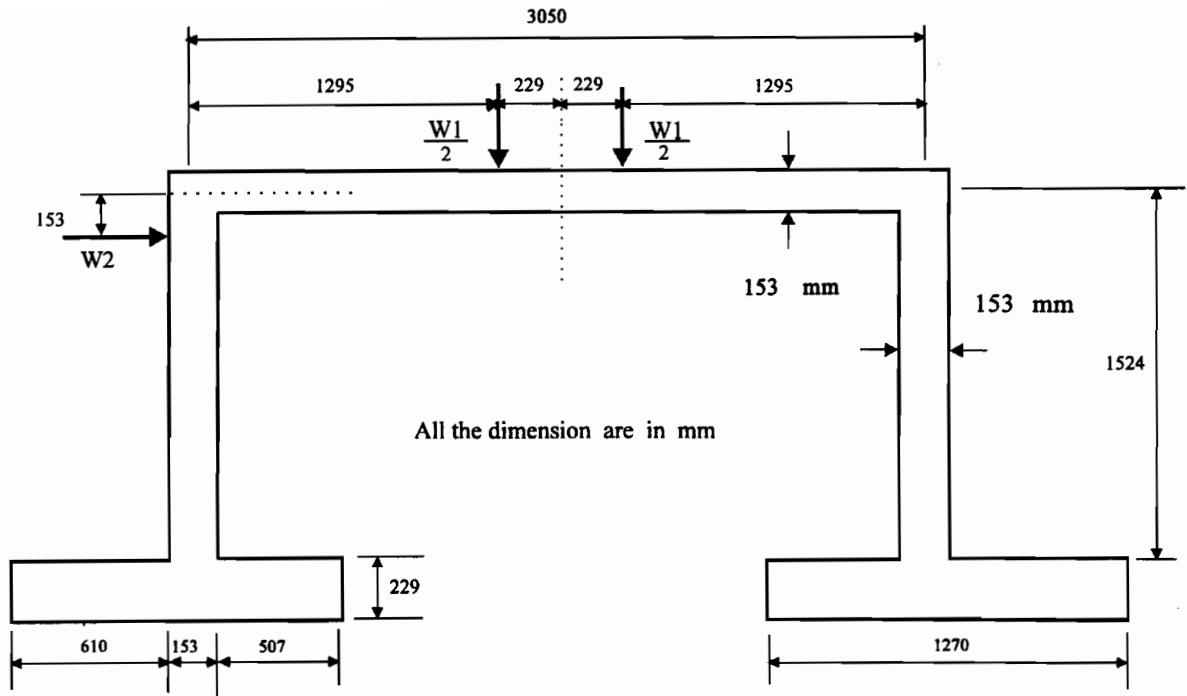


Figure 8.1: Geometry of frames FP4, FP3, and FP2 tested by Cranston and Cracknell (1969)

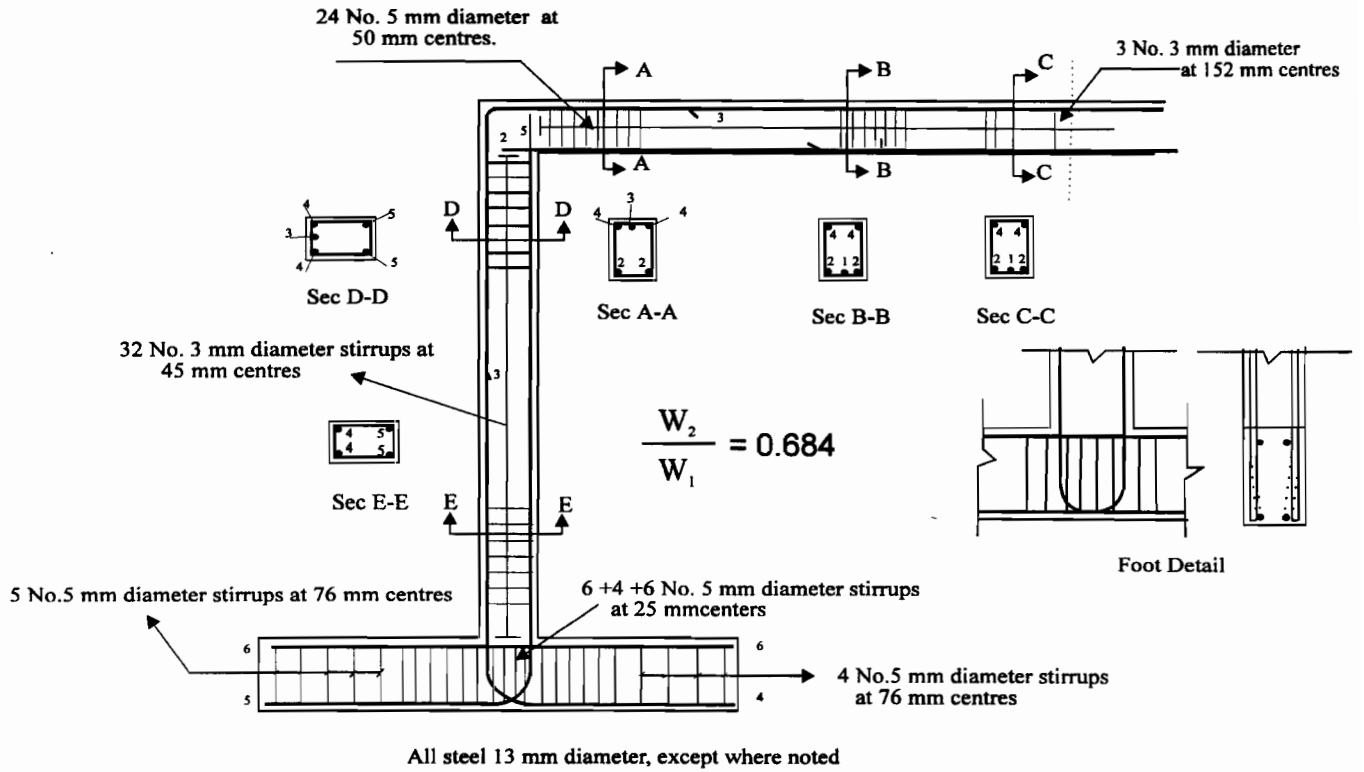


Figure 8.2: Reinforcement details for frame FP4

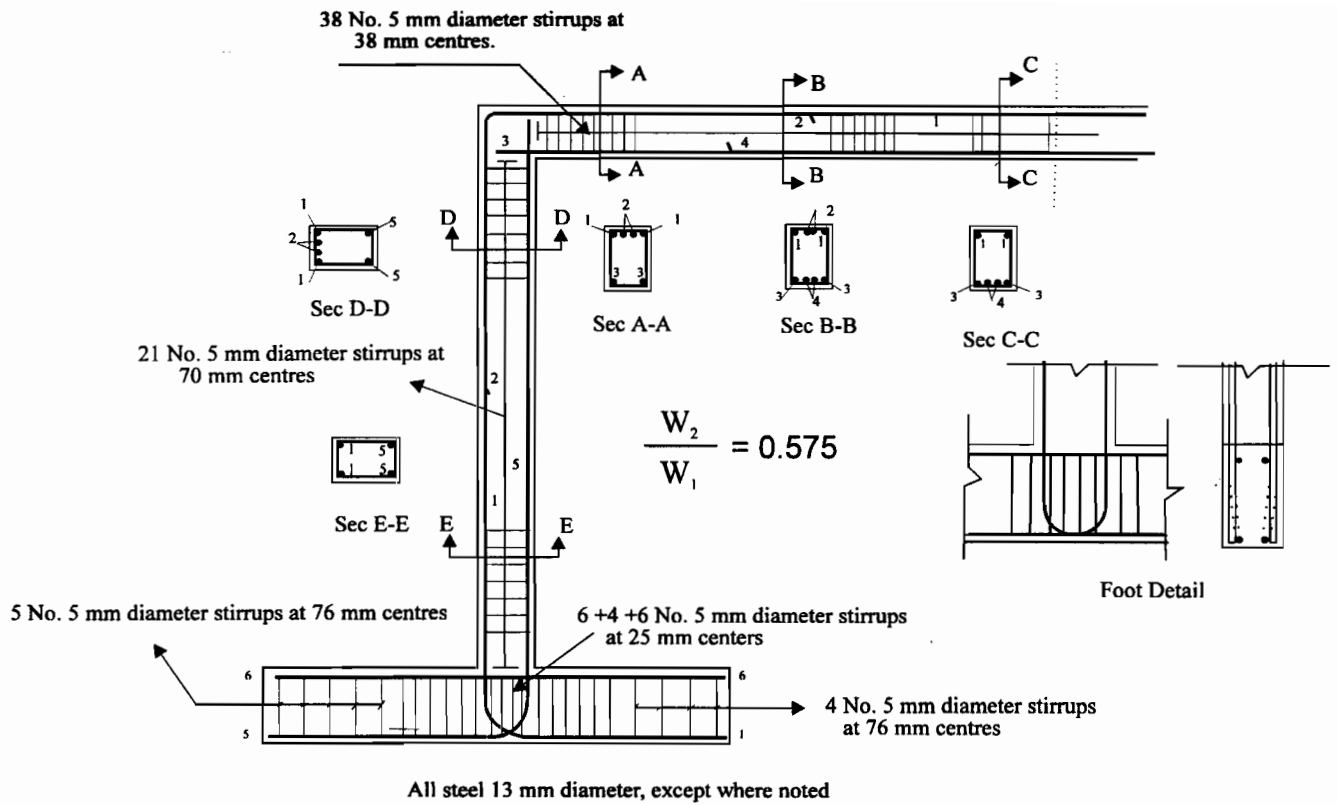


Figure 8.3: Reinforcement details for frame FP3

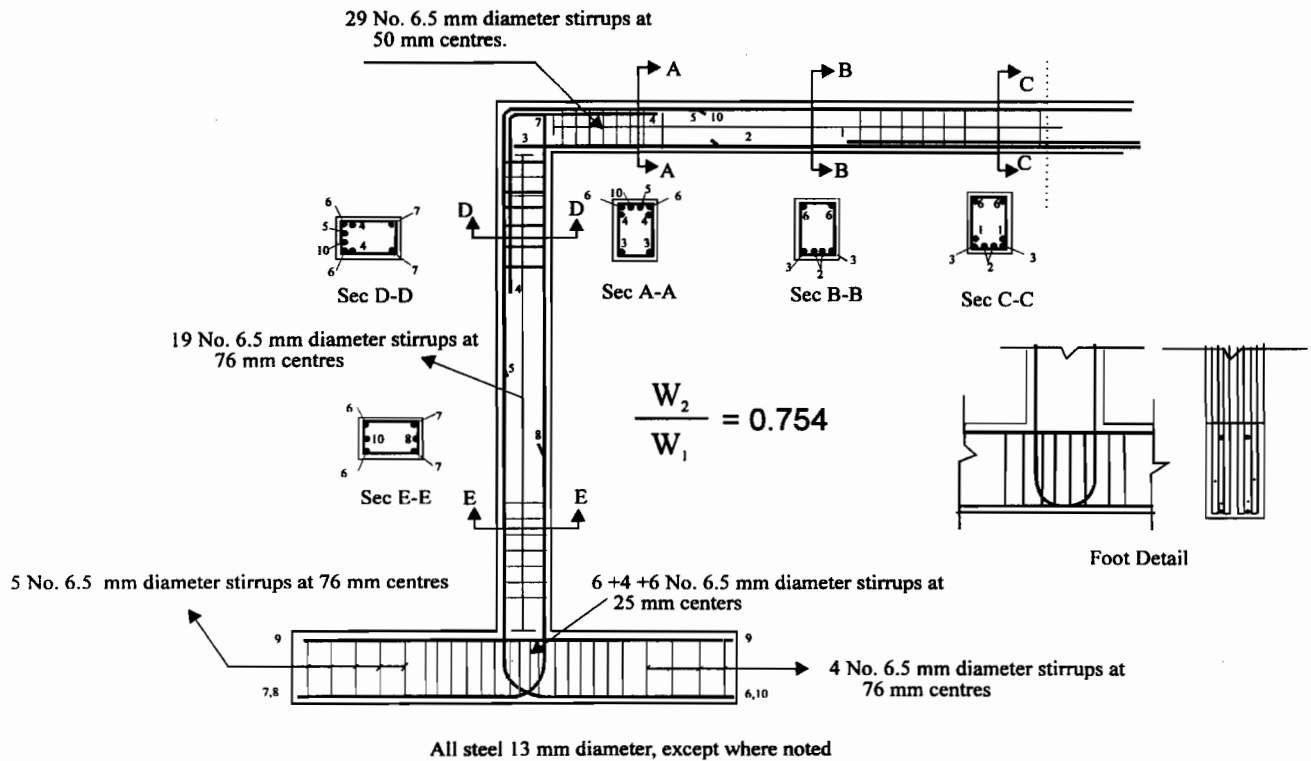
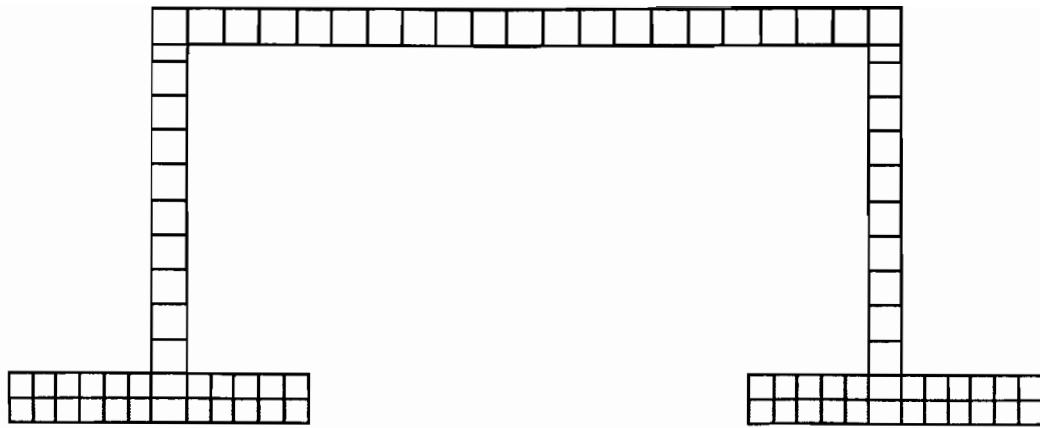
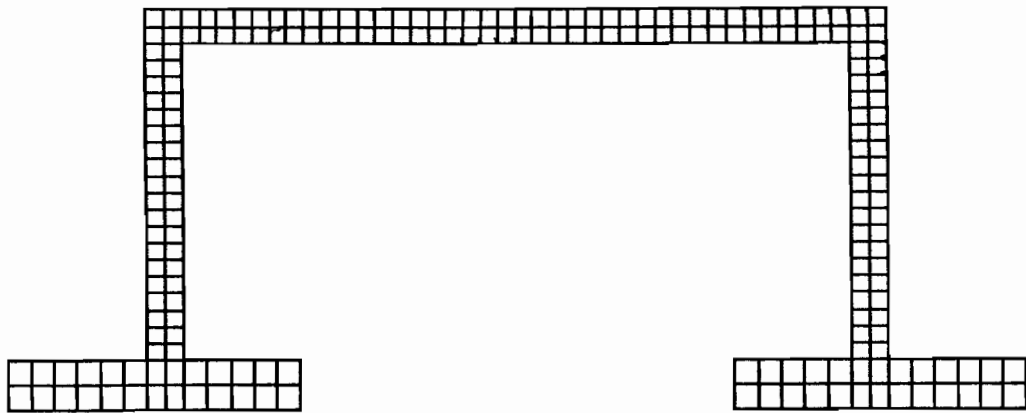


Figure 8.4: Reinforcement details for frame FP2



(a) 89-Element Model



(b) 212-Element Model



(c) 700-Element Model

Figure 8.5: Mesh configurations for frame FP4

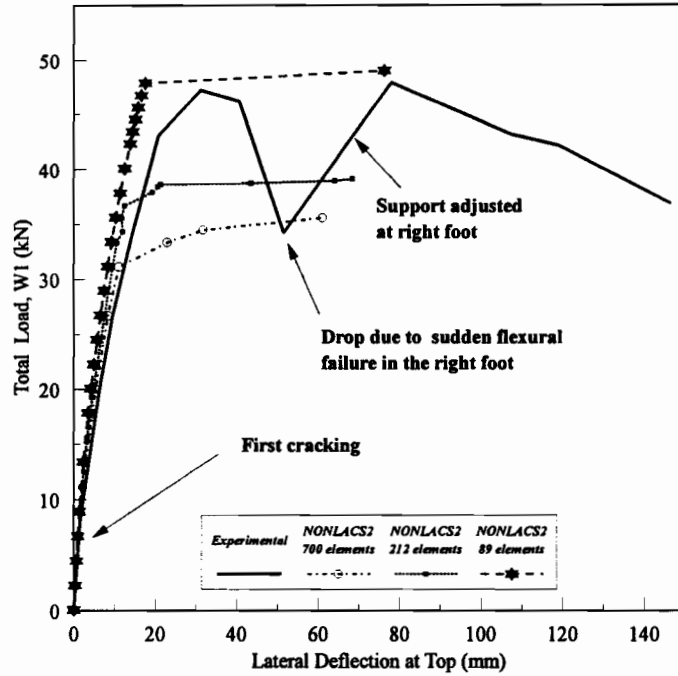


Figure 8.6: Load-deflection curves for different mesh sizes for frame FP4 ($\epsilon_{tu} = 0.0021$).

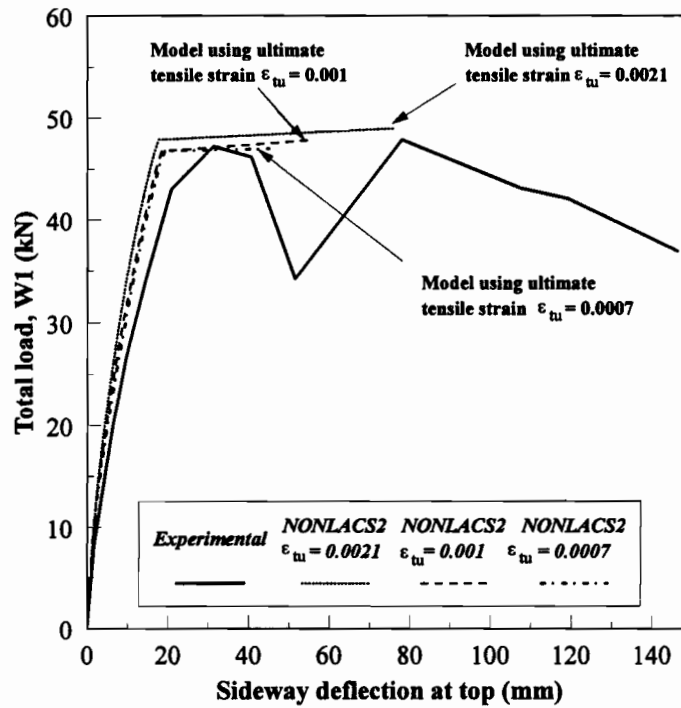


Figure 8.7: Load-deflection curve for frame FP4 idealization 89-elements with different values of the concrete ultimate tensile strain, ϵ_{tu}

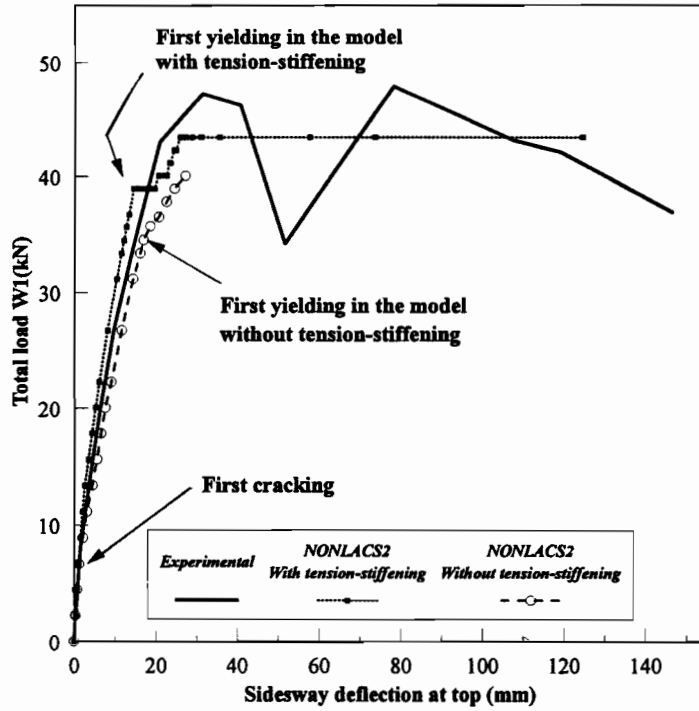
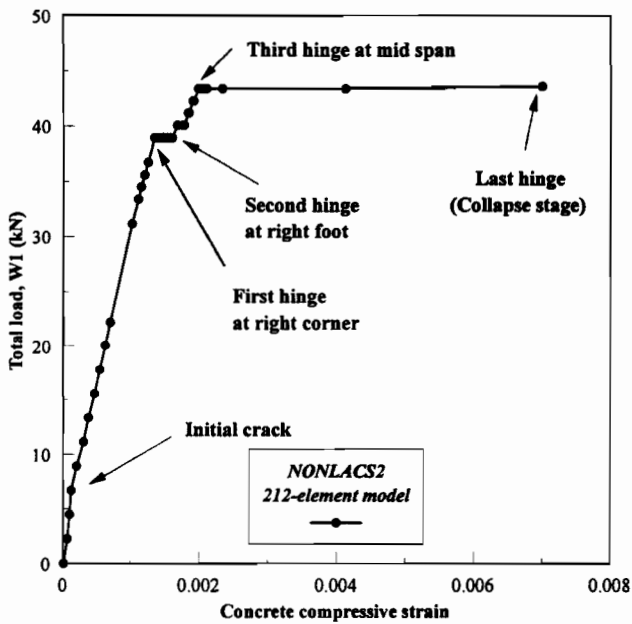
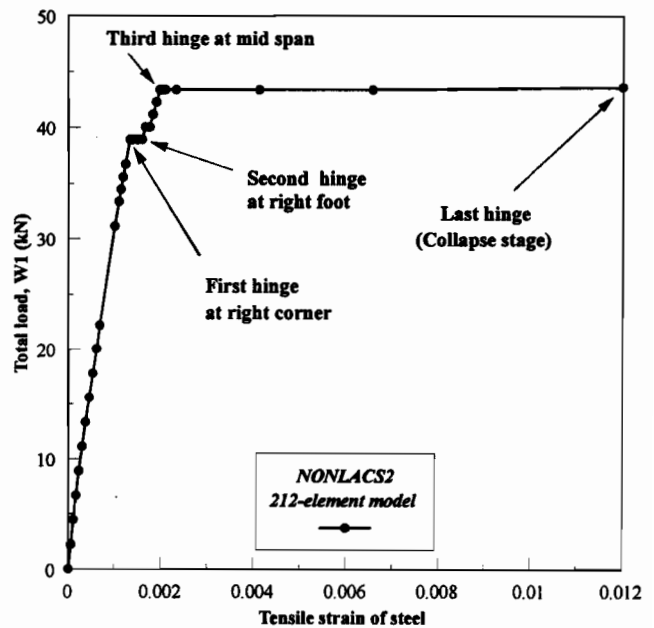


Figure 8.8: Effect of tension-stiffening on the response of the frame FP4 (212-element model)



(a)



(b)

Figure 8.9: Load-steel and concrete strain curves at the mid-span of the beam in the frame FP4

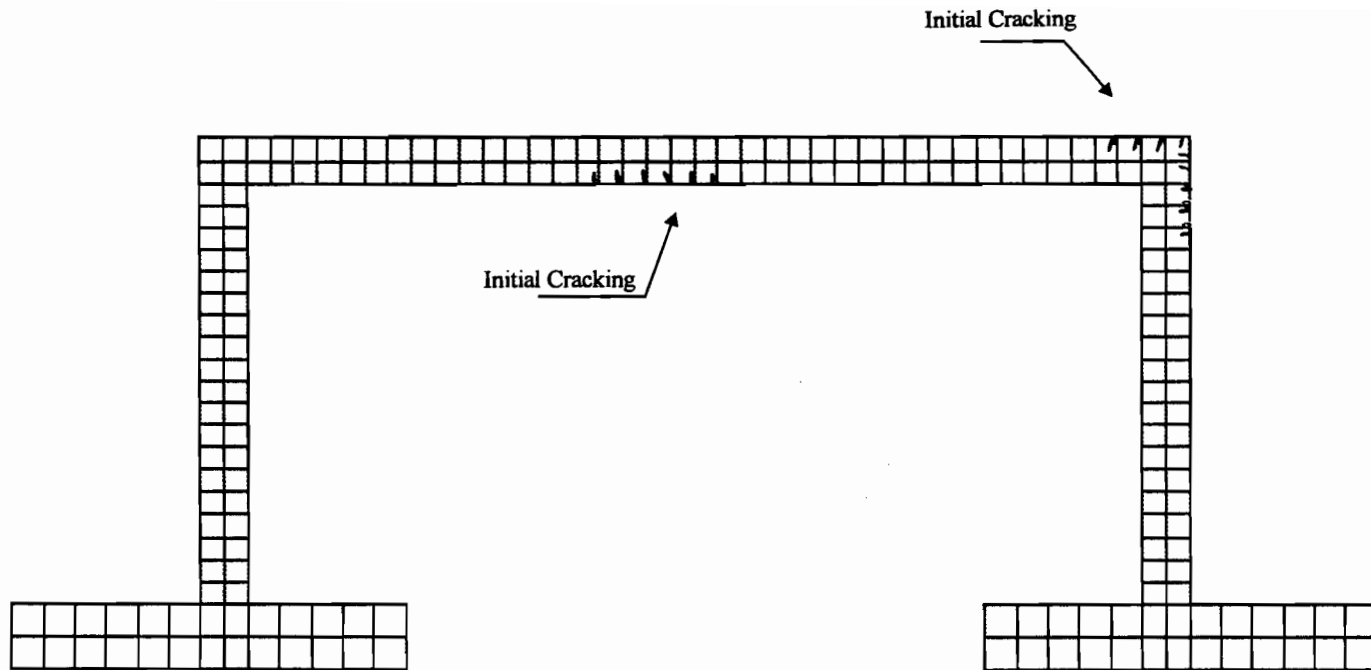


Figure 8.10: Initial crack pattern at load level of 6.67 kN

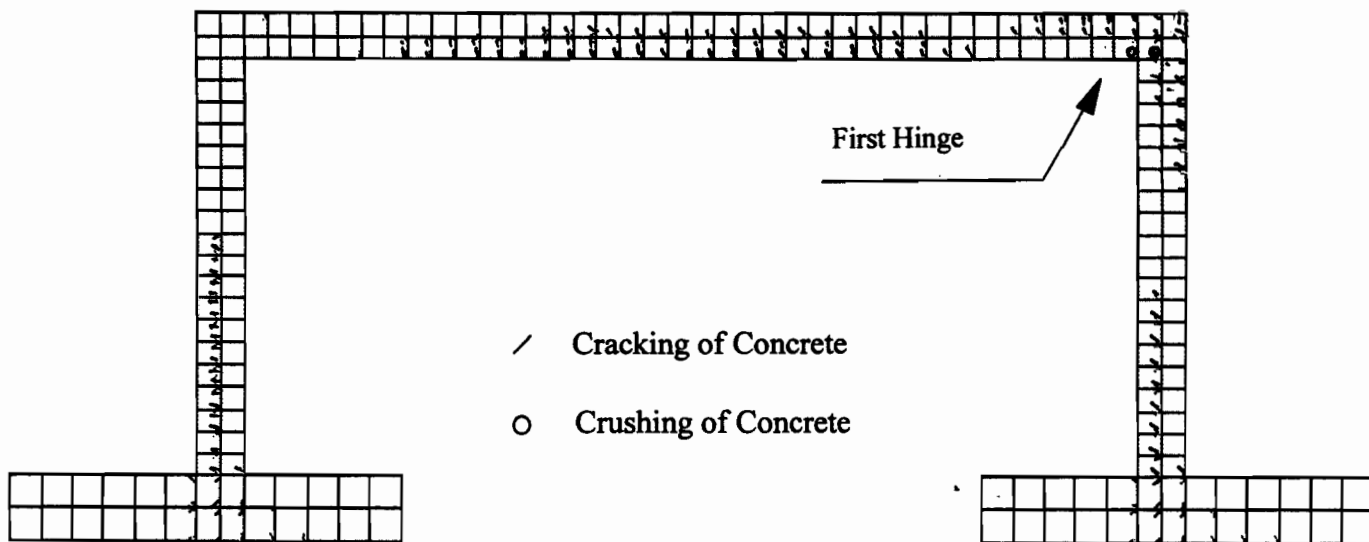


Figure 8.11: First hinge formation at the right hand corner of the frame at load level of 39.4 kN

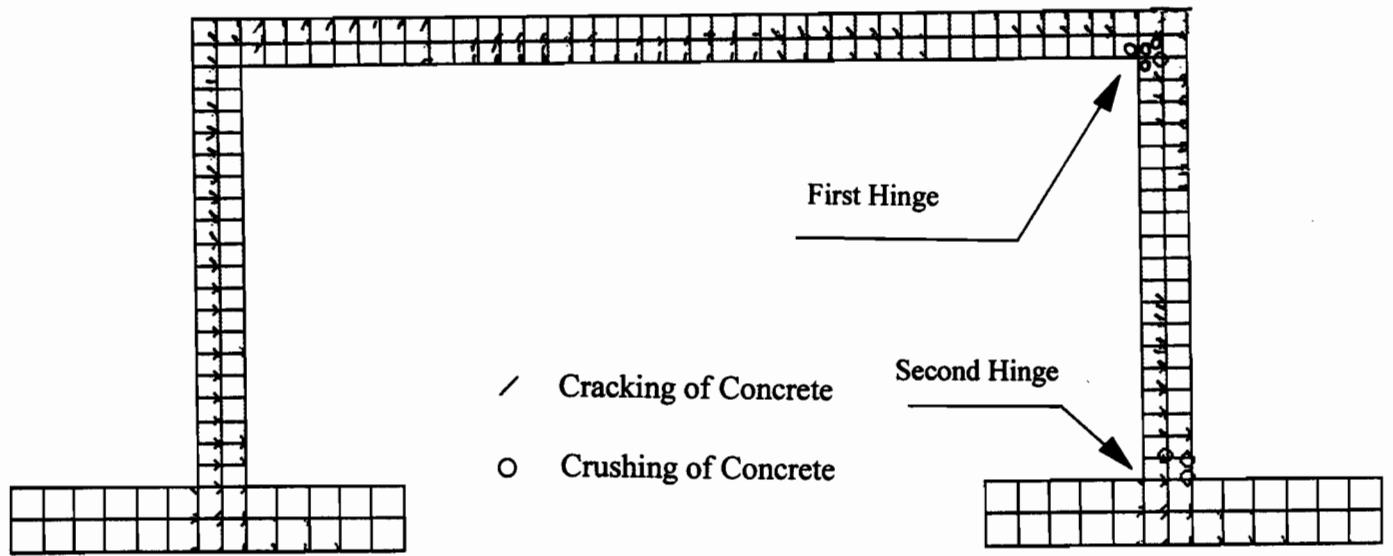


Figure 8.12: Development of the second hinge at the right foot at load level of 41.15 kN

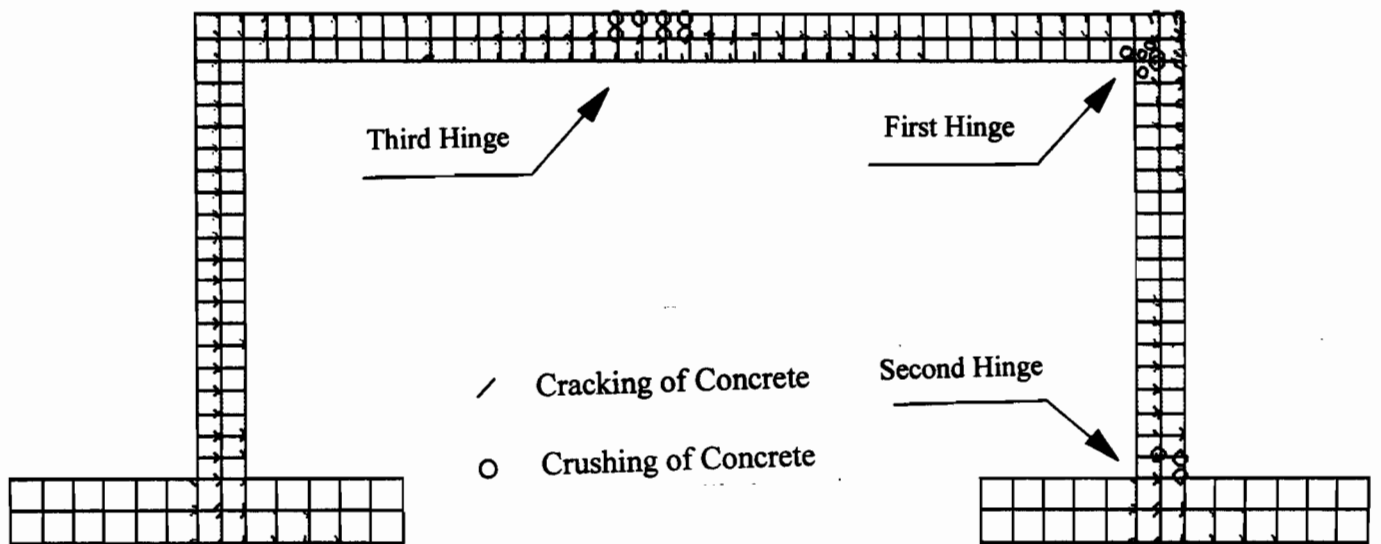


Figure 8.13: Development of the third hinge before the collapse at load level of 42.25 kN

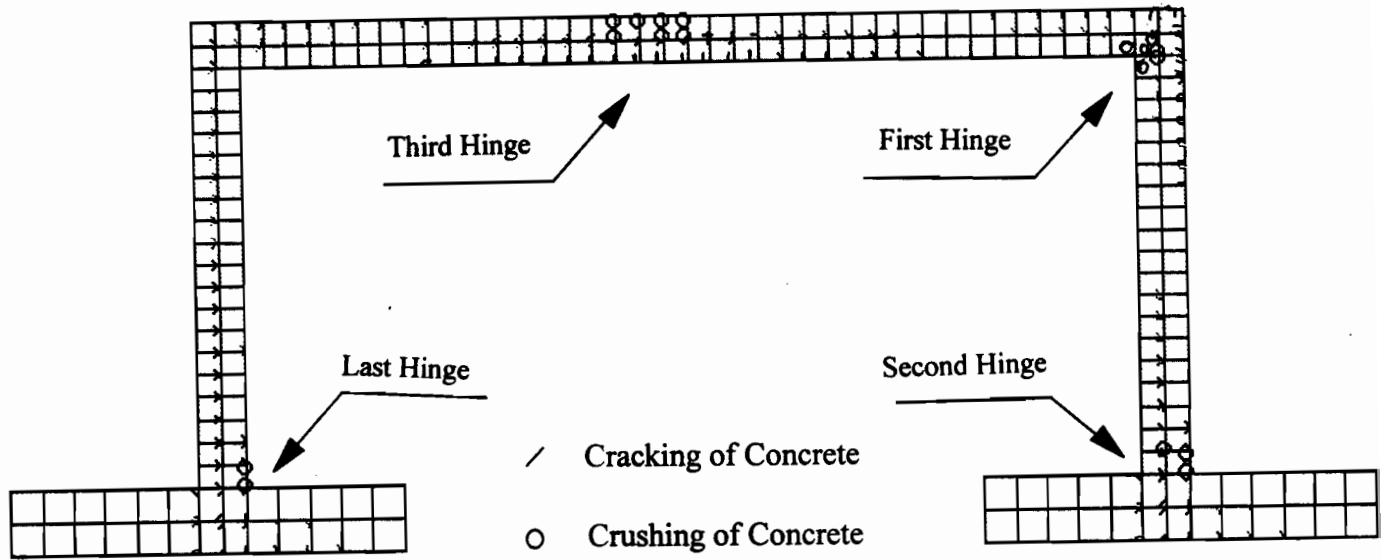


Figure 8.14: Last hinge formed at ultimate load of 43.37 kN

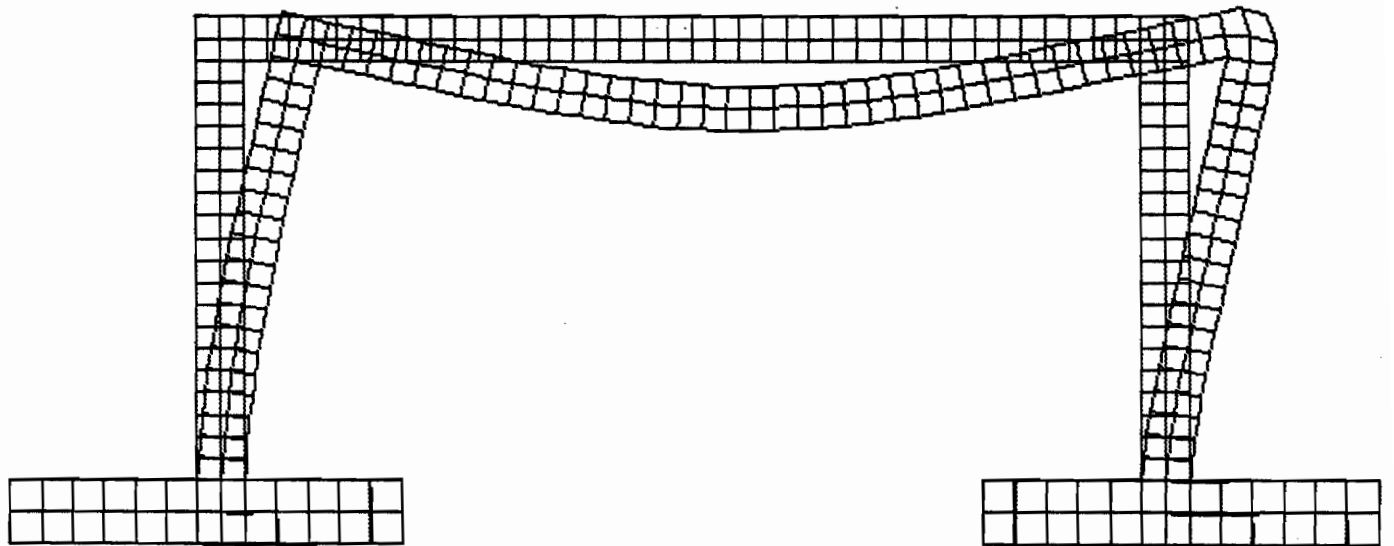


Figure 8.15: Deformed shape of frame FP4 at the failure ($P_u=43.37$ kN)

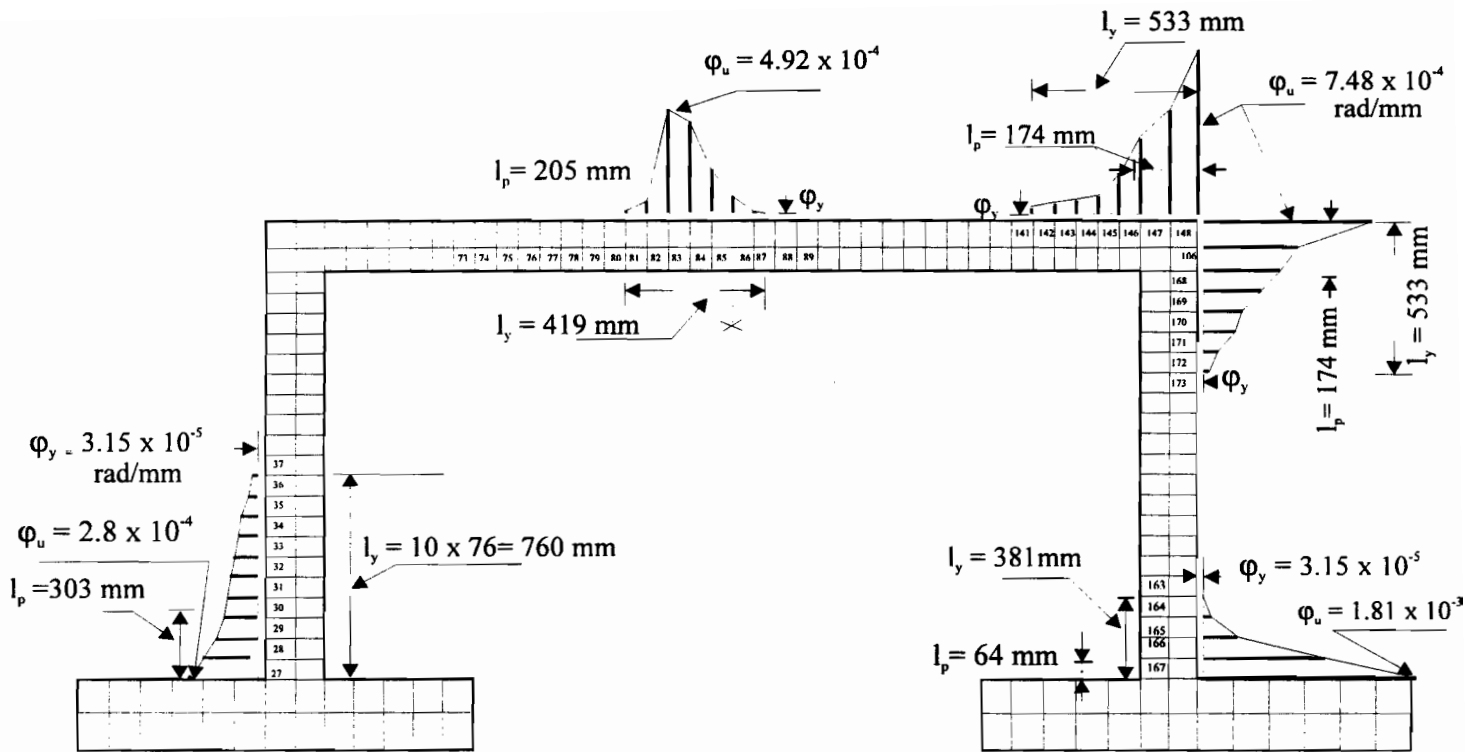


Figure 8.16: Distribution the yield and ultimate curvatures at the critical sections of frame FP4

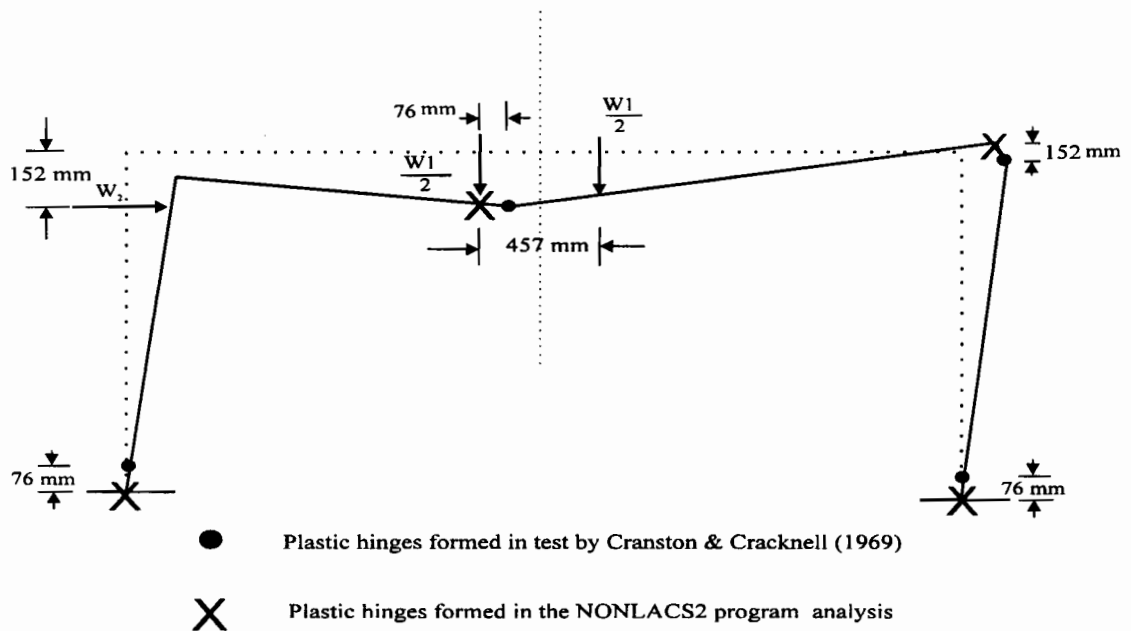


Figure 8.17: Experimental and analytical location of plastic hinges for frame FP4

CHAPTER 9

NAFS- A FINITE ELEMENT PROGRAM FOR NONLINEAR ANALYSIS OF FRAMED STRUCTURES

This chapter presents the key features of a nonlinear finite element analysis computer program, NAFS (Nonlinear Analysis of Frame Structures), as a practical engineering tool based on the displacement formulation of the modified stiffness approach. The variation of flexural rigidity at the section at different loading stages and along the length of element are studied in this chapter. The flexural rigidity equations, proposed in Chapter 5, are utilized to establish the stiffness matrix for the beam element (one-dimensional element). The new 2-node nonlinear beam element with a degrading stiffness matrix is developed to model cracking and other nonlinear effects throughout the entire loading range from zero to the ultimate load. The NAFS program provides a speedy and economical method for analysis of large planar frame structures with an adequate solution accuracy. The computer output gives the complete load-deflection and moment-rotation characteristics, the location and the rotation capacity of the plastic hinges until a collapse mechanism is attained. The accuracy and efficiency of NAFS program is also verified through comparison of the analytical results obtained from both the layered finite element approach (NONLACS2) and the modified stiffness approach (NAFS) with the experimental data from tests on reinforced concrete (R C) frames (FP2, FP3, FP4) and continuous beams (C1 and C2), conducted at the Cement and Concrete Association, and McGill University, respectively.

9.1 MODIFIED STIFFNESS APPROACH

For nonlinear analysis of R C structures using the finite element method, both the modified stiffness and the layered approaches are used widely. In the layered approach, made up

of a series of layers idealized as being in a state of plane stress, leads to greater success than the modified approach, but the time required is too great. Therefore, it is not very efficient to use nonlinear analysis for a wide range of structures using the layered approach. In the modified stiffness approach, the analysis results are obtained speedily by using the beam elements that account approximately for the nonlinear behaviour of the structural concrete. Previous work on the modified stiffness approach has been reviewed in Section 3.1.3.

This chapter deals with nonlinear finite element analysis of R C continuous beams and framed structures by using the modified stiffness approach. Consideration of shear deformations and shear failures, bond-slip between the steel and the concrete, long-term sustained, and cyclic loadings are not included. Geometric nonlinearities caused by P- Δ effect are also neglected.

9.2 VARIATION OF FLEXURAL RIGIDITY ALONG BEAM LENGTH

Because of the varying amounts of reinforcement and the extent of cracking, the flexural rigidity of R C beam is not constant along the span length of the beam. The variation of the flexural rigidity along the member due to cracking causes the distribution of bending moments to change from that calculated by the elastic theory using a constant flexural rigidity. With further loading, the extent of cracking increases and the distribution of the flexural rigidity, and the resulting bending moments, get modified again. Therefore, it is important to study the distribution and the magnitude of the flexural rigidity along the length of the member through the various load stages.

To investigate the variation of the flexural rigidity along the beam span through the various load stages, Mattock's beam M11 subjected to a concentrated load and M81 subjected to uniform loads are analyzed using the NONLACS2 program. Figures 9.1 and 9.2 show the variation of flexural rigidity ratio, $(EI)_{\text{un}}/(EI)_{\text{cr}}$, with respect to the ratio X/L for beams M11 and M81, respectively, at five different load steps: before and after cracking, at service load and at yielding and the ultimate load stages. In these figures, X is the distance from the left support and L is the span of beam. The flexural rigidity for loads greater than the cracking load varies along the beam with a maximum value near the support where there is no cracking and a minimum value at the midspan of the beam. For the ultimate load, the flexural rigidity decreases rapidly from the support to midspan of the beam. The value of flexural rigidity tends to zero in the midspan where the structures carries the maximum moment. At the ultimate load stage, Branson's

equation gives a constant flexural rigidity and equal to 2.46×10^9 kN.mm² over the length of beam regardless the type of loading.

Comparison of Figures 9.1 and 9.2 (beams M11 and M81) reveals that, at the same level of load (e.g. $P/P_u=0.33$), the cracked length of the beam under concentrated load is 1764 mm which is 16 percent less than that under uniform load.

The variation of flexural rigidity along the length of member is assumed to be linear and defined by its values at the two ends of element as follows:

$$(EI)_A = (EI)_i - \left(\frac{X}{L}\right)[(EI)_i - (EI)_j] \quad (9.1)$$

where $(EI)_A$ is the tangent flexural rigidity of the section A, X is the distance of the section A from the left end (end i), L is the length of element, $(EI)_i$ and $(EI)_j$ are the flexural rigidities at ends i and j of element, respectively (Fig. 9.3). The second term in Eq. 9.1 represents the reduction of flexural rigidity due to cracking along the length of the member. As expected, with a decrease in the length of the finite element, the accuracy of predicted flexural rigidities using Eq. 9.1 increases. The parabolic variation of EI along the length is also assumed and the corresponding equation and the modified stiffness matrix are presented by Kheyroddin and Mirza (1994). The effect of cracking and others types of nonlinearity in the section is taken into account by determining the EI values in accordance with the procedure proposed in Chapter 5. The proposed equations take into account the effect of the tension and compression reinforcement ratios, concrete compressive strength, type of loading, cracking and tension-stiffening. The flexural rigidity of the section at each load step, $(EI)_i$ and $(EI)_j$, is either uncracked when $M_a \leq M_{cr,ani}$, or cracked when $M_a > M_{cr,ani}$. The flexural rigidity in the pre-cracking stage is assumed to be constant and equal to $(EI)_{cr}$ [Eq. 5.4]. The flexural rigidity after cracking is obtained using Eq. 5.7.

9.3 MODIFIED STIFFNESS MATRIX FOR BEAM ELEMENT WITH BOTH ENDS-FIXED

The material nonlinearity is considered in the derivation of an explicit expression for the beam-element stiffness matrix, which considers a linear variation of the flexural rigidity over its length. Figure 9.4 shows the positive directions and numbering of the end forces \bar{p} and the corresponding displacements \bar{u} in the local coordinate systems (xy). For the beam element, the member deflection, w, is assumed to be a cubic polynomial and the axial displacement, u, is considered to be linear. Thus

$$w = C_1 x^3 + C_2 x^2 + C_3 x + C_4 \quad ; \quad u = a_1 x + a_2 \quad (9.2)$$

From the virtual-work basis of finite element method, without considering axial components, the element stiffness matrix can be obtained by

$$k = \int_V B^T E B dV = \int_0^L \begin{bmatrix} 12x-6L \\ 6Lx-4L^2 \\ -12x+6L \\ 6Lx-2L^2 \end{bmatrix} [(12x-6L) \quad (6Lx-4L^2) \quad (-12x+6L) \quad (6Lx-2L^2)] (EI)_{(A)} dx \quad (9.3)$$

where L is the length of element. Finally, by substituting the value of $(EI)_A$ from Eq. 9.1 into Eq. 9.3 and neglecting the coupling between the axial and the flexural rigidities (i.e., the P-Δ effect), the element stiffness matrix in local coordinates for member with both ends fixed is given by:

$$k = R_i \begin{bmatrix} \frac{EA}{2LR_i} & 0 & 0 & -\frac{EA}{2LR_i} & 0 & 0 \\ 0 & 6 & 4L & 0 & -6 & 2L \\ 0 & 4L & 3L^2 & 0 & -4L & L^2 \\ -\frac{EA}{2LR_i} & 0 & 0 & \frac{EA}{2LR_i} & 0 & 0 \\ 0 & -6 & -4L & 0 & 6 & -2L \\ 0 & 2L & L^2 & 0 & -2L & L^2 \end{bmatrix} + R_j \begin{bmatrix} \frac{EA}{2LR_j} & 0 & 0 & -\frac{EA}{2LR_j} & 0 & 0 \\ 0 & 6 & 2L & 0 & -6 & 4L \\ 0 & 2L & L^2 & 0 & -2L & L^2 \\ -\frac{EA}{2LR_j} & 0 & 0 & \frac{EA}{2LR_j} & 0 & 0 \\ 0 & -6 & -2L & 0 & 6 & -4L \\ 0 & 4L & L^2 & 0 & -4L & 3L^2 \end{bmatrix} \quad (9.4)$$

in which EA is the axial rigidity, $R_i = (EI)_i / L^3$, and $R_j = (EI)_j / L^3$. Here, it can be seen from Eq. 9.4, that the use of the constant value of flexural rigidity of cracked transformed section at midspan for entire length of beam based on Branson's equation results a smaller value of stiffness, and consequently, the calculated deflection leads to an overestimation of deflection.

9.3.1 Hinge at Left End

At each load step, the total internal moments at the end of each member is compared with the yielding moment of section, M_y (when the tension reinforcement yields). If the internal moment exceeds M_y , the plastic hinge is assumed to form. When an additional hinge is installed, it is necessary to modify the member stiffness matrix.

When a plastic hinge is present at the left hand of member ij (end i), by letting \bar{p}_3 (moment at end i) equal to zero in Fig. 9.4, the stiffness matrix can be modified to:

$$k = R_j \begin{bmatrix} \frac{EA}{LR_j} & 0 & 0 & -\frac{EA}{LR_j} & 0 & 0 \\ 0 & 3 & 0 & 0 & -3 & 3L \\ 0 & 0 & 0 & 0 & 0 & 0 \\ -\frac{EA}{LR_j} & 0 & 0 & \frac{EA}{LR_j} & 0 & 0 \\ 0 & -3 & 0 & 0 & 3 & -3L \\ 0 & 3L & 0 & 0 & -3L & 3L^2 \end{bmatrix} \quad (9.5)$$

It can be noted that when the plastic hinge forms at end i, the modified stiffness matrix is independent of the flexural rigidity at end i. The axial stiffness of the element is unaffected by the plastic hinge.

9.3.2 Hinge at Right End

When a plastic hinge is present at the right hand of member ij (end j), by letting \bar{p}_6 (moment at end j) equal to zero, the stiffness matrix can be modified to:

$$k = R_i \begin{bmatrix} \frac{EA}{LR_i} & 0 & 0 & -\frac{EA}{LR_i} & 0 & 0 \\ 0 & 3 & 3L & 0 & -3 & 0 \\ 0 & 3L & 3L^2 & 0 & -3L & 0 \\ -\frac{EA}{LR_i} & 0 & 0 & \frac{EA}{LR_i} & 0 & 0 \\ 0 & -3 & -3L & 0 & 3 & 0 \\ 0 & 0 & 0 & 0 & 0 & 0 \end{bmatrix} \quad (9.6)$$

9.4 COMPUTER PROGRAMMING AND SOLUTION PROCEDURE

The linear elastic stiffness method from the conventional matrix structural analysis is modified to accommodate the effects of the material nonlinearity of concrete. An incremental/iterative solution technique is used to solve the problem incorporating the material nonlinearity. It implies that the total load can be applied in 30 load steps, and in each load step, a maximum of 15 iterations is carried out until the convergence is reached. The origin of the NAFS program can be traced back to the earlier linear elastic program developed by the author (Kheyroddin 1991). Because of space limitation, only the modifications of the NAFS program is

explained here and the key features of the linear matrix structural analysis program can be found in the work by Kheyroddin (1991) and in standard matrix structural analysis texts (e.g. Weaver and Gere 1990).

9.4.1 Solution Procedure

A flowchart for the NAFS program is shown in Fig. 9.5. The procedure for the nonlinear analysis used here is as follows:

- a) Discretize the structure into one dimensional beam elements considering the reinforcement details, material properties, and the location of loading.
- b) Total load vector is divided and applied in a number of load increments ($F_i = \sum \Delta F_i$).
- c) Calculate the stiffness matrix, k , of each element using the cracking flexural rigidity, $(EI)_{cr}$, assuming that all sections are uncracked in first load step.
- d) Assemble the structure stiffness matrix K .
- e) An elastic analysis of the structure subjected to incremental external loads $\{\Delta F_i\}$ is performed and the incremental nodal displacements are calculated as:

$$\{\Delta \delta_i\} = [K_{i-1}]^{-1} \{\Delta F_i\} \quad (9.7)$$

- f) For each element, obtain the incremental internal forces at ends i and j and calculate the total internal forces.
- g) Apply the next load step.
- h) Determine the values of $M_{cr,anal}$ and M_y and check the condition of the section (cracking or yielding).
- i) Calculate $M_a/M_{cr,anal}$ (M_a obtained in step f) and use the proposed EI formulations to determine the value of EI at the beginning of each load step.
- j) Update the stiffness matrix k using $(EI)_i$ and $(EI)_j$ for each element.
- k) Repeat steps d through j until the value of EI for each element has converged to within a specified tolerance (a maximum of 15 iterations in each load step).
- l) If the value of M at the end of each element exceeds the moment corresponding to the yielding moment, M_y , plastic hinge is assumed to be formed at that section. For this element, a stiffness matrix with an end hinge is used (Equations 9.5 and 9.6).
- m) The amount of incremental plastic hinge rotation, $\Delta \theta_p$, at each load step is calculated.
- n) For divergence, displacement divergence criteria are used. If any of the nodal displacements exceeds the corresponding maximum displacement values input as the divergence values, the

solution is terminated.

The NAFS program can analyze any steel and R C indeterminate frame structures with different loading types (uniform loads, concentrated loads) with different support conditions (fixed, pinned, and spring support or a support with a known displacement). Also, it has the ability to predict the response of a structure subjected to temperature variations. The computer output gives the complete load-deflection and moment-rotation characteristics, the location and the sequence of hinge formation, and the rotation capacity of the plastic hinges until a collapse mechanism is attained. In the service load range, this program can be used for predicting the instantaneous deflections of R C beams. A detailed description of the input data required to run the program is presented in Appendix B.

9.4.2 Plastic Hinge Rotation

When the plastic hinge forms, the incremental moment in the hinge is assumed to be equal to zero and the total moment at the hinge regions is constant and equal to M_y . After calculation of nodal displacement and rotations and internal forces for a given member, the slope-deflection method is used to determine the amount of incremental plastic rotation, $\Delta\theta_p$, in each load step. At the ultimate stage, the total plastic hinge rotations are determined by summation of the incremental plastic rotations at each section. It is postulated that a structure statically indeterminate to degree N will develop $(N+1)$ hinges before final collapse unless a local collapse mechanism is formed first.

For calculation of yielding moment, M_y , depending on the given values of axial load and strains at the edges of the cross-section, an iterative scheme (trial and error) is used to locate the position of the neutral axis. The stresses are then integrated over the cross section to determine the value of yielding moment. For calculation of yielding moment in the column section with a certain value of axial load, at first the neutral axis depth, c , is assumed. Then the values of steel and concrete strains and stresses are calculated. Based on the integration of the area of stress-strain curve of concrete in the compression zone and the internal forces, the value of axial load is determined (equilibrium). This procedure is repeated until, the axial load converges to the value of the axial load obtained from the NAFS program. After convergence, the yield moment, M_y , is calculated for the section.

9.5 APPLICATION OF NAFS PROGRAM

The reliability and accuracy of the NAFS program is demonstrated by comparison of experimental and analytical results obtained from NAFS and NONLACS2 program. The following two experimental test series are studied.

9.5.1 Analysis of Two-Span Continuous Beams

Adaszkievicz (1977) tested three continuous beams subjected to uniformly distributed loads, and two of them, C1 and C3, are selected for analysis using the NONLACS2 and the NAFS programs. Figure 9.6a shows the geometry and the loading condition of these beams. Considering symmetry, only one half of each beam is analyzed using the layered finite element method (NONLACS2 program) and the modified stiffness approach (NAFS program). The sectional and the material properties are presented in Table 9.1. In the modified stiffness approach, one half of beam is divided into only 3 elements (Fig. 9.6b), while using the layered finite element analysis, one half of the beam is discretized into 192 elements as shown in Fig. 9.6c.

Since the experimental load-deflection curves were obtained for the point which is located a distance of $3/8$ of the span length from the end supports (i.e. 857 mm from the left support), one node in the finite element model is selected at this section. The computed load-deflection curves of beams C1 and C3 using layered finite element approach (NONLACS2) and the modified stiffness approach (NAFS) are compared with the results experimentally obtained by Adaszkievicz (1977). As can be seen in Fig. 9.7, the load-deflection curve for beam C1 obtained from NAFS program is stiffer compared with the experimental load-deflection curve until a load intensity equal to 12 N/mm and then it is softer than the experimental load-deflection curve until failure. The layered finite element approach shows stiffer response compared with the experimental values until the yielding load which is equal to 16.57 N/mm. A summary of the analytical and the experimental results at cracking, yielding and the ultimate load stages for the continuous beams is presented in Table 9.2. The ultimate load obtained from the NONLACS2 program is 17.54 N/mm, which underestimates the ultimate load by 17.6 percent, while the value obtained from NAFS program is 19.76 N/mm, which is close to the experimental value of 21.30 N/mm with a discrepancy of 7.2 percent. The yield load from the NAFS and the NONLACS2 programs are 18.38 N/mm and 16.57 N/mm, with a deviation of +8.6 and -2 percent from experimental value, respectively.

The load-deflection curves for the beam C3 using the NAFS and the NONLACS2 programs are compared with the experimental findings in Fig. 9.8. The load-deflection curve obtained from these two programs follow the same general pattern and are quite close to the experimental response. The load-deflection curve obtained using the NAFS program is stiffer than the experimental and NONLACS2 load-deflection curves until a load intensity equal to 12.5 N/mm and then exhibits softer response, very close to experimental response until load level equal to 15.00 N/mm. At high load levels, more than 12.5 N/mm, the beam response obtained from NONLACS2 program is stiffer than the other curves with yielding at a load of 14.62 N/mm which is very close to the yielding load obtained from NAFS program and a deviation of only 4.5 percent from experimental value of 15.32 N/mm. As can be seen from Table 9.2, the ultimate load value obtained using the NAFS and the NONLACS2 programs are approximately the same and underestimate the experimental ultimate load by about 11.5 percent.

The sequence and location of analytical hinge formation is shown in Fig. 9.9. In the experiment program, for beam C1, the first plastic hinge form at central support, followed by second hinge at midspan. As can be seen in Fig. 9.9a, the first plastic hinge for beam C1 using the NAFS program forms at the support and the second plastic hinge forms at midspan with an increase in the applied load, as observed in the experimental program. In the layered finite element method, first yielding of steel (plastic hinge) occurs at the top of central support at a load 16.57 N/mm where the negative moment is a maximum, and then at a load equal to 17.54 N/mm, the collapse mechanism develops with hinging at the midspan. For beam C3, the experimental results show that the ultimate moment at both the midspan and the support are reached almost simultaneously. The first plastic hinge using the NAFS program occurs at midspan followed by the second plastic hinge at the support with a very small increase in the value of applied load which shows a discrepancy from the experimental results. Using the NONLACS2 program, the first plastic hinge is predicted at the support at a load level of 14.62 N/mm followed by the second plastic hinge at the midspan at a load of 15.6 N/mm. Each beam is statically indeterminate to degree one and the formation of two plastic hinges causes its failure. The values of the experimental plastic hinge rotations are not available for comparison of the results. Both beams C1 and C3 subjected to uniform loads demonstrate considerable ductility. This can be attributed to the low steel percentages and the confining nature of the applied load which prevents spalling at mid-span.

It is obvious that the NAFS program can be used with reasonable accuracy for nonlinear

analysis of continuous beams with saving in the required computational time. It is shown that the NAFS program while providing considerable modelling advantages, leads to significant computational saving, with 95 percent reduction in CPU time achieved for beam C1 compared with the NONLACS2 program.

Table 9.1: Sectional and material properties of beams C1 and C3 (Adaszkiewicz 1977)

Beam	Section	b (mm)	d (mm)	d' (mm)	A _s (mm ²)	A _s ' (mm ²)	f _c ' (MPa)	f _{yt} (MPa)	f _{yc} (MPa)	E _s (MPa)	Spacing* (mm)
C1	Support	100	136	21.6	258	142	41	371.6	330	195000	38.1
	Span	100	134	16.3	142	38.7	41	330	482	190000	63.5
C3	Support	100	136	21.6	258	142	41.2	371.6	330	195000	63.5
	Span	100	134.6	16.3	103.2	38.7	41.2	391	330	200000	63.5

* Closed stirrups with diameter of 4.1 mm and yield strength of 255 MPa.

9.5.2 Analysis of Fixed-Base Portal Frames

Cranston and Cracknell (1969) conducted seven tests on fixed-base portal frames and three of them, FP4, FP3, and FP2, are chosen for analysis. These specimens were tested under monotonically increasing vertical load (W_1) and lateral load (W_2). The reinforcing details, material properties and loading conditions of these frames are described in Chapter 8. In the analysis of these frames using the NAFS program, the entire frame is discretized into 12 elements as shown as Fig. 9.10. For the NONLACS2 program, the mesh configuration with 212 elements is used (Fig. 8.2). For determination of the ultimate tensile strain, ϵ_{tu} , the proposed equation 4.1 is utilized. A summary of the cracking, yielding and ultimate loads computed for the different models for frames FP4, FP3, and FP2 are presented in Table 9.3.

The vertical load-sideway deflection curve for the frame FP4 using the different models is shown in Fig. 9.11. The ultimate load from the NAFS and the NONLACS2 programs are 43.66 kN and 43.37 kN, which underestimate the experimental ultimate load by about 9.1 percent and 9.7 percent, respectively. The load-deflection curve obtained from these two programs follow the

same general pattern and are quite close to the experimental response. As can be seen from Fig. 9.11, the ultimate lateral deflection using NAFS program is very close to the experimental value of 146.3 mm, while the NONLACS2 program underestimates this value by about 16 percent.

Figure 9.12 shows the analytical and experimental load-deflection curves for frame FP3. Both NAFS and NONLACS2 program exhibit stiffer response in comparison with the experimental finding. The ultimate load of the frame FP3, however, is somewhat underestimated by both the modified stiffness approach and the layered finite element method. The NONLACS2 program exhibits stiffer response at higher load levels, but it predicts the ultimate load of the frame quite accurately with a difference of 3.6 percent from the experimental value of 66.24 kN.

As can be seen from the load-deflection curve for the frame FP2 (Fig. 9.13), the analytical cracking load, using the NAFS program, is 5.00 kN, while the values of yielding load and ultimate load are $P_y=50.26$ kN and $P_u=62.20$ kN, respectively. The experimental yielding and ultimate loads for this frame are $P_y=57.8$ kN and $P_u=64.27$ kN, respectively. The analytical load-deflection curves obtained from the NAFS and the NONLACS2 programs follow the experimental curve quite closely. The model using the NONLACS2 program underestimates the ultimate load of the structure by 11.8 percent and behaves in a relatively less ductile manner. The NAFS program predicts the ultimate load very well with a deviation of only 3.2 percent from the experimental value and gives a softer response than that the experimental one at higher load levels (after a load equal to 45 kN). This phenomenon is explained here. Before cracking, it is assumed that the variation of flexural rigidity along the length of element is constant and equal to $(EI)_{cr}$. When one section of the member cracks, it is assumed that the entire length is cracked and a linear variation of flexural rigidity is assigned. This results in the stiffness matrix being underestimated compared with the "real" situation. A decrease in the length of finite element will lead to a decrease in this error.

Figure 9.14 shows a comparison between the position and sequence of plastic hinges obtained from the experimental and the analytical work using the NAFS program. The analytical and experimental hinge locations agree exactly for all of the frames.

For the frame FP4, using the NAFS program, the first plastic hinge forms at right foot (node 13) at a load level of $W_1=34.12$ kN, followed by the second plastic hinge which occurs at the right corner (node 11) at $W_1=40$ kN. The third plastic hinge forms at the left foot (node 1) at $W_1=43.37$ kN, and finally the frame collapses after last hinge occurs at mid-beam section (node 7) at ultimate load equal to $W_1=43.66$ kN. The results obtained from NONLACS2 program have

been presented in Chapter 8. As can be seen from Fig. 9.14, the sequence of formation of hinges in frame FP3 is the same as for frame FP4. The first hinge forms at load level of $W_1=50.26$ kN, and the collapse stage is reached at $W_1=62.2$ kN. For the frame FP2, the first yielding of steel occurs at $W_1=51.40$ kN, leading to formation of the first plastic hinge at the right foot of frame. The second hinge forms at the left foot at $W_1=58.94$ kN, while the third hinge occurs at right corner at $W_1=62.03$ kN. The fourth hinge forms at the mid-beam section of the frame. At this stage the frame collapses. Since the fixed-based portal frames (FP4, FP3 and FP2) have a degree of indeterminacy equal to three, with the formation of four plastic hinges each frame becomes a mechanism, and its stiffness matrix becomes singular (analytical failure).

The plastic hinges rotation calculated using the NAFS program are compared with the experimental values in Table 9.4. For frames FP4 and FP3, the maximum deviation between the analytical and experimental results is 30 percent, while the minimum deviation is 0.8 percent. For frame FP2, the NAFS program predicts the value of plastic hinge rotations with reasonable accuracy except at the left foot where a discrepancy of -58 percent is noted from experimental finding.

Although the NAFS program can predict the location of plastic hinges very well, the capability of the program to evaluate the value of plastic hinge rotations is less accurate than that of the NONLACS2 program. The NAFS program is based on concentrated rotations at discrete sections, while the NONLACS2 program is based on the spreadity of the inelasticity over the yielding length, (l_y). However, it should be noted that the value of plastic rotations obtained from NAFS and NONLACS2 program are quite sensitive to the load step increments, especially near the yielding and ultimate loads.

It is apparent that the response of the frames under investigation are predicted with reasonable accuracy by the modified stiffness approach at all loading stages. The proposed method (NAFS program) reduces the computational time by about 90 percent and save about 66 percent memory (storage requirements) in comparison with layered finite element method (NONLACS2 program). This comparison is made on the personal computer (Pentium 90) with 16 MB RAM. The modified stiffness approach (NAFS program) provides a more efficient, speedy, and economical method, for a complete analysis of large R C frame structures, than the program by using the layered approach. The full-range of behaviour including cracking, moment redistribution with hinge formation, and collapse are fully depicted by the method.

Table 9.2: Summary of analytical and experimental results at cracking, yielding and ultimate stage of continuous beams tested by Adaszkiwicz (1977)

Continuous beams	Cracking, Uniform Load (N/mm) *		Yielding, Uniform Load (N/mm)			Ultimate, Uniform Load (N/mm)		
	NONLACS2	NAFS	Experiment	NONLACS2	NAFS	Experiment	NONLACS2	NAFS
C1	5.88	6.90	16.92	16.57	18.38	21.30	17.54	19.76
C3	5.88	6.90	15.32	14.62	14.36	17.81	15.60	15.75

* Experimental cracking loads are not available

Table 9.3: Summary of analytical and experimental results at cracking, yielding and ultimate of frames

Frame	Cracking load W_1 (kN) *		Yielding load W_1 (kN) **			Ultimate load W_1 (kN)		
	NONLACS2	NAFS	Experimental	NONLACS2	NAFS	Experimental	NONLACS2	NAFS
FP4	6.67	5.60	44.0	39.5	34.12	48.04	43.37	43.66
FP3	5.60	5.60	58.5	53.37	50.26	66.94	64.50	58.02
FP2	5.60	5.00	57.8	53.37	51.40	64.27	56.70	62.20

* Experimental cracking loads are not available

** Experimental yielding load obtained from load-deflection curve

Table 9.4: Comparison of experimental and analytical plastic hinge rotation

Plastic Hinge Location (Node Number)	Plastic hinges rotation, θ_p (rad)					
	FP4		FP3		FP2	
	Experimental	NAFS	Experimental	NAFS	Experimental	NAFS
Right foot (13)	0.13	0.09	0.08	0.089	0.08	0.064
Right corner (11)	0.13	0.131	0.14	0.12	0.12	0.05
Left foot (1)	0.08	0.083	0.07	0.079	0.06	0.055
Mid-transom (7)	0.09	0.078	0.12	0.14	0.09	0.07

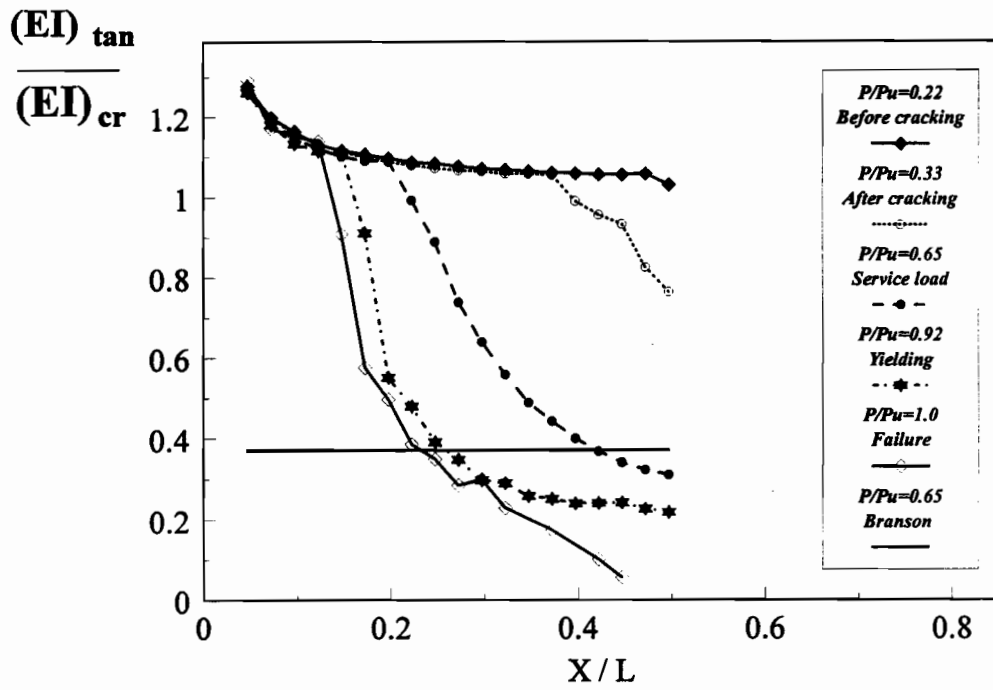


Figure 9.1: Variation of flexural rigidity over half of beam M11 subjected to concentrated loads

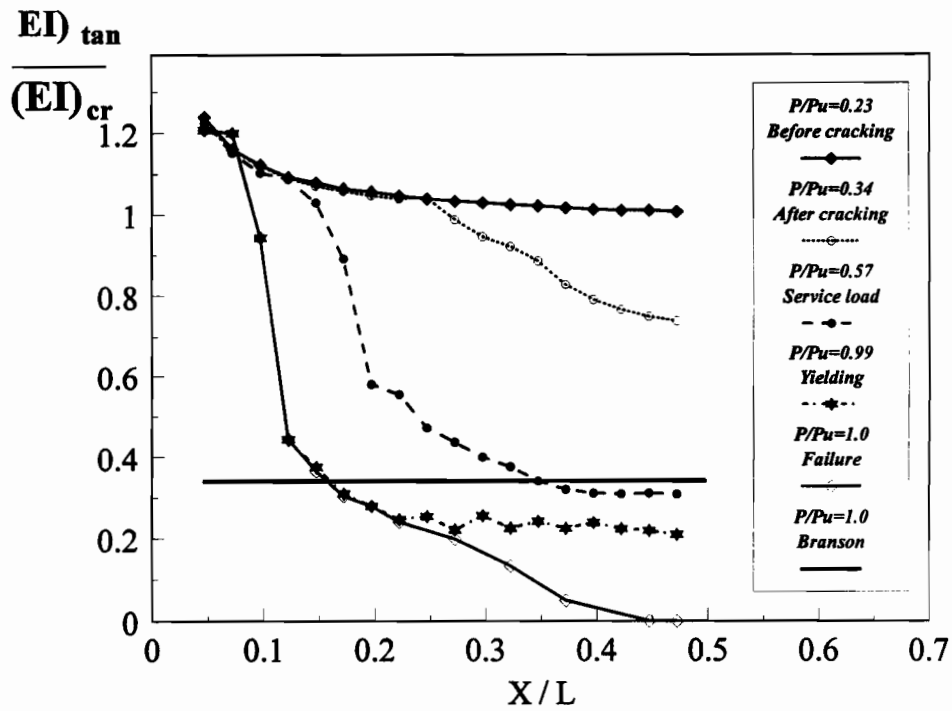


Figure 9.2: Variation of flexural rigidity over half of beam M81 subjected to uniform loads

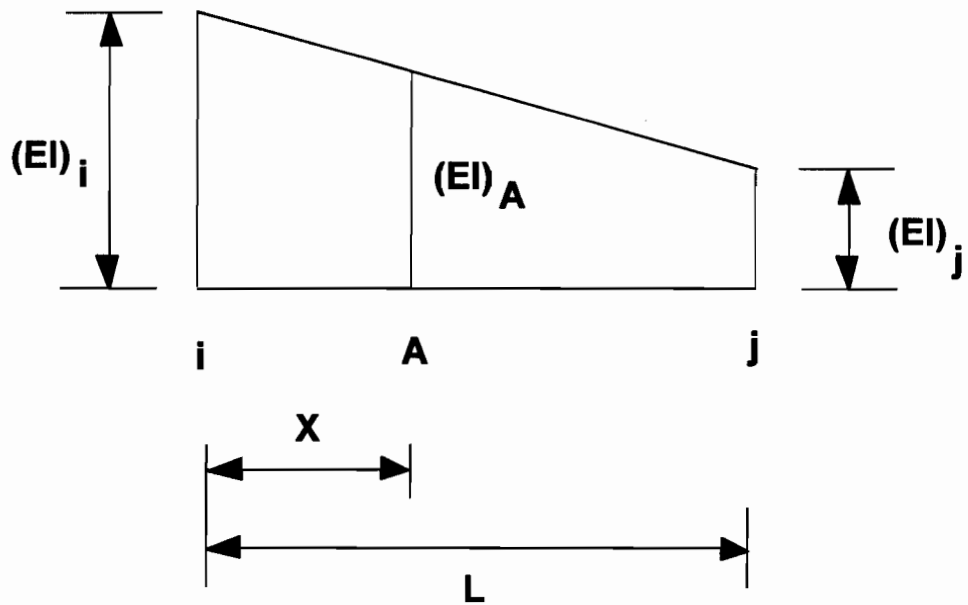


Figure 9.3: Linear variation of flexural rigidity over the length of element

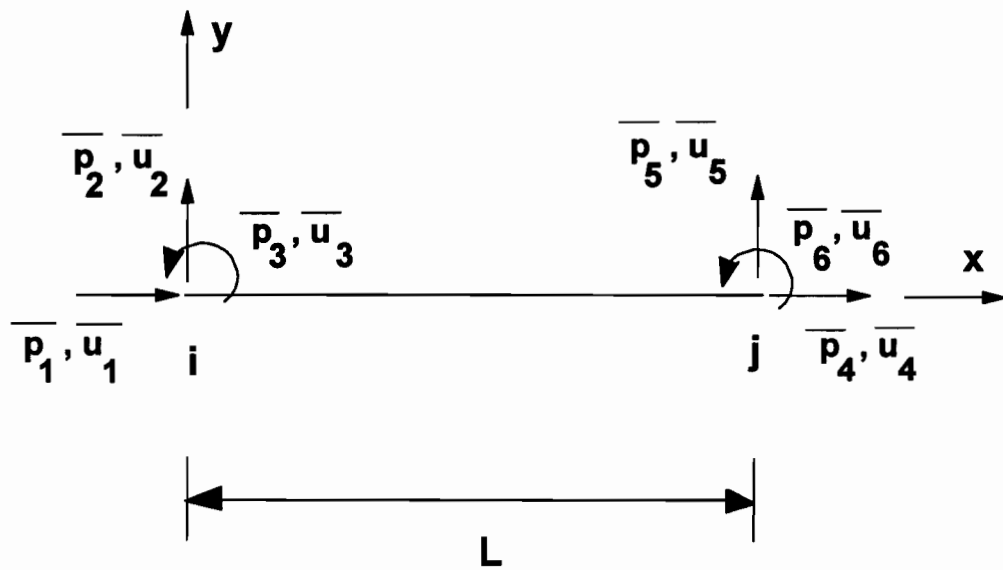


Figure 9.4: Numbering of member end forces and end displacements in local axes.

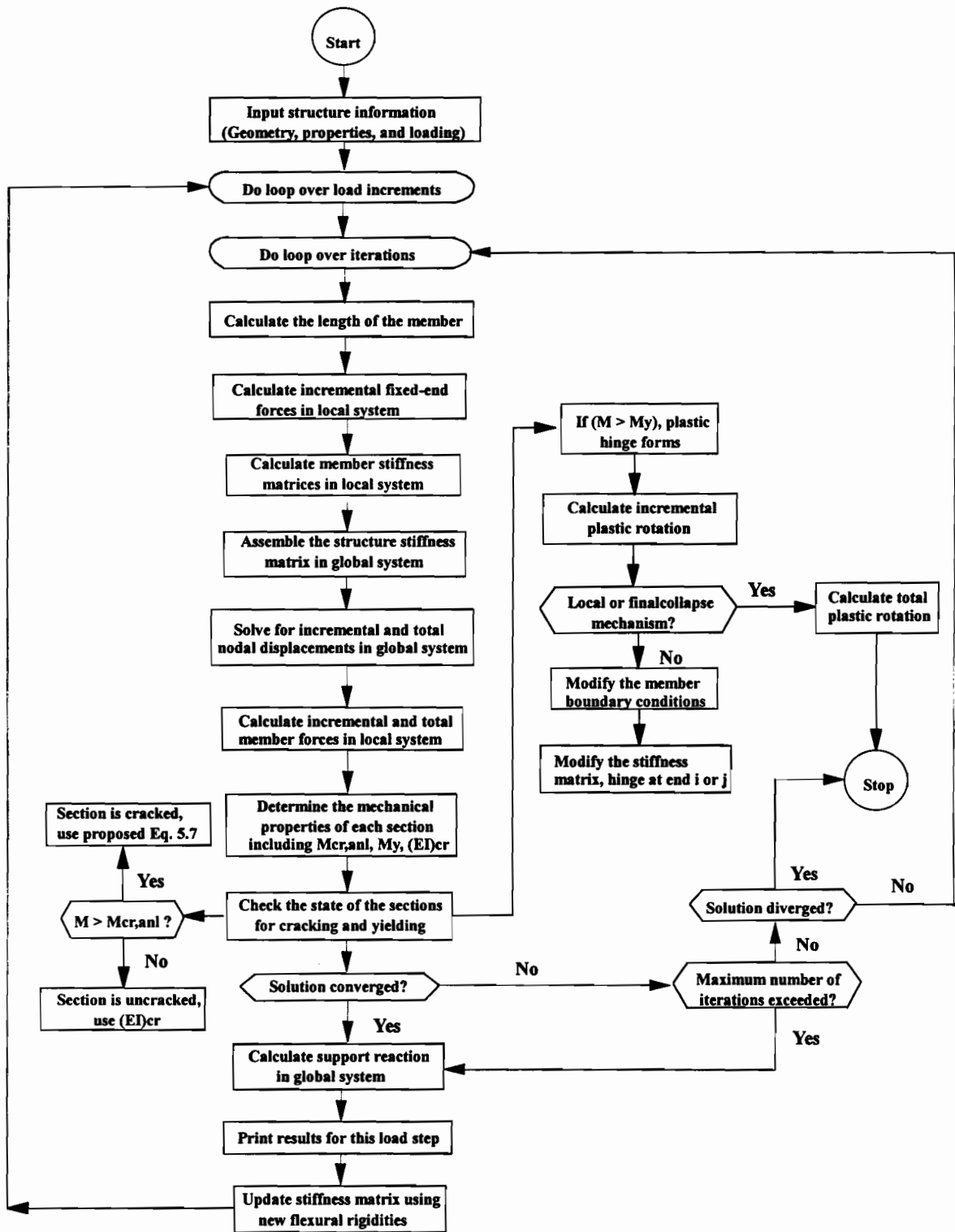


Figure 9.5: Flow chart for the NAFS program

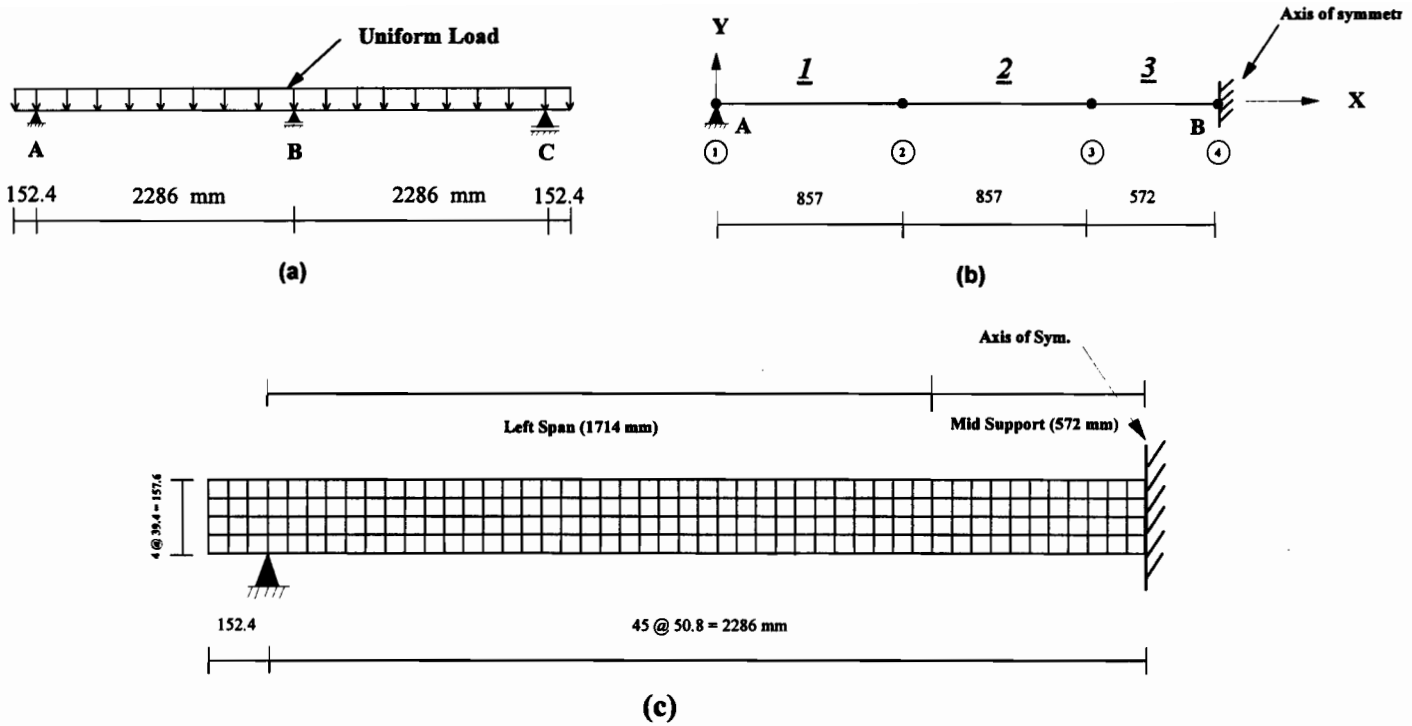


Figure 9.6: Analysis of continuous beams (a) geometry and loading, (b) finite element model using NAFS program, and (c) finite element model using NONLACS2 program

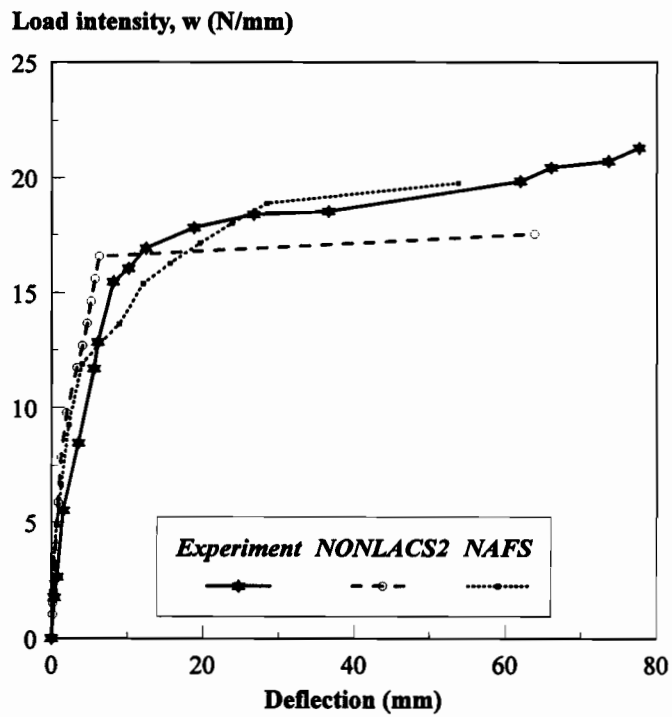


Figure 9.7: Comparison of analytical and experimental load-deflection curves for beam C1

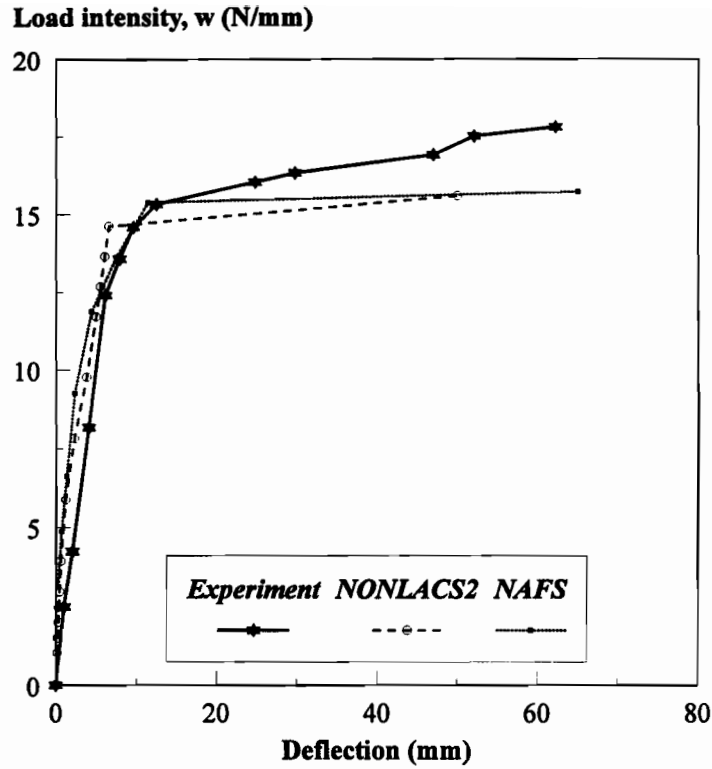


Figure 9.8: Comparison of analytical and experimental load-deflection curves for beam C3

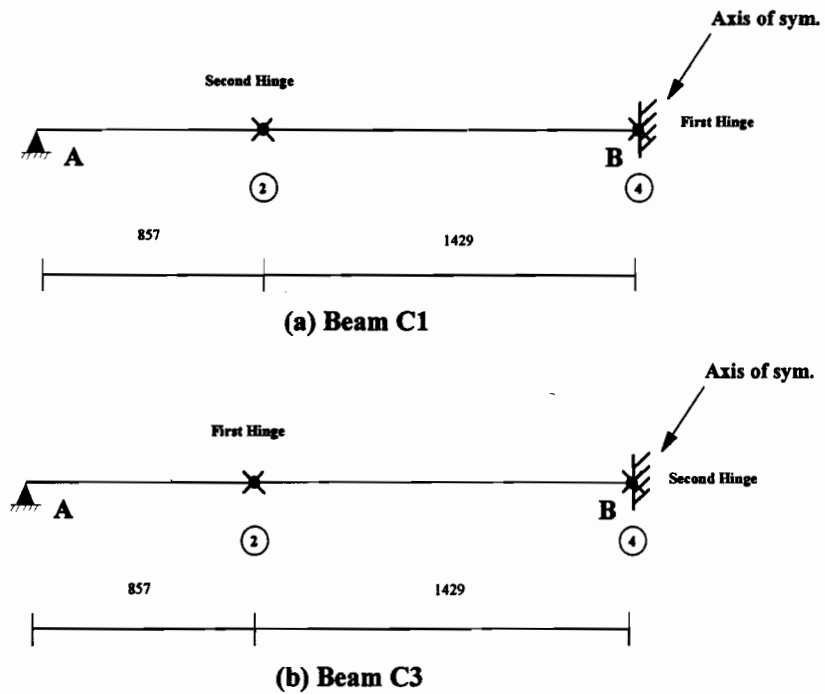


Figure 9.9: Location and sequence of the plastic hinges for continuous beams

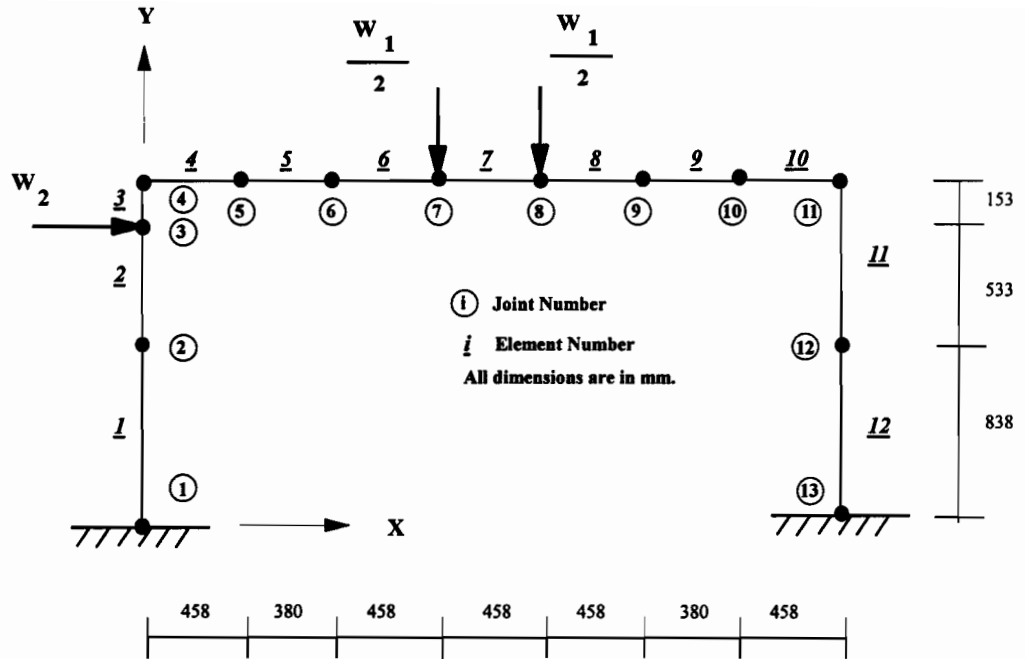


Figure 9.10: Finite element mesh for analysis of portal frames using NAFS program

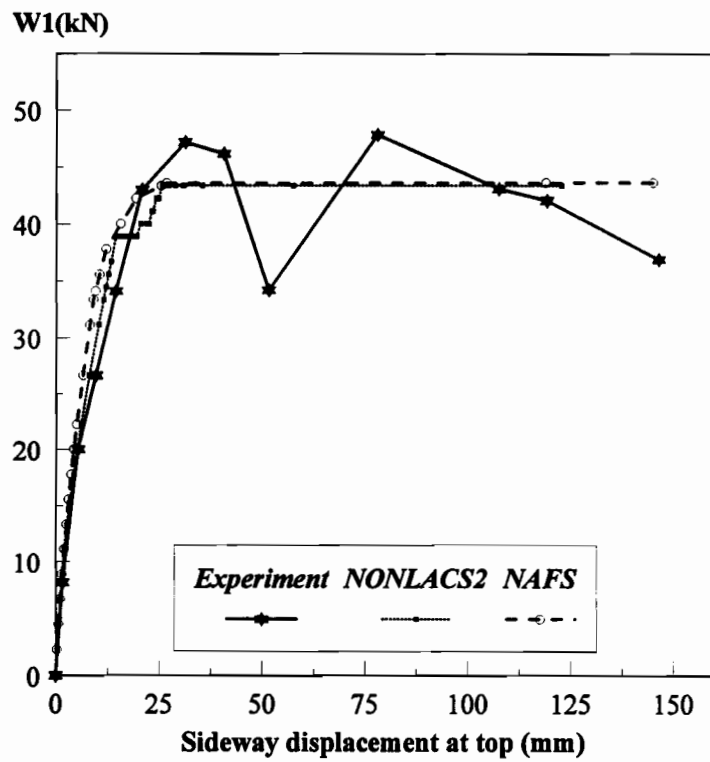


Figure 9.11: Comparison of analytical and experimental load-deflection curves for frame FP4

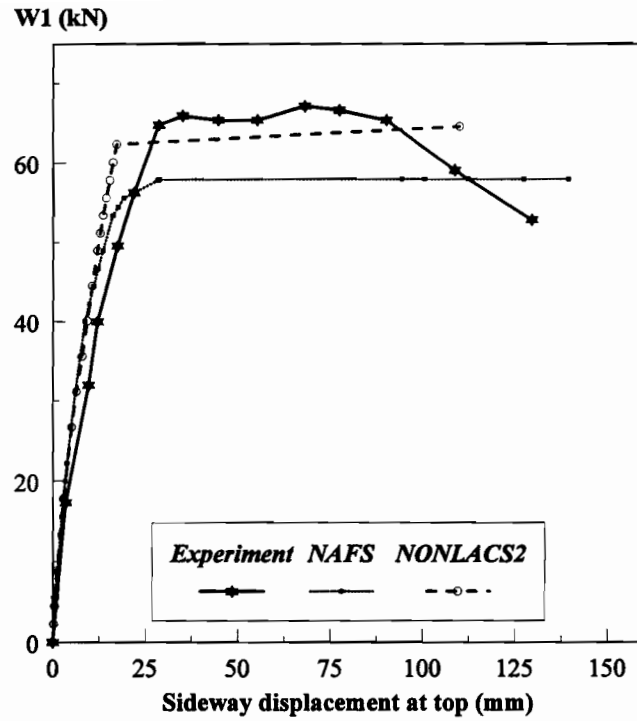


Figure 9.12: Comparison of analytical and experimental load-deflection curves for frame FP3

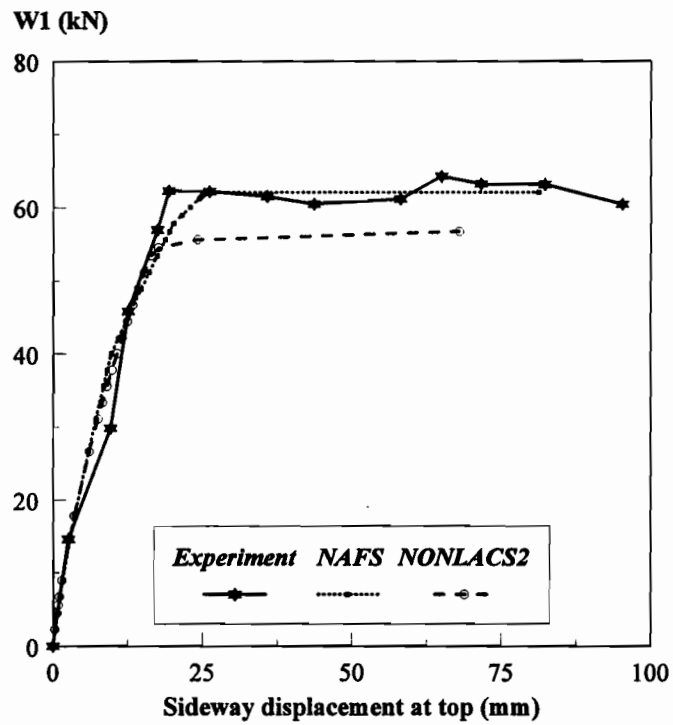
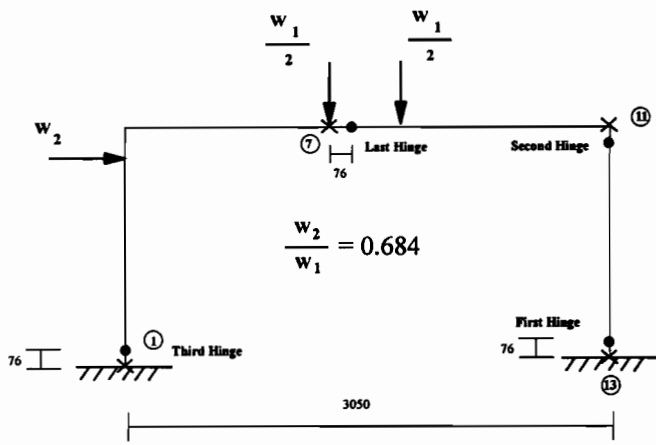
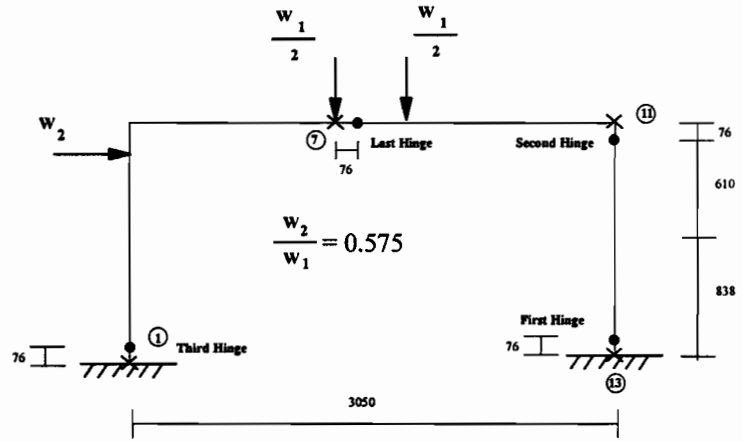


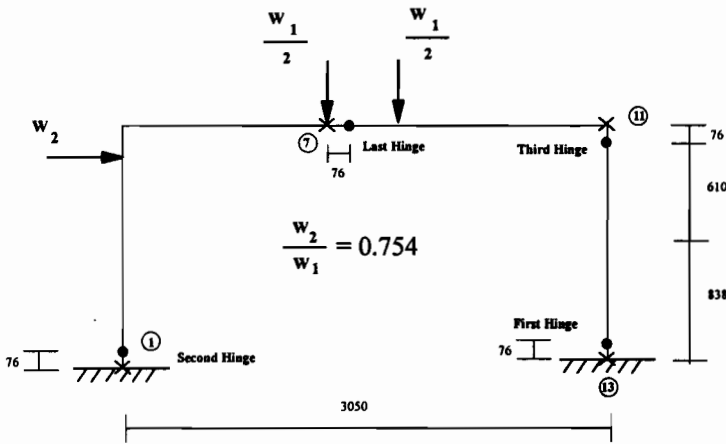
Figure 9.13: Comparison of analytical and experimental load-deflection curves for frame FP2



a) Frame FP4



b) Frame FP3



c) Frame FP2

All dimensions are in mm.

- ① Joint number indicates the position of the computed plastic hinge
- Plastic hinges formed in test by Cranston and Craknell (1969)
- × Plastic hinges obtained using NAFS program

Figure 9.14: Experimental and analytical locations of the plastic hinges for portal frames

CHAPTER 10

SUMMARY AND CONCLUSIONS

This chapter summarizes the highlights of the analytical studies undertaken using the NONLACS2 and the NAFS programs developed in the current study. The analytical results show good correlation with the available experimental results and indicate the usefulness of the nonlinear finite element analysis as a powerful tool to study the behaviour of different types of structural elements subjected to monotonically increasing loads until failure. Some new areas are also recommended for further investigation and future research.

10.1 SUMMARY

The present work is aimed at demonstrating the capabilities of the finite element method as a tool for predicting the nonlinear response of reinforced concrete (R C) structures. The NONLACS2 program, developed in the present study, employs a layered finite element approach, with the concrete modeled as an orthotropic nonlinear material and steel idealized as an elasto-plastic strain hardening material. Cracking of the concrete is idealized using the smeared cracking model. Aggregate interlock and dowel action between the reinforcing steel and the concrete are considered using the shear retention factor. Nonlinear analysis is performed using an incremental-iterative tangent stiffness approach.

A parametric study is conducted to examine the effects of the influencing parameters including the size of the finite element, tension and compression reinforcement ratios and strengths, loading types and stages, tensile and compressive strengths of the concrete, cracking and tension-stiffening on the flexural response of different structural elements. The effect of these parameters on different behavioral aspects of R C structures including the load-displacement,

moment-curvature and load-strain characteristics, flexural rigidity, cracking pattern, cracking, yielding and the ultimate loads, mode of failure, plastic hinge rotations, equivalent plastic hinge length, yielding length and ductility are discussed along with a comparison with the experimental data where available.

Based on the analytical results, a simple formula, as a function of the element size, is proposed for determination of the ultimate tensile strain of the concrete, ϵ_{un} , and elimination of the mesh dependency phenomenon. Also, new equations are proposed to calculate the analytical cracking moment, $M_{cr,anal}$, cracking flexural rigidity, $(EI)_{cr}$, tangent flexural rigidity, $(EI)_{tan}$ and the deflection of R C beams. In addition, new simple equations as a function of tension reinforcement index, ω , and the loading type are proposed to evaluate the rotation capacity of plastic hinges.

The proposed flexural rigidity equations are utilized to develop a nonlinear finite element program, NAFS, as a practical engineering tool based on the modified stiffness approach. A new 2-node nonlinear beam element with a degrading stiffness matrix is developed to model cracking and other nonlinear effects throughout the entire loading range from zero load to the ultimate load.

The applicability and reliability of both the NONLACS2 and the NAFS programs and the validity of proposed methods, including the proposed model for mesh dependency phenomenon, the compressive stress-strain curves of normal and high-strength concrete, new models for concrete in tension and tension-stiffening, and the concrete ultimate compressive and tensile strains is verified using the numerical analysis of several well documented tests. The numerical applications, which are investigated under monotonically increasing loads, are as follows:

- 1) Simply supported normal-strength concrete beams tested by Gaston et al. (1952), Mattock (1964), and Abrishami et al. (1995).
- 2) Simply supported high-strength concrete beams tested by Leslie et al. (1976) and Abrishami et al. (1995).
- 3) Reinforced concrete shear panel tested by Cervenka (1970).
- 4) Two-span continuous beams tested by Adaszkievicz (1977).
- 5) Fixed-base portal frames tested by Cranston and Cracknell (1969).

10.2 CONCLUSIONS

Based on the results of this investigation, the following conclusions can be drawn:

10.2.1 Finite Element Size Effect

1) When the mesh size dependency analysis is ignored (MDEP=1), the computed response of selected R C members is influenced by the size of the finite element. If a fine mesh is used to idealize a R C element for nonlinear finite element analysis, the ultimate load is underestimated. From energy considerations, a decrease in the mesh size increases the rate of crack propagation in the structure, and consequently its energy dissipation capacity decreases. This leads to a lower value of the ultimate load than the experimental one. In this case, the structure exhibits a less ductile response. However, if a coarser mesh is used instead, the ultimate load is overestimated and the structure behaves in a more ductile manner. From a physical point of view, with an increase in the finite element size, the rate of crack progression will decrease and the capacity of the structure to dissipate energy and consequently the ultimate load will increase.

2) The various analyses indicate that the value of the ultimate concrete tensile strain, ϵ_u , has a considerable influence on the computed values of the ultimate load. It is shown that the value of f'_c does not have a significant effect on the value of the ultimate load, compared with the value of ϵ_u . An empirical equation is proposed to predict an appropriate value of ϵ_u as a function of the element size, h . For a finer mesh, the proposed formula gives a large value for ultimate tensile strain of concrete, ϵ_u , which increases the energy dissipation capacity of the structure and reduces the crack propagation within the element and consequently it prevents failure of the structure at an early stage of loading. The proposed formula is used in conjunction with the crack band model proposed by Bazant and Oh (1983), and implemented into the NONLACS2 program to analyze different structural elements. The results using these models show good agreement with the experimental findings in the prediction of the ultimate load, load-deflection and load-concrete and steel strain curves, and the cracking pattern. The proposed model can be used effectively with relatively large finite element sizes with reasonable accuracy, besides saving computational time. The results also show that the proposed model can be used for nonlinear finite element analysis of R C beams with different amounts of reinforcement and detailing.

3) The computed results for the over-reinforced beams show that the effect of mesh size is not so significant on the prediction of the ultimate load, because at higher load levels, the response of the concrete elements in compression governs the overall behaviour, and the response of the

concrete and the influence of the tension reinforcement and tension-stiffening is not as significant as in the under-reinforced concrete beams.

10.2.2 Flexural Rigidity and Deflection of Reinforced Concrete Beams

1) In the pre-cracking stage, the analytical cracking moment and the cracking flexural rigidity increase with an increase in the value of the tension and compression reinforcement ratios. Flexural cracks normally appear at load values between 15 and 20 percent of the ultimate load. Since the analytical cracking moment and the cracking flexural rigidity are sectional properties, the value of f_y and the type of loading do not have any effect on these values.

2) In the post-cracking stage, the following conclusions are made:

a) The heavily reinforced section has a higher EI value compared with that for the lightly reinforced section. An increase in the value of ρ by about 50 percent increases the flexural rigidity by about 33 percent.

b) The compression reinforcement ratio and the compressive strength of concrete have a significant effect on the EI values for heavily reinforced beams and this effect decreases with a decrease in the tension reinforcement ratio.

c) At the same level of moment, the flexural rigidity for beams loaded at midspan is found to be about 8 percent and 18 percent more than that for beams subjected to the third-point loading and uniformly distributed loading, respectively. The effect of loading type on the EI value for heavily reinforced beams is not as significant as for the lightly reinforced beams.

3) The proposed flexural rigidity equations take into account the effect of the tension and compression reinforcement ratios, concrete compressive strength and the type of loading. For the prediction of the short-term deflection, comparison of the results obtained using Branson's equation and the proposed model show that the proposed model is more accurate, especially for the beams with the third-point loading. In Branson's equation, the evaluation of the cracking second moment of area, I_{cr} , is very time-consuming, especially for flanged sections, while the proposed model is independent of the evaluation of I_{cr} . This model is simple and can be used to estimate the values of flexural rigidity and deflection of R C beams with reasonable accuracy.

4) In the post-yielding stage, an increase in the tension and compression reinforcement ratios results in an increase in the yield and ultimate moments. The effect of f'_c and ρ' on the values of M_y and M_u decrease with a decrease in the tension reinforcement ratio. In fact, the flexural strength of R C beams with a small amount of tension reinforcement is little affected by the concrete compressive strength. The effect of f_y on the yield and ultimate moments increase with an increase in tension reinforcement ratio. The effect of the loading type is not considerable on the yield and ultimate moments.

10.2.3 Rotation Capacity of Plastic Hinges

1) The cracking, yielding and the ultimate loads increase with the tension reinforcement index, ω . The ultimate deflection and the deflection ductility ratio, $\mu_\Delta = \Delta_u / \Delta_y$, decrease with an increase in the value of ω . The deflection ductility ratio varies between 3.71 to 15.1, as ω changes from 0.412 to 0.103.

2) At the yielding stage, the value of neutral axis depth, c , calculated assuming a linear distribution of the concrete stress over the depth of section is smaller than the "actual" value of the depth of the compression zone, c , if the concrete stress distribution is nonlinear, which will lead to an underestimation of the curvature at first yield, ϕ_y , and an overestimation of the curvature ductility ratio, $\mu_\phi = \phi_u / \phi_y$. As the tension reinforcement index is increased, the yielding curvature increases.

3) At the ultimate stage, the values of ϵ_{cu} and ϵ_{su} decrease with an increase in the value of ω . For a given z/d ratio, the ultimate curvature decreases with an increase in the tension reinforcement index. The analytical ultimate curvatures are about 2.35, 1.31, and 0.84 times the values obtained using the ACI, Corley's, and Mattock's methods, respectively. The ACI 318-83 Building Code predicts the ultimate curvature very conservatively as compared with the other methods. This Code also underestimates the curvature ductility ratio (up to 2.5 times) compared with the analytical results. The curvature ductility ratio varies from 4.88 to 21.9, when the value of ω changes from 0.412 to 0.103.

4) The advantage of the present study is that the yielding length and the "exact" value of

plastic rotation can be determined without using the concept of an equivalent plastic hinge length. The spread of plasticity (yielding length), ultimate curvature and consequently the plastic hinge rotation for the lightly reinforced beam are greater than that for heavily reinforced beam. It is observed that an increase in ω by about 2.68 times decreases the yielding length and the plastic hinge rotation by about 20 percent and 50 percent, respectively.

5) Compared with CEB-FIP MC90, the analytical results and Corley's theory are found to give safe values except in one case ($\omega=0.103$) and yet they are not as conservative as Baker and Amarakone's and Riva and Cohn's formulations. The plastic rotation capacity predicted by the formula given by Riva and Cohn appear to represent a fairly safe estimate of the actual rotation capacities available up to the maximum load.

6) The Corley's, Mattock's, and Sawyer's theories give a constant plastic hinge length regardless the reinforcement index, while the analytical value of l_p and the value of l_p obtained from Baker and Amarakone's, and Riva and Cohn's formulations is not constant for different values of tension reinforcement indices. The average value of the analytical plastic hinge length on one side of the critical section is 69 percent of the effective depth ($0.69 d$).

7) The plastic hinge rotation increases in going from the concentrated load to the third-point loading, and it is a maximum for the case of the uniformly distributed load. For the beam with $\omega=0.103$, uniformly distributed loads on a simply supported beam lead to θ_p values varying from 1.90 to 1.35 times as high as those corresponding to the beams loaded with a midspan concentrated load or a third-point loadings on the same beam, respectively. These ratios for heavily reinforced beam with $\omega=0.412$ are 1.59 and 0.88, respectively. Thus it can be concluded that the effect of the loading type on the plastic rotation capacity of the heavily reinforced beams is not as significant as for the lightly reinforced beams. It is concluded that the reinforcement index and the loading type have a significant effect on the plastic hinge rotation and length.

8) The analytical results indicate that the NONLACS2 program and the proposed equations (as a function of tension reinforcement index, ω , and the loading type) can be used for analysis of ultimate deformation of R C beams with sufficient accuracy.

10.2.4 High-Strength Concrete Beams

1) The cracking behaviour and stiffness of a concrete beam are strongly influenced by the concrete tensile strength. With an increase in the value of f_t , the cracking moment value increases and the structure behaves in a stiffer manner. In addition, the energy dissipation capacity increases and the crack propagation of the structure decreases, resulting in stiffer load-deflection response. The decrease in the concrete tensile strength does not decrease the ultimate load significantly. It should be pointed out that by decreasing the value of modulus of rupture, the deflection ductility ratio, μ_Δ , decreases and for the value of f_t recommended by the ACI 363 ($f_t=0.94\sqrt{f_c}$), the agreement with the experimental findings is not so good. The model with the value of f_t recommended by the ACI 363 exhibits a very stiff response, but it predicts the ultimate load of the beam quite accurately with a small difference from the experimental value. The analytical predictions are in good agreement with the experimental results when a value of $f_t=0.62\sqrt{f_c}$, recommended by the ACI Committee 318, is used for the concrete tensile strength. It can be concluded that if the experimental cracking moment is not available, the ACI 318 equation for the modulus of rupture can be used for the finite element analysis of high-strength concrete beams with reasonable accuracy. The effect of f_t on the response of heavily reinforced high-strength concrete beams is less than on that of the lightly reinforced beams.

2) A sudden drop in the concrete tensile strength is found to have a significant effect on the member stiffness but it has a less significant effect on the ultimate load. The load-deflection curves are closer to the experimental results when a smaller value of the softening branch factor, α_2 , is used. The model with $\alpha_2=1.0$ (no stress drop at the cracking point) exhibits a very stiff response but results in an accurate value for the beam ultimate load. It can be observed that with an increase in the value of α_2 , the energy dissipation capacity of the beam and consequently the yielding and the ultimate loads and the ductility ratios increase. The results also indicate that decreasing the value of α_2 is acceptable up to a value of 0.2. For α_2 less than 0.2, the analytical results do not correlate well with the experimental findings. The analytical predictions for the beam stiffness, strength and the ductility ratio are in good agreement with the experimental results when a value of $\alpha_2=0.2$ is assumed. The factor α_2 has a significant effect on the cracking pattern, so that with an increase in the value of α_2 the dissipation of energy increases and the progress of cracks decreases. The number of cracks for model with $\alpha_2=1.0$ is minimum, while it is a

maximum with $\alpha_2=0$.

3) The model with $\alpha_2=0$ (no tension-stiffening) underestimates the ultimate load and gives a softer response than that for the experimental one at an early stage of loading, which is not acceptable. If the tension-stiffening is ignored, the structure becomes more flexible and fails in brittle manner with a displacement ductility ratio, $\mu_\Delta=1.0$.

4) As expected, the high-strength concrete beam has higher stiffness, cracking moment, yielding and ultimate loads than the normal-strength concrete beam. With an increase in the value of f'_c by a factor of about 2.8, the analytical cracking moment, yielding and ultimate loads increase by about 34 percent, 5.3 percent and 8.7 percent, respectively. An examination of the under-reinforced beams UCB and HUCB ($\rho=0.0088$) shows that, as expected, the ultimate load capacity is not very sensitive to the value of f'_c . Although the high-strength concrete as a material is more brittle, and it has a lower value of the ultimate concrete compressive strain, ϵ_{cu} , compared with the normal-strength concrete, the curvature ductility and deflection ductility ratios may be the same or greater for the high-strength R C beam.

5) The analytical load-deflection curves obtained from NONLACS2 program follow the same general pattern and are quite close to the experimental responses. The capability of the NONLACS2 program using the proposed model (Eq. 4.1) for determination of the value of concrete ultimate tensile strain, ϵ_w , and the appropriateness of the Popovics' equation for representation of the concrete uniaxial compressive stress-strain characteristics is demonstrated for nonlinear finite element analysis of high-strength concrete beams.

10.2.5 Nonlinear Analysis of Frame Structures

1) The analytical results based on no provision to account for the mesh size dependency (MDEP=1) show that the computed response and the ultimate load for frame FP4 depend on the size and the number of elements. The finer meshes give lower values of the ultimate load and vice versa for the coarser meshes. With an increase in the number of elements, the structure is slightly more flexible than for the case for the coarse mesh idealization, and the frame tends to be less ductile. The pre-cracking behaviour and the cracking load are the same for the different mesh

configurations.

2) It is found that the change of the concrete ultimate tensile strain, ϵ_{tu} , does not appear to have a significant effect on the load-deflection characteristics of the frame. The frame tends to be more flexible due to the lower value of the ultimate tensile strain. Although for nonlinear analysis of the frame FP4, the proposed model gives reasonable results for 89 and 212-element models, however, more analytical work is needed for the frame with a very fine mesh (700-element model).

3) For the frame FP4, the model without tension-stiffening ($\epsilon_{tu} = \epsilon_{cr}$) exhibits softer response than the experimental findings and the mode of failure is brittle without any ductility. The difference in the deflection values between the two models at the failure stage shows the importance of considering the tension-stiffening in the analysis in increasing the ductility of the structure.

4) The location of the plastic hinges obtained for the frame FP4, using the NONLACS2 program, is the same as observed in the experimental work by Cranston and Cracknell (1969). The failure mechanism obtained analytically is in good agreement with the experimental results. Although the analytical plastic hinge rotation values are slightly lower than the experimental values, the agreement between the two sets of results is very good. The maximum deviation between the analytical and the experimental values of the plastic hinge rotations is approximately 13%, while the minimum deviation is 4%.

5) The NONLACS2 program is verified to be sufficiently powerful to adequately predict the complete deformational response of the frame FP4 up to failure including the load-deflection and strain characteristics, failure mechanism, the location of plastic hinges and their rotations, equivalent plastic hinge and yielding lengths which is difficult to obtain in the tests.

10.2.6 Modified Stiffness Approach (NAFS Program)

1) The tangent flexural rigidity equations can be incorporated in the modified stiffness approach for nonlinear finite element analysis of R C frame structures subjected principally to

flexure which will save the computational time considerably.

2) Comparison of the analytical results using the NAFS program with the experimental data from tests on R C frames FP2, FP3, FP4 tested by Cranston and Cracknell (1969) and continuous beams C1 and C2 tested by Adaszkievicz (1977) show that the load-deflection curves obtained from the NAFS program are stiffer than the experimental load-deflection curve at early stages of the loading and then they are softer than the experimental load-deflection curves at higher load levels until failure. The responses of the frames and the continuous beams are predicted with sufficient accuracy by the modified stiffness approach at all loading stages until failure.

3) Although the NAFS program can predict the location of plastic hinges very well, the capability of the program to evaluate the value of plastic hinge rotations is less accurate than that of the NONLACS2 program. In the NAFS program, the structure is idealized as linear elements, where the rotation is concentrated at the nodes, while the NONLACS2 program uses planar elements, where the plastic hinge rotation spreads over the yielding length, (l_y). However, it should be noted that the value of plastic hinge rotations obtained from the NAFS and the NONLACS2 programs are quite sensitive to load increments, especially near the yielding and the ultimate loads. Very small load increments must be used near the critical loading stages such as cracking, yielding and the ultimate load.

4) The new method based on the modified stiffness approach provides a more efficient, speedy, and economical method, for a complete analysis of large frame structures. The computer output gives the complete load-deflection and moment-rotation characteristics, the location and the rotation capacity of the plastic hinges until a collapse mechanism is attained. In the service load range, this program can be used for predicting the instantaneous deflections of R C beams. It is shown that the NAFS program while providing considerable modelling advantages, leads to significant saving in the computational time and memory (storage requirements) in comparison with layered finite element method (NONLACS2 program).

10.3 RECOMMENDATIONS FOR FUTURE RESEARCH

The following suggestions are made for further research:

- 1) The proposed model for eliminating the mesh-dependency phenomenon is mainly concerned with some structural elements exhibiting plane stress behaviour such as, beams and shear panels. A similar investigation is recommended in connection with some other structural elements such as slabs, shear walls, cores, frames, deep beams, etc. to examine the validity of the proposed formula, or for developing new formulas, if needed.
- 2) All new equations proposed in the course of this study are appropriate for structural elements constructed using normal concretes. However, because of the increasing use of high-strength concrete, more analytical work is needed for structural elements built using high-strength concretes.
- 3) More specific information is needed on the behaviour of joints with emphasis on joint stiffness, shear transfer through the joints and the influence of the column and transverse framing members on the joint performance.
- 4) The NONLACS2 program employs a layered finite element approach and its element library does not include the beam element. Further research is suggested to implement the NAFS program as subroutines into the layered finite element program. The new version would be very useful for nonlinear analysis of any R C structures having shell and beam elements such as coupled shear walls and shear wall-frame structures.
- 5) Present limits of the analytical models are related to the fact that only flexural, static actions and material nonlinearities are considered. Further investigations are needed to examine the influence of shear and axial forces, bond slip, geometric nonlinearities, and dynamic and reversing loads.

STATEMENT OF ORIGINALITY

An analytical study has been conducted in order to investigate the nonlinear flexural response of normal and high-strength concrete structures. Two nonlinear finite element programs, NONLACS2 and NAFS, are developed to analyze nineteen reinforced concrete specimens including thirteen simply supported normal and high-strength concrete beams, two continuous beams, one shear panel and three portal frames. Based on the analytical results, new equations are proposed for determination of concrete ultimate tensile strain, ϵ_{tu} , flexural rigidity, deflection and plastic hinge rotations. The applicability and reliability of both NONLACS2 and NAFS programs and the validity of proposed methods is verified using the numerical analysis of several well documented experimental tests. The original contributions in this thesis are:

- 1) A layered finite element program, NONLACS2, is developed and includes the different modelling options including the proposed model for mesh size dependency phenomenon, the compressive stress-strain curves for normal and high-strength concretes, new models for concrete in tension, tension-stiffening, and the concrete ultimate compressive and tensile strains.
- 2) The influence of the element size on the different behavioral aspects of R C beams, shear panel, and frames is investigated and a new model is proposed to determine the concrete ultimate tensile strain, ϵ_{tu} , and remove the mesh size dependency drawback from nonlinear finite element analysis of R C structures.
- 3) Extensive parametric study is conducted to examine the effects of the various influencing parameters on the flexural response of different structural elements, and the analytical results are compared with the experimental data where available.
- 4) Based on the analytical results, new equations are proposed to calculate the analytical cracking moment, cracking flexural rigidity, tangent flexural rigidity, and the deflection of R C beams.
- 5) At the ultimate load stage, new simple equations are derived to consider the effect of tension reinforcement index, ω , and the loading type on the plastic hinge rotations.
- 6) The proposed flexural rigidity equations are utilized to develop a nonlinear finite element program, NAFS, as a practical engineering tool based on the modified stiffness approach.
- 7) The performance of the tension-stiffening model with discontinuous softening on the response of high-strength concrete beams is verified.

REFERENCES

- Abdel-Rahman, H.H. (1982). "Computational Models for the Nonlinear Analysis of Reinforced Concrete Flexural Slab Systems", Ph.D. Thesis, University College of Swansea, United Kingdom.
- Abrishami H.H., Cook, W.D., and Mitchell, D. (1995). "Influence of Epoxy Coated Reinforcement on Response of Normal and High-Strength Concrete Beams", *ACI Structural Journal*, V. 92, No. 2, pp. 157-166.
- ACI Committee 435, Committee Chairman, Branson, D.E. (1966). "Deflection of Reinforced Concrete Flexural Members", *ACI Journal, Proceedings* V. 63, No. 6, pp. 637-674.
- ACI Committee 435, Subcommittee 1, Subcommittee Chairman, R.S., Fling, Committee 435 chairman, D.E., Branson, (1968). "Allowable Deflections", *ACI Journal, Proceedings* V. 65, No. 6, pp. 433-444.
- ACI Committee 318, (1963). "Building Code Requirements for Reinforced Concrete," and commentary, American Concrete Institute, Detroit, Michigan.
- ACI Committee 318, (1971). "Building Code Requirements for Reinforced Concrete (ACI 318-71)", American Concrete Institute, Detroit, 78 pp.
- ACI Committee 435, Subcommittee 2, Branson, D.E. (1972). "Variability of Deflections of Simply Supported Reinforced Concrete Beams", *ACI Journal, Proceedings* V. 69, No. 1, pp. 29-35.
- ACI Committee 435, Chairman, G.M. Sabnis, (1974). "Bibliography on the Deflection of Concrete Structures, Deflection of Concrete Structures", *ACI, SP 43-23*, pp. 573-631.
- ACI Committee 435. (1974). "Deflection of Concrete Structures", SP-43, American Concrete Institute, Detroit.
- ACI Committee 318 (1983). "Building Code Requirements for Reinforced Concrete (ACI 318-83)", American Concrete Institute, Detroit, 111pp.
- ACI Committee 318 (1989). "Building Code Requirements for Reinforced Concrete (ACI 318-89) and Commentary - ACI 318R-89", American Concrete Institute, Detroit, 353 pp.
- ACI Committee 363 (1992), "State of the Art Report on High Strength Concrete", ACI 363R-92, American Concrete Institute, Detroit.
- ACI Committee 435. (1995). "Control of Deflection in Concrete Structures" ACI 435R-95, American Concrete Institute, Detroit.
- ACI-ASCE Committee 428 (1968). "Progress Report on Code Clauses for Limit Design", *Journal ACI*, V. 65, No. 9, pp. 713-720.
- ASCE Task Committee (1982). "Finite Element Analysis of Reinforced Concrete", State-Of-The-Art Report, ASCE, New York, USA.
- ASCE/ ACI Committee 447 (1991). "Finite Element Analysis of Reinforced Concrete Structures II",

Edited by J. Isenberg, American Society of Civil Engineers, New York, USA.

- Adaszkievics, M. (1977). "Behaviour of Continuous Reinforced Concrete Beams under Uniform Loads", M.Eng. Thesis, McGill University.
- Adenot, A. (1970) "Behaviour of Double Bay One Storey Reinforced Concrete Frame Subjected to Horizontal and Vertical Loading", Structural Concrete Series No. 70-4, McGill University, Montreal.
- Ahmad, H. (1996). "Nonlinear Finite Element Analysis of a R C Portal Frame", M.Eng. Project, Department of Civil Engineering and Applied Mechanics, McGill University, Montreal.
- Al-Manaseer, A.A., and Phillips, D.V. (1987). "Numerical Study of Some Post-Cracking Material Parameters Affecting Nonlinear Solutions in R C Deep Beams", Canadian Journal of Civil Engineering, V. 14, No. 5, 655-666.
- Al-Shaikh, A.H., and Al-Zaid, R.Z. (1993). "Effect of Reinforcement Ratio on the Effective Moment of Inertia of Reinforced Concrete Beams", ACI Structural Journal, V. 90, No.2, pp. 144-149.
- Al-Zaid,R.Z.; Al-Shaikh,A.H.; and Abu-Hussein,M.M. (1991). "Effect of Loading Type on the Effective Moment of Inertia of Reinforced Concrete Beams,"ACI Structural Journal, V.88.No.2,PP. 184-190.
- American Concrete Institute. (1991). "Fracture Mechanics of Concrete: Concepts, Models and Determination of Material Properties", ACI 446.1R, Reported by ACI Committee 446 on Fracture Mechanics of Concrete.
- Appleton, J., Camara, j., and Almeida, J.F. (1983). "Elastoplastic Analysis and Design of Partially Prestressed Concrete Beams", International Symposium on Nonlinearity and Continuity in Prestressed Concrete, Preliminary Publication, Vol. 2, University of Waterloo, Waterloo, Ontario, Canada, pp. 185-204.
- Aziz, O. (1988). "A Mechanism Free Plane Quadrilateral Element with Rotational Degree of Freedom and the Associated Facet Shell Element," M. Eng. Thesis, Dept. of Civ. Engrg., Carleton Univ., Ottawa.
- Bahlis, J.B., and Mirza, M.S. (1987). "Nonlinear Analysis of Planar Reinforced Concrete Structures, "Canadian Journal of Civil Engineering, V. 14, No. 6, pp. 771-779.
- Baker A.L.L. (1956). "The Ultimate-Load Theory Applied to the Design of Reinforced and Prestressed Concrete frames", Concrete Publications Ltd., London.
- Baker, A.L.L. (1962). "Ultimate Load Theory for Concrete Frame Analysis" , Transactions of the ASCE, Paper No. 3386, Vol. 127.
- Baker, A.L.L., and Amarakone, A.M.N. (1964). "Inelastic Hyperstatic Frames Analysis", Proceedings of the International Symposium on Flexural Mechanics of Reinforced Concrete, Miami, Florida, ASCE 1965-50, ACI SP-12, pp. 85-142.

- Balakrishnan, S., and Murray, D.W. (1986). "Finite Element Prediction of R C Behaviour," Struct. Engrg. Report No. 138, University of Alberta, Edmonton, Canada.
- Balakrishnan, S., and Murray, D. W. (1988). "Concrete Constitutive Model for NLFE Analysis of Structures", J Struct. Engrg. ASCE, V. 114, No.7, pp. 1449-1465.
- Balakrishnan, S., Elwi, A. E. and Murray, W. (1988). "Effect of Modelling of NLFE Analysis of Concrete Structures", ASCE, J. Struct. Engrg., V. 114, No. 7, pp. 1467-1487.
- Barzegar, F., and Schnobrich, C.W. (1986). "Nonlinear FE Analysis of R C Under Short Term Monotonic Loading", Structural Research Series No. 530, University of Illinois, Urbana, Illinois.
- Bazant, Z. P. (1976). "Instability, ductility and size effect in strain-softening concrete". J. Engng. Mech. Div., ASCE, V.102, No. EM2, pp. 331-344.
- Bazant, Z. P., and Cedolin, L. (1979). "Blunt Crack Band Propagation in F. E. Analysis", J. Engng. Mech. Div., ASCE, V. 105, No.EM2, Proc. paper 1452, pp. 297-315.
- Bazant, Z.P., and Cedolin L. (1980). "Fracture Mechanics of Reinforced Concrete", J. Engng Mech. Div., ASCE 106, pp. 1287-1306.
- Bazant, Z.P. (1983). "Comment on Orthotropic Models for Concrete and Geomaterials", Journal of Engineering Mechanics Division, ASCE, V. 109, No. 3, pp. 849-865.
- Bazant, Z. P., and Cedolin, L. (1983). "Finite Element Modelling of Crack Band Propagation", J. Struct. Engrg., ASCE, V. 109, No.ST2, pp. 69-92.
- Bazant, Z. P., and Oh, B.H. (1983). "Crack Band Theory for Fracture of Concrete", Material and Structures, V. 16, No. 93, pp. 155-177.
- Bazant, Z. P. (1986). "Mechanics of Distributed Cracking", Appl. Mech. Rev., ASME, V. 39, No.5, pp. 675-705.
- Bazant, Z. P., Pan, J., and Pijaudier-Cabot, G. (1987). "Softening in R C Beams and Frames". J. of Structural Engineering, V. 113, No. 12, pp. 2333-2347.
- Bazant, Z. P., and Lin, F. B. (1988). "Nonlocal Smeared Cracking Model for Concrete Fracture", J. Struct. Eng., ASCE, V. 114, No. 11, pp. 2493-2510.
- Bazant, Z.P., and Ozbolt, J. (1990). "Nonlocal Microplane Model for Fracture, Damage, and Size Effect in Structures", ASCE, J. Engng Mech., vol.116, No.11.
- Bazant, Z. P. (1992). "Fracture Mechanics of Concrete Structures", First International Conference on Fracture Mechanics of concrete structures, Colorado, USA, 1-5 June 1992.
- Bazant, Z.P., and Li, Z. (1995). "Modulus of Rupture: Size Effect to Fracture Initiation in

- Boundary Layer", ASCE, Journal of Structural Engineering, V. 121, No. 4, pp. 739-746.
- Becker, J. M. (1967). "Inelastic Analysis of Reinforced Concrete Frames", M. Sc. Thesis, Cornell University.
- Beeby, A.W. (1968). "Short-Term Deformations of Reinforced Concrete Members", Cement and Concrete Association, Technical Report TRA 408, London.
- Bello, H. (1992). "Nonlinear Finite Element Analysis of Planar R C Structures", M.Eng. Project Report, Department of Civil Engineering and Applied Mechanics, McGill University, Montreal.
- Bertero, V.V., and Felippa, C. (1964). Discussion on "Ductility of Concrete", Proceedings of the International Symposium on Flexural Mechanics of Reinforced Concrete, Miami, Florida, Nov. 1964, ASCE 1965-50, ACI SP-12, PP. 227-234.
- Bigaj, A., and Walraven, J.C. (1993). "Size Effect on Rotational Capacity of Plastic Hinges in Reinforced Concrete Beams", CEB Bull. Inf., No. 218.
- Bosco, C., Carpinteri, A., and Debernardi, P.G. (1990). "Fracture of Reinforced Concrete: Scale Effects and Snap-Back Instability", Engng. Fracture Mechanics, V. 35, pp. 665-677.
- Bosco, C., and Debernardi P.G. (1993). "Influence of Some Basic Parameters on the Plastic Rotation of Reinforced Concrete Elements", CEB Bull. d' Inf., No. 218, pp. 25- 44.
- Branson, D.E., (1977). "Deformation of Concrete Structures", McGraw-Hill, New York.
- Branson, D.E. (1963). "Instantaneous and Time-Dependent Deflections of Simple and Continuous Reinforced Concrete Beams", H P R Publication 7, Part 1, pp. 1-78, Alabama Highway Department, Bureau of Public Roads.
- Burnett, E.F.P. (1973). "Rotation Capacity of Reinforced Concrete Flexural Elements", Symposium on Inelasticity and Nonlinearity in Structural Concrete, University of Waterloo, Waterloo, Ontario, Canada, 1972, SM Study 8, University of Waterloo Press, pp. 181-210.
- Carrasquillo, R.L., Nilson, A.H., and Slate, F.O. (1981). "Properties of High Strength Concrete Subject to Short-Term Loads", ACI Journal, V. 78, No. 3, pp. 171-178.
- Cauvin, A. (1983). "Nonlinear Analysis of P.C. Continuous Beams and Frames", International Symposium on Nonlinearity and Continuity in Prestressed Concrete, Preliminary Publication, Vol. 2, University of Waterloo, Waterloo, Ontario, Canada, pp. 107-124.
- CEB (1961), Levi, F. "Work of the European Concrete Committee", ACI Journal, Proceedings V 57, No. 9, pp. 1041-1070.
- CEB (1968). Commission IV, New 1968 Version Worked out by Commission IVb,

- "Deformations", Portland Cement Association, Foreign Literature Study 547.
- CEB-FIP (1978), "Model Code for Concrete Structures", Paris.
- CEB-FIP Model Code 1990- Chapter 1-3, Final Draft. CEB Bull.d' Inf., 1991, No. 203.
- Cedolin, L., Crutzen, Y.R.J., and Dei Poli, S. (1977). "Triaxial Stress-Strain Relationship for Concrete", Journal of Engineering Mechanics Division, ASCE, 103(EM3), pp. 423-439.
- Cervenka, V. (1970). "Inelastic Finite Element Analysis of Reinforced Concrete Panels Under In-plane Loads", Ph. D. Dissertation, Department of Civil Engineering, University of Colorado.
- Cervenka, V. (1985). "Constitutive Model for Cracked Reinforced Concrete", Journal of the American Concrete Institute, V. 82, No. 6, pp. 877-882.
- Chan, W.W.L. (1955). "The Ultimate Strength and Deformation of Plastic Hinges in Reinforced Concrete Frameworks", Magazine of Concrete Research, V. 7, No. 21, pp. 121-132.
- Chan, W.W.L. (1962). "The Rotation of Reinforced Concrete Plastic Hinges at Ultimate Load", Magazine of Concrete Research, V. 14, No. 41, pp. 63-72.
- Chandrasekhar, C.S. and Falkner, H.A. (1974). "Influence of the Width of Loading Plate on the Rotation Capacity of Reinforced Concrete Members", Journal of the ACI, pp. 49-54.
- Chen, W.F. (1982). "Plasticity in Reinforced Concrete," McGraw-Hill, New York, USA.
- Chinniah, J. (1985). "Finite Element Formulations for Thin Plates and Shell Structures", Ph.D thesis, Department of Mechanical and Aeronautical Eng., Carleton University, Ottawa.
- Choi, C. K., and Kwak, H.G. (1990). "The Effect of F.E. Mesh Size in Nonlinear Analysis of R. C. Structures", Computer & Structures, V. 36. No. 5, pp. 807-815.
- Chung, W., and Ahmad, S.H. (1994). "Model for Shear Critical High-Strength Concrete Beams", ACI Structural Journal, V. 91, No. 1, pp. 31-41.
- Cohn, M.Z. (1969). "Limit Design for Reinforced Concrete Structures: An Annotated Bibliography", Solid Mechanics Division, University of Waterloo, Report No. 12, Ontario, Canada.
- Cohn, M.Z, and Riva, P. (1991), "Flexural Ductility of Structural Concrete Sections", PCI Journal, V. 36, No. 2, pp. 72-87.
- Cohn, M.Z. (1964), "Rotation Compatibility in the Limit Design of Reinforced Concrete Continuous Beams", Proceedings of the International Symposium on Flexural Mechanics of Reinforced Concrete, Nov. 1964, ASCE-ACI, Miami, pp. 359-382.

- Cohn, M.Z. (1968). "Limit Design of R C Frames", Proceedings, ASCE, V. 94, No. ST. 10, pp. 2467-.
- Cohn, M.Z. (1965). "Optimum Limit Design for R C Continuous Beams", Proceedings ICE, V. 30, pp. 675-707.
- Cohn, M.Z., and Franchi, A. (1979). "STRUPL: A Computer System for Structural Plasticity", ASCE Journal of the Structural Division, V. 105, No. ST 4, pp. 789-804.
- Collins, M.P., Mitchell, D., MacGregor, J. G. (1993), "Structural Design Considerations for High-strength Concrete", Concrete International, the Magazine of ACI, pp. 27-34.
- Collins, M.P., and Mitchell, D. (1991). "Prestressed Concrete Structures", Prentice-Hall Inc., England Cliffs, New Jersey, 766 pp.
- Collins, M.P., and Porasz, A. (1989). "Shear Design for High Strength Concrete", CEB Bulletin d'Information, No. 193, pp. 77-83.
- Cope, R.J., Rao, P.V., and Clark, L.A. (1979). "Nonlinear Design of Concrete Bridge Slabs Using Finite Element Procedures", CSCE-ASCE-ACI-CEB International Symposium, University of Waterloo, Ont., pp. 331-357.
- Cope, R.J., Rao, P.V., and Clark, L.A. (1980), "Modelling of Reinforced Concrete Behaviour for Finite Element Analysis of Bridge Slabs", Numerical Methods for Nonlinear Problems, C. Taylor et al., Vol. 1, Pineridge Press, Swansea, U. K., pp. 457-470.
- Corley, W.G., and Sozen, M.A. (1966). "Time-Dependent Deflections of Reinforced Concrete Beams", ACI Journal, Proceeding 63,3, pp. 373-386.
- Corley, W.G. (1966). "Rotation Capacity of Reinforced Concrete Beams", Proceedings of the ASCE Structural Journal, V. 92, No. ST-4, pp. 121-146.
- Cosenza, E. (1990). "Finite Element Analysis of Reinforced Concrete Elements in a Cracked State", Comput. & Struct., V. 36, No. 1, pp. 71-79.
- Cranston, W.B., and Cracknell, J.A. (1969). "Tests on Reinforced Concrete Frames 2: Portal Frames with Fixed Feet", Cement and Concrete Association, London, TRA/420.
- Cranston, W. B. (1965). "A Computer Method for Inelastic Analysis of Plane Frames ". TRA 386, Cement and Concrete Association, London.
- CSA Standard. (1984). "Design of Concrete Structures for Buildings (CAN3-A23.3-M84)", Canadian Standard Association, Ontario, 281 p.
- Darvall, P.L. (1984). "Critical Softening of Hinges in Portal Frames", ASCE Journal of Structural Engineering, V. 110, No. 1, pp. 157-162.

- Darwin, D., and Pecknold, D.A. (1977). "Nonlinear Biaxial Stress-Strain Law for Concrete", ASCE Journal of the Engineering Mechanics Division, V. 103, No. EM4, pp. 229-241.
- Darwin, D. (1985). "Concrete Crack Propagation - Study of Model Parameters", Proc. F.E. Analysis of R. C. Structures, eds. Meyer, C., and Okamura, H., ASCE, New York, pp. 184-203.
- Darwin, D., and Pecknold, D.A. (1976). "Analysis of R C Shear Panels Under Cyclic Loading," ASCE Journal of the Structural Division, V. 102, No. ST2, pp. 355-369.
- Desai, C. S. and Abel, J. F. (1972). "Introduction to the Finite Element Method, a Numerical Method for Engineering Analysis", Van Nostrand Reinhold Company, New York.
- El-Metwally, S.E., and Chen, W.F. (1989). "Nonlinear Behaviour of R/C Frames", Computers & Structures, V. 32, No. 6, pp. 1209-1989.
- El-Metwally, S.E.E. (1994). "Method of Segment Length for instability Analysis of reinforced Concrete Beam-Columns", ACI Structural Journal, V. 91, No. 6, pp. 666-677.
- Eligehausen R., Fabritius E., Li L., and Zhao R. (1993). "An Analysis of Rotation Capacity Tests", CEB Bull. d' Inf., No. 218.
- Eligehausen R., and Langer P. (1987a). "Rotation Capacity of Plastic Hinges and Allowable Degree of Moment Redistribution", CEB Bull. d' Inf., No. 175.
- Eligehausen R., and Langer P. (1987b), "The Rotation Capacity of Plastic Hinges in Reinforced Concrete Beams and Slabs", CEB Bull. d' Inf., No. 178/179.
- Ernst, G.C., Smithe, G.M., Riveland, A.R and Pierce, D.N. (1973). "Basic Reinforced Concrete Frame Performance Under Vertical and Lateral Loads", ACI J.70, pp. 261-269.
- Gaston, J. R., and Siess, C. P. and Newmark, N. M. (1952). "An Investigation of the Load-Deformation Characteristics of Reinforced Concrete Beams up to the Point of Failure", Structural Research Series, No. 40, University of Illinois, Urbana.
- Gerstle, K.H. (1981). "Simple Formulations of Biaxial Concrete Behaviour", Journal of the American Concrete Institute, V. 78, No. 1, pp. 62-68.
- Ghoneim, G.A.M., and Ghali, A. (1982). "Nonlinear Analysis of Concrete Structures." Canadian J. Civ. Engrg., V. 9, No. 3, pp. 489-501.
- Ghoneim, G. A. M. (1978). "Nonlinear Analysis of Concrete Structures", Ph.D Thesis, Department of Civil Engineering, University of Calgary, Calgary, Canada.
- Ghosh, S.K. (1971). Discussion of "Effects of Reinforcements on Ductility of Concrete", by Shah S.P. and Rangan B.V. , Journal of Structural Division, ASCE, Vol. 97, No. ST3, pp. 988-995.

- Ghosh, S.K. (1972). "Some Aspects of Non-Linear Analysis of Reinforced Concrete Continuous Beams", Ph.D. Thesis, University of Waterloo.
- Gilbert, R.I., and Warner, R.F. (1978). "Tension Stiffening in R C Slabs". J. Struct. Div., ASCE 104, pp. 1885-1900.
- Glanville, W.H., and Thomas, F.G. (1935). "The Redistribution of Moments in Reinforced Concrete Beams and Frames", J. of the Institution of Civil Engineers, V. 3, No. 5061.
- Gopalaratnam, V. S., and Shah, S. P., (1985). "Softening Response of Plain Concrete in Direct Tension", ACI Journal, pp. 310-323.
- Granholm, H. (1965). "A General Flexural Theory of Reinforced Concrete", John Wiley & Sons, New York.
- Grossman, J.S. (1981). "Simplified Computations for Effective Moment of Inertia I_e and Minimum Thickness to Avoid Deflection Computations," ACI Journal, Proceedings V. 78. No. 6, pp.423-439.
- Gunnin, B. Rad, F. and Furling, R. (1977). "A General Non-Linear Analysis of Concrete Structures and Comparison with Frame Tests", Computers and Structures, V. 7, pp. 257-265.
- Gupta, A. K., and Akbar, H. (1984). "Cracking in Reinforced Concrete Analysis," ASCE Journal of the Structural Division, V. 110, No. 8, pp. 1735-1746.
- Hadj-Arab, A. (1987). "Behaviour of a One-cell Prestressed Concrete Box Girder Bridge-Experimental Study", M.Eng. thesis, Department of Civil and Applied Mechanics, McGill University, Montreal, Que.
- Hanna, Y.G. (1983). "Finite Element Modelling of Reinforced Concrete Structures", Ph.D. Thesis, Department of Civil Engineering and Applied Mechanics, McGill University, Montreal.
- Hanna, Y.G., and Mirza, M.S. (1983). "Post-Cracking Behaviour of Planar Concrete Structures," Canadian Structural Concrete Conference, Ottawa, Ont., pp. 107-127.
- Hillerborg, A. (1989). "The Compression Stress-Strain Curve for Design of Reinforced Concrete Beams", Fracture Mechanics: Application to Concrete, ACI SP-118.
- Houde, J. (1973). "Study of Force-Displacement Relationships for the Finite-Element Analysis of Reinforced Concrete", Ph.D. Thesis, Department of Civil Engineering and Applied Mechanics, McGill University, Montreal.
- Hsu, C.T. (1974). "Behaviour of Structural Concrete Subjected to Biaxial Flexure and Axial Compression", Ph.D. Thesis, Department of Civil Engineering and Applied Mechanics, McGill University, Montreal.

- Razaqpur, A.G., Nofal, M., and Mirza, M.S. (1989). "Nonlinear Analysis of Prestressed Concrete Box Girder Bridges Under Flexure", *Canadian Journal of Civil Engineering*, V. 16, No. 6, pp. 845-853.
- Razaqpur, A.G., and Nofal, M. (1990). "Analytical Modelling of Nonlinear Behaviour of Composite Bridges", *ASCE Journal of the Structural Division*, V. 116, No. ST6, pp. 1715-1733.
- Risha, W.A. (1991). "Analysis and Design of Reinforced Concrete Coupled Structural Walls", M.Eng. Project Report, Department of Civil Engineering and Applied Mechanics, McGill University, Montreal.
- Riva, P., and Cohn, M.Z. (1990), "Engineering Approaches to Nonlinear Analysis of Concrete Structures", *ASCE J. Struct. Engng. Div.*, V. 116, No. 8, pp. 2162-2186.
- Riva, P., and Cohn, M.Z. (1994). "Rotation Capacity of Structural Concrete Members". *Magazine Concrete Research*, V. 46, No. 168, pp. 223-234.
- Riva, P. (1988). "Engineering Approaches to Nonlinear Analysis of Concrete Structures", Ph.D. Thesis, Dept. of Civil Engineering, University of Waterloo, Waterloo, Ontario, Canada.
- Rots, J. G., Nauta, P., Kusters, G. M. A. and Blaauwendraad, J. (1985). "Smearred Crack Approach and Fracture Localization in Concrete", *HERON*, V.30, No.1.
- Rots, J. G. (1988), "Computational Modelling of Concrete Fracture", Ph. D. Dissertation, Civil Engineering Department, Delft University of Technology, Delft, The Netherlands.
- Sader, W.H. (1967). "Ultimate Strength of Single Bay One Storey Reinforced Concrete Frames Subjected to Horizontal and Vertical Loading", M.Eng. Thesis , McGill University.
- Saenz, L.P. (1965). "Equation for the Stress-Strain Curve of Concrete in Uniaxial and Biaxial Compression of Concrete", *ACI Journal*, V. 61, No. 9, pp. 1229-1235.
- SAS User's Guide (1982). "Statistical Analysis System", SAS Institute Inc., Cary, North Carolina, USA.
- Sawyer, H.A. (1964). "Design of Concrete Frames for Two Failure States", *Proceedings of the International Symposium on Flexural Mechanics of Reinforced Concrete*, ASCE-ACI, Miami, pp. 405-431.
- Sawyer, H.A., Stephens, j., and Alling, E.S. (1956). "The Behavior of Under-reinforced Concrete Beams under Long-term Loads", Publication No. 2, Engnrg. Experiment sta., Univ. of Connecticut, 32 p.
- Scanlon, A., Philips, D.V., and Green, D.R. (1986). "Tests on Reinforced Concrete Specimens for Calibrating Finite Element Models", *Cement and Concrete Association Research Seminar on the Behaviour of Concrete Structures*, Slough, U.K.

- Scanlon, A. (1971). "Time Dependent Deflections of Reinforced Concrete Slabs", Ph. D. Dissertation, University of Alberta, Edmonton, Canada.
- Scholz, H. (1993), "Deflection and Ductility of Continuous R C Beams", Magazine of Concrete Research, V. 45, No. 164, pp. 197-202.
- Scordelis, A.C. (1972). "Finite Element Analysis of Reinforced Concrete Structures", Proceedings, Specialty Conference on Finite Element Methods in Civil Engineering, Montreal, pp. 71-113.
- Scott, B.D., Park R., and Priestly, M.J.N. (1982). "Stress-Strain Behaviour of Concrete Confined by Overlapping Hoops at Low and High Strain Rates", ACI Journal, V. 79, No. 1, Jan./Feb., pp. 13-27.
- Shah, S.P., and Ahmad, S.H. (1994). "High Performance Concrete: Properties and Applications", McGraw-Hill Inc., New York, USA.
- Shah, S.P., and Rangan, B.V. (1970). "Effects of Reinforcements on Ductility of Concrete", ASCE Journal of Structural Division, V. 96, No. ST-6, pp. 1167-1184.
- Shaikh, M.F., Mirza, M.S., and McCutcheon, J.O. (1971). "Limit Analysis of Reinforced Concrete Frames", Transactions of the Engineering Institute of Canada, V.14, No. A-6.
- Shareef, S.S., and Buyukozturk, O. (1983). "Constitutive Modelling of Concrete in Finite Element Analysis", Research Report No. R83-16, Department of Civil Engineering, Massachusetts Institute of Technology, Cambridge, MA.
- Shariatmadar, H. (1992). "An Investigation of Seismic Response of Connections in Precast Concrete Double-Tees", M.Eng. Thesis, Department of Civil Engineering and Applied Mechanics, McGill University, Montreal.
- Shayanfar, M.A., Kheyroddin, A., and Mirza, M.S. (1993). "Finite Element Size Effect in Nonlinear Analysis of R C Structures", Structural Engineering Report No. 93-3, Department of Civil Engineering and Applied Mechanics, McGill University, Montreal.
- Shayanfar, M.A., Kheyroddin, A., Mirza, M.S. (1996). "Element Size Effects in Nonlinear Analysis of Reinforced Concrete Members", Computers & Structures, London, U. K. (In press).
- Shayanfar, M.A. (1995). "Nonlinear Finite Element Analysis of Normal and High Strength Concrete Structures", Ph.D. Thesis, Department of Civil Engineering and Applied Mechanics, McGill University, Montreal.
- Shin, S.W., Ghosh, S.K., and Moren, J. (1989). "Flexural Ductility of Ultra-High-Strength Concrete Members", ACI Structural Journal, V. 86, No.4, pp. 394-400.

- Sisodiya, R.G., Cheung, Y.K., and Ghali, A. (1972). "New Finite Elements with Application to Box Girder Bridges", *Journal of the Institution of Civil Engineers*, Paper No.7479.
- Siviero, E. (1974). "Rotation Capacity of Monodimensional Members in Structural Concrete", *CEB Bull. d'Inf.*, No. 105, pp. 206-222.
- Smith, G. M., and Young, L. E. (1955). "Ultimate Theory in Flexure by Exponential Function", *J. of Am. Concr. Inst.*, V. 52, No. 3, pp. 349-359.
- Sun, C.H., Bradford, M.A., and Gilbert, R.I. (1994). "A Reliable Numerical Method for Simulating the Post-Failure Behaviour of Concrete Frame Structures", *Computers & Structures*, V. 53, No. 3, pp. 579-589.
- Swamy, R.N., and Anand, K.L. (1974). "Influence of Steel Stress and Concrete Strength on the Deflection Characteristics of Reinforced and Prestressed Beams", *Deflection of Reinforced Concrete Structures*, ACI, SP 43, pp. 443-471.
- Tasuji, M.F., and Slate, F.O., and Nilson, A.H. (1978). "Stress-Strain Response and Fracture of Concrete in Biaxial Loading," *ACI Journal*, V. 75, No.7, pp. 306-312.
- Thorenfeldt, E., Tamaszecz, A., Jenson, J.J. (1987), "Mechanical Properties of High Strength Concrete and Application in Design", *Proceedings of the Symposium on Utilization of High Strength Concrete*, Tahir, Trondheim, pp. 149-159.
- Ueda, M., and Kawai, T. (1985). "Discrete Limit Analysis of R/C Shear Walls", *Finite Element Analysis of Reinforced Concrete Structures*, ASCE, pp. 277-287.
- Vecchio, F.J. (1989), "Nonlinear Finite Element Analysis of Reinforced Concrete Membranes", *ACI Structural Journal*, pp. 26-35.
- Wang, J. L. (1970). "Matrix Methods of Structural Analysis", International Textbook Company, Penn., 2nd.
- Weaver, W.J., and Gere, J.M. (1990). "Matrix Analysis of Framed Structures", Van Nostrand Reinhold, New York.
- Yu, W.W., and Winter, G. (1960). "Instantaneous and Long-Time Deflections of Reinforced Concrete Beams Under Working Loads", *ACI Journal*, V. 57, No. 1, pp. 29-50.
- Zienkiewicz, O.C. (1983). "The Finite Element Method", 3rd Edition, McGraw-Hill Book Company, Berkshire, United Kingdom, pp. 234-240.
- Zienkiewicz, O. C., Valliappan, S., and King, I. P. (1969). "Elasto-Plastic Solutions of Engineering Problems-Initial Stress- Finite Element Approach", *International Journal for Numerical Methods in Engineering*, Vol. 1.

APPENDIX A

INPUT DATA FILE FOR THE NONLACS2 PROGRAM

INPUT DATA FILE FOR SPECIMEN (9-1) TESTED BY LESLIE ET AL. (1976)

HSC, Specimen (9-1, LS1) tested by Leslie et al., Third-Point Loading, 80 Elements, $\alpha_2=0.2$

```
105 1 0 1 0 0 0 1 1 1 3 1
2 3 0.2 0.0 2 1 0.0
0 0 0 1 0 1
0 0 1 0 0 0 0 0 1 0 0 0 0 0 0 0
0.001 0.001 0.001 0.005 0.005 0.005
0 0 0 0 0 0
28.0
30 0
1 1 1 1 1 1 1 1 1 1 1 1 1 1 1
1 1 1 1 1 1 1 1 1 1 1 1 1 1 1
1 0 0 1 1 1 0 0.0 0.0 0.0 0
2 0 0 1 1 1 0 38 0.0 0.0 0
3 0 1 1 1 1 0 76 0.0 0.0 0
4 0 0 1 1 1 0 135.17 0.0 0.0 0
5 0 0 1 1 1 0 194.33 0.0 0.0 0
20 0 0 1 1 1 0 1081.8 0.0 0.0 1
21 1 0 1 1 1 1 1141 0.0 0.0 0
22 0 0 1 1 1 0 0.0 77.50 0.0 0
23 0 0 1 1 1 0 38 77.50 0.0 0
24 0 0 1 1 1 0 76 77.50 0.0 0
41 0 0 1 1 1 0 1081.8 77.50 0.0 1
42 1 0 1 1 1 1 1141 77.50 0.0 0
43 0 0 1 1 1 0 0.0 155.0 0.0 0
44 0 0 1 1 1 0 38 155.0 0.0 0
45 0 0 1 1 1 0 76 155.0 0.0 0
62 0 0 1 1 1 0 1081.8 155.0 0.0 1
63 1 0 1 1 1 1 1141 155.0 0.0 0
64 0 0 1 1 1 0 0.0 232.50 0.0 0
65 0 0 1 1 1 0 38 232.50 0.0 0
66 0 0 1 1 1 0 76 232.50 0.0 0
83 0 0 1 1 1 0 1081.8 232.50 0.0 1
84 1 0 1 1 1 1 1141 232.50 0.0 0
85 0 0 1 1 1 0 0.0 310 0.0 0
86 0 0 1 1 1 0 38 310 0.0 0
87 0 0 1 1 1 0 76 310 0.0 0
104 0 0 1 1 1 0 1081.8 310 0.0 1
105 1 0 1 1 1 1 1141 310 0.0 0
```



```
read(55,*) 11[I5]
```

C

```
numnp = number of nodes
neltyp = number of element types (3 max)
-- quadrilateral facet shell element
-- boundary element
-- one-dimensional bar element
nquad = quadrilateral shell element type
-- 0 = QLC3 + RBE
-- plane stress + bending
-- linear n and cubic e
-- beam behaviour problems
-- 1 = RQUAD4 + IDKQ4
-- membrane + thick/thin bending
-- cubic field both n and e
-- general behaviour
ntime = number of time intervals for
time-dependent or load reversal analyses
-- 30 time intervals (max)
-- 1 for instantaneous monotonically increasing load
icreep = creep analysis indicator
-- 0 = not required
-- 1 = is required
ishrink = shrinkage analysis indicator
-- 0 = not required
-- 1 = is required
itemp = temperature analysis indicator
-- 0 = not required
-- 1 = is required
norm = convergence and divergence criteria indicator
-- 0 = force norm -- maximum allowable forces
-- Fx , Fy , Fz , Mx, My, Mz
-- 1 = displacement norm -- maximum allowable displacements
--  $\delta x$  ,  $\delta y$  ,  $\delta z$  ,  $\theta x$  ,  $\theta y$  ,  $\theta z$ 
knorm = type of norm values input
-- 0 = percentages of forces/displacement
-- 1 = actual magnitude of norm values of forces/displacements
kult = ultimate analysis indicator
-- 0 = linear/nonlinear elastic analysis
-- at one load interval
-- use 1 load step and 1 iteration
-- 1 = nonlinear inelastic analysis
kinteg = order of numerical integration
-- gauss integration grid element points
-- 1 = 1 integration point (min)
-- 2 = 2 by 2 integration points
```


C

vmax = six tolerable divergence components
 maximum permissible values
 one = x- force/displacement = 10 times elastic results (mm)
 two = y- force/displacement
 three = z- force/displacement
 four = x- moment/rotation = 15 times elastic results (rad)
 five = y- moment/rotation
 six = z- moment/rotation

CC

C READ INPUT CARD # 7 -- TIME-DEPENDENT ANALYSIS

read(55,*) 8[F10.0]

C

(days(i), i=1,ntime)
 = time in days at which time-dependent analysis required
 -- 30 times (max)
 -- 28.0 days = instantaneous analysis

CC

C READ INPUT CARD # 7-A -- LOAD STEPS AND TYPE 2 NODES LOADED

read(55,*) 2[I5]

C

nlstps = number of load steps for analysis (30 max)
 njl2 = number of type 2 nodes loaded
 -- Type 2 nodes = A different set of nodes loaded in
 load steps j-steps
 used for live loads, truck loads, etc
 different set of loads from Type 1 nodes loaded

CC

C nlstep=nlstps

CC

C READ INPUT CARD # 7-B -- OUTPUT RESULTS AT REQUIRED LOAD STEPS

read(55,*) 40[I2]

C

(lstpop(i), i=1,nlstps)
 = output results at load steps required:
 -- enter a number of 0's or 1's for every load step
 for a total equal to NLSTPS
 -- 0 not required
 -- 1 is required

CAUTION : Does not work correctly!!
 Always enter NLSTPS of 1's

CC

```
C READ INPUT CARD # 8 -- REFERENCE TEMPERATURE For ZERO STRESSES
  if(itemp .eq. 1)    omit if ITEMP = 0
  read(55,*) 8[F10.0]
```

```
C
  contemp = concrete reference temperature for zero stresses
```

```
CS
```

```
C SUBROUTINE INPUTJ
```

```
CS
```

```
C READ INPUT CARD # 9 -- NODAL POINT DATA
```

```
  read(55,*) 7[I5] 3[F10.0] [I5]
```

```
C
```

```
  n      = node number
  (id(i,n), i=1,6) = boundary conditions for degrees of freedom:
  delta x = 0 or 1
  delta y = 0 or 1
  delta z = 0 or 1
  theta x = 0 or 1
  theta y = 0 or 1
  theta z = 0 or 1
  -- 0 = unrestrained DOF
  -- 1 = restrained DOF
  x(n)   = x-coordinate -- global axes
  y(n)   = y-coordinate -- global axes
  z(n)   = z-coordinate -- global axes
  kn     = generation
```

```
CS
```

```
C SUBROUTINE ELEMK
```

```
CS
```

```
C READ INPUT CARD -- ELEMENT TYPE IDENTIFICATION
```

```
C   # 10 -- SHELL ELEMENT -- STIF1
```

```
C   (# 19 -- BOUNDARY ELEMENT -- STIF2)
```

```
C   (# 22 -- BAR ELEMENT -- STIF3)
```

```
C   Input cards required for element type(s) needed only
```

```
CR
```

```
C READ INPUT CARD # 10 -- Quadrilateral Facet Shell Element
```

```
  read(55,*) [I5]
```

```
C
```

```
  ntype(i) = element type identification
           = 1 = shell element
```

```
CS
```

```
C SUBROUTINE STIF1
```

```
CS
```

```
C READ INPUT CARD # 11 -- SHELL ELEMENT MATERIAL AND LAYER DATA
```


ecu(i) = maximum compressive strain
 gf(i) = fracture energy for concrete type number i
 --recommended value of 0.5 lb/in (0.1 N/mm)
 amagr(i) = maximum aggregate size for concrete system type number i
 --recommended value of 1.0 in (25.4 mm)

CC

C READ INPUT CARDS # 12 (c) (i), (ii), (iii), (iv), (v) -- CREEP DATA

C Omit creep input data if JCR(I) = 2 or = 0

C

if(jcr(i).eq.0) go to 300

if(jcr(i).eq.2) go to 200

C-----

read(55,*) nage(i), nser(i)

C-----

na=nage(i)

nb=nser(i)

C-----

read(55,*) (sage(i,j), j=1, na)

C-----

jj=na*nb

C-----

read(55,*) (aci(i,j), j=1, jj)

C-----

read(55,*) (w1(i,j), j=1, nb)

C-----

read(55,*) (w2(i,j), j=1,4)

CC

C READ INPUT CARDS # 12 (d), (e) -- SHRINKAGE DATA

C Omit shrinkage input data if JSH(I) = 2 or = 0

if(jsh(i).eq. 0) go to 80

if(jsh(i).eq.2) go to 80

C-----

read(55,*) (tepss(i,n), n=1, ntime)

C-----

continue

C-----

read(55,*) slump(i), size(i), rh(i)

CC

C READ INPUT CARD # 13 -- REINFORCING STEEL MATERIAL PROPERTIES

C -- NUMST (6 max)

C Omit if NUMST = 0

read(55,*) [I5] 5[F10.0]

C

APPENDIX B

INPUT DATA FILE FOR THE NAFS PROGRAM

INPUT DATA FILE FOR CONTINUOUS BEAM C3 TESTED BY ADASZKIEWICZ (1977)

Adasziewicz (Continuous Beam C3), MSA, AC3SDU, 3 Elements, Uniform Loads

```
4 3 0 1 1.00 3 1 0 1
0.001 0.001 0.005
65 65 0.15
1 41.2 3.98 28210 0.007 391.0 330 200000 7580 0.15
2 41.2 3.98 28210 0.007 391.0 330 200000 7580 0.15
3 41.2 3.98 28210 0.007 371.6 330 195000 7580 0.15
1 103.2 38.7 100 157.6 134.6 16.3 1 2
2 103.2 38.7 100 157.6 134.6 16.3 1 2
3 258.0 142 100 157.6 136.0 21.6 1 2
1 0.0 0
2 857 0
3 1714 0
4 2286 0
1 1 2 1
2 2 3 1
3 3 4 1
0
2
1 0 1 0
4 1 1 1
1 30 15
3
1 1
1 1 1.0 157.6 0 0
2 1
1 1 1.0 157.6 0 0
3 1
1 1 1.0 157.6 0 0
1.75 3.50 5.25 6.90 7.88 10.0 12.25
13.0 13.50 14.0 14.35 14.5 14.7 14.88
15.1 15.40 15.6 15.75 15.9 16.0 17.0
17.1 17.3 17.5 17.7 18.0 18.3 18.5
18.7 19.0 19.3 19.5 19.7 20.0 21.0
0
```

```
CSXXXXXXXXXXXXXXXXXXXXXXXXXXXXXXXXXXXXXXXXXXXXXXXXXXXXXXXXXXXXXXXXXXXX
C MAIN PROGRAM
CSXXXXXXXXXXXXXXXXXXXXXXXXXXXXXXXXXXXXXXXXXXXXXXXXXXXXXXXXXXXXXXXXXXXX
C READ INPUT CARD # 1 -- TITLE HEADING IDENTIFICATION CARD
```


C READ INPUT CARD # 8 -- NUMBERING OF MEMBERS

read(*,*) 4[I5]

C

i = member number
jc(i) = near end
kc(i) = far end
kzh(i) = from of story

CC

C READ INPUT CARD # 9 -- BOUNDARY CONDITION OF MEMBERS

read(*,*) [I5]

C

nbm = number of members with boundary condition

CC

C READ INPUT CARD # 10 -- BOUNDARY CONDITION OF MEMBERS

read(*,*) 3[I5]

C omit if NBM = 0 & all end members are prescribed, if nbm = 0

i3 = member number
jfm(i3) = boundary condition (near end)
kfm(i3) = boundary condition (far end)
0: free
1: prescribed

CC

C READ INPUT CARD # 11 -- JOINT BOUNDARY CONDITIONS

read(*,*) [I5]

C

nbn = number of boundary nodes

CC

C READ INPUT CARD # 12 -- JOINT BOUNDARY CONDITIONS

read(*,*) 4[I5]

C omit if NBN = 0

i5 = joint number
ifx(i5) = displacement in x direction
ify(i5) = displacement in y direction
ifr(i5) = rotation about z direction
0: free (unrestrained DOF)
1: prescribed (restrained DOF)
2: flexible support (spring)
3: known displacement

CC

C READ INPUT CARD # 13 -- FLEXIBLE SUPPORT (SPRING)

read(*,*) [I5] 3[F10.5]

